Numerical studies of turbulent and separated flows

by

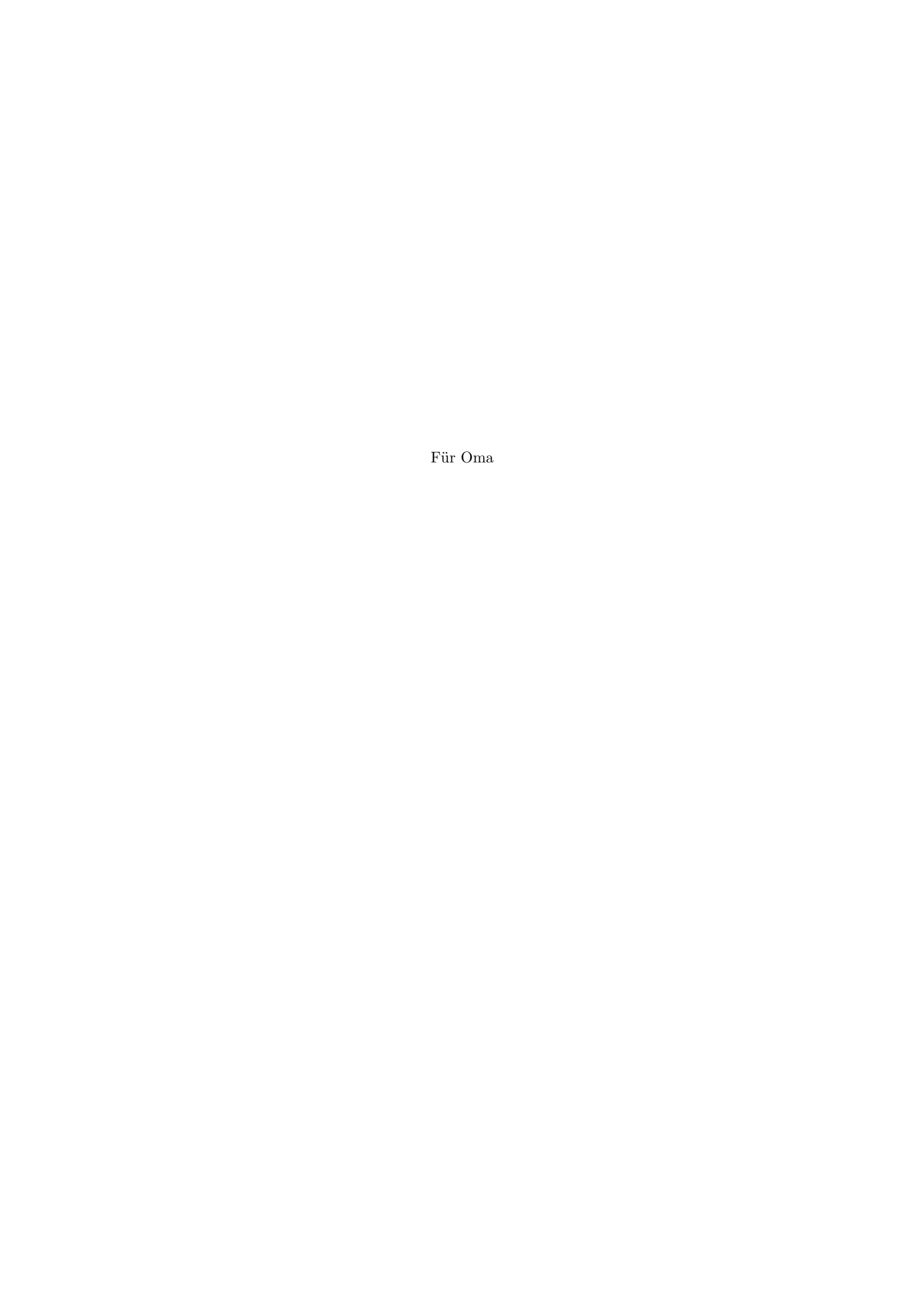
Astrid Herbst

June 2006 Technical Reports from KTH Mechanics SE-100 44 Stockholm, Sweden Typsatt i $\mathcal{A}_{\mathcal{M}}\mathcal{S}\text{-}\mathbb{I}^{A}T_{E}X.$

Akademisk avhandling som med tillstånd av Kungliga Tekniska Högskolan i Stockholm framlägges till offentlig granskning för avläggande av teknologie doktorsexamen fredagen den 16:e juni 2005 kl 10.15 i sal F3, F-huset, Kungliga Tekniska Högskolan, Lindstedsvägen 26, Stockholm.

©Astrid Herbst 2006

Universitetsservice US-AB, Stockholm 2006



Numerical studies of turbulent and separated flows

Astrid Herbst 2006

KTH Mechanics SE-100 44 Stockholm, Sweden.

Abstract

The numerical simulation of time-dependent, inherently three-dimensional flow problems has been employed as a useful and accurate means for prediction and understanding of flow configurations. In particular, direct numerical simulations (DNS) and large-eddy simulations (LES) of highly intermittent flows exhibiting separation and of a turbulent wall jet are performed. For technological applications turbulent flows encountering pressure-driven separation are of great interest. One example of the occurrence of adverse pressure gradients is the flow in the diffuser-like air intake of a modern aircraft, where flow control may be beneficial to improve the flow quality.

As a first step, the effect of periodic excitation on the turbulent boundary layer flow over a flat plate separating due to an adverse pressure gradient is studied as a model problem and investigated through direct numerical simulations. The flow can be forced to remain attached by applying time-periodic perturbation for a certain frequency range at sufficiently high amplitudes. The results show that control with a spanwise periodic input is more effective than with a spanwise homogeneous control input. As a further extension the pressure-induced separation of a turbulent boundary layer on a semi-infinite swept flat plate is studied without periodic forcing.

Going towards a more complex flow geometry exhibiting pressure-driven separation, we consider the planar asymmetric diffuser using LES. A resolution check has been performed highlighting the broad range of the relevant temporal and spatial scales and thus the sensitivity of the simulation results to the computational grid. Regarding the flow physics, the effect of different Reynolds numbers of the inflowing, fully turbulent channel flow on various flow quantities has been studied. The results consistently show that by increasing the Reynolds number a clear trend towards a larger separated region is evident; at least for the studied, comparably low Reynolds-number regime.

Further, the first direct numerical simulation of a turbulent wall jet is performed following the flow through the transition region to its downstream turbulent part. A weak subharmonic behaviour in the transition region is revealed by animations of the flow. Despite the low Reynolds number and a comparably short computational domain, the turbulent flow exhibits a reasonable self-similar behaviour, which is most pronounced in the near-wall region using inner scaling.

Descriptors: Boundary layer, turbulent separation, direct numerical simulation, large-eddy simulation, plane asymmetric diffuser, wall jet.

Preface

This thesis considers numerical simulations in turbulent and separated flows. The thesis is divided in two parts, the first part consists of a short introduction to the field and a summary of the following papers. The papers are re-set in the present thesis format and included in the second part of the thesis.

- **Paper 1.** HERBST, A. H.& HENNINGSON, D. S. 2006 The influence of periodic excitation on a turbulent separation bubble. *Flow, Turbulence and Combustion* **76**, 1-21.
- **Paper 2.** HERBST, A. H., DEUBELBEISS, S., SPEHR, S., HANIFI, A. & HENNINGSON, D. S. 2005 Instability characteristics of harmonic disturbances in a turbulent separation bubble. *Proceedings of XVII Congresso AIMETA di Mechanica Teorica e Applicata*.
- **Paper 3.** HERBST, A. H., BRANDT, L. & HENNINGSON, D. S. 2006 The effect of the sweep angle on the turbulent separation bubble on a flat plate. *Internal report*.
- **Paper 4.** HERBST, A. H. , SCHLATTER, P., & HENNINGSON, D. S. 2005 Simulations of turbulent flow in a plane asymmetric diffuser. *Submitted to Flow, Turbulence and Combustion.*
- **Paper 5.** Levin, O., Herbst, A. H. & Henningson, D. S. 2005 Early turbulent evolution of the Blasius wall jet. *Submitted to Journal of Turbulence in a revised version*.

Division of work between authors

The first paper is on the influence of periodic excitation on a turbulent separation bubble separating from a flat plate due to an adverse pressure gradient. The direct numerical simulations were performed with a numerical code which has already been used in various research projects. The code is based on a pseudospectral technique and originally developed at the Department of Mechanics (DM) by Anders Lundbladh, Arne Johansson and Dan Henningson (DH). The numerical implementations needed for this work was performed by Astrid Herbst (AH). The writing was done by AH with help from DH.

The second paper highlights the instability characteristics of harmonic disturbances in a turbulent separation bubble. The paper is based on the master thesis by S. Spehr with AH and DH as advisors and S. Deubelbeiss with Ardeshir Hanifi (ArH) as advisor. Additional numerical simulations were performed by AH and parts of the analysis were repeated and enhanced. The writing was done by ArH and AH.

The third paper focuses on the effect of the sweep angle on a turbulent separation bubble on a flat plate. The direct numerical simulations were performed by AH using the same simulation code as in the first paper. The analysis of the data was done by AH and Luca Brandt (LB). The figures were prepared by AH and the writing was done by LB and AH with help from DH.

The fourth paper is a numerical study of the flow in the plane asymmetric diffuser using Large Eddy Simulation. The simulations were performed by AH using a code developed at Center of Turbulence Research which was received from Hans-Jakob Kaltenbach. The code is based on a hybrid finite-difference/spectral method. The simulation code was parallelised by AH. The analysis of the data was done by AH and Philipp Schlatter (PS). The figures were prepared by AH and the writing was done by AH and PS with help from DH

The fifth paper is devoted to the early turbulent evolution of the Blasius wall jet. The numerical code for the spatial simulation, carried out by Ori Levin (OL), originates from the same source as the one used in the first paper. All the figures and animations were prepared by OL. The analysis of the statistics were performed by OL and AH. The writing was done by OL and AH with the help of DH.

Contents

Preface	vi
Part 1. Summary	1
Chapter 1. Introduction	3
Chapter 2. Governing equations and simulation techniques	5
2.1. Navier-Stokes equations	5
2.2. Simulation techniques	5
Chapter 3. Application to turbulent separated flows	8
3.1. Aspects of turbulent separated flows	8
3.2. Control of separated flows	9
3.3. Periodic excitation of a turbulent separation bubble on a flat plate	11
3.4. The effect of the sweep angle on a turbulent separation bubble on a flat plate	16
3.5. Flow in a plane asymmetric diffuser	17
Chapter 4. Application to the turbulent wall jet	24
Chapter 5. Conclusions	30
Acknowledgments	32
Bibliography	33
Part 2. Papers	37
Paper 1. The influence of periodic excitation on a turbulent separation bubble	41
Paper 2. Instability characteristics of harmonic disturbances in a turbulent separation bubble	67

x CONTENTS

Paper 3.	The effect of the sweep angle on the turbulent separation bubble on a flate plate	81
Paper 4.	Simulations of turbulent flow in a plane asymmetric diffuser	105
Paper 5	Farly turbulant avalution of the Blacius wall jet	1.45

Part 1 Summary

CHAPTER 1

Introduction

When a fluid flows over a solid body, the fluid slows down due to frictional forces. Prandtl (1904) was first to recognise that the internal friction of a fluid flow, the viscosity, is usually only important in a thin layer adjacent to the body, called the boundary layer. The state of the boundary layer flow can be laminar which can be characterised by a purely steady motion whereas a turbulent flow is characterised by continuously changing flow patterns. The mean flow of a turbulent flow has a distinct direction at the same time as apparently random fluctuations occur. The nature of these fluctuations is chaotic, i.e. the velocity field varies significantly and irregularly in position as well as in time. Under which conditions does turbulence occur? Osborne Reynolds (1883) conducted his classical experiments on the flow in a pipe and found that the state of the flow is characterised by a single non-dimensional parameter, the Reynolds number, which is a measure of the ratio between the inertial and the viscous forces in the flow. For sufficiently high Reynolds numbers, the flow in the boundary layer also becomes turbulent.

The examination of turbulent flows is not an easy task: Experimental investigations are often time and money consuming and computations are also difficult. Although the Navier-Stokes equations provide a complete description of turbulent flow, a full solution is not feasible due to the fact that a large range of scales of motion is present in turbulent flow. Towards higher Reynolds numbers, the range of scales increases. The size of the largest eddies is of the same order of magnitude as the dimensions of the flow geometry whereas our eyes can hardly resolve the smallest eddies without optical help, even though their size is large compared to molecular dimensions. On the one hand, the relevant time scale for the turbulent transport processes is the one determined by the large scales, but small scale motions are important for the dissipation of energy on the other hand. To resolve the large range of turbulent scales in both time and space, the necessary high spatial and temporal resolution requires a large computational effort.

If flow experiences a pressure rise in the direction of the flow, the boundary layer grows and the fluid is slowed down. If the pressure gradient is severe enough, flow in the reverse direction may occur in the region closest to the wall, where the momentum is the lowest. Such a separated region limits the performance in many technical applications and therefore a control acting on the flow may be needed to improve the flow quality. Important factors for

4 1. INTRODUCTION

the occurrence of backflow are the shape of the body surface and the state of the flow in the boundary layer. A turbulent boundary layer can withstand more severe pressure gradients than a laminar one without separating, but if the fluid is slowed down significantly, even a turbulent boundary layer will separate. The simulation of turbulent flow demands a high computational effort, but is even more challenging as separation is encountered. Aiming at controlling a flow for an engineering application increases the computational cost even further since applying and testing different control strategies requests additional computations.

In the present thesis, we first focus on a model problem, namely the influence of control by periodic forcing on a turbulent separation bubble. We consider boundary-layer flow over a flat plate separating due to an adverse pressure gradient which is simulated using direct numerical simulations. The influence of periodic forcing acting on this flow is investigated. An analysis considering the stability of the flow and the response to spanwise varying forcing is carried out. As a further extension the pressure-induced separation of a turbulent boundary layer on a semi-infinite swept flat plate is studied without periodic forcing. As a next step towards a more complex geometry, the turbulent flow in a plane asymmetric diffuser is studied using large-eddy simulations. The thesis also contains a study of the early turbulent evolution of the Blasius wall jet using direct numerical simulation.

CHAPTER 2

Governing equations and simulation techniques

2.1. Navier-Stokes equations

Fluid motion can be described in a mathematical way using Newton's second law of motion and a constitutive relation regarding the viscous forces fluid motion. We assume that the continuum hypothesis is valid, *i.e.* that the molecules are so small and large in number that they constitute a continuum. The relation between the stresses and rates of deformation is assumed to be linear, which is called a Newtonian fluid, such as water and air. Based upon these assumptions the set of equations describing the flow of a fluid, the Navier-Stokes equations for an incompressible fluid, reads:

$$\frac{\partial u_i}{\partial t} + u_j \frac{\partial u_i}{\partial x_j} = -\frac{1}{\rho} \frac{\partial p}{\partial x_i} + \nu \frac{\partial^2 u_i}{\partial x_j \partial x_j}, \quad i = 1, 2, 3$$
 (2.1)

where ρ denotes the density of a fluid, ν the kinematic viscosity of the fluid, u_i the velocity components and p the pressure. The summation convention over repeated indices is applied unless stated otherwise. Here we assume the density of the fluid to be constant, which results in the continuity equation for an incompressible fluid:

$$\frac{\partial u_i}{\partial x_i} = 0 \tag{2.2}$$

The above equations are appropriate when fluid velocity is low compared to the speed of sound and the temperature variations are small. For each flow problem, appropriate initial conditions and boundary conditions have to be specified. The Navier-Stokes equations are non-linear partial differential equations, hence analytical solutions are only known for a small number of laminar flow problems. For other cases one has to resort to numerical solutions.

2.2. Simulation techniques

During the last decade, the numerical simulation of time-dependent, inherently three-dimensional flow problems has been established in the research community as a useful and accurate means for prediction and understanding of complex flow configurations. In particular, numerical simulations of highly intermittent flows as e.g. flows undergoing laminar-turbulent transition or flows exhibiting separation are routinely performed yielding very appealing results when compared to experimental data sets.

The most straightforward simulation approach, referred to as direct numerical simulation (DNS), attempts to numerically solve for all relevant flow structures in both space and time. The need to simulate all scales ranging from the energetically dominant integral length scales down to the smallest, viscous scales is prohibitively expensive even for moderate Reynolds numbers Re. The Reynolds number Re was introduced in the previous chapter as a measure for the ratio between the inertial and the viscous forces in a fluid flow and can be expressed based on a characteristic length scale L such as the integral length scale and a characteristic velocity U as $Re_L = UL/\nu$. An estimate for the smallest viscous scales is the Kolmogorov scale η :

$$\eta = \left(\frac{\nu^3}{\varepsilon}\right)^{1/4} \tag{2.3}$$

where ε denotes the dissipation of the turbulent kinetic energy. For isotropic turbulence, the span of scales that at least needs to be covered by DNS can therefore be estimated as

$$\frac{L}{\eta} = \left(\frac{UL}{\nu}\right)^{3/4} = Re_L^{3/4} \tag{2.4}$$

assuming that $\varepsilon \sim U^3/L$. The number of degrees of freedom is thus proportional to $Re_L^{9/4}$. Taking into account the increasing computational effort for a time accurate solution as a function of Reynolds number, it can been concluded from this simple argument that the computational effort in DNS roughly grows as Re^3 . In particular, when dealing with wall-bounded flows, the computations are expensive (see e.g. Piomelli & Balaras (2002)). Despite the increasing computational power, performing DNS one is at present still restricted to flows in rather simple and generic geometries. Typical problems for which DNS are feasible are channel and pipe flows, boundary-layer flows as well as homogeneous turbulence. DNS is therefore mainly used as a research tool for the detailed study of fundamental processes such as laminar-turbulent transition and turbulence and for validating modelling approaches. A review on the use of DNS as a tool in turbulence research highlighting these issues can be found in Moin & Mahesh (1998).

Conversely, conventional numerical predictions of complex engineering or geophysical turbulent flows are based on the Reynolds Averaged Navier-Stokes (RANS) equations. Starting from the Navier-Stokes equations, decomposing the velocity and pressure fields into a mean and a fluctuating part and applying Reynolds averaging, an equation for the mean velocity is obtained in which the turbulence enters through the Reynolds stresses. In order to solve the resulting RANS equations, statistical turbulence models for the Reynolds stresses are needed. This approach often gives satisfactory results in practical engineering applications. Such computations can, however, only give statistical information about turbulence. The outcome of the simulations is highly model-dependent and the models used often need to be adjusted for the flow configuration under consideration. Severe limitations of existing turbulence models in non-standard

situations, in particular involving separation and laminar-turbulent transition, represent a major obstacle to reliable predictions.

For this reason, the concept of large-eddy simulation (LES) has emerged as an important tool for flows that need to be treated in an unsteady, three-dimensional manner. The fundamental idea is based on the observation that on the one hand the large-scale structures of turbulent flows vary considerably from flow to flow and that on the other hand, the small-scale turbulent structures are nearly isotropic and very universal in character and therefore relatively easy and accurate to model. In LES, only the large-scale, energy-carrying vortices of the flow are accurately resolved on the numerical grid, whereas the effect of the small-scale fluctuations on the (resolved) larger scales enters through a subgrid-scale (SGS) model. Following the traditional LES approach (Leonard (1974)), the three-dimensional Navier-Stokes equations are filtered by a primary LES filter, yielding the LES momentum equations

$$\frac{\partial \overline{u}_i}{\partial t} + \overline{u}_j \frac{\partial \overline{u}_i}{\partial x_j} = \frac{\partial \overline{p}}{\partial x_i} + \frac{1}{Re} \frac{\partial^2 \overline{u}_i}{\partial x_j \partial x_j} - \frac{\partial \tau_{ij}}{\partial x_j} , \qquad (2.5)$$

and the filtered continuity equation

$$\frac{\partial \overline{u}_i}{\partial x_i} = 0 \ . \tag{2.6}$$

Here, \overline{u}_i and \overline{p} denote the filtered velocities and pressure, respectively. To account for the effect of the non-resolved (subgrid, subfilter) scales, the unclosed subgrid-scale stresses $\tau_{ij} = \overline{u_i u_i} - \overline{u_i} \overline{u_i}$ have to be approximated with a subgrid-scale model.

In contrast to the approaches based on the Reynolds-averaged equations described above where all the deviations from the mean velocity field are modelled phenomenologically, only the part of the flow field with scales comparably small to the overall dimensions of the flow is modelled in an LES. Deardorff (1970) was first to apply LES in his pioneering work on the simulation of turbulent periodic channel flow. His approach was based on the ideas of Smagorinsky (1963). For the outcome of an LES, both the underlying numerical scheme for the solution of the large scale, energy containing vortices as well as the subgrid-scale model play an important role and are coupled with each other. Recent reviews on LES and appropriate SGS modelling are given by e.g. Lesieur & Métais (1996); Meneveau & Katz (2000) and in the monograph by Sagaut (2005). However, even for LES the computational cost increases dramatically for higher Reynolds numbers, in particular for wall-resolved LES (i.e. without resorting to wall models (Piomelli & Balaras 2002)).

CHAPTER 3

Application to turbulent separated flows

3.1. Aspects of turbulent separated flows

Separating turbulent flows are one of the main problems in engineering applications of fluid mechanics. The performance of many technical devices suffers from separation, e.g. the flow around vehicles, airfoils, and turbine blades. The design of these devices is always a trade-off. One example is the flow in the diffuser-like air intake of a military aircraft. Here due to stealth and weight considerations it is highly desirable to shorten the section where the flow is decelerating. This exposes the flow to a strong adverse pressure gradient and may lead to separation and flow in the reverse direction limiting the performance due to severe pressure losses.

Separating flows can be distinguished by the state of the boundary layer prior to separation. A turbulent separation bubble means that the boundary layer preceding the separation is turbulent, whereas laminar separation occurs when the incoming flow is laminar. However, even though the flow is laminar before detaching, transition to turbulence may happen in the separation bubble. This is usually referred to as a laminar separation bubble with turbulent reattachment. A major difference between these two categories is that due to the turbulent mixing a turbulent boundary layer can withstand much higher pressure gradients without separating than a laminar boundary layer.

Experiments and numerical simulations of flows in which separation occurs from smooth surfaces rather than induced by sharp edges or obstacles are particularly challenging. In the former case, the separation is caused by an adverse pressure gradient, either arising from geometrical constraints or due to specific freestream conditions. Alving & Fernholz (1996) point out that separation caused by step-like changes in the surface geometry is present at all Reynolds numbers while the separation of flow from a smooth surface due to an adverse pressure gradient may occur under a certain combination of parameters (pressure, gradient, speed etc.). In geometry induced separation, the point of separation is fixed at the step change, while the situation differs for a pressure gradient induced separation. Under such circumstances, both the separation and reattachment points are fluctuating strongly in both time and space. Moreover, the resulting separated flow is highly intermittent and inherently three-dimensional. The whole downstream evolution of the flow is crucially influenced by the processes happening upstream and close to the

separation point. A review highlighting these unsteady processes in separated flows is given by Simpson (1996).

For a pressure-induced separation, another distinction is made according to the magnitude of the pressure gradient. In the case of separation due to a strong adverse pressure gradient, the height of the bubble is of the same order of magnitude as the shear layer prior to separation, whereas it is significantly less for a separation due to a mild adverse pressure gradient. For the separation developing due to a strong adverse pressure gradient, the possibility exists that the flow may not reattach, so that the separation bubble is not closed. For a geometry-induced separation, Alving & Fernholz (1996) note that the height of the bubble is typically larger than the thickness of the separating shear layer.

For a turbulent separating boundary layer, the question arises on which criterion to determine the point of separation and reattachment. Based on the fraction of time that the flow moves backwards, one can define incipient detachment at the point where instantaneous backflow occurs at 1% of the time, intermittent transitory detachment for instantaneous backflow at 20% of the time and transitory detachment for instantaneous backflow at 50% of the time. Transitory detachment collapses in most cases with detachment, defined by vanishing time-averaged shear stress (see Simpson (1996)). A further possibility to define the separated area is the location of the mean dividing streamline, which has the advantage of providing a measure of the extent of the recirculation region. In a direct numerical simulation by Na & Moin (1998) of a turbulent boundary layer separating from a flat plate due to an adverse pressure gradient, similar to the flow case considered in the first paper but without periodic forcing, the separation points determined based on the definition of 50% instantaneous backflow, mean dividing streamline and vanishing mean wall shear stress are in good agreement.

3.2. Control of separated flows

Since separation is limiting the performance in many engineering applications, improved design or flow control to enhance the flow quality, prevent separation and promote reattachment is desirable. However, the idea to increase mixing to assist the flow against an adverse pressure gradient and to delay or to avoid separation is not new. Traditionally, passive control strategies have been applied to suppress separation. A passive control method extracts energy from the flow for control purposes whereas an active control strategy adds energy to control the flow. The first passive device was the vortex generator presented by Taylor (1948). A vortex generator is a rectangular or triangular platform mounted normal to the surface and with an angle to the mean flow direction creating streamwise vortices. Various other designs have been presented in the following years, mostly to delay separation and to improve performance of airfoils and diffusers. Schubauer & Spangenberg (1960) investigated the effect of several different devices on increasing the rate of mixing in turbulent boundary layers in a region of a strong adverse pressure gradient and found that their effect

was equivalent to that of a decrease of the pressure gradient while they differed considerably in effectiveness. Recently, Angele & Klingmann (2005) studied experimentally a turbulent boundary layer subjected to an adverse pressure gradient undergoing separation and reattachment and investigated the effect of passive control by the means of vortex generators and the influence on the turbulent structures of a separating boundary layer.

Other passive control techniques include a permeable reattachment surface, which was investigated by Heenan & Morrison (1998) in the case of turbulent flow downstream a backward-facing step. The influence of surface ribs or groves on the turbulent flow over a backward-facing ramp was examined by Selby et al. (1990). Kalter & Fernholz (1995, 2001) studied the effect of free-stream turbulence on a closed separation bubble and were able to eliminate the separation bubble by a substantial increase in the freestream turbulence level.

Separation control by periodic forcing is attractive because it is an active control strategy affecting the flow at constant mass-flow rate. Periodic excitations have been studied as a means to influence separated flows in various geometries, mainly experimentally. Greenblatt & Wygnanski (2000) review the control of flow separation by periodic excitation as well as control and exploitation of airfoil and diffuser flows, including three-dimensional and curvature effects. Important parameters such as the optimum reduced frequencies and excitation levels are discussed. However, the main focus is on flows which do not reattach unconditionally, e.g. the flow over a deflected flap, which has been studied earlier by Nishri & Wygnanski (1998). Among the naturally reattaching, separated flows, a lot of work concerning the effect of periodic excitations has been carried out on flows where the point of separation does not fluctuate in time but is fixed due to a sudden change in geometry. The backward-facing step is the simplest configuration of this type of flow. Roos & Kegelman (1986) studied the excitation of the flow over a backward-facing step by an oscillating flap positioned at the point of shear-layer separation. The reattachment length was shortened depending on the Reynolds number up to 30% due to the momentum transfer by the vortical structures. The influence of periodic excitations imposed by blowing and suction on this flow was studied experimentally by Yoshioka (2001). He found that large-scale co-rotating spanwise vortices introduced into the shear layer due to the forcing cause an increase in the Reynolds stresses. For the optimum forcing frequency the separated region was shortened by 30 percent. Sigurdson (1995) studied experimentally the effect of periodic velocity perturbations on the separation bubble downstream of the sharp-edged blunt face of a circular cylinder. Forcing at frequencies below the one of the initial Kelvin-Helmholtz instability of the free shear layer, the reattachment length is reduced. He also gives a review on the effect of periodic excitations in various geometries. Kiya et al. (1997) investigated sinusoidal forcing at the corner of a blunt cylinder and found that the optimal frequency scales with the frequency of shedding vortices from the reattachment region of the separated shear layer. He observed that forcing at sufficiently high amplitudes eliminates the recirculation region in a range of forcing frequencies. In an asymmetric plane diffuser, Obi *et al.* (1997) found experimentally that the momentum transfer is promoted by periodic perturbations leading to earlier reattachment.

In addition to time-periodic forcing, Chun et al. (1999) varied the forcing also in spanwise direction by a tape covering parts of the slot through which blowing and suction was applied. They showed that the reattachment length could be further reduced by a suitable spanwise distribution, but the decrease was not substantial compared to the two-dimensional actuation.

Only in very few studies, more advanced control strategies have been applied to separated turbulent flows. Kang & Choi (2002) applied a systematic feedback control method to increase mixing in the large-eddy simulation of the turbulent flow behind a backward-facing step. Spatially and temporally varying blowing and suction with zero-net mass flow rate is provided at the step edge, based on the sensing of the spanwise distribution of the wall pressure fluctuations at a downstream location using a suboptimal feedback control method (see Choi et al. (1993)). The cost functional to be increased is the root-mean square spanwise pressure fluctuations, which is assumed to be associated with mixing behind the backward-facing step. Suboptimal feedback control is capable of decreasing the reattachment length up to 9.7% further than reduction achieved using two-dimensional single frequency actuation which in its turn decreases the reattachment length by up to 19.4% compared to the uncontrolled case.

3.3. Periodic excitation of a turbulent separation bubble on a flat plate

A model problem exhibiting pressure-driven separation which is feasible to study with DNS is the turbulent boundary-layer flow over a flat plate which separates from the wall due to an adverse pressure gradient. This case has been investigated up to the present date in a few studies only, e.g. by Na & Moin (1998). They found that the turbulent structures emanating upstream of the separation point move upwards into the shear layer, and are then advected around the separated region causing the maximum turbulent intensity to be found in the centre of the detached shear layer. Skote & Henningson (2002) conducted a DNS of a turbulent boundary layer separating due to a strong adverse pressure gradient. In comparison with the earlier simulations the flow had a stronger and larger recirculation region. In all studies, the turbulence was found to be intensified above the separated region while it decreased in the backflow itself.

In the first paper we focus on the turbulent boundary layer over a flat plate separating due to an adverse pressure gradient. The effect of periodic excitation on the separation bubble is studied by means of DNS. In contrast to the work by Skote & Henningson (2002), the aim is not to gain further inside into

the nature of separated turbulent flows for the sake of turbulence modelling but to study the effect of periodic excitation on a turbulent separation bubble as a model problem. The direct numerical simulations forming the basis for the first and the second paper are conducted using the same numerical code which was employed in the direct numerical simulations by Skote & Henningson (2002). The simulations of the turbulent boundary layer exposed to an adverse to favourable pressure gradient have been performed using a code developed at the Department of Mechanics by Lundbladh et al. (1999). The code uses a pseudo-spectral method with Fourier discretization in streamwise and spanwise directions and Chebyshev polynomials in the wall-normal direction similar to Kim et al. (1987). A fringe technique enables simulations of spatially developing flows while using Fourier discretization in the streamwise direction (see Nordström et al. (1999)). A fringe region is added in the end of the computational domain, in which the outflow is forced back to the inflow. The fringe region is implemented by the addition of a volume force F to the Navier-Stokes equations:

$$\frac{\partial u_i}{\partial t} + u_j \frac{\partial u_i}{\partial x_j} = -\frac{1}{\rho} \frac{\partial p}{\partial x_i} + \nu \frac{\partial^2 u_i}{\partial x_j \partial x_j} + F_i$$
(3.1)

The force

$$F_i = \lambda(x)(\tilde{u}_i - u_i) \tag{3.2}$$

is non-zero only in the fringe region. \tilde{u}_i is the laminar inflow velocity profile the solution u_i is forced to and λ the strength of the forcing. The form of the fringe function is designed to have minimal upstream influence. The time integration is carried out using a four-step low-storage third-order Runge-Kutta scheme for the nonlinear terms an a second-order Crank-Nicolson method for the linear terms. Aliasing errors from the evaluation of the nonlinear terms are removed applying the $\frac{3}{2}$ -rule when the FFTs are calculated in the wall parallel plane.

The inflow Reynolds number is $Re_{\delta_0^*} = U_\infty \delta_0^* / \nu = 400$ based on the displacement thickness δ_0^* of the boundary layer and the freestream velocity U_∞ at the inflow x=0. All quantities are non-dimensionalized by U_∞ and δ_0^* at x=0. At this position, a laminar Blasius boundary layer profile is assumed. Downstream at x=10 laminar-turbulent transition is triggered by a random volume force near the wall. The computational box is $450 \times 50 \times 24$. A resolution with 480 modes in streamwise, 193 modes in wall-normal and 64 modes in spanwise direction is used, which gives a total of 6 million points. The boundary conditions are no-slip at the wall. Due to the finite size of the computational domain, the flow domain is truncated and an artificial boundary condition is applied at the freestream.

To generate periodic excitation, we use an oscillating wall-normal body force that is centred around x_0 and exponentially decays from the wall. The force to be given by

$$F_y = f_0 e^{-y/c} e^{-[(x-x_0)/x_{scale}]^2} \cos(\omega t) \cos(\beta z) , \qquad (3.3)$$

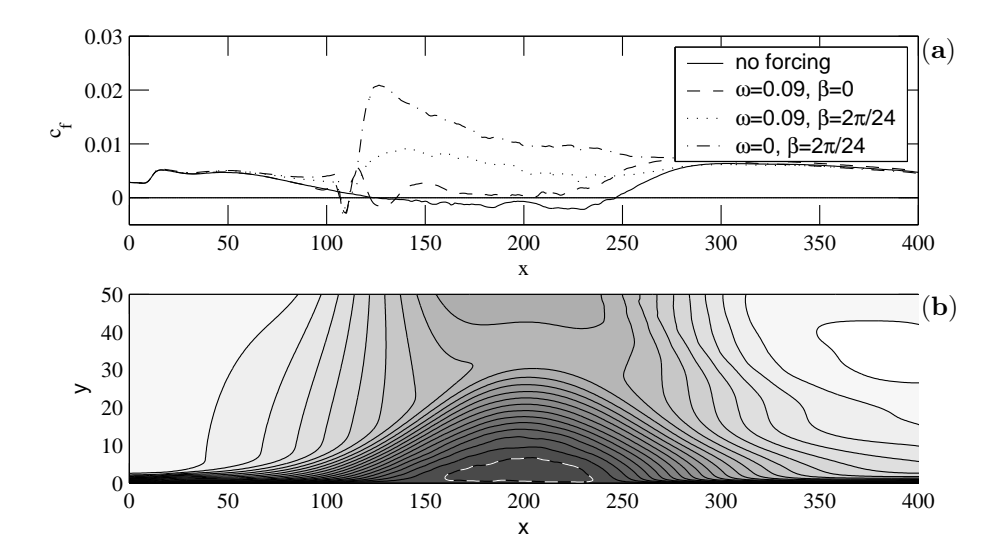


FIGURE 3.1. (a) Mean skin friction coefficient, (b) Contours of streamwise mean velocity for simulation without forcing (neg: dark grey to pos: white, white dashed line: -0.025).

where f_0 is the forcing amplitude, ω the oscillation frequency, x_{scale} a parameter controlling the decay of the forcing in x-direction and c a parameter setting the wall-normal decay. The force causes a flow in wall-normal direction. If the parameter $\beta \neq 0$, the force varies also in spanwise direction.

The contours of constant levels of the mean streamwise velocity from -0.025 to 1.025 averaged in time and spanwise direction are shown for the simulation without forcing in Fig. 3.1b. In the freestream, the streamwise velocity is decelerating between x=50 and x=200 and subsequently accelerating to the value of the freestream velocity at the inlet. This imposes an adverse to favourable pressure gradient on the boundary layer, creating a closed separation bubble. Based on the zeros of the skin-friction coefficient shown in Fig. 3.1a (solid line), the flow separates at $x_{sep}=126$ and reattaches at $x_{att}=247$ for the simulation without forcing, so the total reattachment length is $l_{sep}=121$.

The flow can be forced to remain attached in the region where separation occurs if no forcing is applied by applying time-periodic forcing centred around $x_0 = 110$ upstream of the separated region with a frequency $\omega = 0.09$. This can be seen from the skin friction coefficient in Fig. 3.1a (dashed line). A close-up of the region where the disturbances are generated is shown in Fig. 3.2a. Isosurfaces of the wall-normal velocity component illustrate the two-dimensional character of the perturbations created by the forcing. These structures decay only slowly while travelling downstream and can be seen travelling upwards in the shear layer. This way, mixing is enhanced which can be inferred from larger

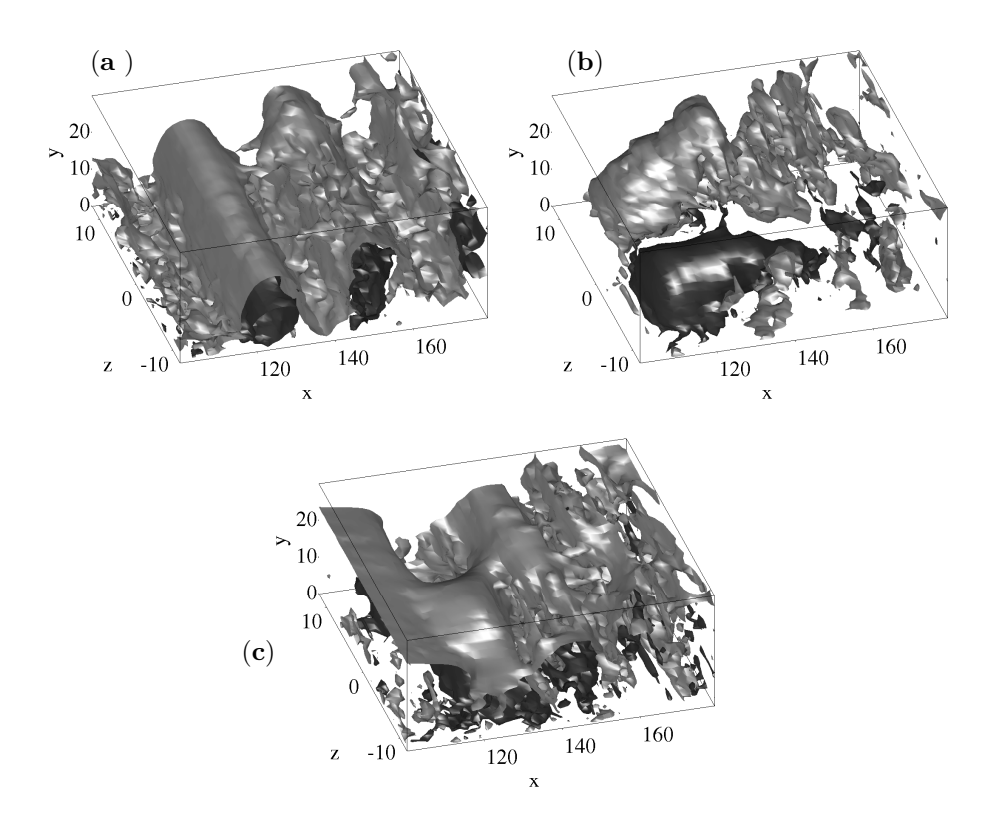


FIGURE 3.2. Instantaneous wall-normal velocity component: (a) Isosurfaces at values of +0.1 (light) and -0.1 (dark) for forcing with $\omega=0.09, \beta=0$ (b) Isosurfaces at values of +0.2 (light) and -0.2 (dark) for forcing with $\omega=0.0, \beta=\frac{2\pi}{24}$ (c) Isosurfaces at values of +0.1 (light) and -0.1 (dark) for forcing at $\omega=0.09, \beta=2\pi/24$.

root-mean-square(rms)-values of the fluctuating component (see Fig. 3.3). We found that the closer to the separation point the forcing is placed the more effective it is in suppressing separation. It is further observed that sufficiently high amplitudes are necessary in order to reduce the reattachment length, here an amplitude $f_0 = 0.1$ has been used.

However, steady spanwise forcing turned out to be very effective in eliminating the separated region. The skin friction coefficient (Fig. 3.1 a, dashed-dotted line) is affected significantly stronger if forcing varies in the spanwise direction ($\omega=0,\ \beta=2\pi/24$) with the same amplitude $f_0=0.1$ as in the time-varying case. The effect of the forcing on the flow is illustrated by the isosurfaces of the wall-normal component shown in Fig. 3.2b. The isosurfaces are displayed for a higher value of v in Fig. 3.2b than in Fig. 3.2a because of

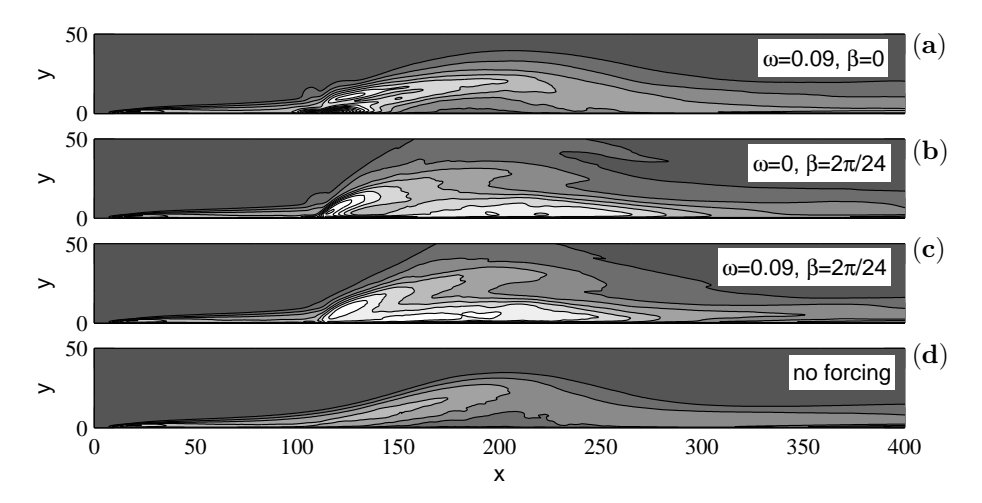


FIGURE 3.3. Contours of streamwise turbulent fluctuation (0.0 to 0.5, spacing 0.03).

the stronger effect on the flow due to the spanwise varying forcing. Even if half the forcing amplitude was used in the case with spanwise varying forcing, the flow was prevented from separating.

The influence of a forcing which varies both in time and the spanwise direction was also investigated. The value of the skin-friction coefficient for that case is shown in Fig. 3.1a (dotted line) and is located between the curves for the forcing only varying in spanwise direction and for the one only varying in time. Structures associated with both types of forcing can be seen in Fig. 3.2c. The fact that spanwise varying forcing shows to be more effective for this flow is possibly due to the low Reynolds number in the simulations. At a higher Reynolds number, time-varying forcing is expected to be more effective, since the two-dimensional disturbances are then expected to be more unstable.

A more detailed analysis considering the stability of the flow and the response to spanwise varying forcing is carried out in the second paper. The data from direct numerical simulations is analysed by means of stability theory and proper orthogonal decomposition (POD) technique (see e. g. Holmes et al. (1996)). The organised wave caused by periodic forcing is extracted by Fourier transform of the phase-averaged data. For the stability analysis, a theoretical model of harmonic perturbations is considered, including the effects of the random turbulent flow. Here, we use an eddy-viscosity approach to model the oscillations of the background Reynolds stresses caused by the organised wave. The equations are derived using the nonlocal stability theory based on the parabolic stability equation (PSE) method. The stability calculations seem to predict the decay rate of the coherent structures correctly, while the shape of disturbances is different. It should be mentioned that due to large forcing

amplitude the nonlinear effects are important in this case and may be able to explain some of the differences.

3.4. The effect of the sweep angle on a turbulent separation bubble on a flat plate

The pressure-induced separation of a turbulent boundary layer evolving over a semi-infinite swept flat plate is considered in the third paper and studied by means of DNS. This preliminary work can therefore be seen as an extension of the studies on the two-dimensional separation of a turbulent boundary layer flow over a flat plate. The subject is of interest since many flows in engineering applications are characterised by three-dimensional mean velocity fields, *i.e.* they are characterised by mean axial vorticity.

The flow under consideration is spanwise invariant: the mean velocity field is characterised by three velocity components but these can be expressed as a function of only two spatial independent variables. Therefore the spanwise derivative of any flow quantity is zero. The configuration is thus a first step in the generalisation from a two-dimensional and coplanar mean flow to the fully three-dimensional case. The spanwise invariant mean flow can still be seen as two-dimensional but it is not coplanar. The few related studies in the literature all consider three-dimensional separation induced by a rapid change in geometry, a sharp edge (e.g. Kaltenbach (2004)), and no studies on turbulent three-dimensional pressure-induced separation seem to be available. The spanwise invariant configuration is chosen because owing to the complexity of fully three-dimensional separation and to the lack of a reference co-planar case it can be difficult to isolate the effects of skewing. Therefore a systematic approach to identify the effect of increasing mean axial vorticity of the base flow is needed. In the simulations presented in the third paper, the spanwise velocity therefore is increased in two steps from zero to the value of its streamwise counterpart U, corresponding to a largest inflow sweep angle of 45°, leaving the remaining flow parameters unchanged. Apart from the introduction of the sweep, the numerical method and setup is the same as in the first paper.

It is found that the location of separation is not changed by the introduction of sweep for the angles examined. The reduction of the separated region is in agreement with previous studies on spanwise invariant three-dimensional separation, where deviations from the sweep-independence principle are observed for angles $\alpha>40^\circ$. A significant increase in the turbulent intensities in the separated region beneath the detaching shear layer and downstream of reattachment is clearly seen for the flow configuration with largest sweep angle. As observed in previous studies, it is not possible to find a universal scaling for the mean flow quantities and statistics of the turbulent fluctuations valid at all locations. However, it can be deduced from the data that , in general, the velocity C of the external streamline seems to provide the best scaling for the flow quantities at separation and inside the separated region, whereas the streamwise velocity U yields a better data collapse in the reattachment

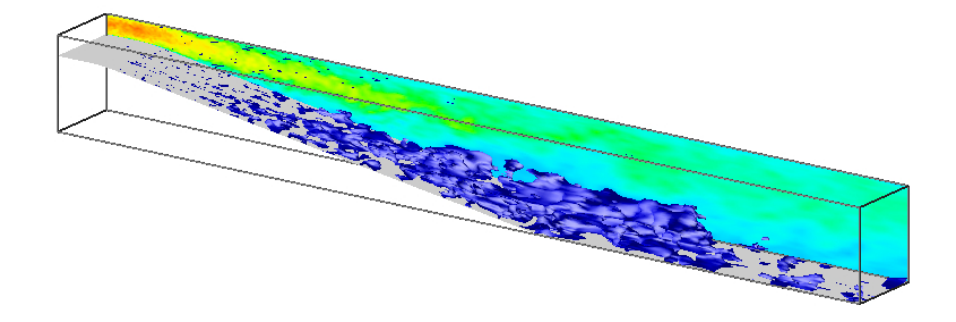


FIGURE 3.4. Isosurface (blue) of zero streamwise velocity for the full diffuser geometry, $Re_b = 9000$, and instantaneous streamwise velocity in a wall normal plane.

region. The latter can be explained by the fact that U is more directly related to the external pressure distribution. Comparison with the simulations of three-dimensional boundary layers subjected to a weak adverse pressure gradient indicates that strength of the pressure gradient, the strain rate and the occurrence of separation have a deeper impact on the turbulence structure than the skewing of the mean flow.

3.5. Flow in a plane asymmetric diffuser

Considering turbulent separation in more complex geometries than the flow case studied in the previous section, one has to resort to modelling approaches. A recent review of different modelling approaches including LES and RANS for separated flows found in industrial applications is given by Leschziner (2006). In particular, the case of turbulent separated flow in a channel with streamwise periodic constrictions, the so called periodic hill, has emerged as a benchmark case. Flow separation is induced by a smooth, yet sharp expansion of the channel, reaching an opening angle of approximately 45° after the smoothly rounded edge. Fröhlich et al. (2005) present a careful comparison of different modelling strategies, e.g. suitable SGS models, wall-functions, resolution requirements etc. Recent results on this test case are presented by Breuer et al. (2006), who compare data obtained from a number of different simulations, including various Reynolds numbers, resolutions and simulation approaches (LES, DNS).

In the fourth paper, we consider the planar asymmetric diffuser, which has already been studied in a number of numerical and experimental works as a model problem for pressure-driven separation. The pressure distribution is no longer chosen separately as in the first paper but is connected to the geometry, which is a step towards a more complex flow problem than the one studied in the first paper. The performance of diffuser-like flows occurring in many technical applications is strongly affected by separation of the boundary layer close to the wall. Therefore, a thorough understanding of the involved flow physics is necessary, especially considering additional engineering applications as, e.g.,

improved diffuser design or flow control to improve the flow quality, prevent separation and promote reattachment. The main difference of the diffuser flow studied in the fourth paper to the above mentioned periodic-hill case is that the inflow conditions are prescribed as fully-developed turbulent channel flow, and the opening angle is significantly lower (approximately ten degrees). With that, the prediction of the separation point is expected to be more sensitive to a proper modelling.

In the fourth paper, large-eddy simulations (LES) of an incompressible planar, asymmetric diffuser flow are presented. Adopting the numerical method already successfully used by Kaltenbach $et\ al.\ (1999)$, the diffuser with an opening angle of 8.5° is considered. For this configuration, recent experimental data is available at $Re_b=20000$ (Törnblom 2003). Compared to previous numerical and experimental studies, the setup is slightly modified, i.e. featuring a marginally decreased opening angle compared to the 10° angle used by Obi $et\ al.\ (1993)$ and Kaltenbach $et\ al.\ (1999)$. The change of setup is adopted in order to create a test case that is more sensitive and thus better suited to compare the results at different Reynolds numbers.

The computations of the diffuser flow are performed using a simulation code based on the hybrid second-order finite-difference/spectral method described by Kaltenbach et al. (1999). The three-dimensional Navier-Stokes equations are filtered to the grid, yielding the LES momentum equations in the primitive variables (velocity and pressure). Equations (2.1) and (2.2) are solved in generalised coordinates using central finite differences of second order in the streamwise (x) and the wall-normal (y) direction, and a Fourier collocation scheme is applied in the spanwise (z) direction. No numerical dissipation is introduced by the numerical scheme due to conservation of kinetic energy. In the wall-normal (x/y) plane a staggered mesh is used with decomposition in contravariant velocity components, whereas the spanwise velocity is computed at the pressure nodes. Dealiasing based on phase-shifting is applied in the spanwise (Fourier) direction to enhance stability and accuracy. The time integration is carried out using a standard semi-implicit low-storage three-stage Runge-Kutta/Crank-Nicolson scheme, in which the viscous terms are treated implicitly in the wall-normal direction. The continuity equation is enforced by a fractional step algorithm of second-order accuracy in time. The Helmholtz equations arising after spanwise Fourier transform are solved by a multigrid algorithm. The code has been parallelised using explicit OpenMP shared-memory directives. The calculations have been performed on the vector computers NEC SX-6 and SX-8 of the HLRS, Stuttgart, Germany.

For the present results, the dynamic Smagorinsky model (Germano et al. (1991), Lilly (1992)) has been used, and a resolution study has been performed, highlighting the broad range of the relevant scales and thus the sensitivity of the simulation results to the grids used. Extensive simulations of the diffuser have been conducted at three different Reynolds numbers, namely $Re_b = 4500$, $Re_b = 9000$ and $Re_b = 20000$ based on the bulk velocity $U_b = 1/2\delta \int_0^{2\delta} U dy$

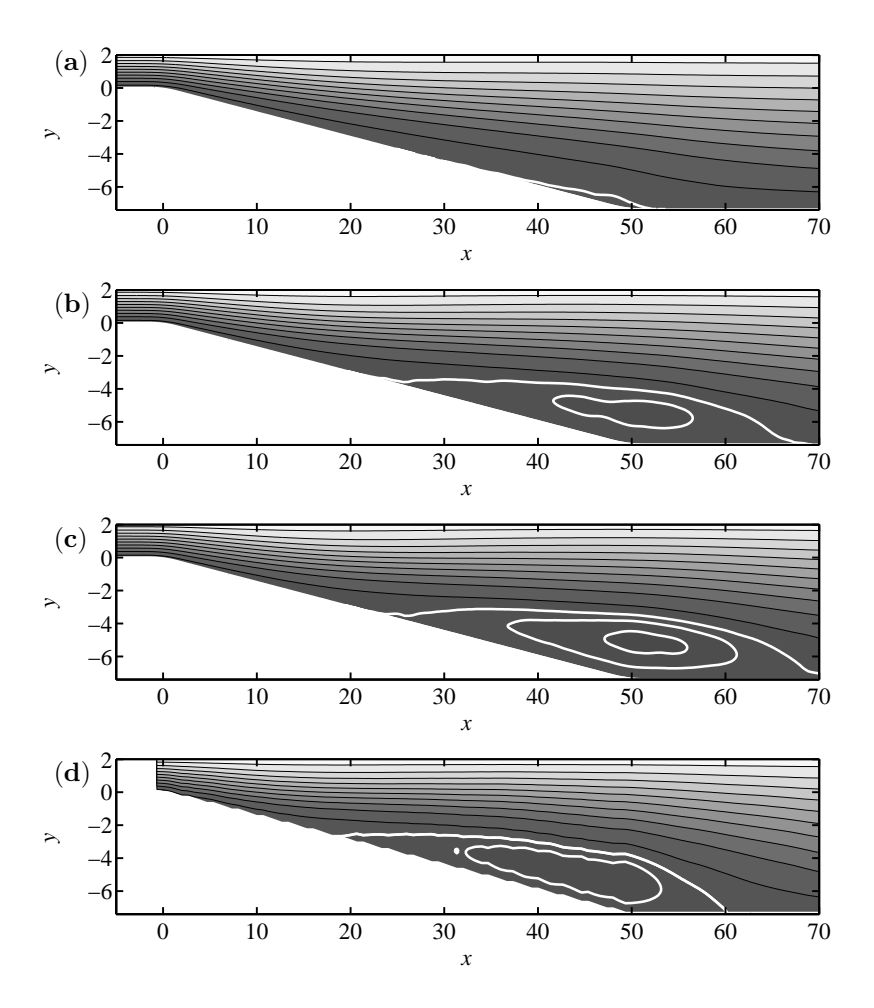


FIGURE 3.5. Reynolds-number dependence of the separation bubble visualised by contours of the stream function: (a) $Re_b = 4500$ (case L3), (b) $Re_b = 9000$ (case M3), (c) $Re_b = 20000$ (case H1), (d) Experiment by Törnblom (2003), $Re_b = 20000$. White contour levels range from -0.2 to -0.05 with spacing 0.05, black contours from 0.1 to 1.9 with spacing 0.2.

and the channel half width δ . That corresponds to a friction Reynolds number Re_{τ} of the inflowing fully-turbulent channel flow of approximately 260, 480 and 980, respectively. These Reynolds numbers are well above the critical value for laminar-turbulent transition and allow sustained turbulent channel flow.

Regarding the flow physics, we focus on quantifying the influence of the Reynolds number on various diffuser-flow characteristics, in particular the extent of the separated region, the internal layer at the upper wall and the size of the turbulent scales. To our knowledge, there is no detailed study in the literature clarifying these influences. Obi et al. (1999) studied experimentally the Reynolds-number effect on the separated flow in the Obi diffuser in the range of $Re_b \approx 2200$ to 9000. Their results show that the extent of the separated region increases with higher Re_b . There is some uncertainty in the data due to the presence of secondary flow caused by a relatively small aspect ratio in the experimental setup.

Comparing the results for $Re_b = 4500$ and $Re_b = 9000$ in Fig. 3.5a and 3.5b we find a considerable increase in the separated region for the higher Reynolds number. This trend also holds comparing the results for $Re_b = 9000$ to those of the simulation for the highest Reynolds number $Re_b = 20000$ shown in Fig. 3.5c. However the differences are much smaller between the medium and the highest Reynolds number, which might indicate that a levelling-off has been reached. At the highest Reynolds number only one simulation (H1) with a resolution corresponding to the medium resolution at the medium Reynolds number has been performed. However, it seems evident from the resolution study at $Re_b = 4500$ and $Re_b = 9000$ that the separated region increases in size with a finer computational grid. Similar trends have also been reported by Kaltenbach et al. (1999). It is therefore expected that the separation bubble at $Re_b = 20000$ will be of the same size or slightly larger if the resolution was increased even further. We thus conclude that for the studied Reynoldsnumber regime a clear trend is observed that the size of the separated region in the rear part of the expanding section of the diffuser increases with higher Reynolds number. This Reynolds-number dependence agrees well with the results reported by Obi et al. (1999).

In figure 3.6 contours of streamwise turbulent intensity are shown. Close to the inflow and in the first part of the expanding section of the diffuser one observes that the region of high turbulent intensity is more confined to the wall for higher Re_b , similar to turbulent channel flow. Further downstream, where the flow separates, the highest turbulence intensities are found in the separated shear layer just above the mean position of the bubble. This feature has also been observed for separation from a solid wall due to an adverse pressure gradient (Skote & Henningson 2002). Comparing the streamwise turbulence intensities for the different Reynolds numbers we observe that the region dominated by the features similar to those of the incoming channel flow extends further into the diffuser as the Reynolds number is increased. This indicates that the incoming channel flow penetrates further in a 'jet-like' manner into the expanding diffuser section. For the highest Reynolds number, also the turbulence intensities measured in the experiments by Törnblom (2003) at $Re_b = 20000$ are shown in Fig. 3.6d. A generally higher level of fluctuations is apparent in the experiments, however the gross features are captured reasonably well by

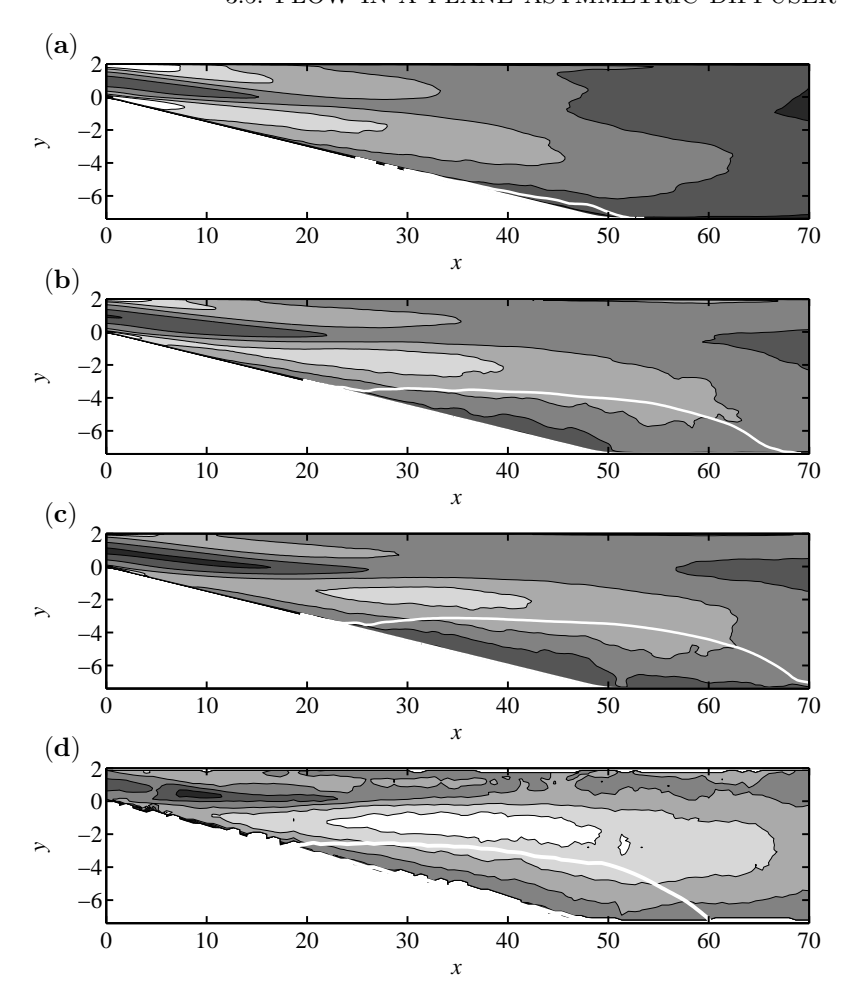


FIGURE 3.6. Reynolds-number dependence of the streamwise turbulence intensity: (a) $Re_b = 4500$, (b) $Re_b = 9000$, (c) $Re_b = 20000$, (d) Experiment by Törnblom (2003). Contour levels range from 0.0 to 0.12 with a spacing of 0.2; white: mean dividing streamline.

the LES results as seen in Fig. 3.6c. Further, the Reynolds number trend shows that the small separated region occurring at the diffuser throat around x=0 has the opposite behaviour as the main separation region, *i.e.* the boundary layer at the diffuser throat has less tendency to separate as the Reynolds number is increased. The spatial extent of the small separated region at the diffuser throat is mainly determined by the state of the local turbulent boundary layer and its ability to withstand separation.

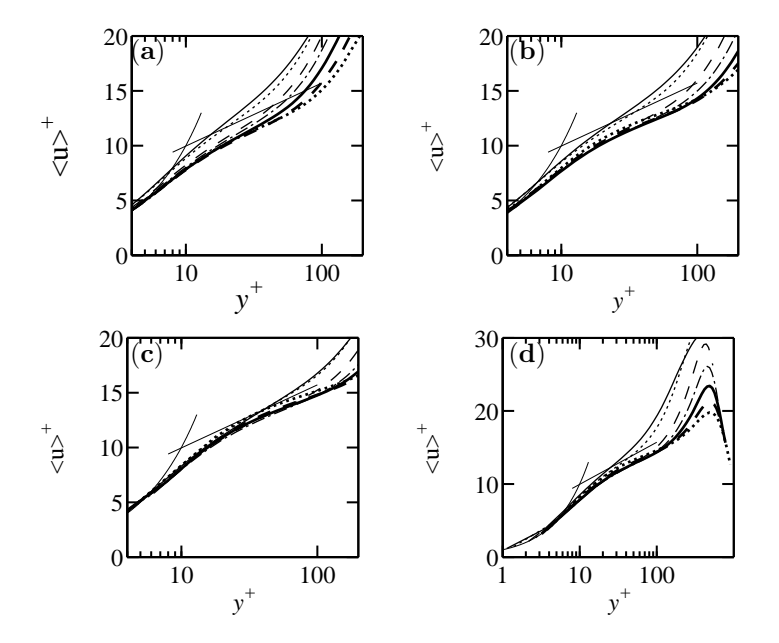


FIGURE 3.7. Reynolds number dependence of the internal layer: (a) $Re_b = 4500$, (b) $Re_b = 9000$, (c) $Re_b = 20000$, (d) $Re_b = 9000$, diverging angle $\phi = 10^{\circ}$. Wall normal profile of mean streamwise velocity at positions x = 6.4 (thin solid line), x = 10.4 (thin dotted line), x = 18.4 (thin dashed line), x = 22.4 (dash-dotted line) x = 26.4 (thick solid line), x = 30.4 (thick dotted line) and x = 34.4 (thick dotted line). The analytical correlations $u^+ = y^+$ and $u^+ = 2.5 \log(y) + 4.2$ are included in the plots for reference.

The internal layer occurring at the non-inclined wall has been described in a recent study by Wu et al. (2006). The Reynolds-number dependence of the internal layer has also been examined in the fourth paper. In order to detect whether the mean streamwise velocity profiles follows a well defined logarithmic layer within the internal layer, we present in figure 3.7 profiles of \overline{u}^+ scaled in viscous units at different streamwise positions in dependence of the Reynolds number. On the semilogarithmic scale adopted, the different profiles collapse well at different streamwise stations for $Re_b = 20000$ (Fig. 3.7c), and also, however less pronounced, for $Re_b = 9000$ (Fig. 3.7b). At this Reynolds number the results agree well with the findings of Wu et al. (2006) who considered the Obi diffuser at the same Re_b , for which we show our own results in figure 3.7(d). Conversely, at the lowest Reynolds number such a collapse is clearly not observed, as can be seen from Fig. 3.7a. It can be concluded that the establishment of an internal layer close to the upper, straight wall, is more distinct for larger Re_b .

Additionally, the influence of temporal correlations arising from the commonly used periodic turbulent channel flow as inflow condition for the diffuser is assessed. These time correlations are clearly related to turbulent events that survive while they are convected downstream. It is however found that this does not have a significant impact on the low-order statistics. Nevertheless, the examination of the power spectra at various positions in the diffuser shows that the low-frequency content of spectrum is enhanced when the inflow data is taken from a longer periodic channel.

In general, reasonable agreement between statistical data computed from LES and the corresponding experimental measurements is obtained, e.g. for the velocity profiles and turbulent fluctuations. However, also the experimental data show a variation between different experiments and setups. Thus, there seems to be a need for more refined measurements in order to create a consistent and accurate data base. In particular, the observed Reynolds number dependency needs to be backed by new experimental studies. In addition, a DNS study at a higher Reynolds number than previously possible would be valuable validation of the present findings.

CHAPTER 4

Application to the turbulent wall jet

A plane wall jet is the flow which is created by the injection of high-velocity fluid in a thin layer close to a wall. The wall jet consists of an inner region, which is similar to a boundary layer, and an outer region in which the flow resembles a free shear layer. These layers interact strongly and form a complex flow pattern. Apart from the interesting physics, wall jets are of great interest from an engineering point of view, for instance in film cooling of gas turbine blades, in combustion chambers in defrosters and for separation control on airfoils.

Turbulent wall jets are challenging cases for flow computations. Recently Dejoan & Leschziner (2005) performed an LES of a turbulent wall jet at Re = 9600 matching the experiments by Eriksson $et\ al.$ (1998). The profiles of velocity and turbulent stresses in the self-similar region are compared to the experimental data and agree well. However, in an LES, the transition process in the outer shear layer and especially in the boundary layer is extremely difficult to reproduce with high accuracy, as also pointed out in that study. Therefore, there are some discrepancies in comparison with the experimental data. Direct numerical simulations seem to have so far only been performed and published for transitional wall-jets. Wernz & Fasel (1996, 1997) studied the importance of three-dimensional effects in the transitional process and Visbal $et\ al.$ (1998) investigated the breakdown process in a finite-aspect-ratio wall jet by the means of DNS. Levin $et\ al.$ (2005) studied the breakdown initiated by the interaction between waves and streaks.

The objective of the fifth paper is to study the early turbulent evolution of the wall jet, which is triggered to undergo transition through the interaction between unstable waves and streaks, the transition scenario studied in Levin et al. (2005). The numerical code (see Lundbladh et al. 1999) for the direct numerical simulation is the same as the one used for the computations of the turbulent separated boundary layer in the first paper, however a slightly different version with a shared-memory parallelisation is used. The Reynolds number is Re = 3090, based on the inlet velocity and the nozzle height b. A Reynolds number matching the experimental investigations (Abrahamsson et al. 1994; Schneider & Goldstein 1994; Eriksson et al. 1998) is not feasible at the present stage, however as opposed to an LES, all scales are resolved and the transitional behaviour is reproduced more reliably. A grid of about 62.3 million

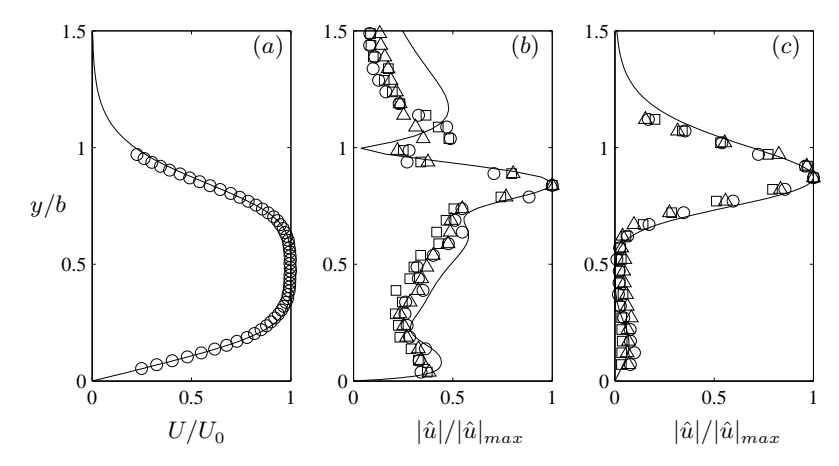


FIGURE 4.1. Comparison between calculations (solid lines) and experiments (symbols) from Levin et al. (2005) at x/b=5.3 for Re=3090. (a) Blasius wall jet. (b) Streamwise wave amplitude for $\omega b/U_0=1.49$. Experimental amplitudes are 0.3% (\circ), 1.1% (\square) and 1.7% (\triangle). (c) Streamwise streak amplitudes. The spanwise wavenumber for the PSE is $\beta b=3.77$ and for the experiments $\beta b=3.15$ (\circ), 3.90 (\square) and 4.72 (\triangle).

modes with 900 streamwise modes, 541 wall-normal modes and 128 spanwise modes is used.

The base flow consists of the Blasius wall jet, which is a solution to the boundary-layer equations with a combination of the Blasius boundary layer and the Blasius shear layer as an initial condition. The flow is matched to an experimental set-up (Levin et al. 2005). Fig. 4.1a shows the computed base flow compared to data measured 16 mm downstream of the nozzle outlet. In the experiment, the Kelvin–Helmholtz instability and naturally appearing streaks were observed to lead to breakdown. Two-dimensional waves and optimal streaks corresponding to the most unstable scales were calculated with the parabolized stability equations and introduced in the DNS. Figures 4.1b and 4.1c show the computed amplitude functions of the wave and the streak, respectively, compared to measured data by Levin et al. (2005).

The area in which the flow quantities are well represented is restricted to the upstream half of the computational box $(x/b \lesssim 25)$ due to a large external vortex that exists in the downstream part of the box. It evolves from a start-up vortex that slowly convects downstream and then remains in the ambient flow in front of the fringe region. Such an external flow exists for wall jets in experimental set-ups as well, but as the computational box is not as large as the surrounding space in an experiment, the problem is more prominent. It is possible to avoid the vortex by specifying the entrainment velocity at the upper boundary. Dejoan & Leschziner (2005) used such a boundary condition

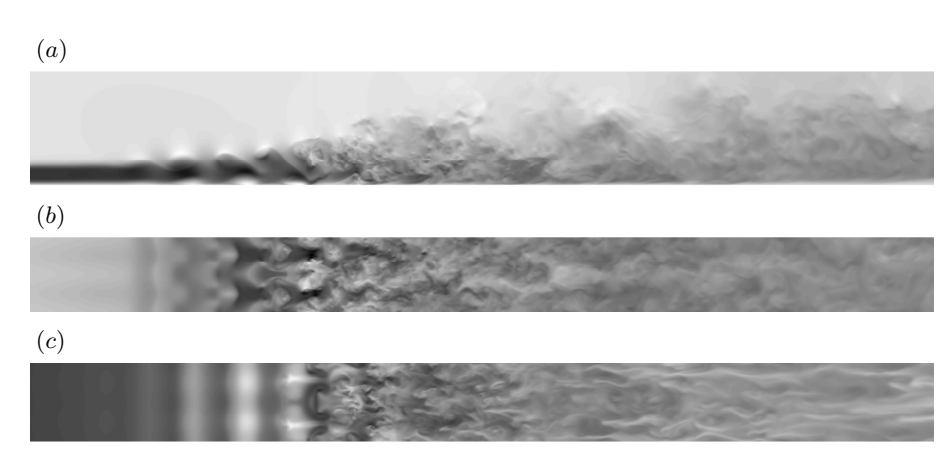


FIGURE 4.2. Visualisation of streamwise velocity with dark areas displaying high velocity and white areas displaying regions of backflow. The flow is from left to right and the streamwise extend of the planes are from the nozzle outlet to 38.5b. (a) (x,y)-plane at the middle of the box, the height of the plane is 4.8b. (b) Horizontal plane at y/b = 0.96. (c) Horizontal plane at y/b = 0.19.

based on the laminar free plane jet. However, we have chosen not to constrain the wall jet by prescribing the entrainment velocity since the laminar growth of a jet differs from its turbulent growth. Evaluation of spanwise two-point correlations of the computed streamwise velocity component showed that the box was sufficiently wide in the upstream half of the box.

In order to visualise the whole wall jet from its laminar part in the vicinity of the nozzle outlet where the waves and the streaks grow, through the transition region to its downstream turbulent part, three two-dimensional planes of an instantaneous flow field are shown in figure 4.2, (which are taken from three corresponding animations). Figure 4.2(a) shows the (x, y)-plane in the middle of the computational domain, where the low-velocity streak is present in the outer shear layer. The height of the plane is y/b = 4.8. In the shear-layer region, anti-clockwise rotating rollers are created by the Kelvin-Helmholtz instability and follow the flow downstream. In the boundary-layer region, clockwise rotating rollers are formed and are associated with small separation bubbles. It can be seen from the animations that the boundary-layer rollers in this plane move faster than the rollers in the shear-layer region. This is due to the spanwise modification of the flow by the streaks with a low-velocity streak in the shear-layer region and a weak high-velocity streak in the boundary-layer region. The shear-layer and boundary-layer rollers move at the same rate in the plane located half a spanwise wavelength to the side of where a high-velocity streak is present in the outer shear layer. Breakdown to turbulence appears first in

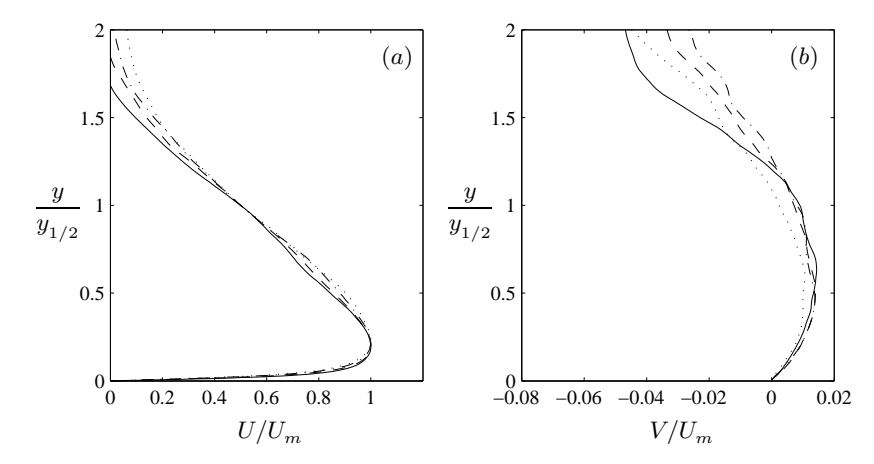


FIGURE 4.3. Mean velocity at x/b = 17 (solid line), 20 (dashed line), 23 (dashed-dotted line) and 26 (dotted line). (a) Streamwise component. (b) Wall-normal component.

the shear-layer region and then spreads down to the boundary-layer region. In the part of the box where the flow is turbulent is the velocity higher in the inner region and lower in the outer region, as expected. Further downstream, the whole wall jet slows down while it spreads and the largest scales increase. Figures 4.2(b) and 4.2(c) show the horizontal planes at y/b=0.96 and 0.19, respectively, which are in the middle of the outer shear layer and the inner boundary layer of the laminar part of the wall jet. The width of the planes shows the entire spanwise extend of the computational box.

Turning attention to the flow characteristics averaged in both time and the spanwise direction, the data is presented in both inner and outer scaling in order to identify self-similar behaviour. However, due to the low Reynolds number and the short computational domain, the data is not sufficient to contribute to a discussion of different approaches to scaling as presented recently by Wygnanski et al. (1992) and George (2000). Scaling with outer variables is used to identify self-similar behaviour in the outer shear layer. Here we apply traditional scaling using the maximum velocity of the wall jet U_m and the half-width $y_{1/2}$. When comparing with data at higher Reynolds numbers, it has to be taken into account that the shear stress in the outer layer, and therefore also the other properties, are dependent on the Reynolds number.

Figures 4.3(a) and 4.3(b) show the streamwise and wall-normal mean velocities, respectively, scaled in outer scaling. The streamwise velocity profiles between x/b=17 and 26 collapse reasonably well up to $y/y_{1/2}=1$. Further away from the wall, the profiles deviate from each other owing to a secondary flow induced by the large external vortex. For the wall-normal velocity profiles, the self-similar behaviour is only obtained between x/b=20 and 23. Further upstream, the deviation originates from the transition to turbulence.

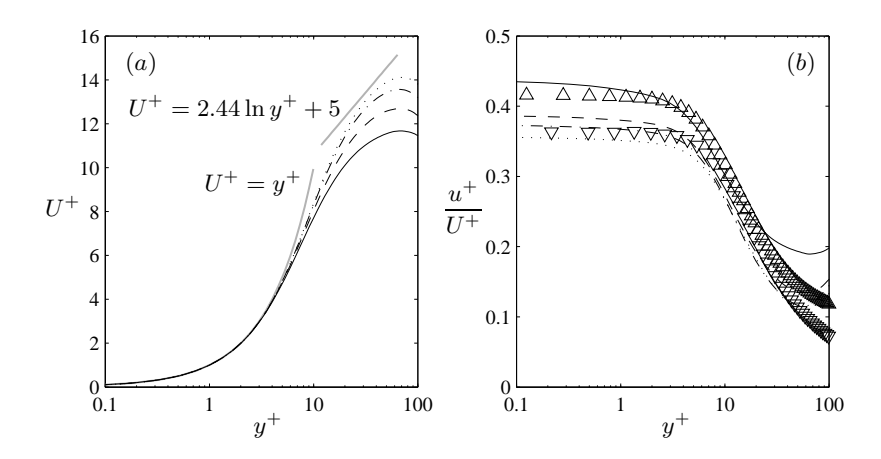


FIGURE 4.4. Near-wall behaviour of (a) streamwise mean velocity and (b) u^+/U^+ . Data from Kim et al. (1987) (∇) and Del Alamo et al. (2004) (\triangle). Lines as in figure 4.3.

The outer vortex in the ambient flow compresses the downstream part of the wall jet slightly, causing the profile at x/b = 26 to deviate towards lower values. This deviation is larger than for the streamwise component indicating that the wall-normal velocity is affected to a higher degree than the streamwise velocity.

Figure 4.4(a) shows the near-wall region of the streamwise mean velocity presented in inner scaling, using the viscous length scale $\eta = \nu/u_{\tau}$ and the friction velocity u_{τ} . Within the viscous sublayer, the profiles follow a linear law $U^+ = y^+$, shown as the grey curved line, up to about $y^+ = 4$. Further away from the wall, the profiles start to deviate from the linear behaviour, earlier than for a turbulent boundary layer that typically starts to deviate for values $y^+ \geq 8$. This observation agrees well with the behaviour inferred from the data measured by Eriksson et al. (1998) at Re = 9000. Due to the low Reynolds number, the data does not follow the classical logarithmic law $U^+ = 2.44 \ln y^+ + 5$, shown as the grey straight line in the figure.

In figure 4.4b, the ratio between the fluctuating streamwise velocity u_{rms} and the mean streamwise velocity is shown. This value has previously been shown to be constant in the viscous sublayer, up to about $y^+ = 5$, and Alfredsson et al. (1988) found the value to be 0.4 in turbulent boundary-layer and channel flows. This value seems to approximately hold even for the turbulent wall jet as can be seen in the figure. A comparison has been made with numerical data for turbulent channel flow computed by Kim et al. (1987) for a low Reynolds number and by Del Alamo et al. (2004) for a higher Reynolds number. The data for the low Reynolds number shows a good agreement with the present simulation.

The turbulent stresses are scaled with inner scaling and displayed in figure 4.5. The profiles collapse reasonably well for the streamwise positions

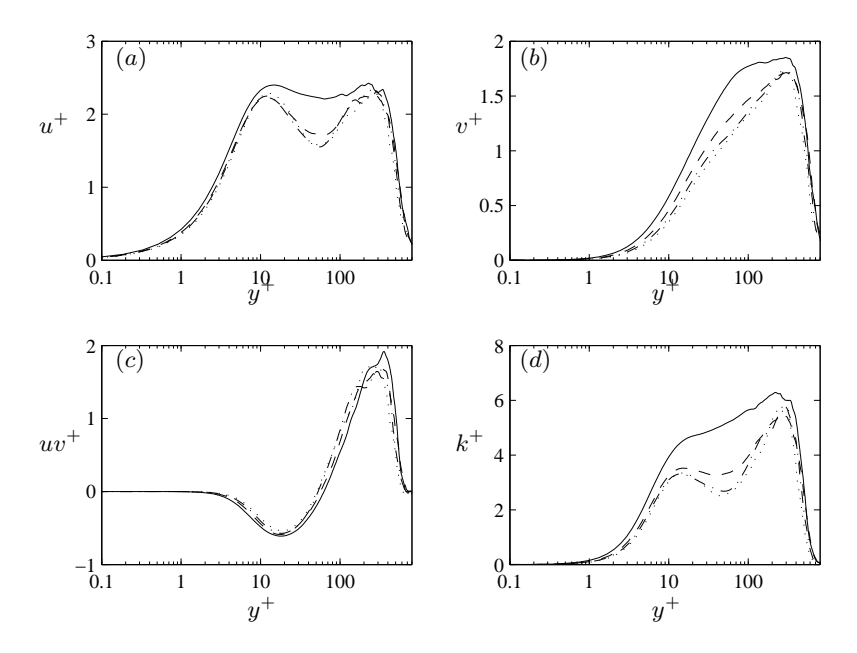


FIGURE 4.5. Profiles of (a) u_{rms} , (b) v_{rms} , (c) Reynolds shear stress and (d) turbulence kinetic energy. Lines as in figure 4.3.

x/b=20 to 26 indicating that the flow has started to exhibit a self-similar behaviour. It should be mentioned that the collapse achieved with inner scaling is much better than with outer scaling. The profile at the position x/b=17 is, however, still close to the transitional region and deviates from the other profiles. Downstream of position x/b=26, the vortex present in the end region of the computational domain causes the flow to depart from the self-similar behaviour and profiles from this region are therefore not shown in the figures.

Unfortunately, recent measurements of turbulent stresses are not available for the Reynolds number at which our simulation is performed. As discussed in more detail in the fifth paper itself, the recent measurements of the turbulent quantities with the Laser-Doppler technique show significant discrepancies from the earlier hot-wire measurements. The difference can be explained as being due to the occurrence of reverse flow resulting in too low values for these components in the hot-wire measurements (Schneider & Goldstein 1994; Eriksson *et al.* 1998). However, in comparison with the data presented by Eriksson *et al.* (1998) at Re = 9000, the positions of the inner maxima of u^+ and u^+ agree well, whereas the levels of the turbulent fluctuations are lower due to the lower Reynolds number. The profiles of the Reynolds shear stress collapse very well in inner scaling but the inner negative peak occurs closer to the wall than in the measurements by Eriksson *et al.* (1998).

CHAPTER 5

Conclusions

In this thesis, the numerical simulation of time-dependent, inherently three-dimensional flow problems has been employed as a useful and accurate means for prediction and understanding of flow configurations. In particular, direct numerical simulations and large-eddy simulations have been performed of highly intermittent flows, exhibiting separation, and of a turbulent wall jet.

A model problem exhibiting pressure driven separation, which is feasible to study with DNS, is the turbulent boundary-layer flow over a flat plate which separates from the wall due to an adverse pressure gradient. The aim was to investigate the effect of periodic excitations on the separated region occurring in this flow as a means of controlling the flow. Linear stability analysis is used to analyse the sensitivity of the flow with respect to the periodic excitations. The dependence of the effect of two-dimensional forcing on position, amplitude and frequency of the forcing is investigated. We have shown that the flow in the region where it separates without forcing can be made to remain attached by applying time-periodic perturbations upstream the separated region for a certain frequency range at sufficiently high amplitudes. The results show further that control with a spanwise periodic input is more effective than with a spanwise homogeneous control input. At a higher Reynolds number, time-varying forcing is expected to be more effective, since the two-dimensional disturbances are then expected to be more unstable, and do not have to be forced with such high amplitudes. Investigations of such forcing combinations together with more advanced feedback control schemes would be interesting in future investigations.

As a further extension the pressure-induced separation of a turbulent boundary layer on a semi-infinite swept flat plate has been considered. The reduction of the size of the separated region is in agreement with previous studies on spanwise invariant three-dimensional separation, where deviations from the sweep-independence principle are observed for angles $\alpha>40^\circ$. Comparison with the simulations of three-dimensional boundary layers subjected to a weak adverse pressure gradient indicates that strength of the pressure gradient, the strain rate and the occurrence of separation have a deeper impact on the turbulence structure than the skewing of the mean flow.

Considering turbulent separation in more complex geometries, one has to resort to modelling approaches due to the increasing computational effort.

Large-eddy simulations (LES) of an incompressible planar, asymmetric diffuser flow have been presented. The pressure distribution is no longer chosen separately as in the first paper but is connected to the geometry, which is a step towards a more realistic flow problem. Compared to previous numerical and experimental studies, the setup is slightly modified, in order to create a test case that is more sensitive and thus better suited for comparisons of results at different Reynolds numbers. A resolution study has been performed, highlighting the disparity of the relevant scales and thus the sensitivity of the simulation results to the grids used. Regarding the flow physics, we focused on quantifying the influence of the Reynolds number on various diffuser-flow characteristics. In particular it is consistently shown that by increasing the Reynolds number a clear trend towards a larger separated region is evident; at least for the studied, comparably low Reynolds number regime. The results suggest that the size of the main separated region is governed by the 'jet-like' inflow which penetrates further into the diffuser. A small separated region occurring at the diffuser throat shows the opposite behaviour compared to the main separation region, i.e. the boundary layer at the diffuser throat has a lower tendency to separate as the Reynolds number is increased. The spatial extent of the small separated region at the diffuser throat is mainly determined by the state of the local turbulent boundary layer and its ability to withstand separation. Moreover, the influence of the Reynolds number on the internal layer occurring at the non-inclined wall has been examined and it can be concluded that this region close to the upper, straight wall, is more distinct for larger Reynolds numbers. In general, reasonable agreement between statistical data computed from LES and the corresponding experimental measurements is obtained, e.g. for the velocity profiles and turbulent fluctuations. However, the experimental data show also a variation between different experiments and setups. Thus, there seems to be a need for more refined measurements in order to create a consistent and accurate data base. In particular, the observed Reynolds number dependence needs to be confirmed an reinforced by new experimental studies. In addition, a DNS study at a higher Reynolds number than previously possible would be valuable validation of the present findings.

The first direct numerical simulation that is sufficiently large to study the self-similar behaviour of a turbulent wall jet has been performed using the same numerical method as used for the turbulent boundary layer on a flat plate. The simulation provides detailed visualisations of the flow structures. The statistical results have been presented in both inner and outer scaling in order to identify self-similar behaviour. Despite the low Reynolds number and the short computational domain, the turbulent flow exhibits a reasonable self-similar behaviour, which is most pronounced using inner scaling in the near-wall region. Despite the large computational cost, the simulation is still too small to study a fully-developed turbulent wall jet. The early turbulent state in the present simulation is governed by the streaks imposed upstream. The study of the fully-developed turbulent wall jet in a larger computational domain and at higher Reynolds numbers is left for future work.

Acknowledgments

First of all, I would like to thank my supervisor, Prof. Dan Henningson, for giving me the opportunity to work as his student and to develop my knowledge within the subject of fluid dynamics. His interest in fluid phenomena is always inspiring.

I would like to thank all the people I had the pleasure to work with during the past years: Dr. Luca Brandt, Dr. Ardeshir Hanifi, Dr. Ori Levin, Dr. Philipp Schlatter, Dr. Martin Skote and Saskia Spehr. Thanks to Dr. Stefan Wallin for fruitful discussions. I learned from all of them.

I would like to thank my teachers during the years at the department of mechanics at KTH: Prof. Arne Johansson, Prof. Henrik Alfredsson, Prof. Gustav Amberg, Dr. Tony Burden, Dr. Anders Dahlkild and Prof. Lars Söderholm.

Thanks to Prof. Ulrich Rist and the staff at the Institute for Aero- and Gasdynamics (IAG) for making my stays in Stuttgart pleasant. I enjoyed the nice atmosphere and the discussions about almost everything at the ÖZ. The financial support for the visits was provided by STINT and HPC Europe.

Many thanks to the people at KTH, especially to those at Mechanics for providing a nice atmosphere at the Department. In particular I would like to thank Anne-Mari Olofsson, Arnim Brüger, Carl-Gustav Unckel, Christer Johannesson, Davide Medici, Erik Lindborg, Erik Stålberg, Espen Åkervik, Fredrik Lundell, Geert Brethouwer, Gustaf Mårtensson, Jan Pralits, Jens Fransson, Jérôme Hæpffner, Kristian Angele, Linus Marstorp, Luca Brandt, Markus Högberg, Martin Byström, Martin Skote, Mattias Chevalier, Olof Grundestam, Ori Levin, Olaf Marxen, Philipp Schlatter, Pär Ekstrand and Veronica Eliasson.

This work has been funded by the Vinnova competence centre PSCI at NADA, KTH. Partial funding from Statens Energimyndighet (STEM) is also acknowledged. The direct numerical simulations were performed at the Center for Parallel Computers at KTH and the large-eddy simulations at the Höchstleistungsrechenzentrum (HLRS), Stuttgart.

Finally, I want to thank everybody in my family who supported me during my education and all my friends for cheering me up during the less productive times.

Bibliography

- ABRAHAMSSON, H., JOHANSSON, B. & LÖFDAHL, L. 1994 A turbulent plane two-dimensional wall-jet in a quiescent surrounding. *Eur. J. Mech. B/Fluids* **13** (5), 533–556.
- Alfredsson, P. H., Johansson, A. V., Haritonidis, J. H. & Eckelmann, H. 1988 The fluctuating wall-shear stress and the velocity field in the viscous sublayer. *Phys. Fluids* **31** (5), 1026–1033.
- ALVING, A. E. & FERNHOLZ, H. H. 1996 Turbulence measurements around a mild separation bubble and downstream of reattachment. *J. Fluid Mech.* **322**, 297–328
- Angele, K. A. & Klingmann, B. 2005 The effect of streamwise vortices on the turbulence structure of a separating boundary layer. *Eur. J. Mech. B/Fluids* 24, 539–554.
- Breuer, M., Jaffrézic, B., Peller, N., Manhart, M., Fröhlich, J., Hinterberger, C., Rodi, W., Deng, G., Chikhaoui, O., Šarić, S. & Jakirlić, S. 2006 A comparative study of the turbulent flow over a periodic arrangement of smoothly contoured hills. In *Direct and Large-Eddy Simulation VI*. To appear.
- Choi, H., Teman, R., Moin, P. & Kim, J. 1993 Feedback control for unsteady flow and its application to the stochastic burgers equation. *J. Fluid Mech.* **253**, 509–543.
- Chun, K., Lee, I. & Sung, H. 1999 Effect of spanwise varying local forcing on turbulent separated flow over a backward facing step. *Exps. Fluids* **26**, 437–440.
- DEARDORFF, J. 1970 A numerical study of the three-dimensional turbulent channel flow at large Reynolds numbers. *J. Fluid Mech.* 41, 453–480.
- Dejoan, A. & Leschziner, M. A. 2005 Large eddy simulation of a plane turbulent wall jet. *Phys. Fluids* 17, 025102.
- Del Alamo, J., Jimenez, J., Zadonade, P. & Moser, R. 2004 Scaling of the energy spectra in turbulent channels. *J. Fluid Mech.* **500**, 135–144.
- ERIKSSON, J. G., KARLSSON, R. I. & PERSSON, J. 1998 An experimental study of a two-dimensional plane turbulent wall-jet. *Exps. Fluids* **25**, 50–60.
- Fröhlich, J., Mellen, C. P., Rodi, W., Temmerman, L. & Leschziner, M. A. 2005 Highly resolved large-eddy simulation of separated flow in a channel with streamwise periodic constrictions. *J. Fluid Mech.* **526**, 19–66.
- George, W. K. 2000 A similarity theory for the turbulent plane wall jet without external stream. J. Fluid Mech. 425, 367–411.

- GERMANO, M., PIOMELLI, U., MOIN, P. & CABOT, W. H. 1991 A dynamic subgrid-scale eddy viscosity model. *Phys. Fluids A* 3 (7), 1760–1765.
- GREENBLATT, D. & WYGNANSKI, I. J. 2000 The control of flow separation by periodic excitation. *Prog. Aerosp. Sci.* **36**, 487–545.
- HEENAN, A. & MORRISON, J. 1998 Passive control of backstep flow. *Exp. Therm. Fluid Sci.* **16** (1-2), 122–132.
- Holmes, Lumley & Berkooz 1996 Turbulence, Coherent Structures, Dynamical Systems and Symmetry. Cambridge Monographs on Mechanics.
- Kaltenbach, H.-J., Fatica, M., Mittal, R., Lund, T. S. & Moin, P. 1999 Study of flow in a planar asymmetric diffuser using large-eddy simulation. *J. Fluid Mech.* **390**, 151–185.
- Kaltenbach, H.-J. 2004 Turbulent flow over a swept backward-facing step. Eur. J. Mech. $B/Fluids~{f 23},~501-518.$
- Kalter, M. & Fernholz, H. 1995 The influence of freestream turbulence on an axisymmetric turbulent boundary layer in, and relaxing from, an adverse pressure gradient. In *Advances in Turbulence V. Proc. 5th Eur. Turb. Conference (Siena, Italy, 1994)*, pp. 261–265. Kluwer.
- Kalter, M. & Fernholz, H. H. 2001 The reduction and the elimination of a closed separation region by free-stream turbulence. *J. Fluid Mech.* 446, 271–308.
- KANG, S. & CHOI, H. 2002 Suboptimal feedback control of turbulent flow over a backward facing step. *J. Fluid Mech.* **463**, 201–227.
- KIM, J., MOIN, P. & MOSER, R. 1987 Turbulence statistics in fully developed channel flow at low Reynolds number. J. Fluid Mech. 177, 133–166.
- Kiya, M., Shimizu, M. & Mochizuki, O. 1997 Sinusoidal forcing of a turbulent separation bubble. *J. Fluid Mech.* **342**, 119–139.
- Leonard, A. 1974 Energy cascade in large eddy simulation of turbulent fluid flows. *Adv. Geophys.* **18** (A), 237–248.
- LESCHZINER, M. A. 2006 Modelling turbulent separated flow in the context of aero-dynamic applications. *Fluid Dynamics Research* **38**, 174–210.
- Lesieur, M. & Métais, O. 1996 New trends in large-eddy simulations of turbulence. *Annu. Rev. Fluid Mech.* **28**, 45–82.
- Levin, O., Chernoray, V. G., Löfdahl, L. & Henningson, D. S. 2005 A study of the Blasius wall jet. *J. Fluid Mech.* **539**, 313–347.
- LILLY, D. K. 1992 A proposed modification of the Germano subgrid-scale closure method. *Phys. Fluids A* 4 (3), 633–635.
- Lundbladh, A., Berlin, S., Skote, M., Hildings, C., Choi, J., Kim, J. & Henningson, D. S. 1999 An efficient spectral method for simulation of incompressible flow over a flat plate. *Tech. Rep.* KTH, Department of Mechanics, Stockholm, Sweden.
- Meneveau, C. & Katz, J. 2000 Scale-invariance and turbulence models for large-eddy simulation. *Annu. Rev. Fluid Mech.* **32**, 1–32.
- Moin, P. & Mahesh, K. 1998 Direct numerical simulation: A tool in turbulence research. *Annu. Rev. Fluid Mech.* **30**, 539–78.
- NA, Y. & Moin, P. 1998 Direct numerical simulation of a separated turbulent boundary layer. *J. Fluid Mech.* **374**, 379–405.
- Nishri, B. & Wygnanski, I. J. 1998 Effects of periodic excitation on turbulent flow separation from a flap. AIAA J. 36 (4), 547–556.

- NORDSTRÖM, J., NORDIN, N. & HENNINGSON, D. S. 1999 The fringe region technique and the Fourier method used in the direct numerical simulation of spatially evolving viscous flows. SIAM J. Sci. Comput. 20 (4), 1365–1393.
- Obi, S., Aoki, K. & Masuda, S. 1993 Experimental and computational study of turbulent separating flow in an asymmetric diffuser. In *Proc. Ninth Symposium on Turbulent Shear Flows, Kyoto, Japan*, pp. P305.1–P305.4.
- Obi, S., Ishibashi, N. & Masuda, S. 1997 The mechanism of momentum transfer in the periodically perturbed turbulent separated flow. In 2nd Int. Symposium on Turbulence, Heat and Mass Transfer (eds. K. Hanjalić & T. Peeters), pp. 835–844. Delft University Press.
- Obi, S., Nikaido, H. & Masuda, S. 1999 Reynolds number effect on the turbulent separating flow in an asymmetric plane diffuser. In *ASME/JSMR Fluids Engineering Division Summer Meeting 1999*, *FEDSM* 99-6976. ASME.
- PIOMELLI, U. & BALARAS, E. 2002 Wall-layer models for large-eddy simulations. *Annu. Rev. Fluid Mech.* **34**, 349–374.
- PRANDTL, L. 1904 Über die Flüssigkeitsbewegung bei sehr kleiner Reibung. In Verhandlungen des III. internationalen Mathematikerkongresses, pp. 484–491. Heidelberg.
- REYNOLDS, O. 1883 An experimental investigation of the circumstances which determine whether the motion of water shall be direct or sinuous, and of the law of resistance in parallel channels. *Phil. Trans. Royal Soc.* **174**, 935–982.
- Roos, F. W. & Kegelman, J. 1986 Control of coherent structures in reattaching laminar and turbulent shear layers. AIAA J. 24, 1956–1963.
- SAGAUT, P. 2005 Large Eddy Simulation for Incompressible Flows, 3rd edn. Springer, Berlin, Germany.
- Schneider, M. & Goldstein, R. 1994 Laser Doppler measurement of tubulence parameters in a two-dimensional plane wall jet. *Phys. Fluids* **6** (9), 3116–3129.
- Schubauer, G. & Spangenberg, W. 1960 Forced mixing in boundary layers. *J. Fluid Mech.* 8, 10–32.
- Selby, G., Lin, J. C. & Howard, F. 1990 Turbulent flow separation control over a backward-facing step. *Trans. ASME: J. Fluids Engng* **112**, 238–240.
- Sigurdson, L. 1995 The structure and control of a turbulent reattaching flow. J. Fluid Mech. 298, 139–165.
- SIMPSON, R. L. 1996 Aspects of turbulent boundary-layer separation. *Prog. Aerospace Sci.* 32, 457–521.
- Skote, M. & Henningson, D. S. 2002 Direct numerical simulation of a separated turbulent boundary layer. *J. Fluid Mech.* **471**, 107–136.
- SMAGORINSKY, J. 1963 General circulation experiments with the primitive equations. *Mon. Weath. Rev.* **91** (3), 99–164.
- Taylor, H. D. 1948 Design criteria for and application of the vortex generator mixing principle. *Tech. Rep.* M-15038-1. United Aircraft Corp.
- TÖRNBLOM, O. 2003 Experimental study of the turbulent flow in a plane asymmetric diffuser. Licentiate thesis, Department of Mechanics, KTH Stockholm, Sweden.
- VISBAL, M. R., GAITONDE, D. V. & GOGINENI, S. P. 1998 Direct numerical simulation of a forced transitional plane wall jet. *AIAA Paper* 98-2643.
- Wernz, S. & Fasel, H. F. 1996 Numerical investigation of unsteady phenomena in wall jets. $AIAA\ Paper\ 96\text{-}0079$.

- Wernz, S. & Fasel, H. F. 1997 Numerical investigation of forced transitional wall jets. $AIAA\ Paper\ 97\text{-}2022.$
- Wu, X., Schlüter, J., Moin, P., Pitsch, H., Iaccarino, G. & Ham, F. 2006 Computational study on the internal layer in a diffuser. *J. Fluid Mech.* **550**, 391–412.
- Wygnanski, I., Katz, Y. & Horev, E. 1992 On the applicability of various scaling laws to the turbulent wall-jet. *J. Fluid Mech.* **234**, 669–690.
- Yoshioka, S. 2001 Control of separated flow over a backward-facing step by periodic forcing. Ph.d.thesis, Department of Mechanical Engineering, Keio University, Keio.

Part 2

Papers

Paper 1

The influence of periodic excitation on a turbulent separation bubble

By Astrid H. Herbst and Dan S. Henningson

Department of Mechanics, KTH, SE-100 44 Stockholm, Sweden

Published in Flow, Turbulence and Combustion 2006 **76:** 1-21 DOI 10.1007/s10494-005-9004-4

Turbulent separation limits the performance in many engineering applications, for example creating pressure losses in diffuser like flows or stall on aircraft wings. In the present study the turbulent boundary layer flow over a flat plate separating due to an adverse pressure gradient is studied as a model problem and the effect of periodic excitation in both time and space is investigated through direct numerical simulations. Linear stability analysis is used to analyse the sensitivity of the flow with respect to time-periodic excitations. The dependence on position, amplitude and frequency of the forcing is investigated. For a certain frequency range at sufficiently high amplitudes, it is possible to eliminate the separated region. Furthermore, three-dimensional effects are studied by applying a steady spanwise forcing as well as a both time-dependent and spanwise varying forcing. A forcing varying in spanwise direction is shown to be the most effective in eliminating the separated region, whereas two-dimensional time-periodic excitation was not as efficient as it was expected.

1. Introduction

Turbulent boundary layers under strong adverse pressure gradients are of interest in many technological applications. One example of the occurrence of adverse pressure gradients is the flow in the diffuser like air intake of a military aircraft. Here due to stealth and weight considerations it is highly desirable to shorten the section where the flow is decelerating. This may lead to separation and flow in the reverse direction limiting the performance due to severe pressure losses. Therefore flow control may be needed as to improve the flow quality.

In the present investigation we focus on the turbulent boundary layer over a flat plate separating due to an adverse pressure gradient. The effect of periodic excitation on the separation bubble is studied by the means of direct numerical simulations. It is important to note that the dynamics of a separating boundary layer is different from a laminar boundary layer undergoing separation with turbulent reattachment. A turbulent boundary layer can withstand considerably higher pressure gradients without separation, but if the pressure gradient

is severe enough to cause the turbulent boundary layer to separate it is a much more difficult task to prevent separation.

Separated turbulent boundary layer flow over a flat plate was investigated using direct numerical simulations (DNS) in only in a few previous studies. Spalart & Coleman (1998) performed a DNS of a turbulent separation bubble with heat transfer. They showed that separation has a large effect on the boundary layer and found an increase of Reynolds stresses over the separation bubble which they explained by a lift-up of the turbulent fluid from the wall region. The separation of a turbulent boundary layer has further been numerically analysed by Na & Moin (1998). They found that the turbulent structures emanating upstream the separation move upwards into the shear layer and then turn around the bubble causing a maximum of the turbulence intensities in the middle of the shear layer. Skote & Henningson (2002) conducted a DNS of a turbulent boundary layer separating due to a strong adverse pressure gradient using the same numerical code that was applied in this study. In comparison with the earlier simulations the flow had a stronger and larger recirculation region. Recently, Manhardt & Friedrich (2002) carried out a DNS of the separated turbulent boundary layer comparable to the experiment of Kalter & Fernholz (1995) but at half the Reynolds number of the experiment. They found that the shape and the dynamics of the separation bubble are governed by the large scale vortices reaching from the wall into the shear layer above it. However, in none of these studies the effect of periodic excitations on the turbulent separation bubble was examined.

Many experiments have been carried out on separated flows, for a review see Simpson (1996). However, in many of them the separation is caused by a sharp edge or an obstacle, fixing the location of separation. On the flatplate turbulent boundary layer, Perry & Fairlie (1975), Simpson $et\ al.\ (1977,1981a,b)$, Dengel & Fernholz (1990), Driver (1991) and Alving & Fernholz (1995, 1996) conducted experiments. In all experiments mentioned above, the turbulence was found to be intensified above the separated region while it decreased in the backflow itself. The effect of time dependent forcing on the flow was not subject in any of the these studies. However, Angele (2003) recently studied experimentally a turbulent boundary layer subjected to an adverse pressure gradient undergoing separation and reattachment and investigated the effect of passive control by the means of vortex generators.

Periodic excitations have been studied as a means to influence separated flows in several other geometries. Greenblatt & Wygnanski (2000) review the control of flow separation by periodic excitation as well as control and exploitation of airfoil and diffuser flows, including three-dimensional and curvature effects. Important parameters such as the optimum reduced frequencies and excitation levels are discussed. However, the main focus is on flows which do not attach unconditionally, e.g. the flow over a deflected flap, which was also studied by Nishri & Wygnanski (1998).

Among the naturally reattaching, separated flows, a lot of work concerning the effect of periodic excitations has been carried out on flows where contrary to the present investigation the point of separation does not fluctuate in time but is fixed due to a sudden change in geometry. The fixed location of the separation point simplifies the understanding of the dynamics and the application of a time-dependent forcing. The backward facing step is the simplest configuration of this type of flow. Roos & Kegelman (1986) studied the excitation of the flow over a backward facing step by an oscillating flap positioned at the point of shear layer separation. The reattachment length was shortened depending on the Reynolds number up to 30 percent due to the momentum transfer by the vortical structures. The influence of periodic excitations imposed by blowing and suction on this flow was studied experimentally by Yoshioka (2001). He found large-scale co-rotating spanwise vortices introduced into the shear layer due to the forcing causing an increase in Reynolds stress. For the optimum forcing frequency the separated region was shortened by 30 percent. The most advanced scheme from a control point of view was applied numerically on this type of flow. Kang & Choi (2002) implemented a suboptimal feedback control as to enhance mixing in the turbulent flow behind the backward facing step simulated using Large Eddy Simulations (LES). The reattachment length was significantly reduced compared to both flow with single frequency actuations and uncontrolled flow. For a the separation bubble downstream the sharpedged blunt face of a circular cylinder, Sigurdson (1995) studied experimentally the effect of periodic velocity perturbations. Forcing at frequencies below the one of the initial Kelvin-Helmholtz instability of the free shear layer, the reattachment length was reduced. Kiya et al. (1997) investigated sinusodical forcing at the corner of a blunt cylinder and found that the optimal frequency scales with the frequency of shedding vortices from the reattachment region of the separated shear layer. He observed that forcing of sufficiently high amplitudes eliminates the recirculation region in a range of the forcing frequency. In an asymmetric plane diffuser, Obi et al. (1997) found experimentally that the momentum transfer is promoted by periodic perturbations leading to earlier reattachment.

From an experimental point of view it is important to have suitable control devices to be able to apply the control strategies developed in numerical investigations. Glezer & Amitay (2002) reviewed the use of synthetic jets where momentary ejection and suction of a fluid across an orifice alternate while retaining zero net mass flux and a broad range of time scales. As an example they show their ability to control separation on a cylinder. Plasma actuators described by Corke *et al.* (2002) are another choice for suitable control devices to control separation. Their influence on the flow are well modelled using a volume force Orlov & Corke (2005).

2. Governing equations and numerical methods

2.1. Numerical scheme

The simulations of the turbulent boundary layer exposed to an adverse to favourable pressure gradient have been performed using a code developed at the Department of Mechanics by Lundbladh $et\ al.\ (1999)$. The code uses a pseudo-spectral method with Fourier discretization in streamwise and spanwise directions and Chebyshev polynomials in the wall-normal direction similar to Kim $et\ al.\ (1987)$. A fringe technique enables simulations of spatially developing flows while using Fourier discretization in the streamwise direction (see Nordström $et\ al.\ (1999)$). A fringe region is added in the end of the computational domain, in which the outflow is forced back to the inflow. The fringe region is implemented by the addition of a volume force F to the Navier-Stokes equations:

$$\frac{\partial u_i}{\partial t} + u_j \frac{\partial u_i}{\partial x_j} = -\frac{1}{\rho} \frac{\partial p}{\partial x_i} + \nu \frac{\partial^2 u_i}{\partial x_j^2} + F_i \tag{1}$$

The force

$$F_i = \lambda(x)(\tilde{u}_i - u_i) \tag{2}$$

is non-zero only in the fringe region. \tilde{u}_i is the laminar inflow velocity profile the solution u_i is forced to and λ the strength of the forcing. The form of the fringe function is designed to have minimal upstream influence and given by

$$\lambda(x) = \lambda_{max} \left[S\left(\frac{x - x_{start}}{\Delta_{rise}}\right) - S\left(\frac{x - x_{end}}{\Delta_{fall}}\right) \right]$$
 (3)

where

$$S(x) = \begin{cases} 0 & x \le 0\\ 1/[1 + \exp(\frac{1}{x-1} + \frac{1}{x})] & 0 < x < 1\\ 1 & x \ge 1 \end{cases}$$
 (4)

The time integration is carried out using a four-step low-storage third-order Runge-Kutta-scheme for the non-linear terms an a second-order Crank-Nicolson method for the linear terms. Aliasing errors from the evaluation of the non-linear terms are removed applying a $\frac{3}{2}$ -rule when the FFTs are calculated in the wall parallel plane.

2.2. Box dimensions and boundary conditions

The simulations are performed at an inflow Reynolds number $Re_{\delta_0^*} = U_\infty \delta_0^* / \nu = 400$ based on the displacement thickness δ_0^* of the boundary layer and the freestream velocity U_∞ at the inflow x=0. All quantities are non-dimensionalized by U_∞ and δ_0^* at x=0. At this position, a laminar Blasius boundary layer profile is introduced. Downstream at x=10 laminar-turbulent transition is triggered by a random volume force near the wall. The form of this local volume force normal to the surface which is triggering the transition to turbulence is given by

$$F_2 = \exp[((x - t_{x0}/t_{xsc})^2 - (y/t_{ysc})^2]f(z,t)$$
 (5)

where

$$f(z,t) = t_{ampt}[(1 - b(t))h^{i}(z) + b(t)h^{i+1}(z)],$$
(6)

with $i = \text{int}(t/t_{dt})$, $b(t) = 3p^2 - 2p^3$, $p = t/t_{dt} - i$. The h^i are Fourier series of unity amplitude with nzt = 10 random coefficients. The maximum amplitude of the forcing is $t_{ampt} = 0.2$, the length scales of the trip $t_{xsc} = 4.0$ and $t_{ysc} = 1.0$ and the forcing originates at $t_{x0} = 10$. We use a time interval $t_{dt} = 4.0$ between the change of the random part of the trip.

The computational box is 450 non-dimensional units long including 50 non-dimensional units for the fringe, 50 units high and 24 units wide. A resolution with 480 modes in streamwise direction, 193 modes in wall-normal direction and 64 modes in spanwise direction is used, which gives a total of 6 million points. The parameters of the fringe are $\lambda_{max} = 1.0$, $x_{start} = 400$, $x_{end} = 450$, $\Delta_{rise} = 40$ and $\Delta_{fall} = 10$. The rms-values of the turbulent fluctuations at the inflow have a maximum of 0.2 percent which is two orders of magnitude below the amplitude of the forcing triggering the transition to turbulence and in that sense the forcing is effective. The simulation without the application of time dependent forcing has also been run with double boxsize in spanwise direction giving similar results.

The boundary conditions are no-slip at the wall. Due to the finite size of the computational domain, the flow domain is truncated and an artificial boundary condition is applied at the freestream. A so-called asymptotic boundary condition is used, which is a generalization of the boundary condition used by Malik *et al.* (1985). It takes the form

$$(D+|k|)\hat{v} = (D+|k|)\hat{V}$$

$$(D+|k|)\hat{u} = (D+|k|)\hat{U}$$

$$(D+|k|)\hat{w} = 0$$
(7)

where $\hat{}$ denotes the Fourier transform in the horizontal direction, |k| is the absolute value of the horizontal wavenumber vector and D is the derivative in the wall-normal direction and a capital letter the mean flow component. This boundary condition allows the top of the computational domain to be placed closer to the wall in simulations where e.g. waves are present. Furthermore, in simulations of a transitional separation bubble this boundary condition has shown to give good agreement with the experimental findings as described by Häggmark et al. (2001). However, the asymptotic boundary condition cannot be applied at the start of the simulations because the correct base flow close to the upper boundary is not known in advance. To establish the bubble the simulation is initially performed with the freestream boundary condition that the normal derivative of the streamwise and spanwise component are set to zero and

$$Dv = DV_{APG} = -\frac{\partial U_{APG}}{\partial x} \tag{8}$$

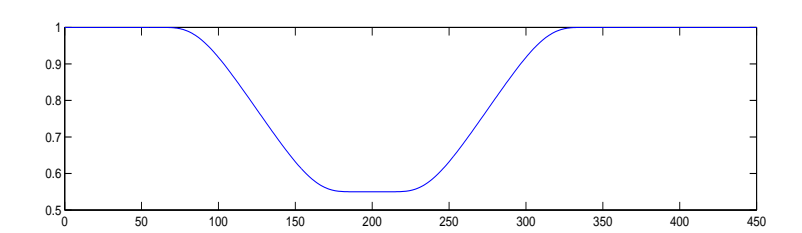


FIGURE 1. Freestream velocity distribution at the beginning of the simulation.

where

$$U_{APG} = 1 - (1 - U_{min})\left(S\left(\frac{x - x_{start}}{x_{fall}}\right) - S\left(\frac{x - x_{end}}{x_{rise}} + 1\right)\right)$$
(9)

and S as defined by (6). The initial freestream velocity distribution U_{APG} with $U_{min}=0.55,\,x_{start}=50,\,x_{end}=350,\,x_{fall}=x_{rise}=150$ used for the present simulation is shown in the fig. 1. The freestream distribution sets the pressure gradient and the chosen parameters are therefore important for the developing flow and its mean flow distribution.

The simulation is initially run with the boundary conditions (4) and (5). When a separation bubble has been established, the flow enters a quasi-equilibrium state but does not get completely statistically stationary. The mean flow is calculated by averaging in time and spanwise direction while the flow is in this quasi-equilibrium. We use this mean flow and switch to the asymptotic boundary conditions. Also in a previous investigation of a transitional separation bubble, Häggmark et al. (2001) used an asymptotic boundary condition, but also applied it at a later time because the correct base flow was not known a priori either. Proceeding in that manner, they achieved good agreement with the experimental results. Recently, Marxen (2004) developed an interaction modell for the simulation of a transitional separation bubble. The interaction model is an iterative implicit method to separate viscous and and inviscid effects based on potential flow theory and source and sink modelling of the separation induced displacement. The values for the boundary condition at the upper boundary are adjusted while the simulation is run until the iterative process has converged. The procedure applied in this study can be viewed as a first step where the boundary condition is retrieved through an iterative process consisting of two steps.

2.3. Disturbance generation

We use an oscillating wall-normal body force that exponentially decays from the boundary layer wall and is centred around the x-position x_0 . We assume the force to be given by

$$F_y = f_0 e^{-y/c} e^{-[(x-x_0)/x_{scale}]^2} \cos(\omega t) \cos(\beta z), \tag{10}$$

where f_0 is the forcing amplitude, ω the oscillation frequency, x_{scale} a parameter controlling the decay of the forcing in x-direction and c a parameter controlling the wall normal decay. The force is causing a wall normal flow. If the parameter $\beta \neq 0$, the force is also varying in spanwise direction. The parameter c controlling the wall normal decay has been chosen in relation to the boundary layer thickness and the parameter x_{scale} had been chosen so that the forcing is kept localized. For a more narrow distribution, the forcing is less effective. The effect of the change of the parameters of the forcing has also been tested on a Blasius boundary layer. The effect of the volume force causes a perturbation with the shape similar to a Tollmien-Schlichting wave. Therefore the body force models any device causing this type of perturbation.

2.4. Linear stability analysis

Linear instability analysis is used to analyse the sensitivity of the flow with respect to periodic excitations. The analysis is performed on the meanflow profile extracted from the DNS after averaging in both time and spanwise direction. The velocity profiles, below denoted U = U(y), are analysed by solving the Orr-Sommerfeld (O-S) equation. The Orr-Sommerfeld equation is an equation for the perturbation derived from the Navier-Stokes equations through linearization and can be written

$$(U-c)(D^{2}-k^{2})\tilde{v} - U''\tilde{v} - \frac{1}{i\alpha \text{Re}}(D^{2}-k^{2})^{2}\tilde{v} = 0$$
 (11)

when assuming a wavelike solution for the wall-normal component v^\prime of the disturbance velocity

$$v'(x, y, z, t) = \tilde{v}(y)e^{i(\alpha x + \beta z - \omega t)}$$
(12)

where α and β denote streamwise and spanwise wave numbers, respectively and $k^2 = \alpha^2 + \beta^2$. The results from the Orr-Sommerfeld equations are only valid as long as the perturbations are small enough and the length scale of the perturbations is smaller than the variation of the mean flow in horizontal direction due to the assumption of parallel mean flow which is made in the derivation. A temporal analysis of the Orr-Sommerfeld equations is performed. In the temporal framework, the equation is solved for a given wavenumber α as an eigenvalue problem in c. The solution is an eigenfunction with a corresponding eigenvalue $c = c_i + c_r$, where c_i is the growth rate and c_r the phase speed. The angular frequency can then be calculated as $\omega = \alpha c$. For a thorough derivation of the equations and further explanations of the stability problem see e.g. the textbook by Schmid & Henningson (2000).

3. Results

3.1. General description of the flow

We first discuss the results for the simulation without forcing. In figure 2a the mean skin friction coefficient and fig. 2b the mean flow in streamwise direction, averaged in both time and spanwise direction are shown. The simulation was

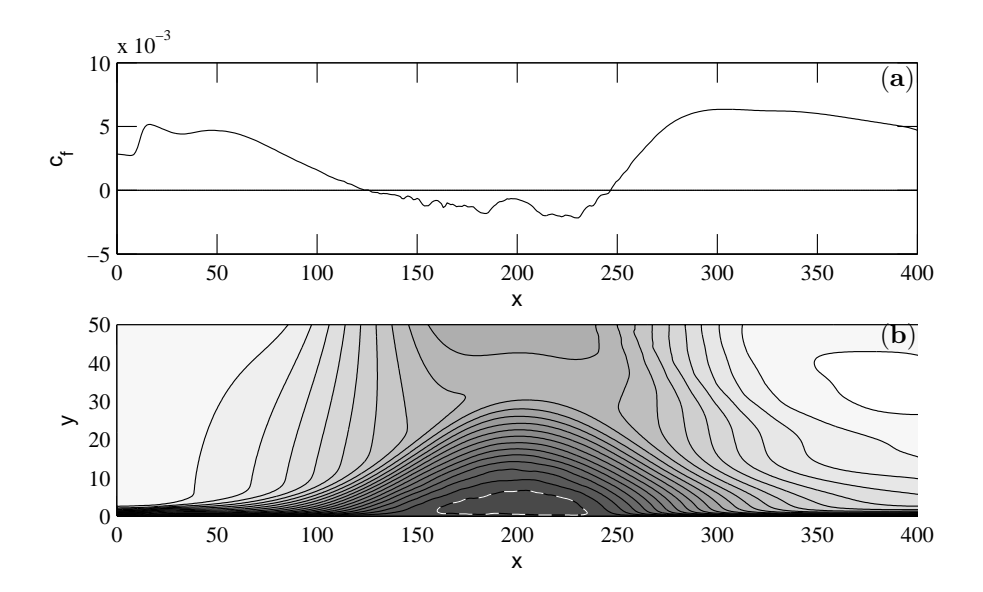


FIGURE 2. Simulation without forcing (a) Mean skin friction coefficient, (b) Contours of streamwise mean velocity (neg: dark grey to pos: white, white dashed line: -0.025, contour spacing 0.05).

run for 6000 time units. The averaged data is based on the data gathered during the last 2000 time units of the simulation. The slow convergence is due to the flapping motion associated with separation bubbles which has be observed in previous studies, e.g. Na & Moin (1998). At the freestream, the streamwise velocity is decelerating between x = 50 and x = 200 and then accelerating to the value of the freestream velocity at the inlet. This imposes an adverse to favourable pressure gradient on the boundary layer, creating a closed separation bubble. From the zeros of the skin friction coefficient which correspond to zero wall-shear stress the points of separation and reattachment can be determined. Na & Moin (1998) found this definition of separation and reattachment for their simulation of a turbulent boundary layer on a flat plate separating due to an adverse pressure gradient in good agreement with the points determined by the mean dividing streamline and the location of 50% backflow. As can been seen from the skin friction coefficient shown in fig. 2a, the flow is separating at $x_{sep} = 126$ and reattaching at $x_{att} = 247$, so the total reattachment length x_r is 121.

$3.2.\ Simulation\ with\ time-periodic\ forcing$

The mechanism of the time-periodic forcing to eliminate separation is demonstrated for forcing with a frequency of $\omega = 0.09$ and $f_0 = 0.1$ which is applied

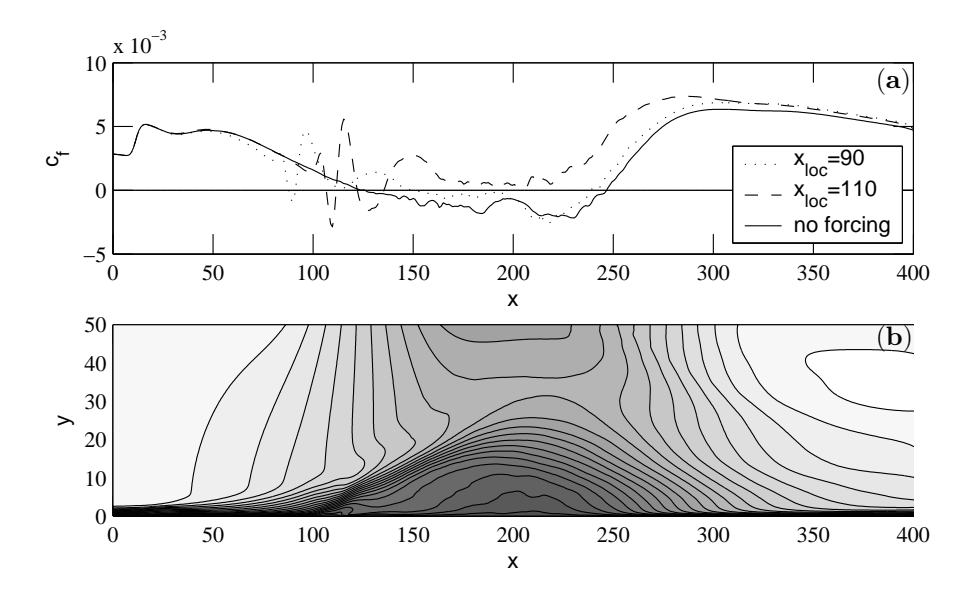


FIGURE 3. (a) Mean skin friction coefficient for case with forcing at $\omega = 0.09$ and $f_0 = 0.1$ and varying forcing position, (b) Contours of streamwise mean velocity for the case with forcing at $\omega = 0.09$ and $f_0 = 0.1$ around $x_0 = 110$. (neg: dark grey to pos: white, contour spacing 0.05).

around an x-position $x_0=110$. Based on phase averaged data, the amplitude of the disturbance in the flow has a maximum of 0.35 and is greater than 0.2 between x=103 and x=117. The forcing does not vary in spanwise direction ($\beta=0$). For all the cases with forcing discussed in this study, c=10 and $x_{scale}=5$ are constant. Both the mean skin friction coefficient and the mean streamwise velocity in fig. 3 show that the backflow region is eliminated. However, in the region where the forcing is applied, backflow occurs locally. From the instantaneous streamwise velocity shown in a x-y-plane at z=0 in fig. 4a large vortices can be seen developing at the origin of the forcing and travelling downstream in the shear layer above the bubble. These vortices are not present in the case without forcing shown for comparison in fig. 4b.

A close up on the region where the disturbances are generated is shown in fig. 5. The isosurfaces of the streamwise and the wall-normal component illustrate the two-dimensional character of the perturbations created by the forcing. These structures decay only slowly while travelling downstream and can be seen travelling upwards in the shear layer which is most clearly seen from the isosurfaces of the streamwise velocity component in fig. 5.

The streamwise turbulence intensity u_{rms} in the streamwise direction in fig. 13d shows a maximum in the shear layer above the detachment region in the

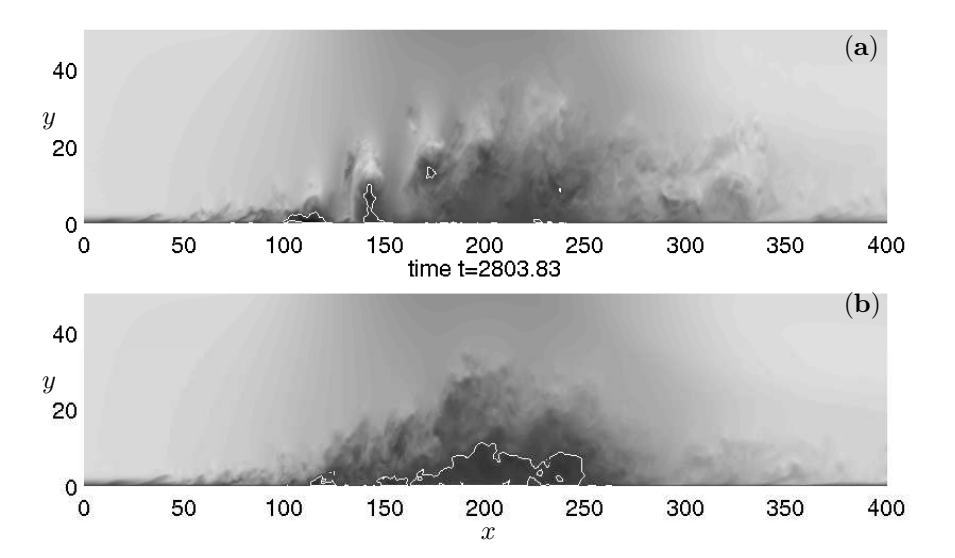


FIGURE 4. Instantaneous streamwise velocity (neg: dark grey to pos: white, white line: zero) for simulation with forcing at $\omega = 0.09$ and $f_0 = 0.1$ around $x_0 = 110$ (a) and without forcing (b).

simulation without forcing. As time periodic perturbations are imposed, the streamwise turbulence intensity shows a significant increase in the region where the forcing is applied and in the shear layer above the bubble (see fig.13a).

3.2.1. Influence of the forcing position

To examine the influence of the streamwise position at which the disturbances are generated the mean skin friction coefficient is shown in fig. 3a for two simulations differing only in the position of the forcing and is compared to the case without forcing.

The amplitude is $f_0 = 0.1$ and the frequency is $\omega = 0.09$ in both cases with forcing. In both cases the separated area is affected by the forcing. If the forcing is centred around $x_0 = 90$, the point of separation which is located at $x_{sep} = 125$ in the simulation without forcing moves downstream to x = 150. The position of reattachment is not significantly affected, it is only slightly promoted to x = 242 compared to x = 245 in the case without forcing. This implies that the reattachment length is reduced by 30%. If the forcing is placed closer to the separation point at x = 110, the skin friction coefficient never becomes negative in the region where we observe separation in the case without forcing. However, we observe a small region of separation where the disturbance is generated.

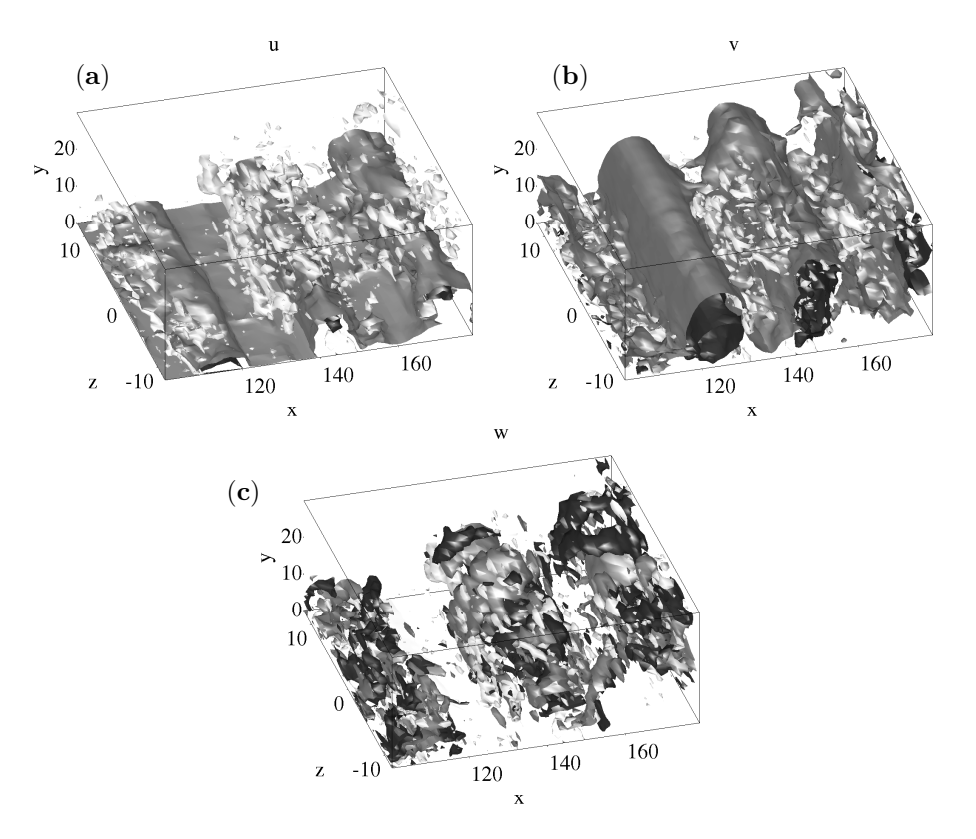


FIGURE 5. Isosurfaces of (a) instantaneous streamwise velocity component at values of +0.1 (grey) and -0.1(dark grey) and spanwise vorticity at 0.2 (light grey) (b) instantaneous wall-normal velocity component at values of +0.1 (grey) and -0.1 (dark grey) and spanwise vorticity at 0.2 (light grey) (c) instantaneous spanwise velocity component spanwise velocity component at values of +0.1 (grey) and -0.1(dark grey) and spanwise vorticity at 0.2 (light grey).

The decrease of the separation bubble in both height and length can be seen from the plot of contours of streamwise mean velocity, see fig. 6.

Comparing the mean velocity profiles in fig. 7, one observes that at x=150 the profiles for both forcing positions deviate from the case without forcing. For the forcing at x=110, the velocity is higher than without disturbances at all y-positions whereas for the forcing centred around x=90 the velocity is lower between y=10 and y=15. At x=200 the profile is still s-shaped for the forcing located at x=110, but follows almost the shape of the profile without disturbances for the forcing centred at x=90.

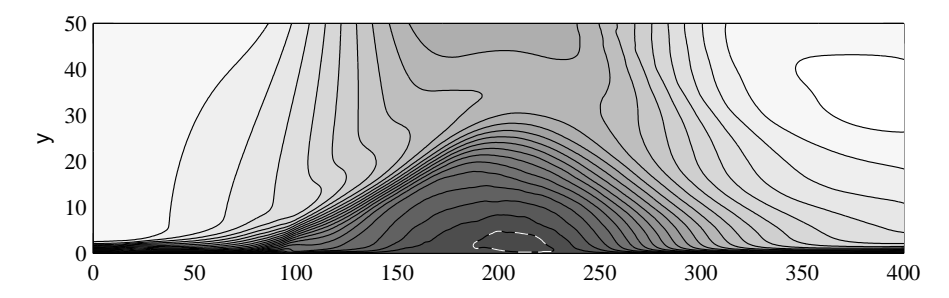


FIGURE 6. Contours of streamwise mean velocity for case with forcing at $\omega = 0.09$ and $f_0 = 0.1$ around $x_0 = 90$. (neg: dark grey to pos: white, white dashed line: -0.025, contour spacing 0.05).

Placing the forcing closer to the separated area effects also the distribution of the streamwise component of the mean velocity at the freestream which can be seen from fig. 7c. The mean freestream velocity is lower between x=150 and x=250 compared to the case without forcing if the forcing is placed as close as $x_0=110$.

3.2.2. Influence of the Forcing Amplitude

An important parameter of the time varying forcing is the forcing amplitude. The influence of the forcing amplitude is examined for a forcing position $x_0 = 110$ and frequency $\omega = 0.09$. The forcing amplitudes $f_0 = 0.01$ and $f_0 = 0.05$ are tested and compared to the results of the case for forcing with an amplitude $f_0 = 0.1$ discussed before.

If the forcing amplitude is reduced to $\frac{1}{10}$ of the basic case, the main parameters as separation and reattachment point and reattachment length are not significantly influenced (see table 1). For half the forcing amplitude, both separation and and reattachment are delayed. The length of the separation bubble x_r is slightly decreased. However, it has been observed that the height of the separation bubble is increased and the value of the skin friction coefficient is lower in the region before reattachment than without forcing (see fig. 8). Therefore relatively high amplitudes are necessary in order to prevent separation.

3.2.3. Influence of the Forcing Frequency

The influence of different forcing frequencies shown in table 1 is examined at a constant x-position $x_0 = 110$ and a constant forcing amplitude $f_0 = 0.1$. The length of the separation x_r is measured behind x = 120, e.g. behind the

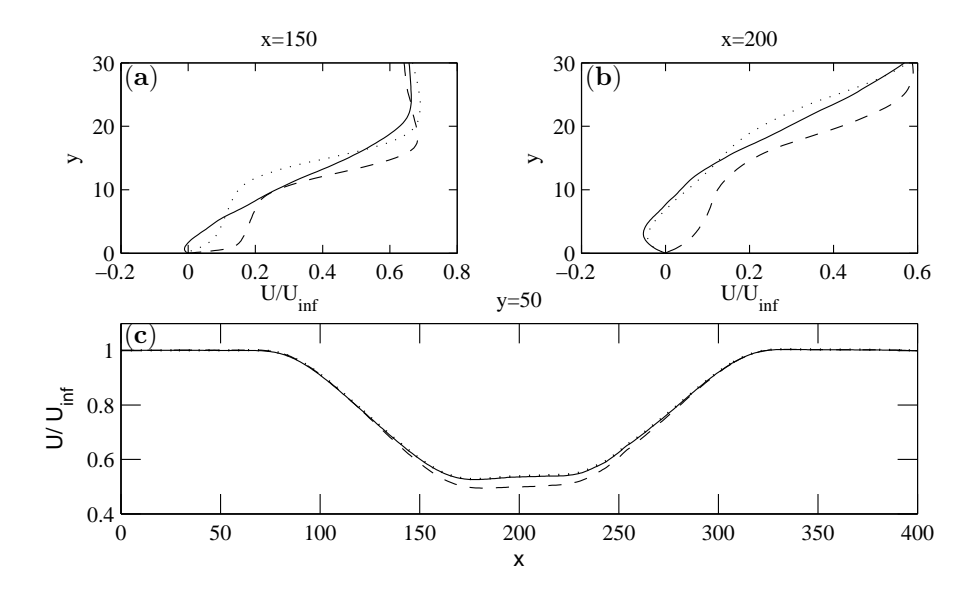


FIGURE 7. Streamwise velocity profiles at (a) x=150 and (b) x=200 for forcing at $\omega=0.09$ and $f_0=0.1; \cdots, x_0=90; ---, x_0=110;$ — no forcing. , (c) Mean streamwise freestream velocity distribution for forcing $\omega=0.09$ and $f_0=0.1,\cdots,x_0=90; ---, x_0=110;$ — no forcing.

centre of the forcing x_0 . The forcing is most effective for frequencies in the range $0.07 \le \omega \le 0.1$. In this range the reattachment length is reduced by 90 %. However, a short bubble due to the forcing is occurring at the location where the forcing is centred. If the frequency is scaled with the mean reattachment length without forcing x_r , and the freestream velocity at the inlet, we compute a most effective reduced frequency $F^+ = fx_r/U_{\infty}$ in the range $1.34 \leq F^+ \leq 1.92$, so $F^+ \approx \mathcal{O}(1)$. For periodic excitation of the separated turbulent flow from a deflected flap also Nishri & Wygnanski (1998) found the most effective frequency $F^+ \approx \mathcal{O}(1)$. Amitay & Glezer (2004) also observed for the actuation of flow over a stalled airfoil an effective frequency range for $F^+ \approx \mathcal{O}(1)$, but found a second even more successful frequency range for $F^+ \approx \mathcal{O}(10)$. In our investigation such a second, more effective frequency band at higher frequencies was not observed. For the frequency $\omega = 0.15$, separation is delayed, but the skin-friction coefficient is decreased to a lower value than without forcing (see fig. 8a). Therefore also reattachment is delayed and the reattachment length is slightly increased in comparison to the case without forcing. For the frequencies 0.2 and 0.3, separation is delayed and the reattachment length is only slightly decreased by 10 %. For frequencies lower

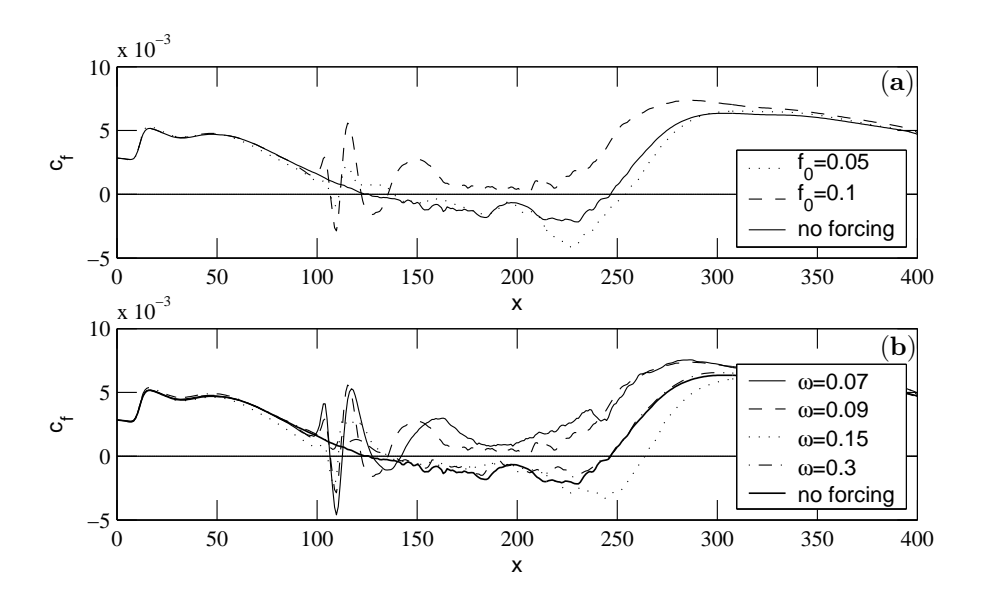


FIGURE 8. (a) Influence of forcing amplitude: Skin friction coefficient for forcing at $\omega=0.09$ and $x_0=110$, (b) Influence of forcing frequency: Skin friction coefficient for forcing with $f_0=0.1$ at $x_0=110$.

ω_t	f_0	x_{sep}	x_{att}	x_r	$U_{\infty}(x=200)$
-	-	126	247	121	0.54
0.07	0.1	128	141	13	0.50
0.09	0.1	122	135	13	0.50
0.10	0.1	121	133	12	0.50
0.15	0.1	135	261	126	0.59
0.20	0.1	146	255	109	0.56
0.30	0.1	135	245	110	0.53
0.09	0.01	126	246	120	0.53
0.09	0.05	138	255	117	0.57
0.09	0.1	122	135	13	0.50

Table 1. Frequency and amplitude dependence for forcing centred at $x_0 = 110$, $\beta = 0$. x_{sep} denotes mean separation point, x_{att} denotes mean reattachment point x_r mean reattachment length.

than the most effective frequency range, separation is delayed, but the reattachment length is decreased less than for the most effective frequency range. However, the results for frequencies below $\omega=0.07$ were not of interest here and are therefore not shown in Table 1. Those lower frequencies correspond to

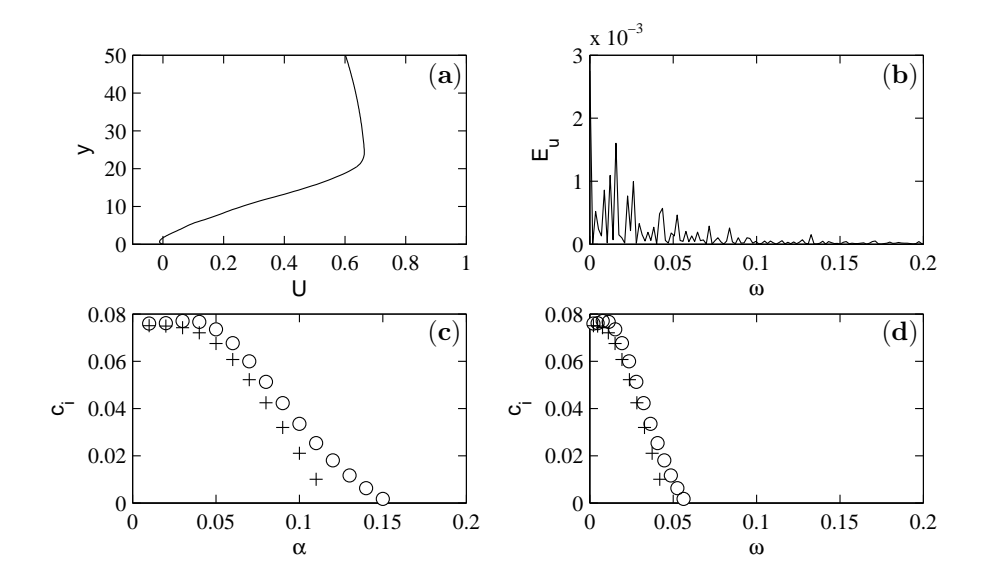


FIGURE 9. (a) Profile of streamwise mean velocity at x=150 $(x=x_{sep}+0.2x_r)$, (b) energy spectrum of streamwise velocity component at x=150, y=7, (c) growth rate c_i for least stable mode versus α and (d) growth rate c_i for least stable mode versus ω . Crosses denote results achieved with, circles without smoothing in Chebyshev space.

wavelengths in the range of the length of the bubble. However, the idea of the forcing is not to intensify motions corresponding to the movement of the entire bubble and therefore higher frequencies are used. In an attempt to understand these results we perform a linear stability analysis which is presented in the section below.

3.2.4. Linear stability analysis

Temporal stability results are presented with the aim of understanding why relatively high amplitudes and low frequencies are necessary in order to eliminate separation by time perodic forcing. The analysis was performed on the mean flow calculated from the DNS data without forcing by averaging in both time and spanwise direction. Due to the fact that turbulent mean profile represents the flow only in an averaged sense and that the boundary layer is growing the results from such an analysis have to be interpreted carefully. A more advanced analysis where the effect of the turbulent stresses are taken into account would contribute further understanding but is out of the scope of the present paper.

The results are shown in fig. 9 for a profile of the streamwise mean velocity which has been extracted at the position x = 150 ($x = x_{sep} + 0.2x_r$). Within

the temporal framework, the wavenumber is given and phase speed and growth rate have to be determined. Therefore the growth rate c_i is shown versus α in fig. 9. Since the frequency is related to the phase speed $\omega = \alpha c$, the corresponding frequency ω is calculated and the dependence of c_i is shown versus the corresponding frequency ω . The growth rate has a maximum at $\omega = 0.01$ and is then decreasing. For frequencies higher than $\omega = 0.06$ no modes are amplified. Comparing these results to the energy spectra of the mean streamwise component, we observe a peak in approximately the same frequency range with a maximum between $\omega = 0.01$ and 0.02, which is in qualitative agreement with the results from the linear stability analysis. The fact that the observed growth rates are very small and that only low frequencies are unstable is possibly due to the low Reynolds number in the simulations. This explanation is supported by the fact that the stability calculations show more unstable frequencies if the analysis is performed for the same profile at a higher Reynolds number.

The results of linear instability calculations can be very sensitive to slight changes in the mean velocity profile. To examine the influence of small deviations still persistent in the mean profile, the mean velocity profile has been smoothed by truncating the associated Chebyshev series. The results of the linear stability analysis performed on the smoothed profile show good agreement with the results for the profile not subjected to the smoothing process (see fig. 9c,d). However, the growth rate decays slightly faster with increasing α for the smoothed profile shown in fig. 9c. Depending on the frequency ω , which is the parameter of interest for the forcing, the growth rates of the two profiles nearly collapse as shown in fig. 9d.

Despite the limitations of performing a linear stability analysis on the turbulent mean flow and the qualitative character due to the growth of the boundary layer, these results give an indication why relatively high amplitudes are needed in order to eliminate separation by time varying forcing. Note that also the unstable frequencies correspond to wavelength on the order of the bubble length. This indicates a possibility of a global instability of the turbulent separation bubble. However, this has to be investigated using a more advanced bi-global stability analysis, see e.g. Theofilis (2003).

3.3. Spanwise varying forcing

The results presented in the previous sections concern the effect of periodic forcing without variation in the spanwise direction. Since time-varying forcing requires unexpected high amplitudes and also the results of the linear stability analysis show only low growth rates, a comparision with forcing varying in the spanwise direction has been performed. Steady spanwise forcing turned out to be very effective in eliminating the separated region. In this section we investigate the influence of the spanwise varying forcing.

Figure 10b shows how the mean flow in streamwise direction is affected by a spanwise varying forcing centered at $x_0 = 110$ varying in spanwise direction

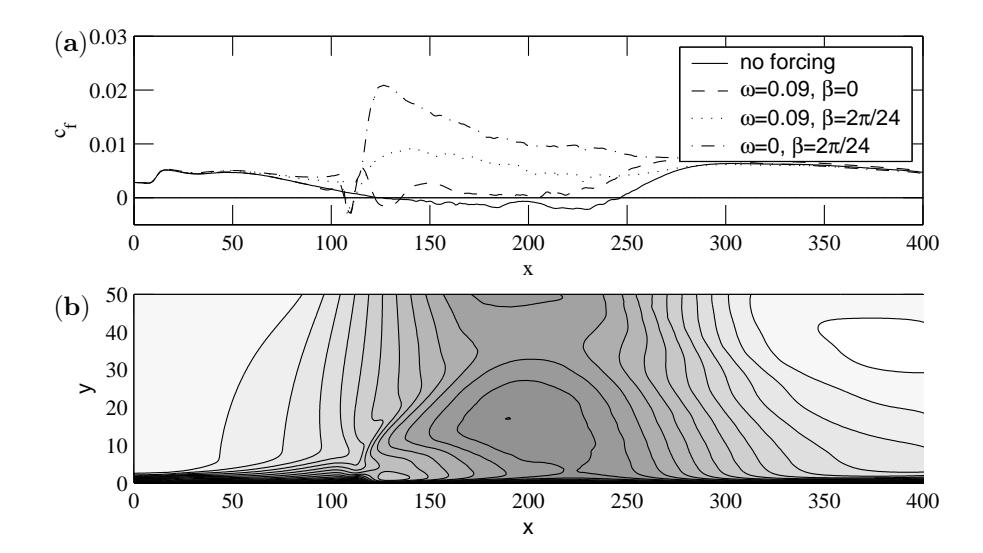


FIGURE 10. Spanwise varying forcing: (a) Mean skin friction coefficient, (b) Forcing with $\omega = 0.0$, $\beta = \frac{2\pi}{24}$, mean streamwise velocity, contour spacing 0.05.

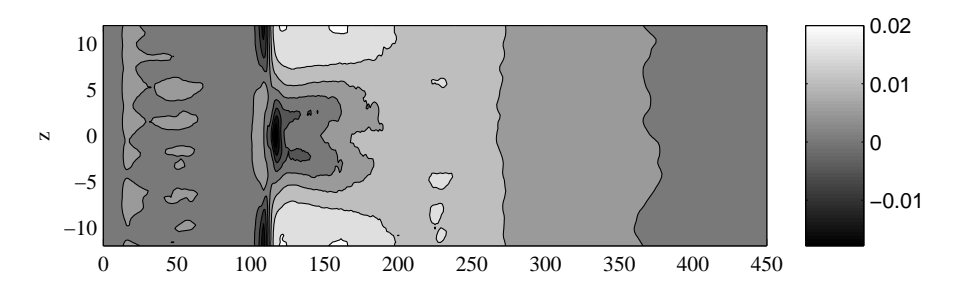


FIGURE 11. Contour plot of skin friction coefficient for spanwise varying forcing with $\omega=0.0,\ \beta=\frac{2\pi}{24}$ and f=0.05, contour spacing 0.005.

with $\beta = \frac{2\pi}{24}$ and an amplitude $f_0 = 0.1$. The flow stays attached in the time- and spanwise averaged mean in the region where the flow separates if no forcing is applied. Figure 10a shows the mean skin friction coefficient averaged in both time and spanwise direction as a measure of how the flow is affected by the forcing for the case of a steady spanwise forcing centered at $x_0 = 110$ varying in spanwise direction with $\beta = \frac{2\pi}{24}$ (dashed-dotted line). The skin friction coefficient is increased significantly compared to a forcing with the same forcing amplitude $f_0 = 0.1$ which varies in time but is homogeneous in spanwise direction (dashed line). Decreasing the amplitude of the spanwise

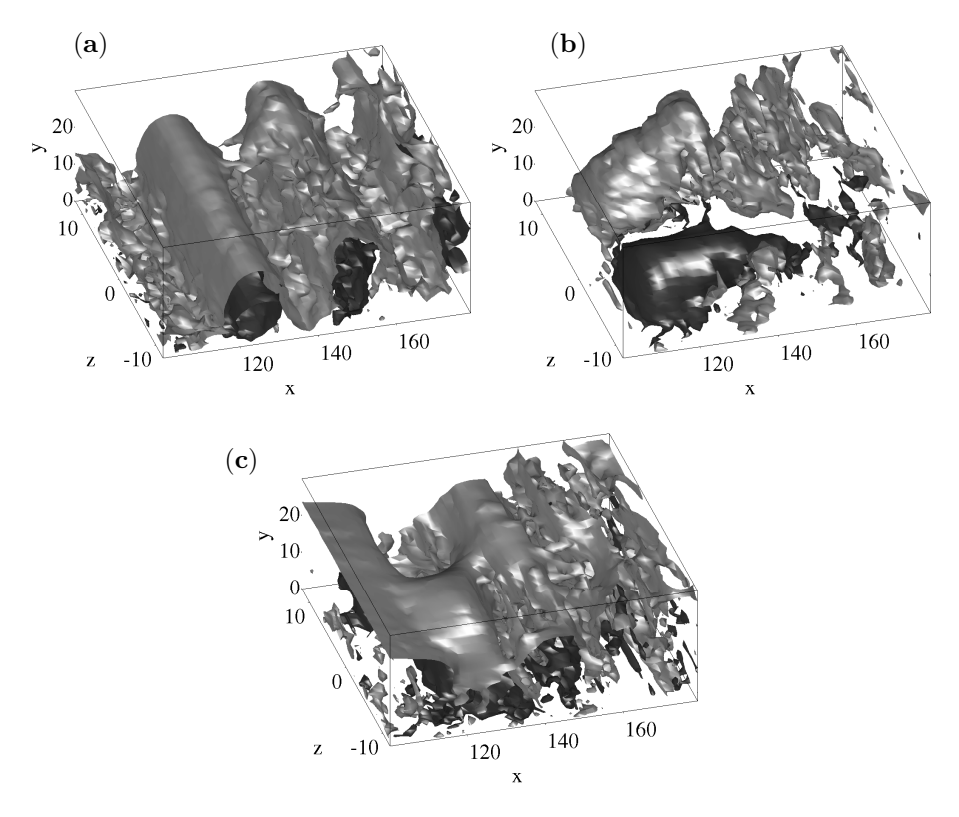


FIGURE 12. Instantenous wall-normal velocity component for different types of forcing: (a) Isosurfaces at values of +0.1 (light) and -0.1 (dark) for forcing with $\omega=0.09,~\beta=0$ (b) Isosurfaces at values of +0.2 (light) and -0.2 (dark) for forcing with $\omega=0.0,~\beta=\frac{2\pi}{24}$ (c) Isosurfaces at values of +0.1 (light) and -0.1 (dark) for forcing at $\omega=0.09,~\beta=\frac{2\pi}{24}$.

varying forcing described above by 50%, the flow has been observed to stay attached in the region where separation occurs if no forcing is applied. Thus the spanwise varying forcing is more effective compared to the two-dimensional time-periodic forcing.

For this case, a contour plot of the skin friction coefficient averaged only in time is shown (fig. 11). The skin friction coefficient is varying in the spanwise

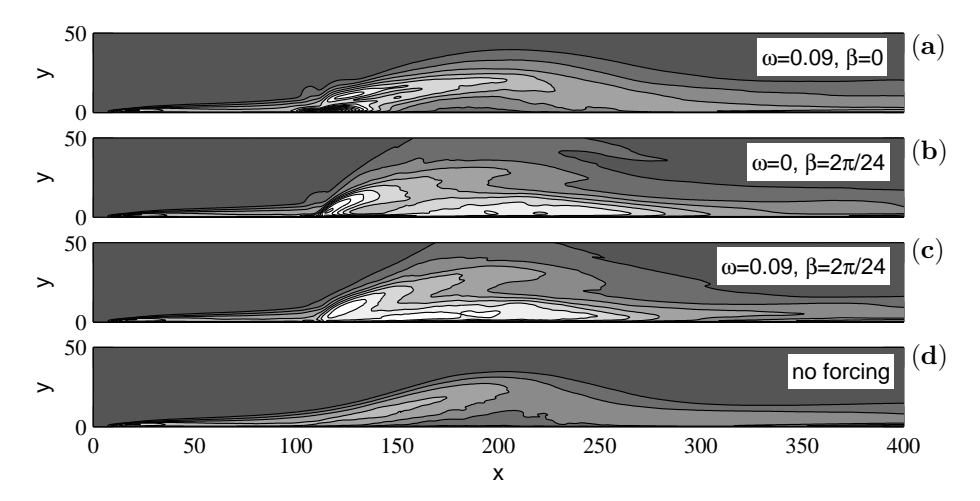


FIGURE 13. Contours of streamwise turbulent fluctuation (0.0 to 0.5, spacing 0.03).

direction in the region where the forcing is applied and the spanwise variation persists downstream towards x=200. However, the flow stays attached downstream x=140 for all spanwise positions judging by the skin friction coefficient.

A combination of the time dependent and spanwise effects has also been tested by applying a forcing which varies both in time and in spanwise direction. The curve of the skin friction coefficient ($dotted\ line$) is located between the skin friction coefficient for the forcing only varying in spanwise direction and the forcing only varying in time with the same forcing amplitude applied at the same forcing position x_0 .

To illustrate the effect of the different types of forcing on the flow, a close up of the region where the forcing is applied, is shown in fig. 12b for the steady spanwise forcing and in fig. 12c for the forcing both in time and in spanwise direction in comparison the only time-dependent forcing 12a. The isosurfaces of the instantaneous wall normal component illustrate the effect of the forcing on the flow. A spanwise varying structure is clearly seen in case the spanwise varying forcing whereas the structures due to the time dependence of the forcing are clearly visible if the forcing is varying in both time and spanwise direction.

To examine the effect of the forcing on the flow further, turbulent fluctuations have been compared for the there cases discussed in this section. As an example, the contour plots of the streamwise fluctuation are shown in fig. 13. For all types of forcing compared here, the streamwise fluctuation is significantly higher than if no forcing is applied. The comparison of the turbulent fluctuations shown in fig.13 reveals that the time-dependent forcing mainly

affects the shear layer whereas in the case of spanwise varying forcing the fluctuations also increase in the area where backflow occurs without forcing.

4. Conclusions

Direct numerical simulations of a turbulent boundary layer separating under a strong adverse pressure gradient have been performed. This flow configuration has been examined as a model problem for separation occurring in the technological applications of interest, e.g. diffuser like flows.

The aim of our study was to investigate the effect of periodic excitations on the separated region occurring in this flow. For time-dependent forcing, we have analysed how the position, the amplitude and the frequency of the forcing affect the flow. The influence of forcing varying in the spanwise direction has been studied for both steady spanwise forcing and in combination with time varying forcing.

We have shown that the flow in the separated region can be forced to stay attached by applying time-periodic perturbation upstream the separated region. This is due to fact that the mixing is enhanced which can be interfered from larger rms-values of the fluctuating component.

Investigating the influence of the position of the forcing, we found that the closer the forcing is located with respect to the separation point, the more effective it is in suppressing separation. When considering the frequency dependence of the forcing we found the frequencies in the range $0.07 \le \omega \le 0.1$ most suitable to reduce the area where backflow occurs. It has been observed that sufficiently high amplitudes are necessary in order to reduce the reattachment length. The order of magnitude needed for the forcing to effect the separation bubble is higher than expected. However with an amplitude $f_0 = 0.1$ nondimensionalized with the freestream velocity at the inlet and the displacement thickness at the inlet, the order of magnitude of the volume force is considerably lower than the other forces in the flow. The turbulent separation on a flat plate investigated here is a result of a strong pressure gradient only and not any geometry changes. It is in this regard different from the cases where timeperiodic excitation was found to be effective for lower amplitudes. Contrary to the present investigation, the point of separation does not fluctuate in the cases where a geometry change fixes the separation point, which simplifies the understanding of the dynamics of the time-dependent forcing.

The temporal linear stability analysis has been carried out on a mean streamwise velocity profile taken at the beginning of separated region and showed that the mean velocity profile is only unstable for frequencies below $\omega=0.06$. The growth rates are small even in the frequency range where the flow is susceptible to perturbations. This is possibly due to low to the Reynolds number in the direct numerical simulations. However, the parallel mean flow assumption in the linear stability analysis means that one has to be careful interpreting the results of the linear stability analysis for lower frequency disturbances. In the experimental investigation of periodic excitation of the

flow over a backward-facing step, Roos & Kegelman (1986) found by varying the Reynolds number that a reduced effectiveness of shear layer excitation was present when the turbulence was not fully developed.

Spanwise variation of the forcing has been shown to be more effective in eliminating the separated region than two-dimensional time-varying forcing. Applying a steady spanwise forcing with half the forcing amplitude used for the time dependent forcing, the flow stays attached in the region where it separates without forcing. At a higher Reynolds number, time-varying forcing is expected to be more effective, since the two-dimensional disturbances are then expected to be more unstable, and do not have to be forced with such high amplitudes. However for the flow over a backward-facing step, Chun et al. (1999) and Kang & Choi (2002) showed that the reattachment length could be reduced the most by a suitable combination of time dependent forcing and forcing varying in spanwise direction. Investigations of such forcing combinations together with more advanced feedback control schemes would be interesting in future investigations.

Acknowledgements

Dr. Luca Brandt is acknowledged for his help with the stability calculations. The work was funded by the Vinnova competence centre PSCI at NADA, KTH. Partial funding from STEM is also acknowledged.

References

- ALVING, A. E. & FERNHOLZ, H. H. 1995 Mean velocity scaling in and around a mild, turbulent separation bubble. *Phys. Fluids* **7**, 1956–1969.
- ALVING, A. E. & FERNHOLZ, H. H. 1996 Turbulence measurements around a mild separation bubble and downstream of reattachment. *J. Fluid Mech.* **322**, 297–328.
- Amitay, M. & Glezer, A. 2004 Role of Actuation Frequency in Controlled Flow Reattachment over a Stalled Airfoil. *Exps. Fluids* **36**, 43–52.
- ANGELE, K. 2003 Experimental studies of turbulent boundary layer separation and control. Ph.D.thesis, Tec. Rep. TRITA-MEK 2003:08, Department of Mechanics, KTH, Stockholm, Sweden.
- Chun, K., Lee, I. & Sung, H. 1999 Effect of spanwise varying local forcing on turbulent separated flow over a backward facing step. Exps. Fluids 26, 437–440.
- CORKE, T., POST, M. L., ORLOV, D. & McLAUGHLIN, T. E. 2002 Application of weakly-ionized plasmas as wing flow-control devices. AIAA Paper 2002, 0350.
- Dengel, P. & Fernholz, H. 1990 An experimental investigation of an incompressible turbulent boundary layer in the vicinity of separation. *J. Fluid Mech.* **212**, 615–636.
- Driver, D. M. 1991 Reynolds shear stress measurements in a separated boundary layer flow. $AIAA\ Paper\ \mathbf{91},\ 1787.$
- GLEZER, A. & AMITAY, M. 2002 Synthetic jets. Annu. Rev. Fluid Mech. 34, 503-529.

- GREENBLATT, D. & WYGNANSKI, I. J. 2000 The control of flow separation by periodic excitation. *Prog. Aerosp. Sci.* **36**, 487–545.
- HÄGGMARK, C. P., HILDINGS, C. & HENNINGSON, D. 2001 A numerical and experimental study of a transitional separation bubble. *Aerosp. Sci. Techol.* **0**, 1–12.
- Kalter, M. & Fernholz, H. 1995 The influence of freestream turbulence on an axisymmetric turbulent boundary layer in, and relaxing from, an adverse pressure gradient. In *Advances in Turbulence V. Proc. 5th Eur. Turb. Conference (Siena, Italy, 1994)*, pp. 261–265. Kluwer.
- Kang, S. & Choi, H. 2002 Suboptimal feedback control of turbulent flow over a backward facing step. *J. Fluid Mech.* **463**, 201–227.
- KIM, J., MOIN, P. & MOSER, R. 1987 Turbulence statistics in fully developed channel flow at low Reynolds number. J. Fluid Mech. 177, 133–166.
- Kiya, M., Shimizu, M. & Mochizuki, O. 1997 Sinusoidal forcing of a turbulent separation bubble. *J. Fluid Mech.* **342**, 119–139.
- Lundbladh, A., Berlin, S., Skote, M., Hildings, C., Choi, J., Kim, J. & Henningson, D. S. 1999 An efficient spectral method for simulation of incompressible flow over a flat plate. Technical Report KTH/MEK/TR-99/11–SE. KTH, Department of Mechanics, Stockholm, Sweden.
- Malik, M. R., Zang, T. A. & Hussaini, M. Y. 1985 A spectral collocation method for the Navier-Stokes equations. *J. Comp. Phys.* **61**, 64–88.
- Manhardt, M. & Friedrich, R. 2002 DNS of a turbulent boundary layer with separation. *Int. J. Heat and Fluid Flow* 23, 572–581.
- MARXEN, O. 2004 Numerical studies of physical effects related to the controlled transition process in laminar separation bubbles. Dissertation, Universität Stuttgart, Stuttgart.
- NA, Y. & Moin, P. 1998 Direct numercial simulation of a separated turbulent boundary layer. J. Fluid Mech. 374, 379–405.
- NISHRI, B. & WYGNANSKI, I. J. 1998 Effects of periodic excitation on turbulent flow separation from a flap. AIAA J. 36 (4), 547–556.
- NORDSTRÖM, J., NORDIN, N. & HENNINGSON, D. S. 1999 The fringe region technique and the Fourier method used in the direct numerical simulation of spatially evolving viscous flows. *SIAM J. Sci. Comput.* **20** (4), 1365–1393.
- Obi, S., Ishibashi, N. & Masuda, S. 1997 The mechanism of momentum transfer in the periodically perturbed turbulent separated flow. In 2nd Int. Symposium on Turbulence, Heat and Mass Transfer (eds. K. Hanjalić & T. Peeters), pp. 835–844. Delft University Press.
- Orlov, D. & Corke, T. 2005 Numerical simulation of aerodynamic plasma actuator effects. AIAA Paper ${f 2005}$, 1083.
- Perry, A. E. & Fairlie, B. D. 1975 A study of turbulent boundary layer separation and reattachment. *J. Fluid Mech.* **69**, 657–672.
- Roos, F. W. & Kegelman, J. 1986 Control of coherent structures in reattaching laminar and turbulent shear layers. AIAA J. 24, 1956–1963.
- Schmid, P. & Henningson, D. S. 2000 Stability and transition in shear flows. Springer.
- Sigurdson, L. 1995 The structure and control of a turbulent reattaching flow. J. Fluid Mech. 298, 139–165.

- SIMPSON, R. L. 1996 Aspects of turbulent boundary-layer separation. *Prog. Aerosp. Sci.* 32, 457–521.
- SIMPSON, R. L., CHEW, Y. T. & SHIVAPRASAD, B. G. 1981a The structure of the separating turbulent boundary layer. Part1. Mean flow and Reynolds stresses. J. Fluid Mech. 113, 23–51.
- SIMPSON, R. L., CHEW, Y. T. & SHIVAPRASAD, B. G. 1981b The structure of the separating turbulent boundary layer. Part2. Higher-order turbulence results. J. Fluid Mech. 113, 53–73.
- SIMPSON, R. L., STRICKLAND, J. & BARR, P. 1977 Features of a separating turbulent boundary layer in the vicinity of separation. *J. Fluid Mech.* **79**, 553–594.
- Skote, M. & Henningson, D. 2002 Direct numercial simulation of a separated turbulent boundary layer. J. Fluid Mech. 471, 107–136.
- SPALART, P. & COLEMAN, G. 1998 Numerical simulation of a separation bubble with heat transfer. *Eur. J. Mech. B./Fluids* **16**, 169–189.
- Theofilis, V. 2003 Advances in global linear instability analysis of nonparallel and three-dimensional flows. *Prog. Aerosp. Sci.* **39**, 249–315.
- Yoshioka, S. 2001 Control of separated flow over a backward-facing step by periodic forcing. Ph.d.thesis, Department of Mechanical Engineering, Keio University, Keio.

Paper 2

2

Instability characteristics of harmonic disturbances in a turbulent separation bubble

By Astrid H. Herbst¹, Steve Deubelbeiss², Saskia Spehr³, Ardeshir Hanifi⁴ and Dan S. Henningson¹

¹KTH Mechanics, SE-100 44 Stockholm, Sweden

²Inst. of Fluid Dynamics, Dept. of Mechanical and Process Engineering,
ETH Zürich, Switzerland

³Inst. f. Strömungslehre, Universität Karlsruhe, Germany

 $^4\mathrm{Division}$ of Systems Technology, Swedish Defence Agency, Stockholm, Sweden

Proceedings of XVII Congresso AIMETA di Mechanica Teorica e Applicata

Keywords: separated flow, direct numerical simulation, flow instability, POD

SUMMARY: The instability characteristics of a turbulent flat plate boundary layer separating under a strong adverse pressure gradient are examined. The analysis is based on the data of direct numerical simulation. A theoretical model of harmonic perturbations is considered, including the contribution of the turbulent part of the flow, to investigate the stability characteristics of the flow. The structure of the organized waves is also investigated by means of Proper Orthogonal Decomposition (POD).

1. Introduction

The understanding of the behavior of a flow in a boundary layer and the knowledge of its physical implications like the wall shear rate or the heat transfer is in many technical and industrial applications often of paramount importance (for example for the design of a turbine blade). These physical properties depend heavily on if the flow is laminar, transitional or turbulent and if there a separation bubble occurs or not. Therefore, Direct Numerical Simulations (DNS) of a turbulent boundary layer separating under a strong adverse pressure gradient have been performed in Herbst (2004) and Herbst & Henningson (2005), which provide a basis for the present work. Flow separation limits the performance of many technical devices due to severe pressure losses. For this reason flow control may be desired to eliminate or reduce the size of the separation bubble. An interesting control approach, investigated in Herbst (2004) and Herbst & Henningson (2005), is to use periodic excitation to eliminate the separation. The turbulent flow over a flat plate with pressure gradient has been chosen as a model for separation and its control for the technological applications of interest, e.g. in diffusers.

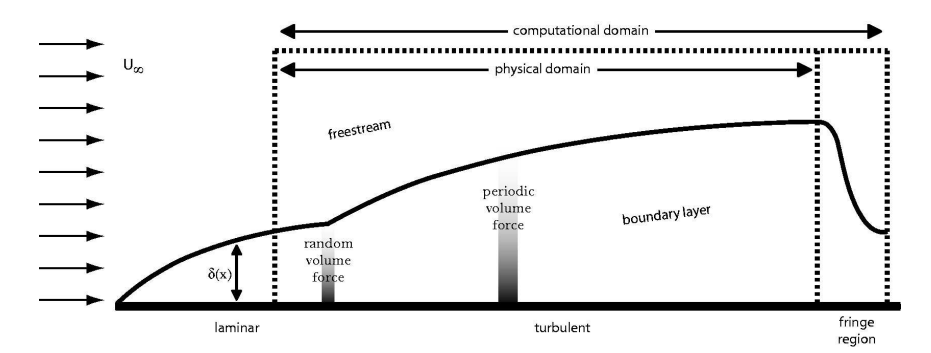


FIGURE 1. The physical and computational domain with the random volume force for the turbulence generation and the periodic volume force for the separation control.

These previous studies showed that the parameters (frequency and spanwise wavenumber) of the most efficient periodic forcing do not correspond to the most unstable mode predicted by the local linear stability analysis. This stability analysis was made based on the time-averaged profiles, ignoring the contribution of the turbulent part of the flow. One of the objective of the present work is to advance the analysis by including the effects of the random turbulent flow. For this matter, we follow the approach of Hussain & Reynolds (1972) who used an eddy viscosity model to calculate the Raynolds stress terms caused by presence of organized waves in a turbulent flow. This approach was also used by Reau & Tumin (2000) to investigate the characteristics of harmonic perturbations in turbulent wakes.

The present article is based on the master thesis of S. Spehr (2004) and S. Deubelbeiss (2005). Since new numerical simulations were performed some parts of the analysis were repeated and enhanced.

2. Direct Numerical Simulations

The flow in a separated boundary layer over a flat plate has been studied by means of numerical simulations. Further, a periodic volume forcing has been used to control the separation bubble.

The computational box (see figure 1) is 450 nondimensional units long including the fringe region with a length of 50, 50 units high and 24 units wide. A resolution with 480 points in streamwise direction, 193 points in wall normal direction and 64 points in spanwise direction is used. Here, the reference length is the displacement thickness at inlet of the box where the Reynolds number Re = 400. For a description of the numerical tools the readers are referred to Herbst (2004).

The streamwise component of the freestream velocity, \overline{u}_e , used to generate the separation bubble, is shown in figure 2. At the leading edge (x = 0) a laminar Blasius boundary layer profile is introduced. Downstream at position

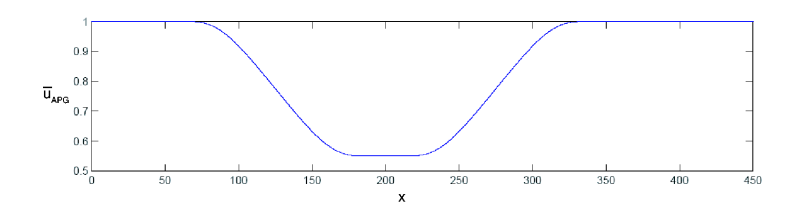


FIGURE 2. Freestream velocity distribution at the beginning of the simulation.

x=10 the laminar-turbulent transition is triggered by a random volume force near the wall (see figure 1). When no control is imposed, the separation of the flow occurs at $x_{sep}=126$ and the reattachment point is at $x_{att}=247$ (reattachement length: $x_r=121$). The control is performed by means of an oscillating volume force F_y in the wall-normal direction. This volume force decays exponentially from the boundary layer wall and is centered around x_0

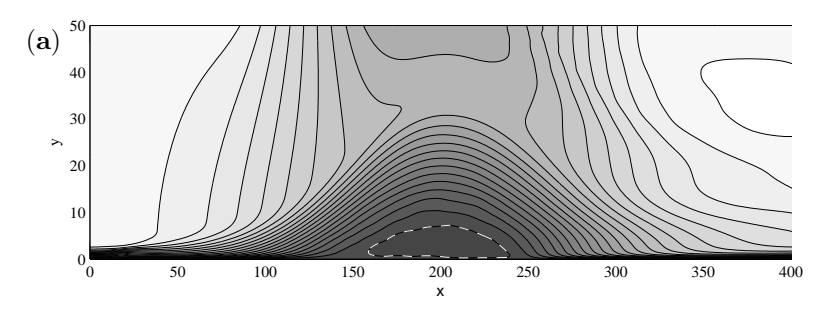
$$F_y = f_0 \exp\left(-\frac{y}{c} - \left[\frac{x - x_0}{x_{scale}}\right]^2\right) \cos(\omega t) \cos(\beta z) , \qquad (1)$$

where f_0 is the forcing amplitude, ω the oscillation frequency, β the spanwise wavenumber, x_{scale} a parameter controlling the decay of the forcing in x direction and c a parameter controlling the wall normal decay. It has been shown by Herbst (2004) and Herbst & Henningson (2005) that the closer the forcing position (for the separation control) is located with respect to the separation point, the more effective it is in suppressing the separation. In the calculations presented here, the location of forcing is $x_0 = 110$, its frequency $\omega = 0.09$ and its amplitude set to either $f_0 = 0.1$ or 0.01.

To give a picture of the flow analyzed here, some plots with fundamental values (from the DNS calculations in Herbst (2004) and Herbst & Henningson (2005)) are shown in figures 3 and 4.

In figure 3 the mean flow component in streamwise direction averaged in time and spanwise direction can be seen. The upper figure shows the unforced case with the separation bubble (white dashed line: negative streamwise velocity) and the lower one shows the forced case with a forcing frequency $\omega = 0.09$ and a forcing amplitude $f_0 = 0.1$. For the latter one the separation bubble almost disappears.

In figure 4 the u_{rms} -velocity is plotted for the unforced and forced cases. It is obvious that the range of fluctuations for the forced case is increased and that its maximum occurs around the forcing position.



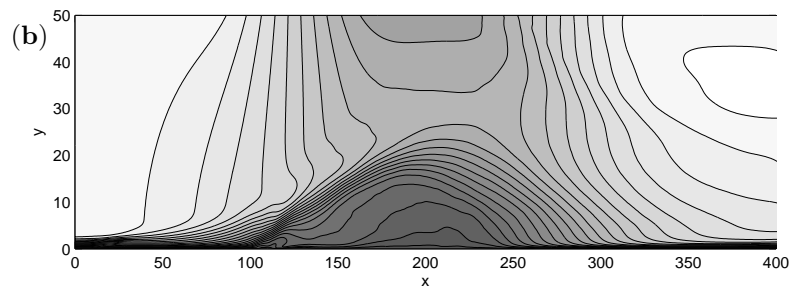


FIGURE 3. Mean velocity component in streamwise direction for the unforced and forced case in contour plots. Contours of mean velocity component in streamwise direction for (a) the unforced and (b) the forced case with the forcing frequency $\omega = 0.09$ and the forcing amplitude $f_0 = 0.1$ (neg: dark grey to pos: white, white dahed line: -0.025, contour spacing 0.05).

3. Stability Analysis

3.1. Equations

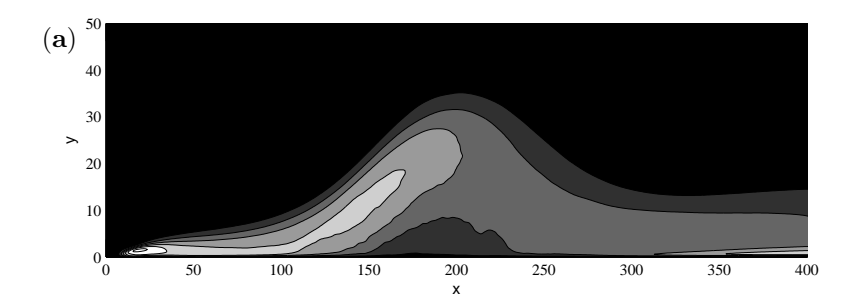
Here, we present the equations describing the evolution of organized waves in a turbulent flow. The derivation follows closely the work of Hussain & Reynolds (1972).

As we are interested in the evolution of coherent structures in a turbulent flow, we introduce the following decomposition of variables

$$\xi(\vec{x},t) = \overline{\xi}(\vec{x}) + \tilde{\xi}(\vec{x},t) + \xi'(\vec{x},t) . \tag{2}$$

where, $\overline{(\cdot)}$ denotes the mean (time-averaged) quantities, $\tilde{(\cdot)}$ the periodic wave and $(\cdot)'$ corresponds to the turbulent motion. The time average $\overline{\xi}$ and phase average are defined as

$$\overline{\xi}(\vec{x},t) = \frac{1}{T} \cdot \int_{-\frac{T}{2}}^{\frac{T}{2}} \xi(\vec{x},t+\tau) d\tau , \qquad (3)$$



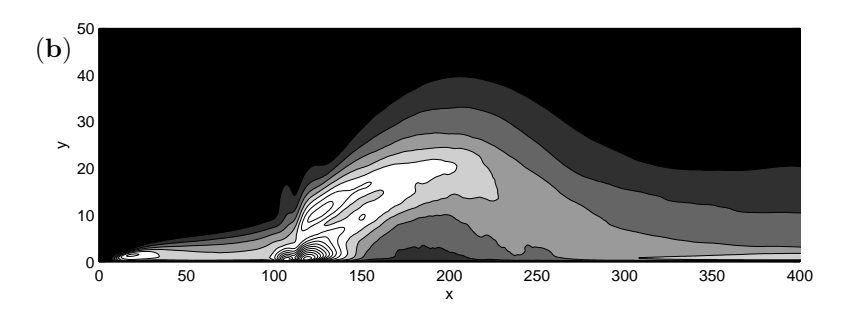


FIGURE 4. Turbulence intensity u_{rms} for the (a) unforced and (b) forced case (zero: $dark\ grey$ to pos: white, contour spacing 0.03).

$$\left\langle \xi(\vec{x},t) \right\rangle = \xi(\vec{x},t^{\varphi}) = \lim_{n \to \infty} \frac{1}{n} \sum_{i=1}^{n} \xi(\vec{x},t^{\varphi} + iT_{P}) , \quad t^{\varphi} = \frac{\varphi}{2\pi} T_{P}, \quad 0 \le \varphi \le 2\pi .$$

$$\tag{4}$$

Here, T_P is the cycle duration and φ the phase angle.

Introducing the triple decomposition (2) into the Navier-Stokes equations, phase averaging and subtracting the time-averaged equations give the dynamical equations for the organized waves which in non-dimensional form are

$$\frac{\partial \tilde{u}_i}{\partial t} + \tilde{u}_j \frac{\partial \overline{u}_i}{\partial x_j} + \overline{u}_j \frac{\partial \tilde{u}_i}{\partial x_j} = -\frac{\partial \tilde{p}}{\partial x_i} + \frac{1}{Re} \frac{\partial^2 \tilde{u}_i}{\partial x_j^2} + \frac{\partial}{\partial x_j} (\overline{\tilde{u}_i \tilde{u}_j} - \tilde{u}_i \tilde{u}_j) - \frac{\partial}{\partial x_j} \tilde{r}_{ij},$$
 (5)

with

$$\tilde{r}_{ij} = \left\langle u_i' u_j' \right\rangle - \overline{u_i' u_j'}. \tag{6}$$

Here, u_i represents the *i*-th component of the velocity vector, p the pressure, t the time. The Reynolds number is defined as $Re = U_{ref}^* L_{ref}^* / \nu_{ref}^*$, where U_{ref}^* , L_{ref}^* and ν_{ref}^* represent a characteristic velocity, length and kinematic viscosity, respectively. Throughout this text, the subscripts 1, 2 and 3 correspond to the streamwise (x), wall normal (y) and spanwise (z) directions, respectively. The velocities in the respective directions will also be denoted by $u = u_1$, $v = u_2$ and $w = u_3$. The term \tilde{r}_{ij} is the difference between the phase and time averages

of the Reynolds stresses of the background turbulence and can be regarded as the oscillation of the background Reynolds stresses due to the passage of the organized disturbance. Following the work of Hussain & Reynolds (1972), we adopt an eddy viscosity model and assume

$$\tilde{r}_{ij} = -\nu_t \left(\frac{\partial \tilde{u}_i}{\partial x_j} + \frac{\partial \tilde{u}_j}{\partial x_i} \right) = -2\nu_t \tilde{s}_{ij}, \qquad \tilde{s}_{ij} = \frac{1}{2} \left(\frac{\partial \tilde{u}_i}{\partial x_j} + \frac{\partial \tilde{u}_j}{\partial x_i} \right) . \tag{7}$$

Here, ν_t is calculated based on the DNS results defined either as

$$\nu_t = \nu_t^e = -\frac{\overline{u_i' u_j'} \overline{s}_{ij}}{2\overline{s}_{kl} \overline{s}_{kl}} \quad \text{or } \nu_t = \nu_t^k = c_\mu \frac{k^2}{\varepsilon} , \qquad (8)$$

with k being the turbulent kinetic energy, ϵ the dissipation rate and $c_{\mu} = 0.09$ a model constant. We assume the organized waves to be normal modes given as

$$\tilde{\xi}(x,y,z,t) = \hat{\xi}(x,y)e^{i\theta}$$
, with $\theta = \int_{x_0}^x \alpha(x')dx' + \beta z - \omega t$, (9)

where α and β are stream- and spanwise wavenumbers, respectively, and ω the angular frequency of the wave. Introducing the ansatz (9) and (7) in equation (5), removing the terms nonlinear in \tilde{u}_i and assuming weak streamwise dependency of flow variables results in a modified set of Parabolized Stability Equations, PSE (see e.g. Bertolotti & Herbert (1992)).

3.2. Analysis

Here we present the results of the stability analysis of the unforced separation bubble. To measure the size of the disturbance, we choose an integral quantity defined as

$$A_{u^2} = \int_0^\infty |\tilde{u}|^2 dy. \tag{10}$$

with corresponding growth rate as

$$\sigma_{u^2} = -\alpha_i + \frac{\partial}{\partial x} ln \left(\sqrt{A_{u^2}} \right) , \qquad (11)$$

In figure 5 the growth rates of disturbance with different β are shown. The data are given for both $\nu_t = \nu_t^k$ and quasi laminar case $\nu_t = 0$. It was observed that for x < 140 the eddy viscosity has a damping effect on the growth rate of the disturbances. However, for x > 140 the effect of eddy viscosity was found to be the opposite for $\beta > 0.1$. The most interesting result is that when the eddy viscosity is taken into the account the damping rate decreases with increasing value of β . The opposite is valid for the quasi laminar case.

In order to make a comparison with the DNS result, we extract the coherent structures corresponding to the frequency of periodic forcing by a Fourier Transform of the spanwise- and phase-averaged data. Figure 6 demonstrates

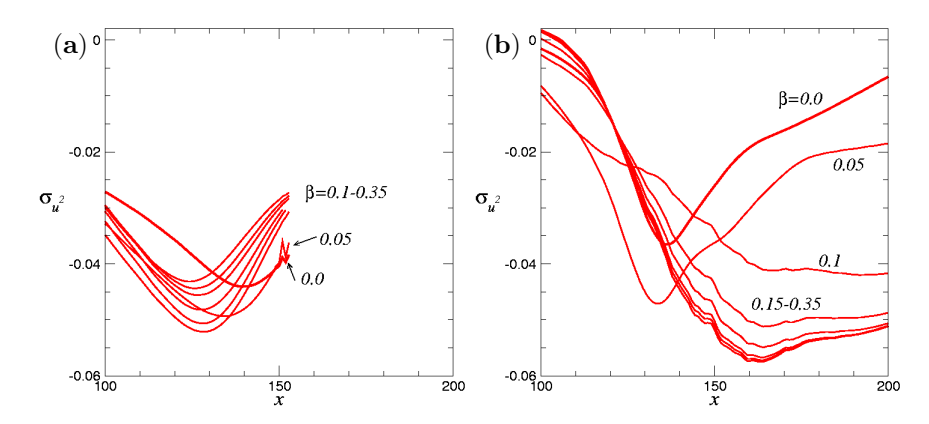


FIGURE 5. Growth rate based on \tilde{A}_{u^2} for different values of spanwise wavenumber β . (a): $\nu_t = \nu_t^k$, (b): $\nu_t = 0$. $\omega = 0.09$.

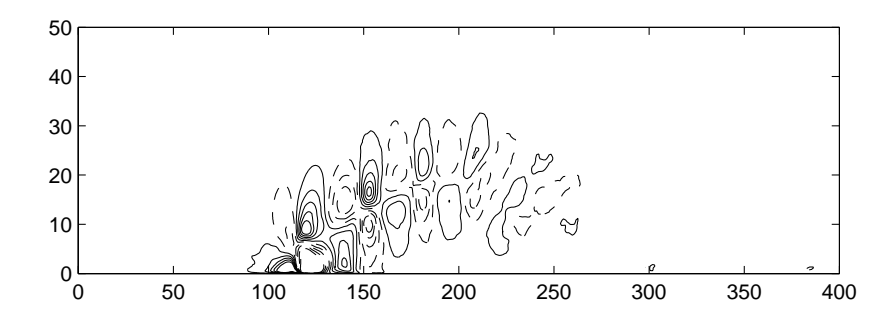


FIGURE 6. Contour plot of the coherent structure. Contours ranging from -0.225 to 0.225, contour spacing 0.05, dashed lines denote neg. values, solid lines denote positive values.

the structure of the organized wave in the separation bubble. As can be seen there, the amplitude of the wave decays as it propagates downstream.

In figure 7(a), the values of A_{u^2} as a function of streamwise position for the low and high amplitude cases are plotted. For comparison, the linear PSE results are also given. The DNS data show an initial growth of the disturbances which is then followed by a long region of decay. The maximum amplitude is reached at $x \approx 120$ which is close to the point of separation in unforced case (x=126). As can be seen, the PSE results seems to predict the decay of low amplitude case correctly. Surprisingly, the quasi laminar results $(\nu_t=0)$ fit better to the DNS data.

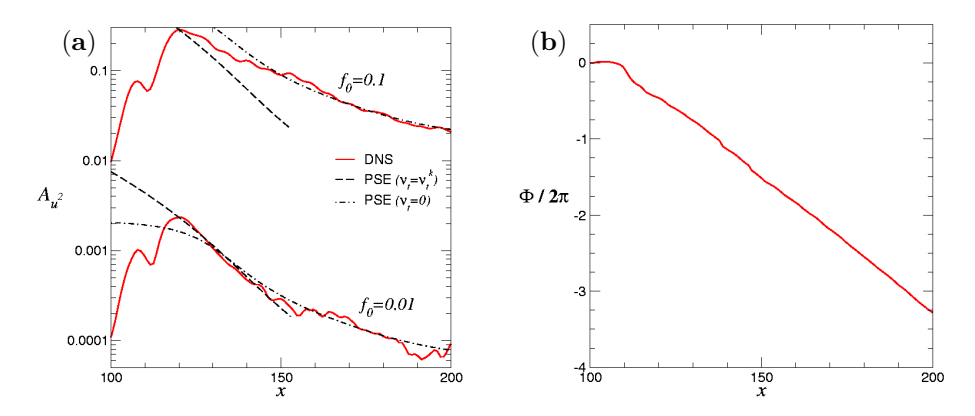


FIGURE 7. (a): Amplitude, (b): phase of the disturbance from DNS.

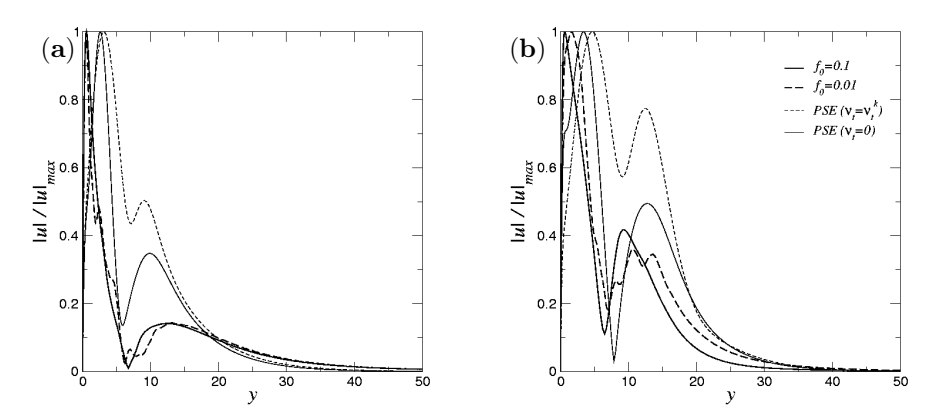


FIGURE 8. Amplitude of disturbances as a function of wall-normal coordinate. (a): x = 102, (b): x = 121.

In figure 7(b) the phase of the disturbance (high amplitude case) measured at the location of its maximum at each streamwise position is shown. Estimating the wavelength of the disturbance as $\alpha = d\Phi/dx$ gives a value of 0.22, which corresponds to a phase velocity of c = 0.41. This value is close to that found in quasi laminar calculations.

In figure 8 the amplitude of disturbances from DNS and PSE calculations at two different streamwise positions are compared to each other. Although the variation of A_{u^2} in PSE and low amplitude forcing DNS are in close agreement, the shape of disturbances are different.

4. Proper Orthogonal Decomposition (POD)

Proper orthogonal decomposition (POD) was introduced by Lumley to identify coherent structures in random turbulent flows. The implementation of the

POD in the manuscript is based on the method of snapshots developed by Sirowich (1987). For a given number M of snapshots of instanteneous velocity fields $u_i(x, y, z, t_p)$ at discrete times t_p , the eigenvectors and eigenvalues of the discrete correlation matrix

$$A_{i,j} = 1/M \sum_{k=1}^{nx} \sum_{l=1}^{ny} \sum_{m=1}^{nz} \sum_{n=1}^{3} u_i(x_k, y_l, z_l, t_i) u_i(x_k, y_l, z_l, t_j)$$
 (12)

are computed. For a thorough derivation of the equations and a detailed treatment of the subject, see e.g. Holmes *et al.* (1996).

The results for POD applied to the periodically excited turbulent separation bubble are presented in this section. POD has been applied to three dimenensional velocity fields, but since the flow is homogeneous in spanwise direction, every POD mode is associated with a Fourier mode in spanwise direction. Consequently contour plots of a selected x-y-plane are sufficient to show the results of the POD. The contour plots belong all to z=0 and are therefore situated in the middle of the domain. The dataset which POD was performed on consists of 150 snapshots taken within one forcing-period and equidistant in time.

Figure 9 shows the eigenfunctions associated with the eight highest eigenvalues. The smaller the magnitude of the corresponding eigenvalues the less energy do the eigenfunctions contain. Therefore we focus on the eigenfunctions corresponding to the highest eigenvalues. The eigenfunction corresponding to the highest eigenvalue (mode 1) is shown in figure 9(a) and can be associated with the baseflow. Mode 2 and 3, shown in figures 9(b) and (c) show almost similar structures, originating around (x = 110, y = 0), the point where the forcing is centred and decaying only slowly while travelling upwards in the shear layer. Figure 10 (a) and (b) show the eigenvalues. The first eigenvalue is four times higher than the second one. Remarkable is that the following eigenvalues occur in pairs, the second and third eigenvalues have the same order of magnitude (0.093 and 0.084) and are more than a factor two larger than the fourth and the fifth eigenvalue (0.04 and 0.03). Apart from a phase shift, the projection of the snapshots on the eigenfunctions representing the time dependence of the expansion coefficient of the highest modes (figure 10 (c) and (d)) is almost the same for the modes 2 and 3 with the frequency of the original forcing and for the modes 4 and 5 which represent the

first harmonic. Since the structures displayed by figures 9(b) and (c) and by the figures 9(d) and (e) are also very similar is it again likely that each pair belongs to one structure that is travelling downstream.

5. Conclusions

A flat plate boundary layer flow under strong adverse pressure gradient causing a separation bubble was considered. The data from direct numerical simulations were analysed by means of stability theory and Proper Orthogonal Decomposition technique.

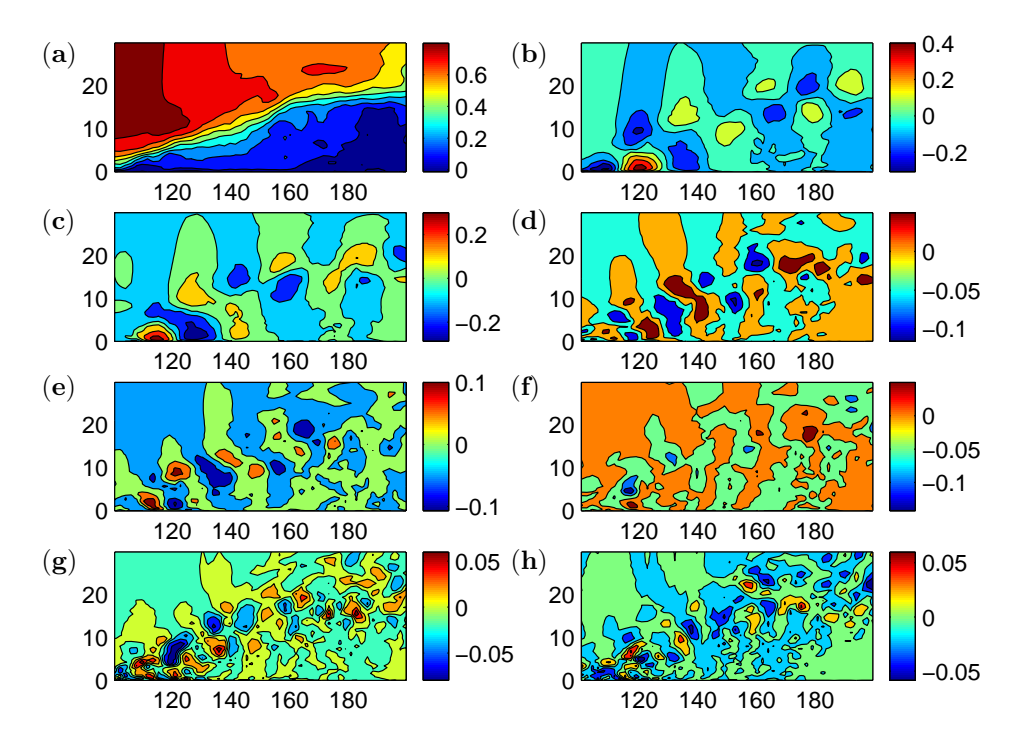


FIGURE 9. Contour plots of the eigenfunctions associated with the eight highest eigenvalues (Mode 1-8) in descending order starting in (a).

The organized wave caused by periodic forcing was extracted by Fourier transform of the phase-averaged data.

For stability analysis, a theoretical model of harmonic perturbations is considered, including the effects of the random turbulent flow. Here, we have used an eddy viscosity approach to model the the oscillations of the background Reynolds stresses caused by the organized wave. The equations were derived using the nonlocal stability theory based on the PSE method. The stability calculations seemed to predict the decay rate of the coherent structures correctly, while the shape of disturbances were different. It should be mentioned once again that due to large forcing amplitude the nonlinear effects are important here and may be able to explain some of the differences.

The POD technique was also used to extract the different structures of the flow. These results show a similarity to the structures found by Fourier transform of phase-averaged data.

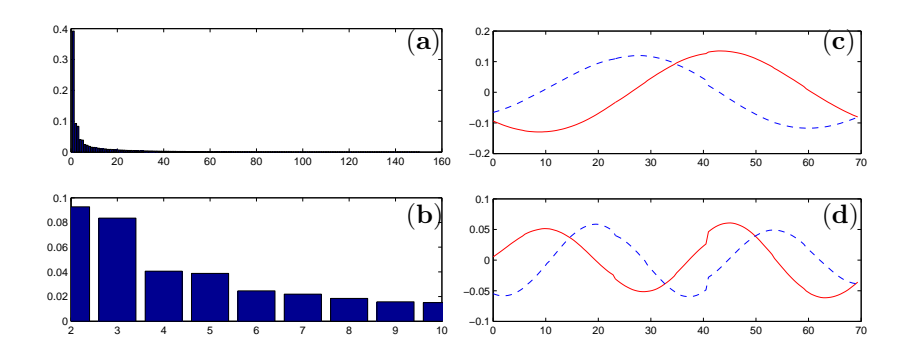


FIGURE 10. Eigenvalues corresponding to (a) mode 1-50 (b) mode 2-8 (c). Projection of the snapshots of the DNS on modes 2 and 3 and (d) modes 4 and 5.

References

Bertolotti, F. & Herbert, T. 1992 Linear and nonlinear stability of the Blasius boundary layer. J. Fluid Mech. 242, 441–474.

Deubelbeiss, S. 2005 Instability characteristics of harmonic disturbances in a turbulent separation bubble. Diploma Thesis, Institute of Fluid Dynamics, Department of Mechanical and Process Engineering, ETH Zürich.

HERBST, A. 2004 Studies of periodic excitation of a turbulent separation bubble. Licentiate thesis. Royal Institute of Technology (KTH), Department of Mechanics, Stockholm, Sweden.

HERBST, A. & HENNINGSON, D. 2005 The influence of periodic excitation on a turbulent separation bubble. $Kluwer\ Academic\ Publishers\ (2005)$.

HOLMES, LUMLEY & BERKOOZ 1996 Turbulence, Coherent Structures, Dynamical Systems and Symmetry. Cambridge Monographs on Mechanics.

Hussain, A. & Reynolds, W. 1972 The mechanics of an organized wave in turbulent shear flow. Part 3. Theoretical models and comparisons with experiments. J. Fluid Mech. **54**, 263–288.

Reau, N. & Tumin, A. 2000 On harmonic perturbations in turbulent wakes. AIAA-2000-2539.

SIROWICH, L. 1987 Turbulence and the dynamics of coherent structures. *Quarterly of applied mathematics* **XLV**, 561–582.

SPEHR, S. 2004 Proper orthogonal decomposition applied to turbulent separation. Master thesis, Stockholm, Royal Institute of Technology (KTH), Department of Mechanics.

Paper 3

3

The effect of the sweep angle on the turbulent separation bubble on a flate plate

By Astrid H. Herbst, Luca Brandt and Dan S. Henningson

KTH Mechanics, SE-100 44 Stockholm, Sweden

Internal report

The effect of the sweep angle on the turbulent separation bubble induced by an imposed adverse-to-favourable pressure gradient is examined by means of direct numerical simulation. To the best of our knowledge, this preliminary work presents the first numerical study of pressure-induced three-dimensional separated boundary layer flow. It is found that the location of separation is not changed by the introduction of sweep for the angles examined here. The reduction of the separated region is in agreement with previous studies on spanwise invariant three-dimensional separation, where deviations from the sweepindependence principle are observed for angles $\alpha > 40^{\circ}$. A significant increase in the turbulence activity in the separated region beneath the detaching shear layer and downstream of reattachment is clearly seen for the flow configuration of largest sweep. As observed in previous studies, it is not possible to find a universal scaling for the mean flow quantities and statistics of the turbulent fluctuations valid at all locations. However, it can be deduced from the data that, in general, the velocity C of the external streamline seems to provide the best scaling for the flow quantities at separation and inside the separated region, whereas the streamwise velocity U yields a better data collapse in the reattachment region. The latter can be explained by the fact that U is more directly related to the external pressure distribution. Comparison with the simulations of three-dimensional boundary layers subject to weak adverse pressure gradient indicates that strength of the pressure gradient, the strain rate and the occurrence of separation have a deeper impact on the turbulence structure than the skewing of the mean flow.

1. Introduction

Many flows encountered in engineering applications are characterised by three-dimensional mean velocity fields, *i.e.* they are characterised by mean axial vorticity. A wide variety of them is further complicated by the occurrence of boundary layer separation. Applications of three-dimensional separated flows can be found among others on airfoils, road vehicles and turbine blades. Separation is still difficult to predict by the presently available turbulence models and it has a deep impact on the performance or lost of functionality of many

devices. This justifies the increasing interest in such flows. The aim of the present work is thus to examine the effect of such skewing of the mean flow on turbulent separation.

The pressure-induced separation of a turbulent boundary layer evolving over a semi-infinite swept flat plate is considered in the present work and studied by means of Direct Numerical Simulation (DNS). The flow under consideration is therefore spanwise invariant: the mean velocity field is characterised by three velocity components but these can be expressed only as a function of two spatial independent variables. Therefore the spanwise derivative of any flow quantity is zero. The present configuration is thus an obvious first step in the generalisation from a two-dimensional and coplanar mean flow to the fully three-dimensional case. The spanwise invariant mean flow can still be seen as two-dimensional but it is not coplanar. The few related studies found in the literature all consider three-dimensional separation triggered by the geometrical configuration, a sharp edge, and to the best of our knowledge no studies on turbulent three-dimensional pressure-induced separation are available. Recently, Hetsch & Rist (2006) studied the effect of the sweep angle on the disturbance amplification and the onset of transition on a laminar separation bubble on a flat plate.

The experiments by Hancock & McCluskey (1997); Hancock (1999) consider separation behind a swept separation line created by a vertical fence mounted on the front of a horizontal splitter plate. The measurements are limited to a swept angle of 25° and the reference case without sweep. These authors find that the outer layers of the separation bubble are essentially independent of sweep angle; the lateral velocity is nearly equal to the velocity in the free-stream. Thus the velocity in the separated region scales with the streamwise component U. It is suggested that the presence of vorticity perpendicular to the separation line has only a negligible effect because the rolling up of the spanwise vorticity is still dominant. Hancock (1999) also notes that the inner layer beneath a separation bubble and downstream of reattachment is thin compared with the bubble height and therefore its motion is driven by the intense motions in the outer shear layer. In a later experimental study, with a similar set-up, Hardman & Hancock (2000) show that the cross-flow layer is substantially thicker than the region where reverse flow is encountered.

For a laminar flow the independence of the separation and reattachment location on the sweep angle, as observed by Hancock (1999), can be derived analytically, known as the sweep independence principle (see e.g. Kaltenbach 2004). The principle states that the streamwise (normal to the leading-edge) and wall-normal velocities are independent of the presence of the spanwise (parallel to the leading-edge) component, which behaves as a passive scalar. However, the sweep independence principle does not necessarily hold for turbulent mean flow owing to the coupling of the Reynolds stresses induced by pressure-strain and dissipation rate terms. Kaltenbach & Janke (2000) performed a DNS study of a transitional separation bubble induced behind a swept backward facing step.

They show that in their case the sweep-independence principle is followed up to a sweep angle of 40° in agreement with previous experimental work. The main deviations from the sweep independence are found to consist in a shortening of the separation region and an increase in the turbulent stresses prior to reattachment when scaled with the step-normal component. The transition is triggered by a Kelvin-Helmholtz type instability of the shear layer. Even though spatial growth rates are found to increase with increasing sweep angle (Lu & Lele 1993), Kaltenbach & Janke (2000) observed only a weak influence of the skewing on the fluctuation amplifications. The same flow configuration but at different Reynolds number was examined by Kaltenbach (2003) with emphasis on the turbulence features inside the separation bubble and downstream of reattachment. It is found that the turbulent boundary layer has a faster recovery for higher sweeps, which was explained by the fact that with increasing sweep angle the edge-parallel component of the mean flow provides sufficiently high wall-normal shear at the wall so that strong turbulent production is observed even close to the attachment line. The turbulent flow over a swept backward-facing step was studied by Kaltenbach (2004) using Large Eddy Simulation (LES). He concluded that no significant influence of the mean flow skewing on the statistical turbulence structure is present inside the outer free shear layer, whereas substantial changes in the near-wall region upstream of reattachment is due to the sweep. It was also observed that the decrease in length of the separation bubble with the sweep angle is less for turbulent than for transitional flow.

Three-dimensional turbulent separation is sensitive to the incoming turbulent boundary layer flow. Numerous studies have considered skewed turbulence and the main results can be summarised as follows. First, the near-wall activity (shear stress and turbulent kinetic energy) is reduced for increasing sweep (Johnston & Flack 1996). As a consequence, a reduction of the structure parameter a_1 is observed when three-dimensional effects are present. The LES study by Kannepalli & Piomelli (2000) indicates that the reduction of turbulent kinetic energy is due to the disruption of the streaky structures and of the outer layer vortical structures induced by the imposition of a transverse shear. However, it should be noted that contrary to previous studies the addition of mean crossflow to the complex flow over a bump did not reduce the vertical mixing relative to the turbulent kinetic energy in the experiments by Webster et al. (1996). Secondly, a misalignment between the shear stress vector and the strain rate vector is observed. This lack of alignment has far reaching consequences for turbulence modelling, refuting the validity of any eddy-viscosity model assumption. Such a misalignment is also observed for three-dimensional separation both for transitional flow (Kaltenbach 2003) and in the LES of a fully turbulent flow in Kaltenbach (2004). In the latter work it is concluded that, however, models which rely on the alignment of shear-stress vector and velocity gradient do not necessary fail in three dimensions since the largest misalignment is concentrated in regions of low turbulence production. Third,

the numerical experiment by Coleman et al. (2000) demonstrate the turbulence in the outer layer of the boundary layer is hardly influenced by a pure skewing strain rate. Apart from the main focus on the effect of sweep on the turbulent separation bubble, simulations of three-dimensional boundary layer under a weak adverse pressure gradient are also presented in this paper in order to compare the characteristics of the incoming flow to those of a fully developed three-dimensional boundary layer and try to separate the effect of mean flow skewing from that of the strong pressure gradient and strain associated to separation.

The spanwise invariant configuration is chosen because owing to the complexity of fully three-dimensional separation and to the lack of a reference coplanar case it can be difficult to isolate the effects of skewing. This advocates the need for a systematic approach to identify the effect of increasing mean axial vorticity of the base flow. In fact, turbulence is found to be more affected by changes in strain rates than by skewing (Coleman $et\ al.\ 2000$). In the simulations presented here, the spanwise velocity therefore is increased in two steps from zero to the value of its streamwise counterpart U, that is a largest inflow sweep angle of 45° is considered, leaving the remaining flow parameters unchanged.

The present work can therefore be seen as an extension of previous studies on the two-dimensional separation of a turbulent boundary layer flow over a flat plate. The latter problem was investigated using direct numerical simulations only in a few previous studies. Spalart & Coleman (1998) performed a DNS of a turbulent separation bubble with heat transfer. They showed that separation has a large effect on the boundary layer and found an increase in the Reynolds stresses over the separation bubble which they explained by a liftup of the turbulent fluid from the wall region. The separation of a turbulent boundary layer has further been numerically analysed by Na & Moin (1998). They find that the turbulent structures emanating upstream the separation move upwards into the shear layer and then turn around the bubble causing a maximum of the turbulence intensities in the middle of the shear layer. Skote & Henningson (2002) conducted a DNS of a turbulent boundary layer separating due to a strong adverse pressure gradient using the same numerical code that was applied in this study. In comparison with the earlier simulations the flow has a stronger and larger recirculation region. Manhardt & Friedrich (2002) carried out a DNS of the separated turbulent boundary layer comparable to the experiment of Kalter & Fernholz (1995) but at half the Reynolds number of the experiment. They find that the shape and the dynamics of the separation bubble are governed by the large scale vortices reaching from the wall into the shear layer above it, similarly to what observed for the swept separation by Hancock (1999). A turbulent separation bubble has also been simulated by Herbst & Henningson (2006). These authors consider the turbulent boundary layer flow over a flat plate separating due to an adverse pressure gradient and reattaching due to the presence of a favourable gradient further downstream.

The focus of the study is on the effect of periodic excitation in eliminating the separated region. The uncontrolled configuration used in Herbst & Henningson (2006) provides the starting point for the present study. Spanwise skewing of the mean flow is in fact imposed to a flow subject to the same streamwise pressure distribution adopted previously. Two sweep angles will be considered here, $\alpha_0 = 11^{\circ}$ and $\alpha_0 = 45^{\circ}$, where α_0 denotes the angle between the incoming free-stream velocity and the direction of the imposed pressure gradient measured in the region of zero pressure gradient upstream of the bubble.

2. Governing equations and numerical methods

2.1. Numerical scheme

The simulations of the turbulent boundary layer exposed to an adverse to favourable pressure gradient have been performed using a code developed at the Department of Mechanics at KTH by Lundbladh $et\ al.$ (1999). The code uses a pseudo-spectral method with Fourier discretization in streamwise and spanwise directions and Chebyshev polynomials in the wall-normal direction. A fringe technique enables simulations of spatially developing flows while using Fourier discretization in the streamwise direction (see Nordström $et\ al.$ 1999). A fringe region is added at the end of the computational domain to force the outflow back to the inflow velocity field and thus satisfy periodic boundary conditions. Therefore the code solves the unsteady three-dimensional Navier–Stokes equations with the addition of a volume force F:

$$\frac{\partial u_i}{\partial t} + u_j \frac{\partial u_i}{\partial x_j} = -\frac{1}{\rho} \frac{\partial p}{\partial x_i} + \nu \frac{\partial^2 u_i}{\partial x_j^2} + F_i \tag{1}$$

The forcing

$$F_i = \lambda(x)(\tilde{u}_i - u_i) \tag{2}$$

is non-zero only in the fringe region. \tilde{u}_i is the laminar inflow velocity profile the solution u_i is forced to and λ the strength of the forcing. The form of the fringe function is designed to have minimal upstream influence (see Herbst & Henningson 2006).

The time integration is carried out using a four-step low-storage third-order Runge-Kutta-scheme for the non-linear terms an a second-order Crank-Nicolson method for the linear terms. Aliasing errors from the evaluation of the non-linear terms are removed applying a $\frac{3}{2}$ -rule when the FFTs are calculated in the wall parallel plane.

2.2. Parameter settings and boundary conditions

The simulations are performed at an inflow Reynolds number $Re_{\delta_0^*} = U\delta_0^*/\nu = 400$ based on the displacement thickness δ_0^* of the boundary layer and the normal-to-leading-edge free-stream velocity U at the inflow x=0. If not otherwise stated, all quantities are non-dimensionalized by U and δ_0^* at x=0. At

this position, a laminar Blasius boundary layer profile is introduced. Downstream at x=10 laminar-turbulent transition is triggered by a random volume force near the wall.

The computational box is 450 non-dimensional units long including 50 non-dimensional units for the fringe, 50 units high and 24 units wide. A resolution with 480 modes in streamwise direction, 193 modes in wall-normal direction and 64 modes in spanwise direction is used, which gives a total of 6 million points.

The boundary conditions are no-slip at the wall. Due to the finite size of the computational domain, the flow domain is truncated and an artificial boundary condition is applied at the free stream. A so-called asymptotic boundary condition is used, which is a generalization of the boundary condition used by Malik *et al.* (1985). It takes the form

$$(D+|k|)\tilde{v} = (D+|k|)\tilde{V}$$

$$(D+|k|)\tilde{u} = (D+|k|)\tilde{U}$$

$$(D+|k|)\tilde{w} = 0$$
(3)

where $\tilde{\ }$ denotes the Fourier transform in the horizontal direction, |k| is the absolute value of the horizontal wavenumber vector and D is the derivative in the wall-normal direction and a capital letter the mean flow component. This boundary condition allows the top of the computational domain to be placed closer to the wall in simulations where e.g. waves are present. Furthermore, in simulations of a transitional separation bubble this boundary condition has shown to give good agreement with the experimental findings as described by Häggmark et al. (2001). However, the asymptotic boundary condition cannot be applied at the start of the simulations because the correct base flow close to the upper boundary is not known in advance. To establish the bubble the simulation is initially carried out imposing in the free stream zero normal derivative of the streamwise and spanwise velocity components and

$$Dv = DV_{APG} = -\frac{\partial U_{APG}}{\partial x} \tag{4}$$

where U_{APG} is the initial free-stream streamwise velocity distribution defining the external pressure gradient. For the simulations reported in this paper U_{APG} is chosen as

$$U_{APG} = 1 - (1 - U_{min})\left(S\left(\frac{x - x_{start}}{x_{fall}}\right) - S\left(\frac{x - x_{end}}{x_{rise}} + 1\right)\right)$$
 (5)

where S is defined by

$$S(x) = \begin{cases} 0 & x \le 0\\ 1/[1 + \exp(\frac{1}{x-1} + \frac{1}{x})] & 0 < x < 1\\ 1 & x \ge 1 \end{cases}$$
 (6)

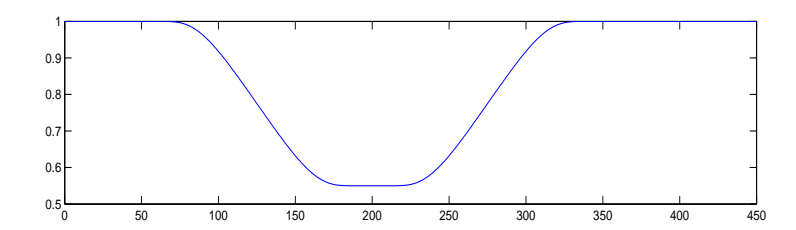


FIGURE 1. Freestream velocity distribution at the beginning of the simulation.

and $U_{min} = 0.55$, $x_{start} = 50$, $x_{end} = 350$, $x_{fall} = x_{rise} = 150$, see figure 1. The free-stream distribution sets the pressure gradient and the chosen parameters are therefore important for the developing flow.

The simulation is thus initially run with the boundary conditions (4) and (5) until a separation bubble has been established and the flow enters a quasi-equilibrium state even though it does not become completely statistically stationary. The mean flow to be used for the asymptotic boundary condition (3) is calculated by averaging in time and spanwise direction while the flow is in this quasi-equilibrium. A similar procedure was also adopted by Häggmark et al. (2001) who switched to an asymptotic boundary condition at a later time because the correct base flow was not known a priori. Proceeding in this manner, a good agreement with the experimental results was achieved. Recently, Marxen (2004) developed an interaction model for the simulation of a transitional separation bubble. The interaction model is an iterative implicit method to separate viscous and inviscid effects based on potential flow theory and source and sink modelling of the separation induced displacement. The values for the boundary condition at the upper boundary are adjusted while the the simulation is run until the iterative process has converged. The procedure applied in this study can be viewed as a first step where the boundary condition is retrieved through an iterative process consisting of two steps. The sweep is introduced at a third stage. Once the two-dimensional turbulent separation bubble with the asymptotic free-stream condition has reached steady state, a non-zero spanwise velocity component is imposed at the upper limit of the computational domain.

Before presenting the main results of our study a brief description of the notation is appropriate. For the infinite swept flat plate considered here, the sweep angle α is defined as the angle between the normal-to-leading-edge direction and the projection in a wall-parallel plane of the direction of the free-stream streamline. Two reference frames can be used to analyse spanwise-invariant three-dimensional flows. The first system is aligned with the flat plate (and the external pressure gradient) while the second is relative to the external streamline. The first will be indicated by x,y,z where x denotes the streamwise (parallel to the pressure gradient) direction, y the wall-normal direction and z the spanwise (parallel to the plate leading edge) direction. The second

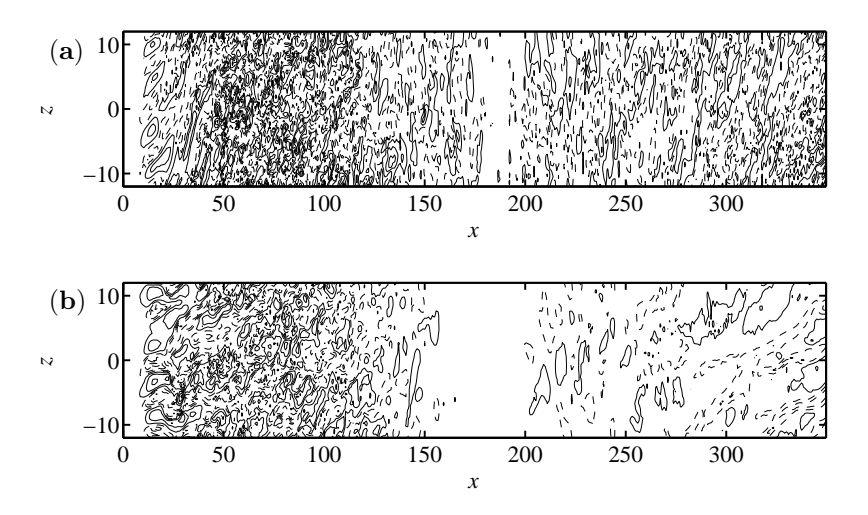


FIGURE 2. Contours of streamwise disturbance velocity at y = 1. Contour levels ranging from -0.45 to 0.45, contour spacing 0.1, with *dashed lines* indicating negative values and *solid lines* positive values. (a) $\alpha_0 = 45^{\circ}$, (b) $\alpha_0 = 11^{\circ}$.

reference frame will be denoted by \hat{x}, y, \hat{z} , with \hat{x} the downstream direction parallel to the external streamline and \hat{z} the cross-flow direction, the wall-normal direction being the same for the two coordinate systems. The corresponding velocities will be denoted (U,V,W) and \hat{u}',v',\hat{w}' where capital letters are used for mean values and primes for the velocity fluctuations. The total wall-parallel velocity is $C=\sqrt{U^2+W^2}$. Quantities denoted with an index zero, e.g. α_0 , refer to values at the inflow of the computational domain. For the normalisation of the velocity in the figures, free-stream values are used. These are simply indicated by the velocity component, e.g. W_0 is the inflow spanwise velocity.

3. Results

3.1. Flow visualisation

Visualisations of the instantaneous flow are shown first in order to provide a picture of the flow under consideration. The instantaneous streamwise velocity perturbation, defined as the difference between the local velocity and its spanwise mean, is shown in a plane parallel to the wall at y=1 in figure 2. The plot in figure 2(a) pertains to the simulation with inflow sweep angle $\alpha_0=45^{\circ}$, whereas the flow with sweep $\alpha_0=11^{\circ}$ is depicted in figure 2(b). Note that the streamwise coordinate x is aligned with the externally imposed pressure gradient and that the plot is not at the actual scale, so that the sweep angle appears to be considerably deformed (increased) by the stretching of the axis. The two-dimensional reference case is not reported here; as discussed below its features are very similar to those observed in the simulation with sweep of 11°.

The incoming flow is laminar and transition to turbulence is triggered at x = 10. The large structures at the transition stage are clearly convected in the direction of the free-stream streamline. Turbulent fluctuations intensify in the region of adverse pressure gradient before the flow separates in the mean at $x \approx 125$. It is evident from the plot that separation is spanwise invariant. In the separated region the maximum of the turbulence activity is occurring in the detaching shear layer and it is therefore observed at distances from the wall much higher than that considered here. However, significant qualitative differences are not observed in the different cases. The important reduction of fluctuations in the near wall region is more pronounced in the case of lower sweep. Probably the most interesting features is the early and larger increase in turbulence activity for the 45°-case. This can be explained by the fact that with increasing sweep angle the spanwise component of the mean flow provides sufficiently high wall-normal shear at the wall so that strong turbulence production is observed. Such observation would suggest earlier reattachment and a faster recovery of the turbulent boundary layer in the case with higher sweep. The latter is confirmed by the analysis of the statistical data (see discussion below), whereas the reattachment position is only slightly upstream in the case with larger skewing. This suggests that for the present configuration reattachment is dictated by the external pressure gradient to a high degree and that the level of turbulent fluctuations has little impact on it.

3.2. Mean flow characteristics

The mean flow characteristics are discussed first, whereas the structure of the turbulence fluctuations are presented in the next session. The results are obtained by averaging in time and in the homogeneous spanwise direction. To give an overview of the flow and the separated region, the streamwise and spanwise friction coefficients are displayed in figure 3. In 3(a) the streamwise wall shear stress $\tau_{w,x}$ is normalised with the free-stream streamwise velocity U as usually reported in several experimental studies, whereas in figure 3(b) $c_{f,x} = \tau_{w,x}/(0.5\rho C^2\cos\alpha)$ is displayed, where C is the free-stream velocity at the corresponding streamwise location and α the local angle between the freestream velocity and the normal-to-leading-edge direction. Such normalisation follows directly from the projection of the total shear $c_f = \tau_w/(0.5\rho C^2)$ in the streamwise direction (see also Kaltenbach 2004). From both plots it can be deduced that the location of the separation point is unchanged by the introduction of sweep, a results which supports the validity of the sweep independence principle at the angles considered here. The reattachment location is basically the same for the case without sweep and the lowest sweep angle, whereas a slightly shorter bubble is obtained for the largest sweep angle. The reduction of bubble length is in agreement with previous studies, even if the effect is not particularly pronounced for the $\alpha_0 = 45^{\circ}$ case considered here. However,

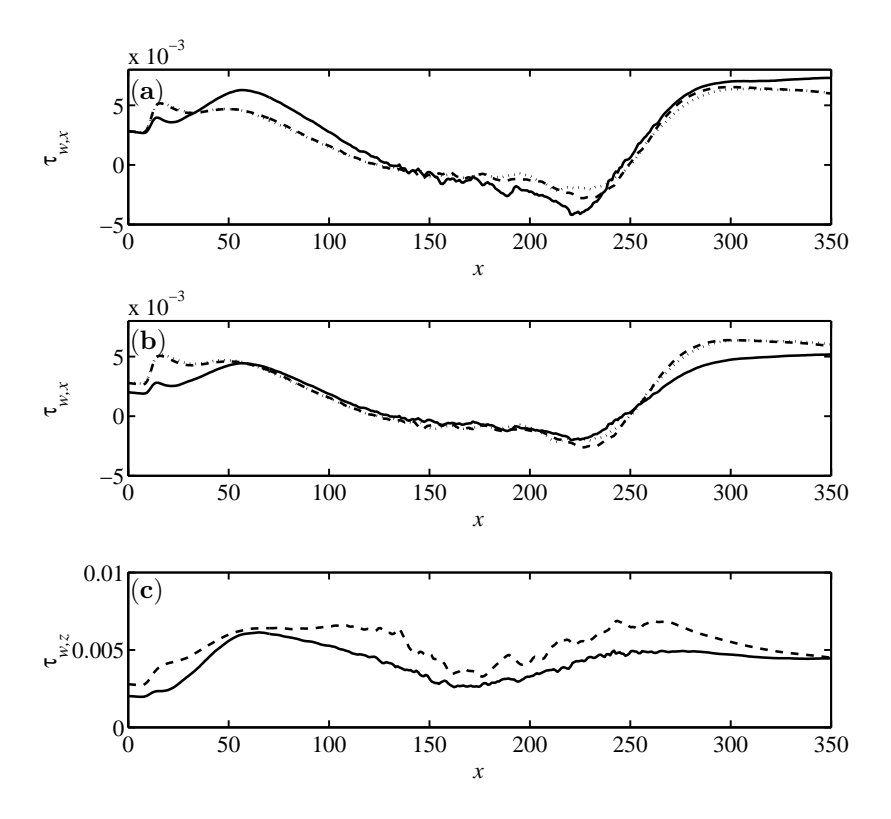


FIGURE 3. Skin friction coefficient (a) $2 * \tau_{wx}/(Re U^2)$ (b) $2 * \tau_{wx}/(Re U C)$ (c) $2 * \tau_{wz}/(Re W C)$. Solid line $\alpha_0 = 45^{\circ}$, dashed line $\alpha_0 = 11^{\circ}$, dotted line $\alpha_0 = 0^{\circ}$.

Kaltenbach (2004) notes that the decrease in length of the separation bubble with the sweep angle is lower for turbulent than for laminar flow.

Considering the streamwise evolution of the friction coefficient, it can be noted that the scaling in figure 3(a) seems to be valid only in the reattachment region ($x \approx 250$), with stronger negative friction for higher sweep inside the separation bubble. However, when scaling the same data with the total freestream velocity, a collapse of the data is observed upstream and for a large part of the separated region. This suggests that the free-stream velocity C is the relevant scale at separation whereas its streamwise counterpart is the relevant scale at reattachment, probably because it is more directly related to the imposed pressure gradient. The differences close to the domain inflow, $x \lesssim 50$ can be due to a different transition development. Note that small differences are found between the no-sweep and the $\alpha_0 = 11^{\circ}$ -case. In the region where the flow remains attached in the presence of the adverse pressure gradient $c_{f,x}$ is larger for higher sweep angle, whereas the opposite is true in the flows subjected to the favourable pressure gradient downstream of the bubble.

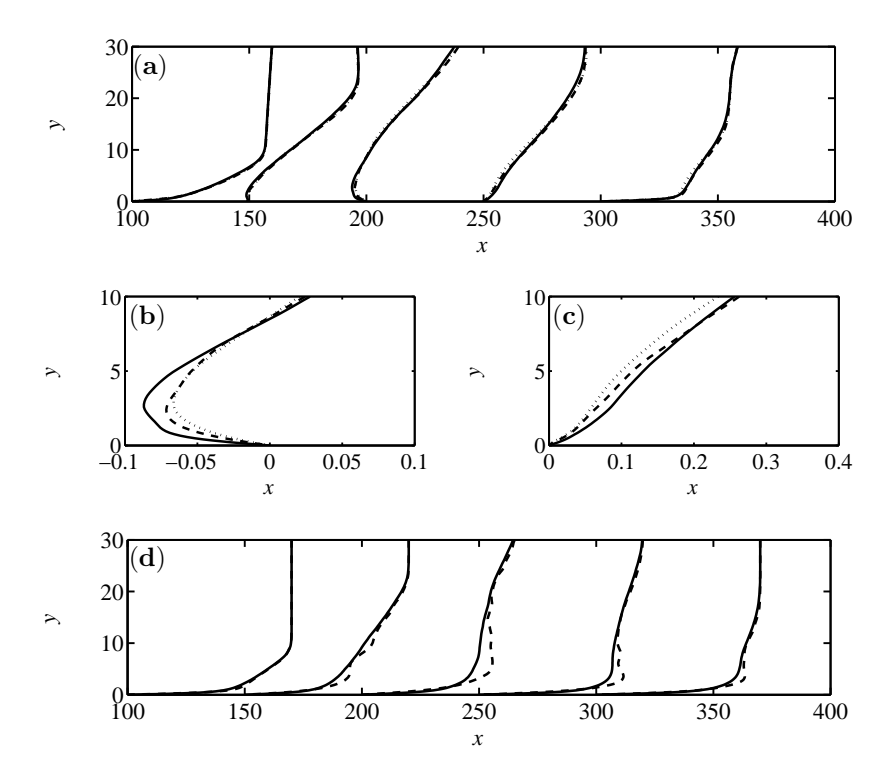


FIGURE 4. Mean velocity profiles for different sweep angles (solid line $\alpha_0 = 45^{\circ}$, dashed line $\alpha_0 = 11^{\circ}$, dotted line $\alpha_0 = 0^{\circ}$) at different streamwise positions (a) $x + 70 * U/U_0$, (b) U/U_0 at x = 200, (c) U/U_0 at x = 250, (d) $x + 70 * W/W_0$.

The spanwise component of the normalised wall-shear stress is depicted in figure 3(c). The scaling appears not to be as appropriate as for the streamwise shear, being the values lower for higher sweep angles. The later finding is in agreement with the LES results in Kaltenbach (2004) for a backward-facing step and the DNS data of a three-dimensional boundary layer subject to a weak adverse pressure gradient reported in the appendix.

The mean flow velocity profiles extracted at five streamwise locations $(x=100,\ 150,\ 200,\ 250,\ 300)$ are shown in figure 4 in the reference frame relative to the pressure gradient (or leading edge). The streamwise component is depicted in figure 4(a), where small differences can be seen among the three simulations under considerations. This finding is agreement with previous studies considering sweep angles lower than 50°. The main differences are highlighted in the enlargements figure 4(b) and figure 4(c). A stronger counterflow in the separated region and a quicker recovery in the near-wall region

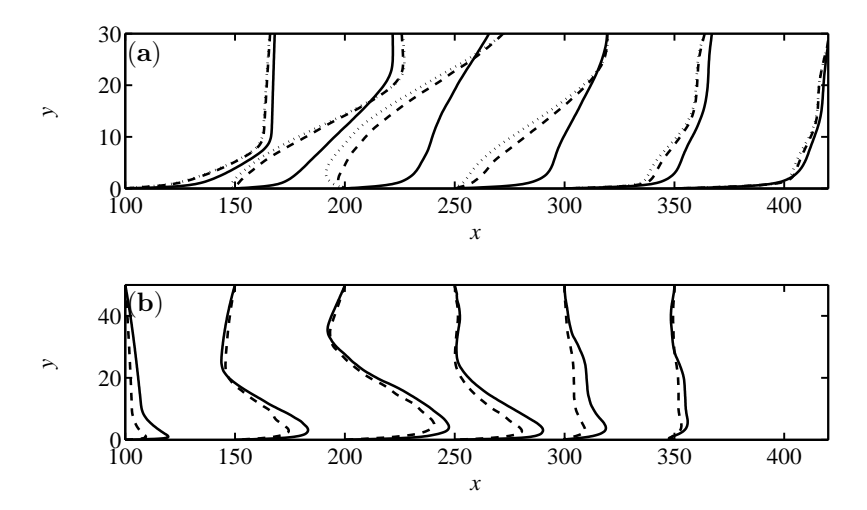


FIGURE 5. Mean velocity profiles in the coordinate system aligned with the free-stream streamline for the different sweep angles under consideration (solid line $\alpha_0 = 45^{\circ}$, dashed line $\alpha_0 = 11^{\circ}$, dotted line $\alpha_0 = 0^{\circ}$) at different streamwise positions. (a) $x + 70 * \hat{U}/C$, (b) $x + 140 * \hat{W}/C$.

downstream of the bubble is observed for the largest sweep. The mean spanwise velocity component is shown in figure 4(d). Larger differences than for the mean streamwise component can be seen in this case, being the profiles fuller for the configuration with lower sweep.

In figure 5(a) the mean velocity profiles in the direction of the local freestream streamline are reported for the three cases under consideration. When increasing the sweep, the profiles appear fuller and no counterflow is observed. This is explained by the fact the angle with respect to the direction of the pressure gradient is increasing and therefore the negative velocity in the streamwise direction is not longer yielding a dominant projection in the streamline direction. The cross-flow mean velocity is reported in figure 5(b). By comparison with 5(a), it can be observed that the thickness of the cross-flow layer is larger than that of the reverse flow region and of the viscous boundary layer relative to the \hat{U} component (see also Hardman & Hancock 2000). The cross flow velocity is higher in the case with larger sweep and no collapse of the data with the data at lower sweep angles is observed when those are presented in the reference frame relative to the free-stream streamline. These differences in the mean spanwise velocity component, also observed in figure 4(d), are most likely due to the presence of a strong pressure gradient, with related rotational strain rate $0.5\partial W/\partial x$ (see Appendix). The spanwise component \hat{W} gives and indication of how the axial vorticity $\Omega_z = \partial \hat{W}/\partial y$ is distributed in the flow.

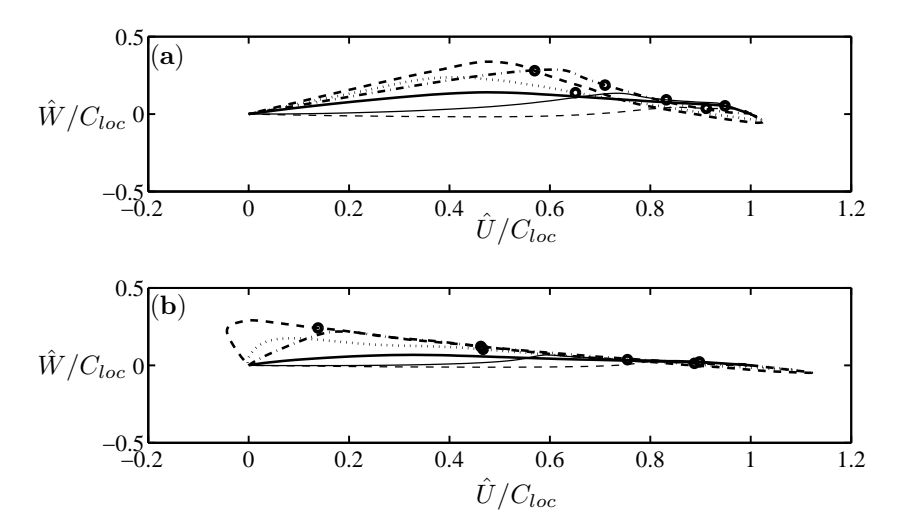


FIGURE 6. Hodographs of mean velocity vector for sweep angle (a) $\alpha_0 = 45^{\circ}$, (b) $\alpha_0 = 11^{\circ}$, at different streamwise positions (thick solid line, x=100, thick dashed line, x=150, thick dotted line, x=200, thick dashed-dotted line, x=250, thin solid line, x=300, thin dashed line, x=350.) The circles denote the values at y=10.

The latter is stronger close to the wall and in the shear layer emanating at separation.

Velocity polar plots, or hodographs, in the reference frame of the local free-stream streamline are displayed in figure 6(a) and (b) for sweep angle of 11° and 45° respectively. The results indicate that the skewing of the mean flow is largest just downstream of the separation point. This is a consequence of the fact that inside the separation bubble the flow is aligned in the spanwise direction. It is also possible to note that the skewing of the profile in the outer part of the boundary layer is reduced when increasing the sweep angle. This reduction can probably be explained by the fact that the separation line becomes more aligned with the inflow direction.

3.3. Turbulence characteristics

In this section the statistical properties of the turbulent fluctuations are presented. The turbulent kinetic energy divided by with U_0C_0 and C_0^2 is shown in figure 7(a) and (b), respectively. The increase in the turbulent fluctuations in the free shear layer limiting the size of the bubble is evident in both plots. In agreement with previous studies on separation it is not possible to find a scaling law which is valid everywhere. The normalisation with U_0C_0 seems to be more appropriate in the outer part of the boundary layer, whereas the scaling with the total velocity C_0 seems to capture the near-wall dynamics for the attached

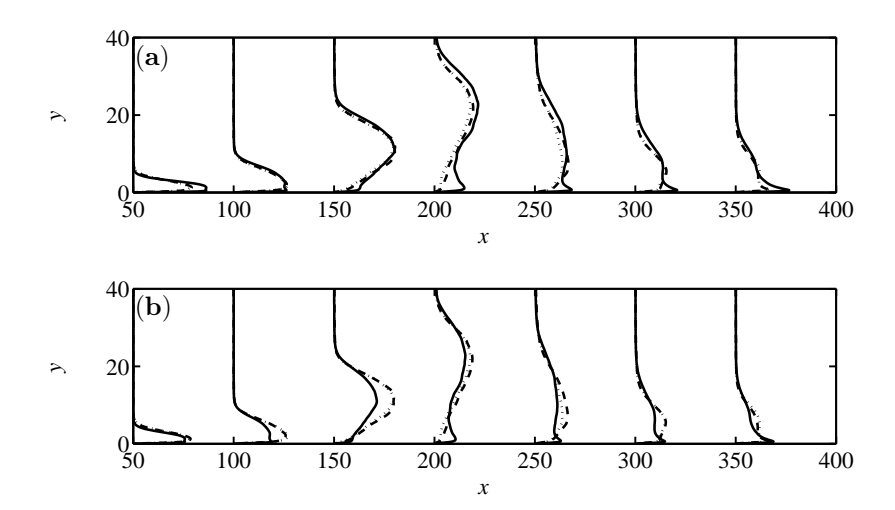


FIGURE 7. Wall-normal profiles of turbulent kinetic energy for the different sweep angles under consideration (solid line $\alpha_0 = 45^{\circ}$, dashed line $\alpha_0 = 11^{\circ}$, dotted line $\alpha_0 = 0^{\circ}$) at different streamwise positions (a) $x+2000*k/C_0U_0$ (b) $x+2000*k/C_0^2$.

flow better. An increased turbulent activity is observed close to the wall in the separated region for the case of largest sweep, yielding a double-peaked structure of the kinetic energy profiles. Such an increase close to the wall can be explained by the fact that with increasing sweep the mean velocity component parallel to the separation line W can provide near-wall shear increasing turbulent production.

The Reynolds stresses responsible for turbulence production in three-dimensional flows, u'v' and v'w', are displayed in figure 8 scaled with C_0U_0 and C_0W_0 respectively. The u'v'-stress are shown to scale well with C_0U_0 at least up to the reattachment region. A better collapse at these later stations is obtained when scaling the data with U_0^2 (not shown), as in Kaltenbach (2004). This might be due to the fact that the imposed pressure gradient is proportional to U_0 . A double-peaked profile is found for the v'w'-stress at the largest sweep. This can be explained by the presence of two regions of larger mean spanwise shear $\partial W/\partial y$, as observed in Kaltenbach & Janke (2000). Unfortunately, significant oscillations are observed in the profiles pertaining to the configuration with lower sweep. The reason is still unclear and it might be related to the length of the time interval of the averaging procedure (see also Appendix).

For three-dimensional flows, the coordinate independent structure parameter $\,$

$$a_1 = \frac{((u'v')^2 + (v'w')^2)^{0.5}}{(u'^2 + v'^2 + w'^2)}$$

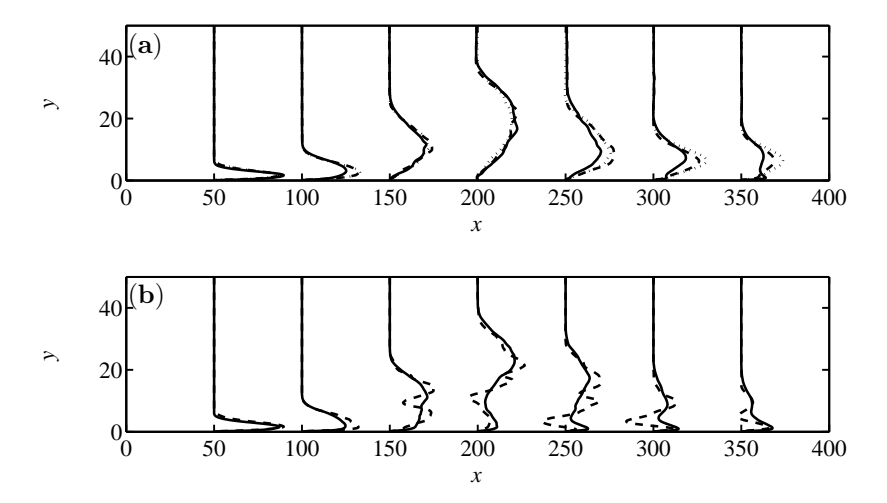


FIGURE 8. Wall-normal profiles of Reynolds stresses for different sweep angles (solid line $\alpha_0 = 45^{\circ}$, dashed line $\alpha_0 = 11^{\circ}$, dotted line $\alpha_0 = 0^{\circ}$) at different streamwise positions (a) $x - 10000 * uv/C_0U_0$ (b) $x - 10000 * vw/C_0W_0$.

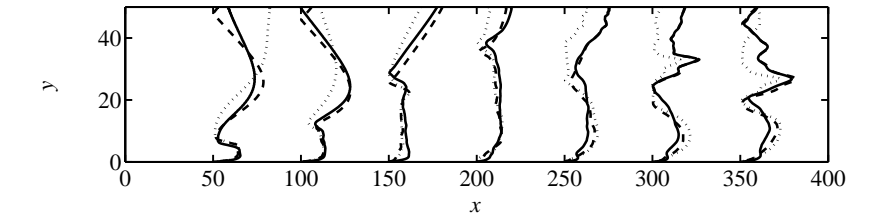


FIGURE 9. Wall-normal profiles of structure parameter a1 at different streamwise positions x + 100 * a1 for different sweep angles (solid line $\alpha_0 = 45^{\circ}$, dashed line $\alpha_0 = 11^{\circ}$, dotted line $\alpha_0 = 0^{\circ}$).

is usually considered. Wall-normal profiles of the parameter a_1 at different streamwise locations are displayed for the three simulations under considerations in figure 9. The largest values, about 0.25, are observed in the shear layer region (to be compared to an equilibrium value of about 0.2 for a free shear layer). These values are comparable in the three cases examined. The slow relaxation of the outer part of the boundary layer, indicated by the outer peak in the profiles, is also hardy dependent on the sweep angle. For the $\alpha_0 = 45^{\circ}$ -case the structure parameter is larger in the near wall region beneath the bubble, whereas it is the lowest after reattachment, as expected from previous studies

on three-dimensional turbulent boundary layers (Johnston & Flack 1996). The values close to the wall are of the order of 0.15.

4. Summary and conclusions

The effect of the sweep angle on the turbulent separation bubble induced by an imposed adverse-to-favourable pressure gradient is examined by means of direct numerical simulation. To the best of our knowledge, this preliminary work presents the first numerical study of pressure-induced three-dimensional separated boundary layer flow. To better identify the effect of the mean flow skewing, the free-stream spanwise velocity component is increased leaving all the other flow parameters unchanged. Having learned from previous studies on three-dimensional turbulent flows with and without geometrically-induced separation that the complicated effects of pressure gradient and strain on the turbulence characteristics are usually larger than those of sweep, simulations of a three-dimensional turbulent boundary layer subject to a weak adverse pressure gradient are also performed in order to try to separate the two competing effects, e.g. the mean flow skewing and the strong pressure gradient and strain rates associated to separation. The main findings can be summarised as follows.

The location of separation is not changed by the introduction of sweep for the angles examined here, whereas the reattachment occurs slightly upstream for the flow with largest sweep. The reduction of the separated region is in agreement with previous studies on spanwise invariant three-dimensional separation, where deviations from the sweep-independence principle are observed for angles $\alpha > 40^{\circ}$.

A significant increase in the turbulence activity in the separated region beneath the detaching shear layer and downstream of reattachment is clearly seen for the flow configuration with largest sweep angle. Such an increase occurring in the near-wall region is explained by the fact that with increasing sweep the mean velocity component parallel to the separation-reattachment line can provide wall-normal shear to feed turbulence production. However, this enhancement of the momentum mixing does not affect the reattachment point significantly, suggesting that the imposed pressure gradient is actually the main parameter determining the flow reattachment in the configuration under consideration. A different distribution of the external pressure can be designed in order to emphasise the effect of the increased turbulent mixing on the flow reattachment. A longer region with a weaker flow acceleration downstream of the bubble would probably help but it would cost in terms of computational efforts.

Profiles of mean flow quantities and statistics of the turbulent fluctuations comparing the three cases under consideration are shown. As observed in previous studies, it is not possible to find a universal scaling valid at all locations. However, it can be generally said that the velocity C of the external streamline seems to provide the best scaling for the flow quantities at separation and inside the separated region, whereas the streamwise velocity U yields a better

data collapse in the reattachment region. The latter can be explained by the fact that U is more directly related to the external pressure distribution.

Comparison with the simulations of three-dimensional boundary layers subject to weak adverse pressure gradient (see appendix) indicates that strength of the pressure gradient, the strain rate and the occurence of separation have a deeper impact on the turbulence structure than the skewing of the mean flow. This result is more evident for pressure-induced boundary-layer separation than for separation induced by the geometrical configuration.

The results presented here provide a first insight into the complicated flow originating by the twofold effect of skewing and pressure-induced separation. To complete the present study future investigations should aim at considering the effect of higher sweep angles. In addition, the evolution of vorticity in the detaching shear layer need to be further examined. In particular, the effect of the sweep on the interaction between the large vortical structure and the near-wall turbulence should be considered.

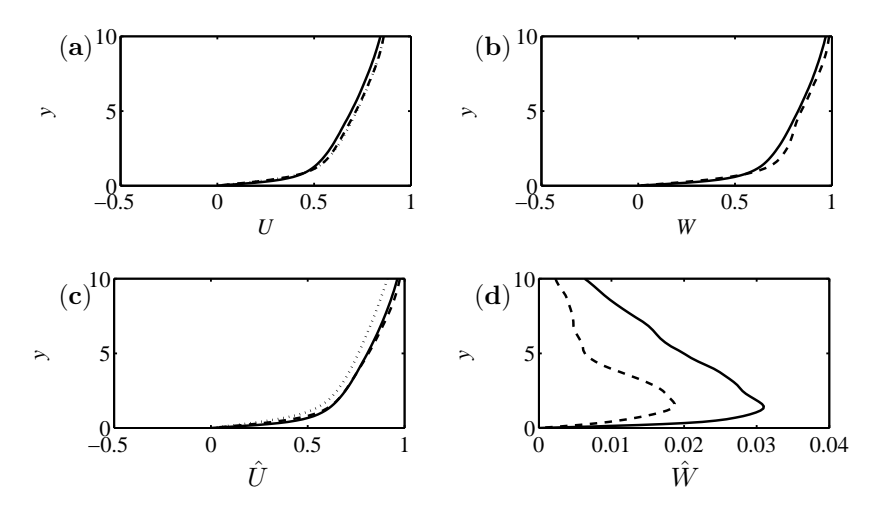


FIGURE 10. Wall-normal profiles of (a) U, (b) W (c), \hat{U} , (d) \hat{W} at x=250 for different sweep angles (solid line $\alpha_0=45^{\circ}$, dashed line $\alpha_0=11^{\circ}$, dotted line $\alpha_0=0^{\circ}$).

Appendix

In this appendix the results of preliminary simulations of a three dimensional turbulent boundary layer subject to weak adverse pressure gradient are presented. The free-stream streamwise velocity is chosen to be $U(x) \propto x^m$ with m=0.077. Simulations are conducted for the same sweep angles $\alpha_0=11^{\circ}$ and $\alpha_0 = 45^{\circ}$ as for the separation bubble presented in the paper. The data for the reference two-dimensional case were produced with the same numerical code by Skote et al. (1998). For the simulations presented in this Appendix, the following parameter setting is used. The computational domain is 450 long, 24 high and 24 wide, with a fringe region of 50. $480 \times 121 \times 96$ modes are used in the streamwise, wall-normal and spanwise direction respectively. The simulation in Skote et al. (1998) were performed in a lower computational domain, only 18 high, with 101 and 121 modes in the wall-normal direction. No-slip is imposed at the wall, whereas the asymptotic free-stream boundary condition described above is used at the upper limit of the computational box (see Skote et al. 1998, for further details). The statistics reported are obtained by averaging in time and in the spanwise direction and the profiles shown are extracted at x = 250, that is sufficiently far downstream of the transition region and upstream of the numerical fringe region.

Analysis of the skin friction coefficient, not shown here, indicates that the effects of separation are more important than those of skewing since a direct analogy with the results in figure 3 is not seen and that the turbulent flow considered above cannot be considered as fully developed as separation is encountered. The mean flow velocities are depicted in figure 10(a) and (b). The

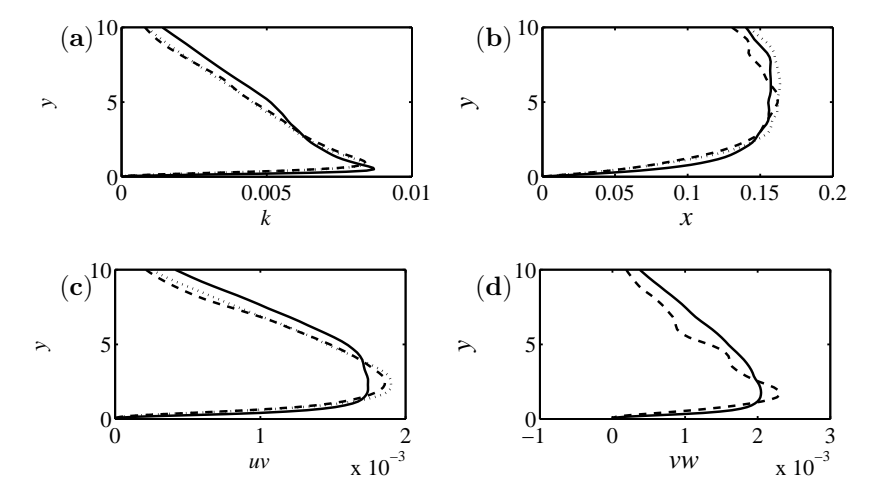


FIGURE 11. Profiles of (a) kinetic energy k/C_0^2 , (b) structure parameter a1 (c) Reynolds stress $u'v'/(U_0C_0)$, (d) Reynolds stress $v'w'/(C_0W_0)$ at x=250 for different sweep angles (solid line $\alpha_0=45^{\circ}$, dashed line $\alpha_0=11^{\circ}$, dotted line $\alpha_0=0^{\circ}$).

streamwise velocity does not show a monotonic behaviour when increasing the sweep, whereas the spanwise velocity profiles show features similar to those observed in the separating flow (figure 4d). The mean velocity in the direction of the local free-stream streamline is reported in figure 10(c) and (d). Good scaling can be observed for the downstream component, whereas the normalised cross-flow component is largest for highest sweep, in agreement with the behaviour for the separated flow presented in figure 5(b). As suggested before, the differences in the cross-flow component may be due to the effect of the $\partial W/\partial x$ strain.

The main features of the turbulent fluctuations are displayed in figure 11. The turbulent kinetic energy normalised with C_0^2 is depicted in figure 11(a), where it can be noticed that the amplitude is almost independent of the sweep angle, whereas the location of the peak is moving closer to the wall when increasing the mean flow skewing. The results cannot be directly compared with those presented in figure 7, suggesting that for pressure-induced boundary-layer separation the separation has a stronger effect on the turbulence than the sweep. The Reynolds stresses $u'v'/(U_0C_0)$ and $v'w'/(C_0W_0)$ are shown in figure 11(c) and (d) respectively. The intensity of the u'v'-stresses decreases with the sweep angle. The same seems to be valid also for the v'w' component of the Reynolds stress tensor, but the results show oscillations for the case with lower sweep, as in the case of the three-dimensional turbulent bubble in figure 8(b). The Townsend structure function a_1 is reported in figure 11(b). Although the results can be affected by the oscillations observed for the v'w' stresses, it seems

possible to conclude that no significant reduction is observed with increasing sweep, as also indirectly shown by the good collapse of the turbulent kinetic energy profiles in figure 11(a). Reduction of the structure parameter is observed in three-dimensional boundary layers induced by spanwise shear but it was not found in the turbulent flows over a swept bump by Webster *et al.* (1996). The data suggests that the reduction in turbulent activity close to the wall observed in skewed turbulent flows is compensated by the effect of the mean flow strain induced by the adverse pressure gradient.

References

- COLEMAN, G. N., KIM, J. & SPALART, P. R. 2000 A numerical study of strained three-dimensional wall-bounded turbulence. *J. Fluid Mech.* **416**, 75–116.
- HÄGGMARK, C. P., HILDINGS, C. & HENNINGSON, D. 2001 A numerical and experimental study of a transitional separation bubble. *Aerosp. Sci. Techol.* **0**, 1–12.
- HANCOCK, P. E. 1999 Measurements of mean and fluctuating wall shear stress beneath spanwise-invariant separation bubbles. *Experiments in Fluids* **27**, 53–59.
- HANCOCK, P. E. & McCluskey, F. M. 1997 Spanwise-invariant three-dimensional separated flow. *J. Expt. Thermal Fluid Sci* 14, 25–34.
- HARDMAN, J. R. & HANCOCK, P. E. 2000 The near-wall beneath a moderately converging three-dimensional turbulent separated and reattaching flow. *Eur. J. Mech. B-Fluids* **19**, 653–672.
- HERBST, A. H. & HENNINGSON, D. S. 2006 The inflence of periodic excitation on a turbulent separation bubble. *Flow, Turb. Combust.* **76**, 1–21.
- Hetsch, T. & Rist, U. 2006 The effect of sweep on laminar separation bubbles. In Sixth IUTAM Symposium on Laminar-Turbulent Transition (ed. R. Govindarajan), pp. 395–400. Printed in the Netherlands: Springer.
- JOHNSTON, J. P. & FLACK, P. A. 1996 Review- Advances in three-dimensional turbulent bounday layers with emphasis on the wall-layer regions. Trans. ASME I: J. fluids Engng. 118, 219–232.
- Kaltenbach, H.-J. 2003 The effect of sweep angle variation on the turbulence structure in a separated three-dimensional flow. *Theoret. Comput. Fluid Dyn.* 16, 187–210.
- Kaltenbach, H.-J. 2004 Turbulent flow over a swept backward-facing step. Eur. J. Mech. $B/Fluids~{f 23},~501-518.$
- Kaltenbach, H.-J. & Janke, G. 2000 Direct numerical simulation of flow separation behind a swept, rearward-facing step at $re_h = 3000$. Phys. Fluids 12, 2320–2337.
- Kalter, M. & Fernholz, H. 1995 The influence of freestream turbulence on an axisymmetric turbulent boundary layer in, and relaxing from, an adverse pressure gradient. In *Advances in Turbulence V. Proc. 5th Eur. Turb. Conference (Siena, Italy, 1994)*, pp. 261–265. Kluwer.
- KANNEPALLI, C. & PIOMELLI, U. 2000 Large-eddy simulation of a three-dimensional shear-driven turbulent boundary layer. *J. Fluid Mech.* **423**, 175–203.
- Lu, G. & Lele, S. K. 1993 Inviscid instability of a skewed compressible mixing layer. $J.\ Fluid\ Mech.\ 249,\ 441-463.$

- Lundbladh, A., Berlin, S., Skote, M., Hildings, C., Choi, J., Kim, J. & Henningson, D. S. 1999 An efficient spectral method for simulation of incompressible flow over a flat plate. Technical Report KTH/MEK/TR-99/11–SE. KTH, Department of Mechanics, Stockholm, Sweden.
- Malik, M. R., Zang, T. A. & Hussaini, M. Y. 1985 A spectral collocation method for the Navier-Stokes equations. *J. Comp. Phys.* **61**, 64–88.
- Manhardt, M. & Friedrich, R. 2002 DNS of a turbulent boundary layer with separation. *Int. J. Heat and Fluid Flow* 23, 572–581.
- Marxen, O. 2004 Numerical studies of physical effects related to the controlled transition process in laminar separation bubbles. Dissertation, Universität Stuttgart, Stuttgart.
- NA, Y. & Moin, P. 1998 Direct numercial simulation of a separated turbulent boundary layer. J. Fluid Mech. 374, 379–405.
- NORDSTRÖM, J., NORDIN, N. & HENNINGSON, D. S. 1999 The fringe region technique and the Fourier method used in the direct numerical simulation of spatially evolving viscous flows. SIAM J. Sci. Comput. 20 (4), 1365–1393.
- Skote, M. & Henningson, D. 2002 Direct numercial simulation of a separated turbulent boundary layer. *J. Fluid Mech.* **471**, 107–136.
- Skote, M., Henningson, D. S. & Henkes, R. A. W. M. 1998 Direct numerical simulation of self-similar turbulent boundary layers in adverse pressure gradients. *Flow, Turb. Combust.* **60**, 47–85.
- Spalart, P. & Coleman, G. 1998 Numerical simulation of a separation bubble with heat transfer. *Eur. J. Mech. B./Fluids* **16**, 169–189.
- Webster, D. R., Degraaf, D. B. & Eaton, J. K. 1996 Turbulence characteristics of a boundary layer over a swept bump. *J. Fluid Mech.* **323**, 1–22.

Paper 4

4

Simulations of turbulent flow in a plane asymmetric diffuser

By Astrid H. Herbst, Philipp Schlatter and Dan S. Henningson

KTH Mechanics, SE-100 44 Stockholm, Sweden

Submitted

Large-eddy simulations (LES) of a planar, asymmetric diffuser flow have been performed. The diverging angle of the inclined wall of the diffuser is chosen as 8.5°, a case for which recent experimental data are available. Reasonable agreement between the LES and the experiments is obtained. The numerical method is further validated for diffuser flow with the diffuser wall inclined at a diverging angle of 10°, which has served as a test case for a number of experimental as well as numerical studies in the literature (LES, RANS). For the present results, the subgrid-scale stresses have been closed using the dynamic Smagorinsky model. A resolution study has been performed, highlighting the disparity of the relevant temporal and spatial scales and thus the sensitivity of the simulation results to the specific numerical grids used. The effect of different Reynolds numbers of the inflowing, fully turbulent channel flow has been studied, in particular, $Re_b = 4500$, $Re_b = 9000$ and $Re_b = 20000$ with Re_b being the Reynolds number based on the bulk velocity and channel half width. The results consistently show that by increasing the Reynolds number a clear trend towards a larger separated region is evident; at least for the studied, comparably low Reynolds-number regime. It is further shown that the small separated region occurring at the diffuser throat shows the opposite behaviour as the main separation region, i.e. the flow is separating less with higher Re_b . Moreover, the influence of the Reynolds number on the internal layer occurring at the non-inclined wall described in a recent study has also been assessed. It can be concluded that this region close to the upper, straight wall, is more distinct for larger Re_b . Additionally, the influence of temporal correlations arising from the commonly used periodic turbulent channel flow as inflow condition (similar to a precursor simulation) for the diffuser is assessed.

1. Introduction

During the last decade, the numerical simulation of time-dependent, inherently three-dimensional flow problems has been established in the research community as a useful and accurate means for prediction and understanding of complex flow configurations. In particular, numerical simulations of highly intermittent flows as e.g. flows undergoing laminar-turbulent transition or flows exhibiting separation are routinely performed yielding very appealing results when compared to experimental data sets.

The most straightforward simulation approach, referred to as direct numerical simulation (DNS), attempts to numerically solve for all relevant flow structures in both space and time. The need to simulate all scales ranging from the energetically dominant integral length scales down to the smallest, viscous scales is prohibitively expensive even for moderate Reynolds numbers Re, in particular when dealing with wall-bounded flows (see e.g. Piomelli & Balaras (2002)). Conversely, conventional numerical predictions of complex engineering or geophysical turbulent flows are based on the Reynolds-averaged Navier-Stokes (RANS) equations for which statistical turbulence models are needed. Such computations can, however, only give statistical information about turbulence, and severe limitations of existing turbulence models in nonstandard situations, in particular involving separation and laminar-turbulent transition, represent a major obstacle to reliable predictions. For this reason, the concept of large-eddy simulation (LES) has emerged as an important tool for flows that need to be treated in an unsteady, three-dimensional manner. In LES, only the large-scale, energy-carrying vortices of the flow are accurately resolved on the numerical grid, whereas the effect of the small-scale fluctuations on the (resolved) larger scales enters through a subgrid-scale (SGS) model. Recent reviews on LES and appropriate SGS modelling are given by e.g. Lesieur & Métais (1996); Meneveau & Katz (2000) and in the monograph by Sagaut (2005). However, even using LES the computational cost increases dramatically for higher Reynolds numbers, in particular for wall-resolved LES (i.e. without resorting to wall models (Piomelli & Balaras 2002)).

Experiments and numerical simulations of flows in which separation occurs from smooth surfaces rather than induced by sharp edges or obstacles are particularly challenging. In the former case, the separation is caused by an adverse pressure gradient, either arising from geometrical constraints or due to specific freestream conditions. Under such circumstances, both the separation and reattachment points are fluctuating strongly in both time and space. Moreover, the resulting separated flow is highly intermittent and inherently three-dimensional. The whole downstream evolution of the flow is crucially influenced by the processes happening upstream and close to the separation point. A review highlighting these unsteady processes in separated flows is given by Simpson (1996).

A model problem exhibiting pressure driven separation which is feasible to study with DNS is the turbulent boundary-layer flow over a flat plate which separates from the wall due to an adverse pressure gradient. This case has been investigated up to the present date in a few studies only, e.g. by Na & Moin (1998). They found that the turbulent structures emanating upstream the separation point move upwards into the shear layer, and are then advected around the separated region causing the maximum of turbulence intensity to

be found in the centre of the detached shear layer. Skote & Henningson (2002) conducted a DNS of a turbulent boundary layer separating due to a strong adverse pressure gradient. In comparison with the earlier simulations the flow had a stronger and larger recirculation region. In all studies, the turbulence was found to be intensified above the separated region while it decreased in the backflow itself.

To study turbulent separation in more complex geometries one has to resort to modelling approaches. A recent review of different modelling approaches including LES and RANS for separated flows found in industrial applications is given by Leschziner (2006). In particular, the case of turbulent separated flow in a channel with streamwise periodic constrictions has emerged as a benchmark case. Flow separation is induced by a smooth, yet sharp expansion of the channel, reaching an opening angle of approximately 45° after the rounded edge. Fröhlich et al. (2005) present a careful comparison of different modelling strategies, e.g. suitable SGS models, wall-functions, resolution requirements etc. Recent results on this test case are presented by Breuer et al. (2006), who compare data obtained from a number of different simulations, including various Reynolds numbers, resolutions and simulation approaches (LES, DNS).

In the present contribution, we consider the planar asymmetric diffuser, which has already been studied in a number of numerical and experimental works as a model problem for pressure-driven separation. The performance of diffuser-like flows occurring in many technical applications is strongly affected by separation of the boundary layer close to the wall. Therefore, a thorough understanding of the involved flow physics is necessary, especially considering additional engineering applications as, e.g., improved diffuser design or flow control to improve the flow quality, prevent separation and promote reattachment. The main difference of the diffuser flow studied in the present contribution to the above mentioned periodic hill case is that the inflow conditions are prescribed as fully-developed turbulent channel flow, and the opening angle is significantly lower (approximately ten degrees). With that, the prediction of the separation point is expected to be more sensitive to a proper modelling approach.

Experimental investigations on the plane asymmetric diffuser have been carried out by Obi et~al.~(1993) and Buice & Eaton (1996) (see also Buice & Eaton (2000)). They both consider a fully developed turbulent inflow with a Reynolds number $Re_b = 9000$ based on the bulk velocity and the inlet channel half-height. The diffuser wall is inclined at the diverging angle of 10° . Recently, new experimental data for the asymmetric diffuser have been obtained by Törnblom (2003) (see also Gullman-Strand et~al.~(2004)) for slightly different conditions. These authors used an increased inflow Reynolds number of $Re_b = 20000$ and a decreased opening angle of 8.5° . For all these cases, velocity signals and velocity fluctuations together with wall measurements of pressure are available.

Results of RANS calculations for the 10° -diffuser using commercial software packages are reported in Iaccarino (2001). A detailed comparison between RANS and experiments for the 8.5° -case is presented in Gullman-Strand *et al.* (2004). It can be concluded from the RANS studies that, provided a suitable model, reasonable agreement with the experimental data can be obtained. However, these studies also show that the RANS results are in fact highly model dependent.

The Obi case has been considered in the numerical LES study by Kaltenbach et al. (1999) yielding generally satisfactory agreement with experimental data. They used the dynamic Smagorinsky model according to Smagorinsky (1963), Germano et al. (1991) and Lilly (1992) to account for the unresolved scales. More recently, the same flow case has been revisited by Schlüter et al. (2005) and Wu et al. (2006), also applying (among others) the dynamic Smagorinsky model, however using a different discretisation scheme than Kaltenbach et al. (1999). Schlüter et al. (2005) and Wu et al. (2006) report consistently that a reasonable prediction of the mean separation is possible on even rather coarse LES grids, however, by increasing the resolution (and thereby enhancing the overall accuracy of the simulation approximation), a trend towards a larger separated region is visible. Regarding the physics of the flow, Wu et al. (2006) identified an internal layer located close to the upper (straight) wall of the diffuser just after the expansion edge at the lower wall. Preliminary results for the Obi diffuser have also been obtained by Gravemeier (2005) in an LES based on the variational multiscale approach. The author reports on encouraging results using these recent modelling strategies on comparably coarse grids, however, the simulations seem to be clearly influenced by the exact details of the SGS model.

A DNS of the Obi diffuser at fairly low Reynolds number $Re_b \approx 2300$ has been reported by Ohta *et al.* (2003). Compared to the experimental data their numerical results considerably overpredict the extent of the separated region at that low Reynolds number. The authors attribute their mismatch to effects due to secondary flow in the experiments, however, they do not comment on possible numerical influences caused by their numerical approach.

In the present contribution, we focus on quantifying the influence of the Reynolds number on various diffuser-flow characteristics, in particular the extent of the separated region and the evolution of the skin friction coefficient, the internal layer at the upper wall and the size of the turbulent scales. To our knowledge, there is no detailed study in the literature clarifying these influences. Obi et al. (1999) have studied experimentally the Reynolds-number effect on the separated flow in the Obi diffuser in the range $Re_{cl} = 2500$, 3750, 5000 and 10000, based on the centreline velocity and the inflow channel half width, corresponding roughly to $Re_b = 2200$, 3350, 4500 and 9000. Their results show that the extent of the separated region increases with higher Re_b . In particular, for the lowest Reynolds number under consideration in the experiment, they find that the separation bubble completely disappears. The

authors thus argue that the diffuser recirculation region vanishes at Reynolds numbers below a certain limit. It should however be noted that the authors mention the presence of secondary flow caused by a relatively small aspect ratio in their experimental setup. As a consequence, the separated region might be underestimated due to the influence of the side wall. However, the issue of the decreasing separation bubble is of relevance, since at present the applicability of DNS is still restricted to fairly low Reynolds numbers. We therefore intend to conduct the investigations by performing large-eddy simulations using the numerical method already used with success by Kaltenbach et al. (1999), however on the slightly modified geometry of the diffuser also considered by Törnblom (2003), i.e. featuring a slightly decreased opening angle of 8.5° compared to 10° used by Obi et al. (1993) and Kaltenbach et al. (1999). This change of setup was motivated by the expected smaller separation bubble for the higher Reynolds number, which can however independently be reduced by a decreased opening angle.

Extensive simulations of the diffuser have been performed at three different Reynolds numbers, namely $Re_b=4500$, $Re_b=9000$ and $Re_b=20000$ corresponding to a friction Reynolds number Re_{τ} of the inflowing fully-turbulent channel flow of approximately 260, 480 and 980, respectively. Note that all Reynolds numbers are well above the limit for transition to turbulence. The Reynolds number effects on the flow statistics and the size of the separation bubble are documented. Power spectra of the temporal velocity fluctuations are calculated. Additionally, the influence of temporal correlations present in the inflow conditions is assessed.

The paper is organised as follows. In section 2 the applied simulation techniques including the discretisation method and the SGS model are introduced. The specific parameter settings and the inflow generation is discussed in section 3. The statistical and instantaneous results obtained for the diffuser flow at different Reynolds numbers are presented in section 4, and conclusions are drawn in section 5.

2. Simulation Technique

The computations of the diffuser flow are performed using a simulation code based on the hybrid second-order finite-difference/spectral method described in Kaltenbach *et al.* (1999). The three-dimensional Navier-Stokes equations are filtered to the grid, yielding the LES momentum equations in the primitive variables (velocity and pressure)

$$\frac{\partial \overline{u}_i}{\partial t} + \frac{\partial \overline{u}_i \overline{u}_j}{\partial x_i} = \frac{\partial \overline{p}}{\partial x_i} + \frac{1}{Re_b} \frac{\partial^2 \overline{u}_i}{\partial x_i \partial x_j} - \frac{\partial \tau_{ij}}{\partial x_i} , \qquad (1)$$

and the filtered continuity equation

$$\frac{\partial \overline{u}_i}{\partial x_i} = 0 \ . \tag{2}$$

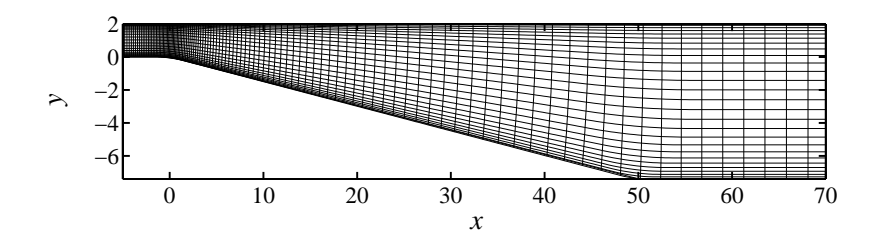


FIGURE 1. Sketch of the diffuser geometry (opening angle $phi = 8.5^{\circ}$) and the grid used for the present cases. Note that the inflow plane is located at x = -5 and the diffuser throat at x = 0.

Here, \overline{u}_i and \overline{p} denote the grid-filtered velocities and pressure, respectively. τ_{ij} are the subgrid-scale stresses computed from the SGS model as described below. The summation convention over repeated indices is applied unless stated otherwise. Equations (1) and (2) are solved in generalised coordinates using central finite differences of second order in the streamwise (x) and the wall-normal (y) direction, and a Fourier collocation scheme is applied in the spanwise (z)direction. No numerical dissipation is introduced by the numerical scheme due to conservation of kinetic energy. In the wall-normal (x/y) plane a staggered mesh is used with decomposition in contravariant velocity components, whereas the spanwise velocity is computed at the pressure nodes. Dealiasing based on phase-shifting is applied in the spanwise (Fourier) direction to enhance stability and accuracy. The time is integrated by a standard semi-implicit low-storage third-stage Runge-Kutta/Crank-Nicolson scheme, in which the viscous terms are treated implicitly in the wall-normal direction. The continuity equation is enforced by a fractional step algorithm of second-order accuracy in time. The Helmholtz equations arising after spanwise Fourier transform are solved by a multigrid algorithm. A sketch of the computational domain and a typical grid are shown in figure 1.

The code has been parallelised using explicit OpenMP shared-memory directives. The calculations have been performed on the vector computers NEC SX-6 and NEC SX-8 of the HLRS, Stuttgart, Germany. The overall performance of the code is 3.5 GFlops on a single processor NEC SX-8.

To account for the effect of the non-resolved (subgrid, subfilter) scales, the dynamic Smagorinsky model (Germano *et al.* 1991) has been adopted. In particular, the deviatoric part of the unclosed subgrid-scale stresses is approximated as

$$\tau_{ij} - \frac{\delta_{ij}}{3} \tau_{kk} \approx -2\nu_t \overline{S}_{ij} , \qquad (3)$$

with the resolved strain rate $\overline{S}_{ij} = 1/2(\partial \overline{u}_i/\partial x_j + \partial \overline{u}_j/\partial x_i)$. The remaining part of the SGS stresses is lumped into a modified pressure term (Lesieur & Métais 1996). The eddy viscosity ν_t is computed according to the Smagorinsky

model (Smagorinsky 1963) as

$$\nu_t = C\Delta^2 |\overline{S}| , \quad |\overline{S}|^2 = 2\overline{S}_{ij}\overline{S}_{ij} .$$
 (4)

The model coefficient C is defined as the square of the original Smagorinsky coefficient C_S . The local grid spacing Δ is given by the cube root of the cell volume $\Delta = (\Delta x \Delta y \Delta z)^{1/3}$. To determine the local model coefficient, the dynamic procedure proposed by Germano et al. (1991) has been applied. For this purpose the top-hat filter has been used in the wall-parallel directions and is approximated by the trapezoidal rule. The ratio of the filter width of the grid and test filter is $\hat{\Delta}/\Delta = \sqrt{6}$. Note that this ratio is the only parameter characterising the test filtering (apart from the actual test-filtered quantities) which enters the dynamic procedure. As commonly used in the literature, the dynamic model coefficient C has been computed using the least-squares approach by Lilly (1992) and is further averaged in the homogeneous spanwise (z) direction. Negative values of the resulting eddy viscosity ν_t are allowed, but restricted by the condition that the total viscosity $\nu_t + \nu$ is positive.

At the solid walls, no-slip boundary conditions are applied. Periodicity is assumed in the spanwise direction. At the inlet plane (x=-5) turbulent inflow is imposed via unsteady Dirichlet boundary conditions for the velocity components. Due to the staggered grid no conditions for the pressure need to be imposed. The inflow data is obtained from a separate LES of a fully-developed turbulent channel flow in a periodic box, which is further described in section 3.2. At the diffuser outflow plane a convective boundary condition of the form

$$\frac{\partial \overline{u}_i}{\partial t} + U_c \frac{\partial \overline{u}_i}{\partial x} = 0 \tag{5}$$

is used. The mean convection speed U_c is obtained as the wall-normal and spanwise average of the streamwise velocity component in the outflow plane.

3. Parameter Settings and Inflow Condition

3.1. Geometry and Parameter Settings

The geometry of the diffuser case is sketched in figure 1. For the present study, various calculations of the diffuser flow have been performed as summarised in table 1. Three different Reynolds numbers Re_b of the inflowing turbulent channel are considered, namely cases L1-L3 (low Re_b) with $Re_b = 4500$, cases M1-M3 with $Re_b = 9000$ (medium Re_b), and $Re_b = 20000$ (H1). For all cases the geometry of the diffuser is unchanged, however, the grid resolution is adapted according to the values given in the table. All quantities are non-dimensionalised by the inflow channel half-height δ and the bulk velocity U_b . Simulations have been performed with an opening angle of the inclined wall of the diffuser of $\phi = 8.5^{\circ}$. This specific geometry is designed to be similar to the setup employed in the experimental study by Törnblom (2003) (see also Gullman-Strand $et\ al.\ (2004)$). The channel inflow height is 2. The expansion starts at x = 0 and ends at x = 49.6 when the channel has reached a height of

TABLE 1. Grid resolution $N_x \times N_y \times N_z$ and Reynolds number Re_b of the inflowing turbulent channel flow for the diffuser cases. ϕ denotes the opening angle of the diffuser.

	Re_b	ϕ	N_x	N_y	N_z	# grid points
L1	4500	8.5	193	43	64	$0.53 \cdot 10^{6}$
L2	4500	8.5	193	65	64	$0.80 \cdot 10^{6}$
L3	4500	8.5	369	97	128	$4.58 \cdot 10^{6}$
M1	9000	8.5	289	65	96	$1.80 \cdot 10^{6}$
M2	9000	8.5	369	65	128	$3.07 \cdot 10^{6}$
М3	9000	8.5	593	129	192	$14.7 \cdot 10^6$
H1	20000	8.5	593	129	192	$14.7 \cdot 10^6$
K1	9000	10	353	65	128	$2.94 \cdot 10^{6}$

9.4 corresponding to an opening coefficient of 4.7. The length of the computational domain is $L_x = 93$ for the cases L1-L3, M1, M2 and K1 allowing the flow to recover over approximately 40 units before exiting the domain. For cases M3 and H1, a slightly increased length of the computational domain to $L_x = 104$ was used. The spanwise width is chosen as $L_z = 8$ for all cases, which is the same as previously adopted by Kaltenbach et al. (1999) and Wu et al. (2006). The edges at x = 0 and x = 49.6 are smoothed with a curvature radius of 20. The streamwise grid resolution is continuously coarsened in the downstream direction according to the increasing size of the expected turbulence. In the wall-normal direction, the grid points are moderately clustered towards both solid walls. As opposed to, e.g., Fröhlich et al. (2005), no wall-functions have been used in order to allow for an accurate prediction of the flow structures even close to the upper (non-inclined) wall.

To validate the present numerical approach, a simulation similar to Kaltenbach et~al.~(1999) featuring an opening angle of $\phi=10^\circ$ has also been performed (case K1). This geometry is described in detail by Obi et~al.~(1993) and Buice & Eaton (1996). It is worthwhile noting that in all studies different smoothing radii of the edges have been employed. In particular, Kaltenbach et~al.~(1999) and Obi et~al.~(1993) chose a value of 8.6, whereas Buice & Eaton (1996) used 19.4. In the 8.5° case considered in Törnblom (2003) a value of 6.6 has been adopted. It is however expected that the dynamics of the separated flow region is only marginally influenced by the specific choice of the rounding radius as long as is it smooth enough to prevent the flow from separating.

3.2. Inflow condition

As described in the previous section 2, the inflow boundary conditions located at x=-5 are specified via an unsteady Dirichlet condition. The time-dependent data is taken from a separate simulation of fully-developed turbulent channel flow. For these simulations, the same numerical scheme and SGS model has been applied as for the diffuser calculations. The different grids employed

TABLE 2. Computational grid and Reynolds numbers of channel flow used to generate the inflow condition for the diffuser. For all simulations, the channel height is $L_y=2$ and the width $L_z=8$. $\Delta y^+|_{\rm w}$ denotes the wall-normal spacing at the wall, $\Delta y^+|_{\rm c}$ the wall-normal spacing at the centreline, Δx^+ the streamwise spacing and Δz^+ the spanwise spacing in viscous units

	Re_b	Re_{τ}	N_x	N_y	N_z	L_x	Δx^+	$\Delta y^+ _{\rm w}$	$\Delta y^+ _{\rm c}$	Δz^+
L1C	4500	254	115	43	64	14.82	32.7	1.2	28.3	31.8
L2C	4500	258	115	65	64	14.82	33.2	0.5	11.5	32.3
L3C	4500	260	230	65	128	14.82	16.8	0.5	11.6	16.3
M1C	9000	473	97	65	96	9.7	47.3	1.5	33.8	39.4
M2C	9000	475	161	65	128	10.13	29.9	1.5	34.0	29.7
M2CL	9000	477	641	65	128	40.38	30.0	1.5	34.1	29.8
M3C	9000	482	193	129	192	9.65	24.1	0.7	16.7	20.1
H1C	20000	973	193	129	192	9.65	48.6	1.4	35.6	40.5

for the periodic channel flow are presented in table 2. The meshes have been chosen to be conforming at the inlet of the diffuser to avoid spatial interpolation. The channel simulations have been run with constant time step, and a Lagrangian interpolation technique has been employed to match the correct time of the diffuser simulation. No recycling of inflow data was used in order to avoid introducing further artificial periodicity.

The channel flow simulations are run with pseudo-periodic boundary conditions, *i.e.* a wall-normal velocity plane well upstream of the outflow boundary condition (usually located at $0.9 \cdot L_x$) is continuously fed back as inlet boundary condition of the channel. By this method, a constant mass flux is maintained throughout the simulation.

In table 2 the different resolutions are summarised. It can be seen that the resolution is sufficient in all spatial directions to allow for an accurate simulation of turbulent channel flow (Piomelli & Balaras 2002). The variation of the computed Reynolds number based on the skin friction Re_{τ} is only minor (below 3%) between the different resolutions.

The averaged properties of the channel flow simulations are shown in figure 2 for the wall-normal profile of the streamwise velocity component in wall units $\langle \overline{u} \rangle$, and the fluctuations

$$u_{\rm rms} = \frac{\sqrt{\langle \overline{u'} \, \overline{u'} \rangle}}{u_{\tau}} , \quad v_{\rm rms} = \frac{\sqrt{\langle \overline{v'} \, \overline{v'} \rangle}}{u_{\tau}} , \quad w_{\rm rms} = \frac{\sqrt{\langle \overline{w'} \, \overline{w'} \rangle}}{u_{\tau}} ,$$
 (6)

and the cross stresses

$$\langle \overline{u'} \, \overline{v'} \rangle / u_{\tau}^2 \ .$$
 (7)

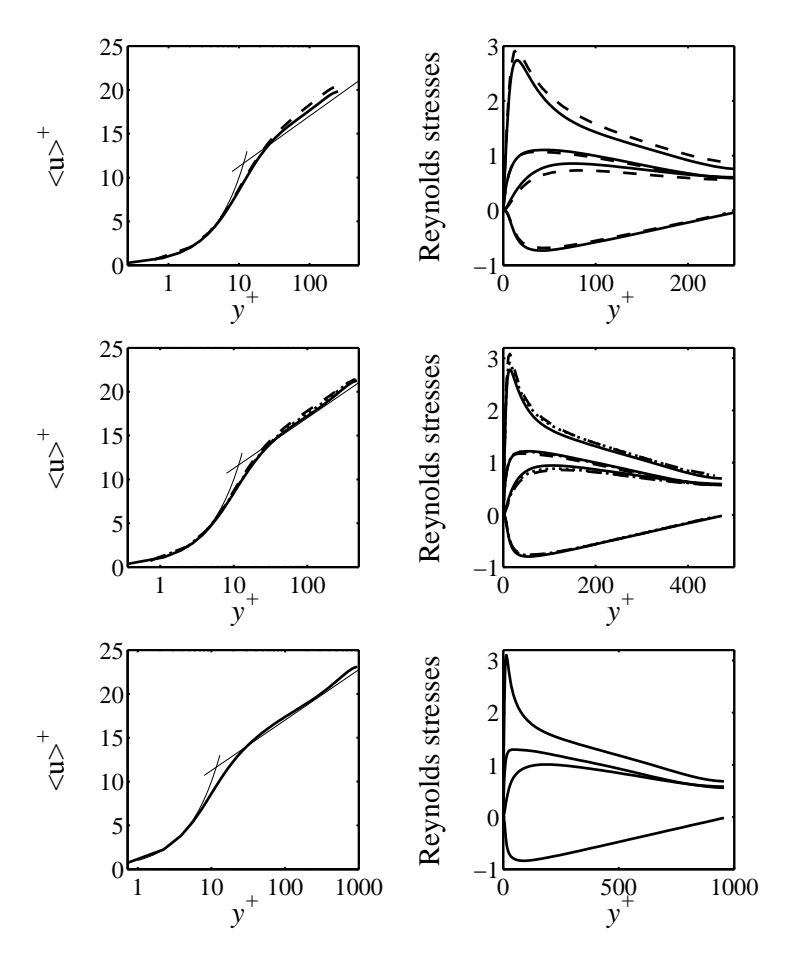


FIGURE 2. Statistics obtained for the fully developed channel flow used as inflow condition for the diffuser simulations. Left column: Streamwise velocity profile $\langle u^+ \rangle (y^+)$ scaled in viscous units. Right column: Fluctuations $u_{\rm rms}, v_{\rm rms}, w_{\rm rms}$ and cross stresses $\langle \overline{u'} \, \overline{v'} \rangle / u_\tau^2$. Top: $Re_b = 4500$, dashed case L1C, solid case L3C; Middle: $Re_b = 9000$, dashed case M1C, dotted case M2C, solid case M3C; Bottom: $Re_b = 20000$, solid case H1C. The analytical correlations $u^+ = y^+$ and $u^+ = 2.5 \log(y) + 5.5$ are included in the plots for reference.

Here, u_{τ} denotes the friction velocity, and the average $\langle \cdot \rangle$ is taken in time and over the homogeneous wall-parallel planes, and the fluctuations are defined as

$$\overline{u'} = \overline{u} - \langle \overline{u} \rangle . \tag{8}$$

The obtained results compare well with available numerical and experimental data sets. In particular, the law of the wall is reproduced accurately for all

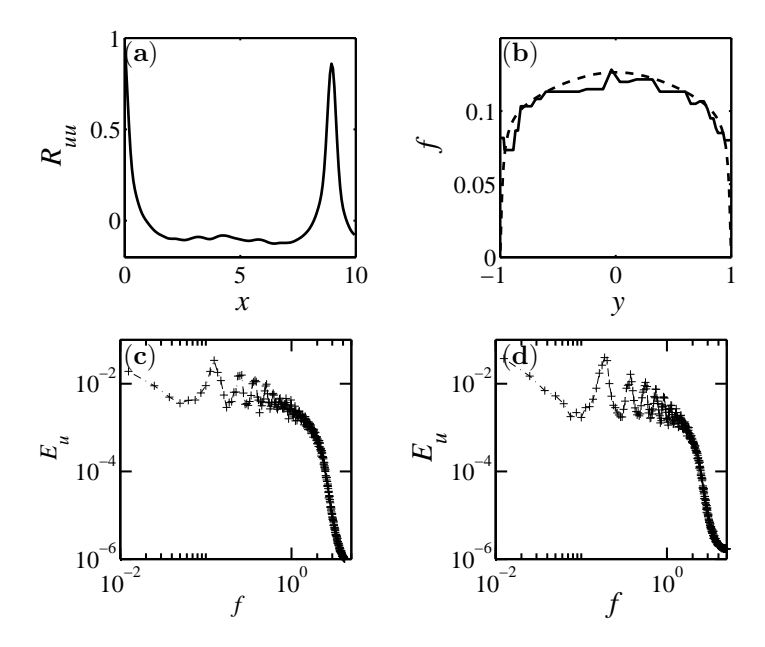


FIGURE 3. (a) Streamwise two-point correlation in the periodic channel; (b) frequency of the first peak in the power spectrum (solid) compared to $\langle \overline{u} \rangle / L_{x,r}$ (dashed); (c) Power spectrum of streamwise velocity at the channel centre for the long channel ($L_x = 40.38$, case M2CL) and (d) short channel ($L_x = 10.13$, case M2C).

simulations even on the coarsest grids. The fluctuations $u_{\rm rms}$ are slightly overpredicted for the lower resolutions. Note that this is a common observation for most LES calculations (see *e.g.* Schlatter *et al.* (2005)). In general a good convergence of the LES results can be observed. This is in particular important since it is suggested that the separation occurring in the diffuser is strongly dependent on an accurate representation of the turbulent inflow conditions (Buice & Eaton 1996).

The streamwise extent of the computational domain is sufficiently long such that the streamwise two-point correlations R_{uu} drop to zero, which is illustrated in figure 3(a) for case M2C. The strong peak visible at x=8.946 is the signature of the recycling station, located at approximately $0.9L_x$. However, looking at a temporal power spectrum of the streamwise velocity component, clear peaks are visible at frequencies $f=k\cdot 0.125,\, k=1,2,\ldots$ These peaks are most pronounced for the power spectra taken at a position in the channel centre. The fundamental frequency of these peaks is $f_0=0.125$ (see figure 3(d)) corresponding to the mean streamwise velocity at this wall-normal position $\langle \overline{u} \rangle$ divided by channel length up to recycling position $\langle \overline{u} \rangle / x_{L,r} = 1.12/8.946 = 0.125$. Since

the mean streamwise velocity varies in the wall-normal direction, the fundamental frequency also varies in y depending on where the power spectrum is recorded. In figure 3(b), the fundamental frequency taken from the power spectra is shown as a function of wall-normal position. The data coincides remarkably well with those obtained analytically from dividing the mean streamwise velocity by the channel length $x_{L,r}$. This clearly indicates that the peaks in the power spectra are associated with streamwise advection. Furthermore, the influence of the channel length on the temporal correlations has been examined by conducting an additional simulation (M2CL in table 2). For that simulation, the recycling position is located at $x_{L,r} = 36.15$ with the total channel length being $x_L = 40.38$. The corresponding power spectrum of the streamwise velocity in the channel centre is depicted in figure 3(c): The fundamental peak at 0.03 agrees with the expected value $\langle \overline{u} \rangle / x_{L,r} = 1.12/36.16 = 0.03$. It is interesting to note that the amplitude of the peak decreases for the longer channel flow simulation compared to the shorter channel length indicating that the overall correlation has decreased. This is of course expected due to the longer convection time. As mentioned above, the appearance of these peaks in the power spectra is clearly related to turbulent events that survive while they are convected downstream through the channel ('frozen turbulence'). It is important to note that the spectral peaks are not an artefact of the pseudoperiodic boundary treatment adopted here. This was checked by considering turbulent channel flow with genuine periodic boundary conditions. In these results obtained by a fully spectral method, the same peaks are visible (not shown).

For the present application, the data obtained by the simulation of the periodic channel are used as inflow condition for the diffuser flow. The question now arises how the artificial frequencies present in the channel data affect the dynamics of the flow in the diffuser. To address this issue we performed two diffuser simulation (case M2) with the inflow data obtained from the channel simulations M2C and M2CL, which differ in the frequency of the dominant spectral peaks. The results of these simulations are further discussed in section 4.4.

4. Results for the Diffuser Flow

4.1. Validation of Diffuser Simulations

The simulations of the flow in a planar asymmetric diffuser have been performed for three different resolutions for each of the two Reynolds numbers $Re_b = 4500$ and $Re_b = 9000$ and could be compared with each other to check convergence. The unsteady inflow conditions for each diffuser simulation are taken from channel simulations that have been performed with a resolution corresponding to the resolution of the diffuser simulation at the inflow (see also section 3.2). The effect of the resolution on the channel flow simulations has already been discussed in section 3.2.

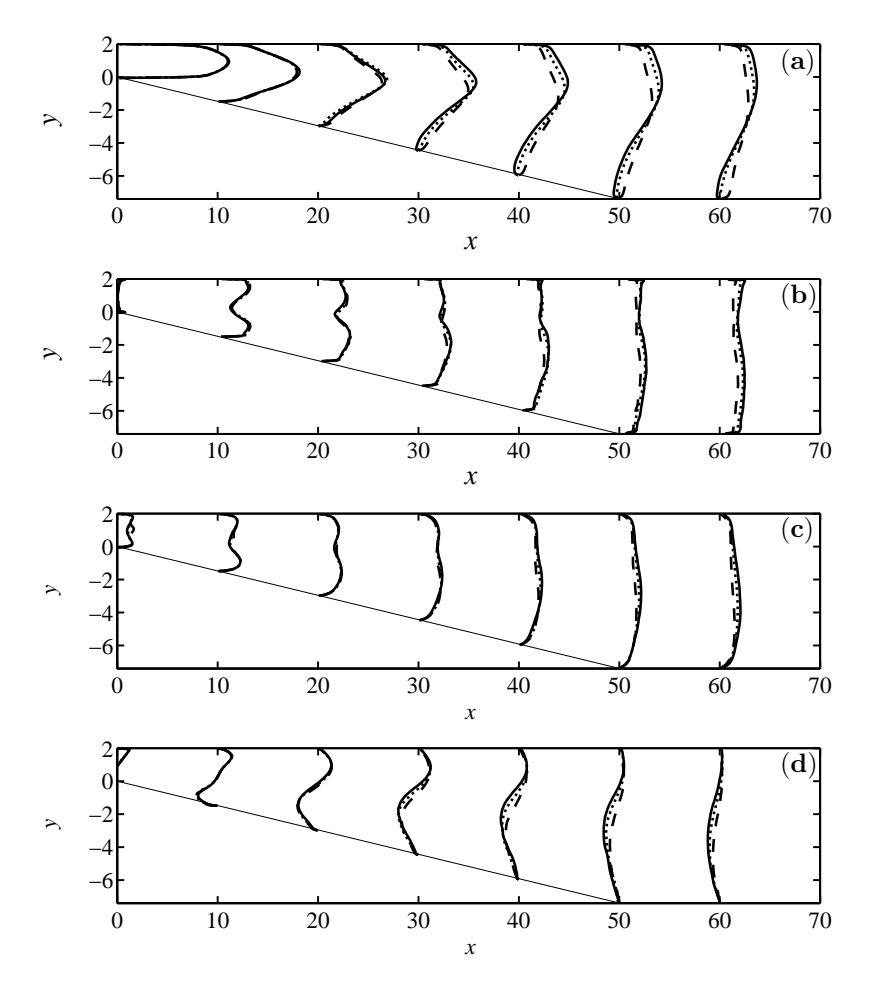


FIGURE 4. Turbulent statistics for the diffuser, $Re_b = 9000$ (dashed case M1, dotted case M2, solid case M3): (a) $10 \cdot \langle \overline{u} \rangle + x$, (b) $30 \cdot u_{rms} + x$, (c) $30 \cdot v_{rms} + x$, (d) $500 \cdot \langle \overline{u'}, \overline{v'} \rangle + x$.

4.1.1. Resolution Study

In figure 4 the evolution of the mean streamwise velocity $\langle \overline{u} \rangle$ and the fluctuations $u_{\rm rms}$, $v_{\rm rms}$ and $\langle \overline{u'} \, \overline{v'} \rangle$ is shown for $Re_b = 9000$ (cases M1-M3) at 7 streamwise positions $x = 0, 10, \ldots, 60$. Note that the average $\langle \cdot \rangle$ is taken over time and the spanwise direction, and (compare to section 3.2)

$$u_{\rm rms} = \sqrt{\langle \overline{u'} \, \overline{u'} \rangle} \;, \quad v_{\rm rms} = \sqrt{\langle \overline{v'} \, \overline{v'} \rangle} \;, \quad w_{\rm rms} = \sqrt{\langle \overline{w'} \, \overline{w'} \rangle} \;.$$
 (9)

The general behaviour of the results shows a good agreement between the medium resolution (simulation M2) and the highest resolution (simulation M3).

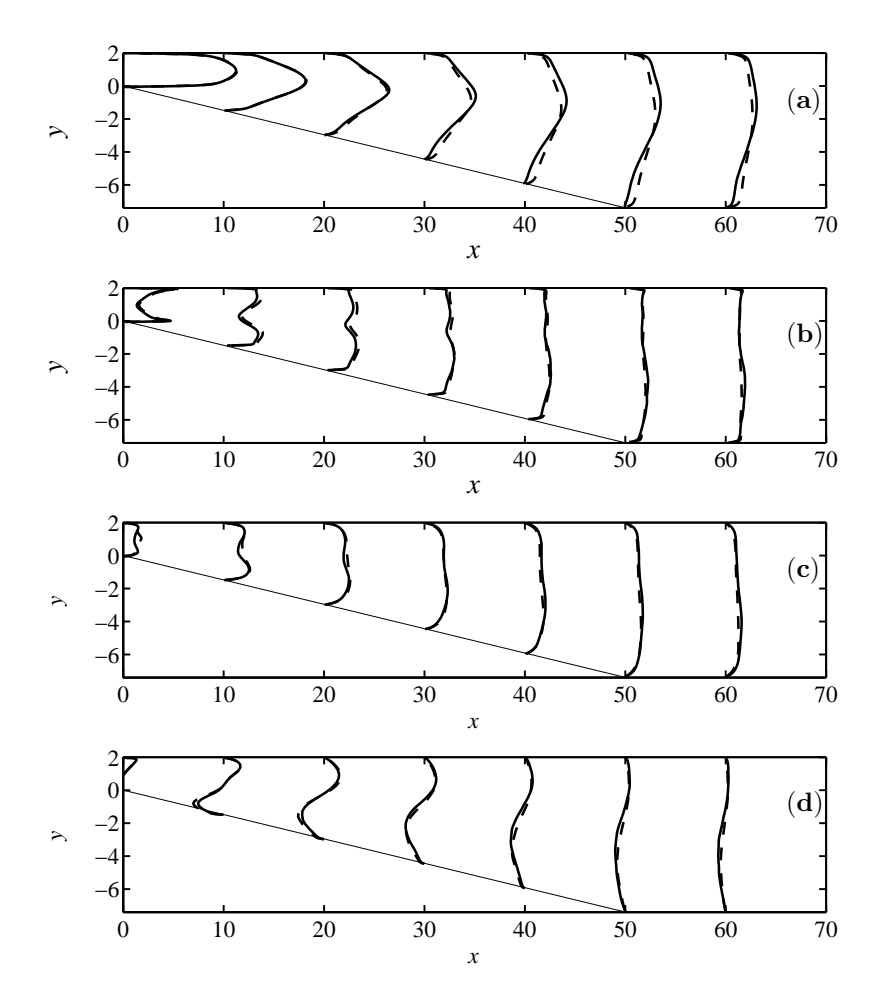


FIGURE 5. Turbulent statistics for the diffuser, $Re_b = 4500$ (dashed case L1, solid case L3): (a) $10 \cdot \langle \overline{u} \rangle + x$, (b) $30 \cdot u_{rms} + x$, (c) $30 \cdot v_{rms} + x$, (d) $500 \cdot \langle \overline{u'} \, \overline{v'} \rangle + x$.

Relevant low-order statistics such as mean streamwise velocity, turbulence intensities and skin friction do not show large differences (see also figure 12). Conversely, the lowest resolution (case M1) fails to predict the correct extent of the separated region (see figure 12), resulting in discrepancies in the mean streamwise velocity as well as the turbulent fluctuations. This particular resolution must clearly be considered as insufficient for the given Reynolds number.

For the lowest Reynolds number $Re_b = 4500$, the comparison between the two simulations L1 and L3 in figure 5 shows differences that originate from the fact that the lower resolution (L1) fails to predict any separated region at all, whereas a shallow separation bubble is present in the rear part of the expanding

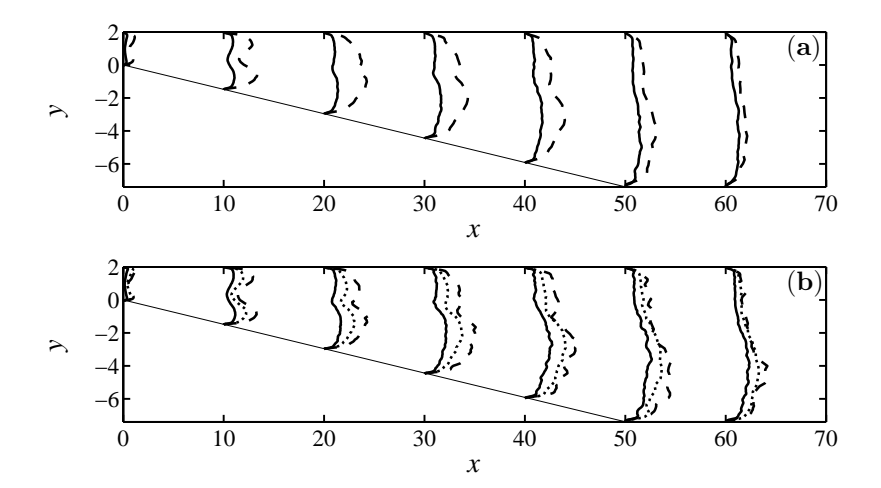


FIGURE 6. Ratio of SGS eddy viscosity and molecular viscosity: (a) $Re_b = 4500$ (dashed case L1, solid case L3); (b) $Re_b = 9000$ (dashed case M1, dotted case M2, solid case M3).

section of the diffuser for case L3. This obvious difference is however not due to an insufficient resolution in the wall-normal direction, since a separate run with the same resolution in x and z as case L1, but increased number of grid points in y (case L2) gave the same results as L1, *i.e.* no separation bubble present in the temporal and spanwise average. Therefore, only the results for L1 and L3 are compared in figure 5. Note that the separation bubble observed in simulation L3 is very shallow only.

The resolution check is conducted only at Re = 4500 and Re = 9000. For the highest Reynolds number solely one simulation (H1) has been performed with the resolution in wall units chosen to be similar as case M2. In section 4.2.1 the results of case H1 are compared to the experimental findings by Törnblom (2003).

4.1.2. SGS Model

By performing an LES, the interaction between the resolved and unresolved (subgrid, subfilter) scales is modelled. It is therefore essential to investigate and quantify the influence of the subgrid-scale model for both Reynolds numbers Re=4500 and Re=9000 at the different resolutions. Figure 6 depicts the ratio between the viscosity provided by the subgrid-scale model and the molecular viscosity. It can be observed that the influence of the subgrid-scale model clearly weakens as the resolution is increased. Close to the inflow of the diffuser, the maximum ratio of modelled to molecular viscosity is approximately 1.5 for the lowest resolution and only 0.4 for the highest resolution. In the separated region, the general influence of the SGS model appears to be more prominent,

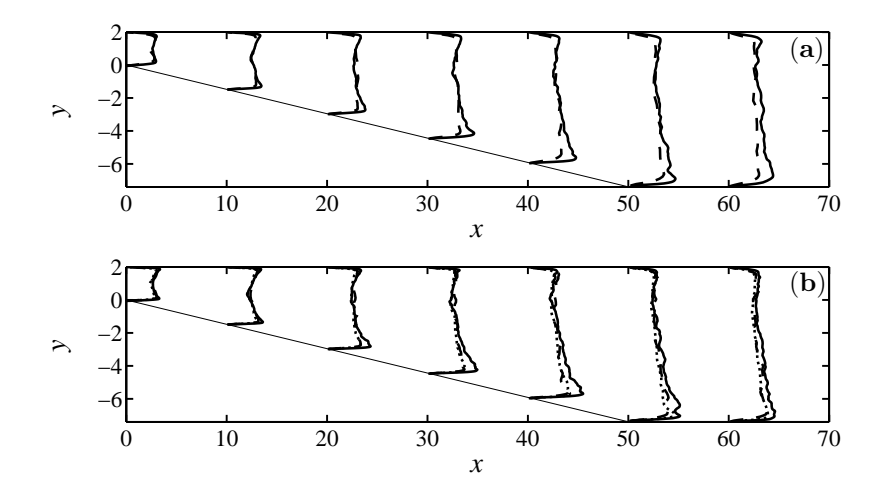


FIGURE 7. Evolution of the Smagorinsky coefficient C_S , shown is $20 \cdot C_S + x$: (a) $Re_b = 4500$ (dashed case L1, solid case L3); (b) $Re_b = 9000$ (dashed case M1, dotted case M2, solid case M3).

with the eddy viscosity being 5 times the molecular viscosity (case M1) and with a ratio of 2 for case M3. It can further be seen that close to the upper wall the effect of the SGS model is much smaller than in the recirculation region. It can thus be concluded that the resolution at the upper wall is sufficient for all cases. For the highest resolution the maximum activity of the SGS model is in the shear layer on top of the separated region, reaching to a ratio of 2.

In order to further assess the role of the subgrid-scale model, we compare profiles of the Smagorinsky coefficient C_S , as computed from the dynamic procedure (see section 2). The results are shown in figure 7 for the different resolutions, averaged in time and spanwise direction. The value of the Smagorinsky coefficient does, as expected, not vary significantly as the resolution is changed. The influence of the dynamic procedure is clearly evident by reducing the model coefficient close to solid walls, reproducing the correct asymptotic near-wall behaviour to account for the decreasing effective Reynolds number close to the walls (Piomelli 1993). In the turbulent channel flow away from the wall a value of $C_S \approx 0.12$ is measured, which is consistent with other studies applying the Smagorinsky model (see e.g. Moin & Kim (1982)). However, for the highest resolution at both Reynolds numbers we note a slight increase of C_S within the separated region.

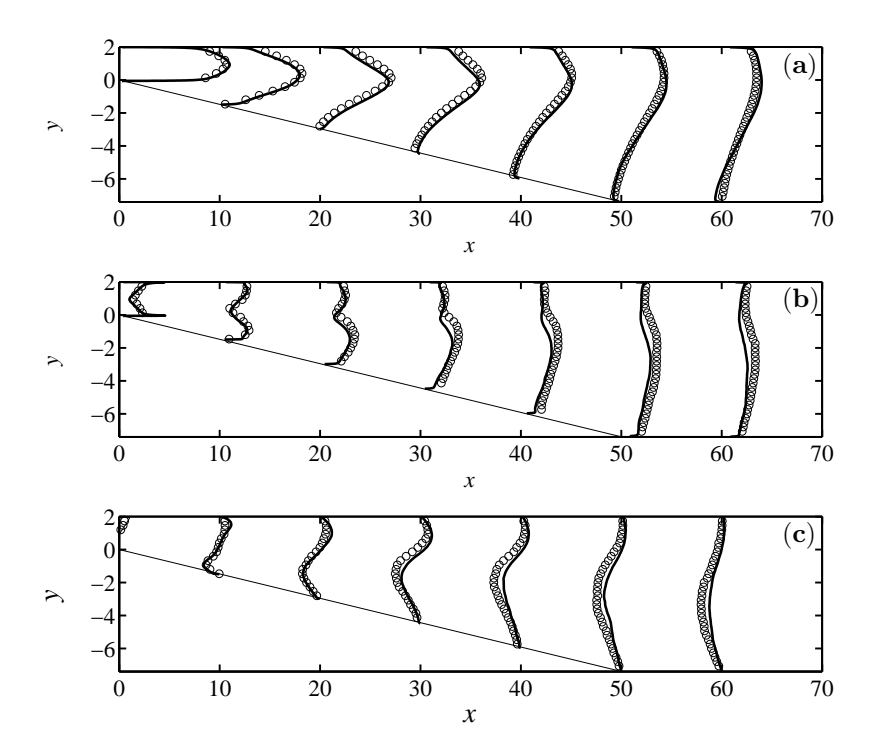


FIGURE 8. Comparison of H1 (solid) with measurements by Törnblom (2003) (circles) at $Re_b = 20000$: (a) $10 \cdot \langle \overline{u} \rangle + x$, (b) $30 \cdot u_{rms} + x$, (c) $500 \cdot \langle \overline{u'} \ \overline{v'} \rangle + x$.

4.2. Statistical Results

In a first part, we focus on the overall properties of the flow in the diffuser. For the presentation of results we use the data obtained with the highest resolution available at each Reynolds number.

4.2.1. Comparison with Experimental Data

Figure 8 shows the comparison of our LES results (H1) at $Re_b = 20000$ with the experimental data by Törnblom (2003) for the mean streamwise velocity $\langle \overline{u} \rangle$, $u_{\rm rms}$ and $\overline{u'}\,\overline{v'}$. For the streamwise velocity a good overall agreement can be seen at all downstream stations. A close inspection of the data however shows that the separated region obtained from the experiment is slightly larger than in the simulations (see also discussion related to figure 9). The turbulent stresses in the rear part of the diffuser are under-predicted in the LES, which is consistent with the results obtained by Kaltenbach *et al.* (1999), however, the difference is more distinct in our case. It should be noted that we did not include the SGS stresses τ_{ij} in the evaluation of $u_{\rm rms}$ and $\overline{u'}\,\overline{v'}$.

4.2.2. Reynolds-Number Effect on the Main Separated Region

For separated flow, one way to define the separated region is to consider the stream function of the mean two-dimensional flow field. Na & Moin (1998) found the definition of separation and reattachment based on the mean dividing streamline for their simulation of a turbulent boundary layer on a flat plate separating due to an adverse pressure gradient in good agreement with the points determined by zeros of the mean skin-friction coefficient and the location of 50% backflow. Moreover, the mean dividing streamline gives a measure for the extent of the recirculation region. Figure 9 gives a two-dimensional view of the extent of the separation region by showing contour lines of the stream function for the different simulations as well as the experimental data by Törnblom (2003).

Comparing the results for $Re_b = 4500$ and $Re_b = 9000$ in figure 9(a) and (b) we find a considerable increase of the separated region for the higher Reynolds number. This trend also holds comparing the results for $Re_b = 9000$ to those of the simulation for the highest Reynolds number $Re_b = 20000$ shown in figure 9(c). However the differences are much smaller between the medium and the highest Reynolds number, which might indicate that a levelling-off has been reached. At the highest Reynolds number only one simulation (H1) with a resolution corresponding to the medium resolution at medium Reynolds number has been performed. However, it seems evident from the resolution study presented in the preceding section for $Re_b = 4500$ and $Re_b = 9000$ that the separated region always increases in size with a finer computational grid. Similar trends have also been reported by Kaltenbach et al. (1999). It is therefore expected that separation bubble at $Re_b = 20000$ will be of the same size or slightly larger if the resolution was increased even further. We thus conclude that for the studied Reynolds-number regime a clear trend is observed that the size of the separated region in the rear part of the expanding section of the diffuser increases with higher Reynolds number. This Reynolds-number dependence agrees well with the results reported by Obi et al. (1999). Their data suggest the existence of a critical Reynolds number below which the flow does not separate in the mean from the inclined wall. However, with their experimental setup they could not prevent separation from the side walls, leading to significant secondary flow and three-dimensional effects. In particular the separation region could thus be underestimated in their data.

If we compare to the measurements by Törnblom (2003), for which the resulting stream function is shown in 9(d), we note that the flow separates slightly later in the simulation (at x = 19.5) than in the experiment (at $x \approx 18$). Downstream of the point of separation, the recirculation region increases in size more rapidly in the experiments than the simulation. However, the flow computed by LES reattaches significantly later than in the measurements. This tendency was also observed for the simulation on the Obi diffuser configuration with a 10° opening angle at the Reynolds number $Re_b = 9000$ in the study by Kaltenbach $et\ al.\ (1999)$.

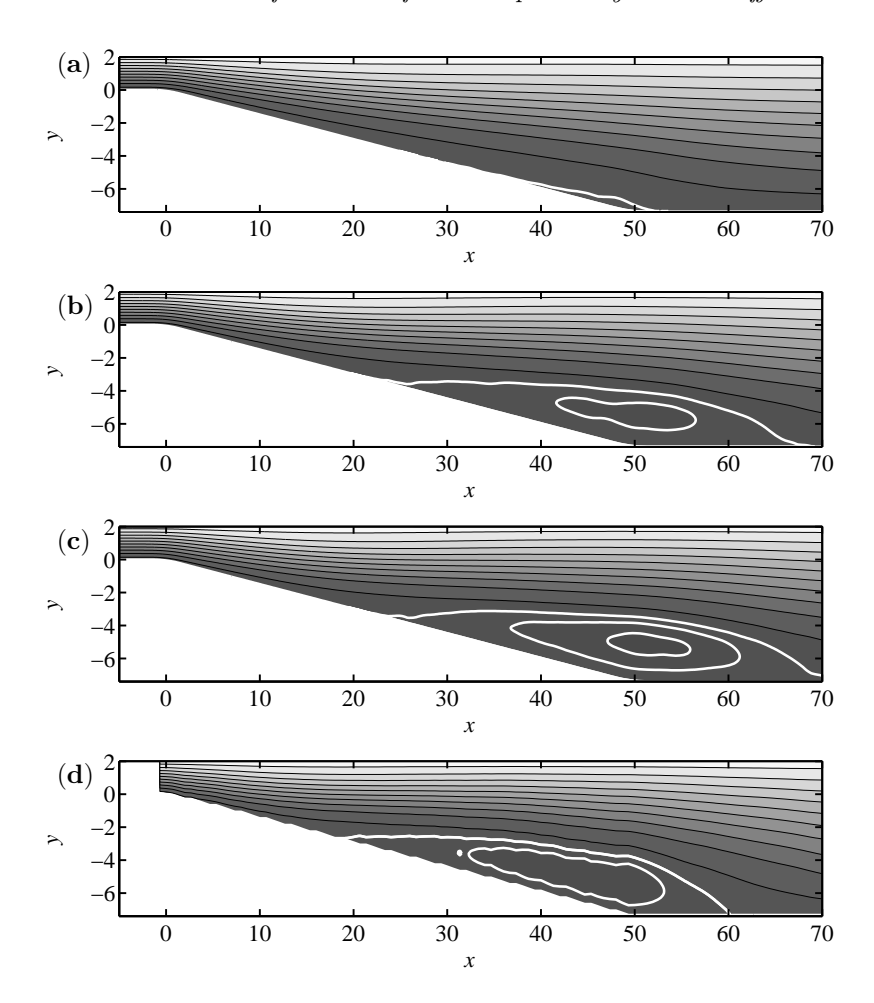


FIGURE 9. Reynolds-number dependence of the separation bubble visualised by contours of the stream function: (a) $Re_b = 4500$ (case L3), (b) $Re_b = 9000$ (case M3), (c) $Re_b = 20000$ (case H1), (d) Experiment by Törnblom (2003), $Re_b = 20000$. White contour levels range from -0.2 to -0.05 with spacing 0.05, black contours from 0.1 to 1.9 with spacing 0.2.

In figure 10 contours of streamwise turbulent intensity are shown. Close to the inflow and in the first part of the expanding section of the diffuser one observes that the region of high turbulent intensity is more confined to the wall for higher Re_b , similar as in turbulent channel flow. Further downstream, where the flow separates, the highest turbulence intensities are found in the separated shear layer just above the mean position of the bubble. This is a

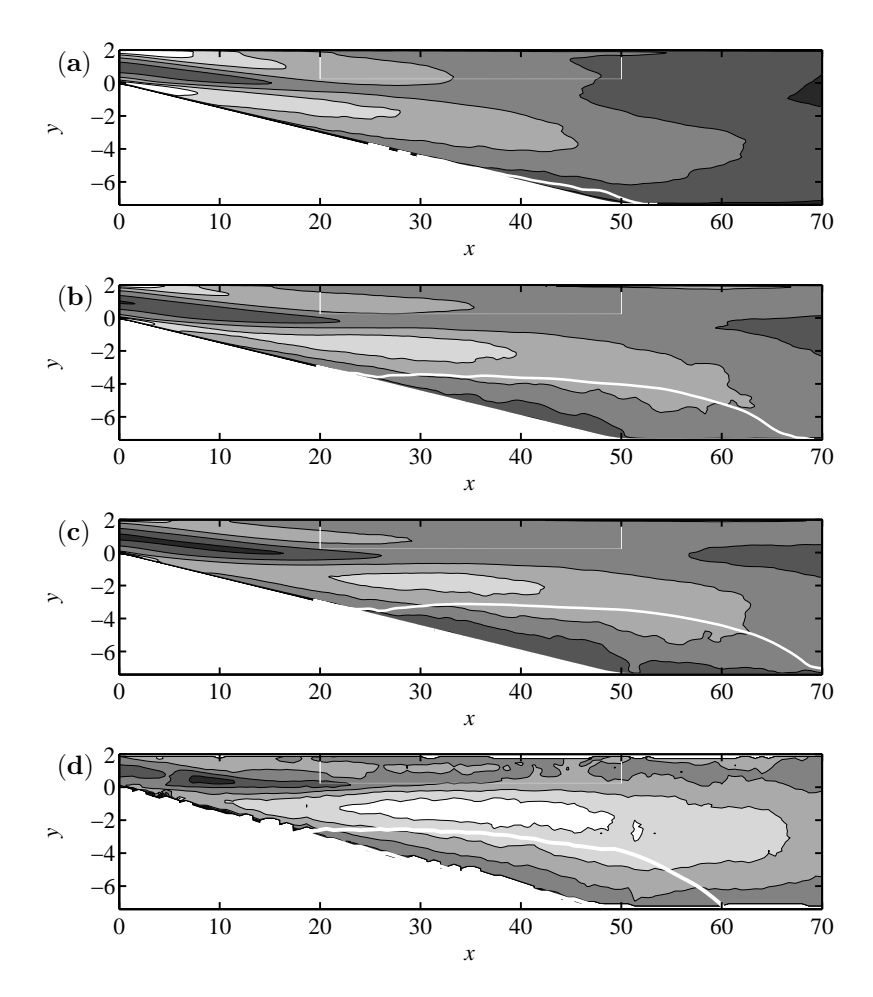


FIGURE 10. Reynolds-number dependence of the streamwise turbulence intensity: (a) $Re_b = 4500$ (case L3), (b) $Re_b = 9000$ (case M3), (c) $Re_b = 20000$ (case H1), (d) Experiment by Törnblom (2003). Contour levels range from 0.0 to 0.12 with a spacing of 0.2; white: mean dividing streamline. The box marked is shown enlarged in figure 13.

feature which has also been observed for separation from a solid wall due to an adverse pressure gradient (Skote & Henningson 2002). Comparing the streamwise turbulence intensities for the different Reynolds numbers we observe that the region dominated by the features similar to those of the incoming channel flow extends further into the diffuser as the Reynolds number is increased. This indicates that the incoming channel flow penetrates further in a 'jet-like' manner into the expanding diffuser section. Also shown in figure 10(d) are

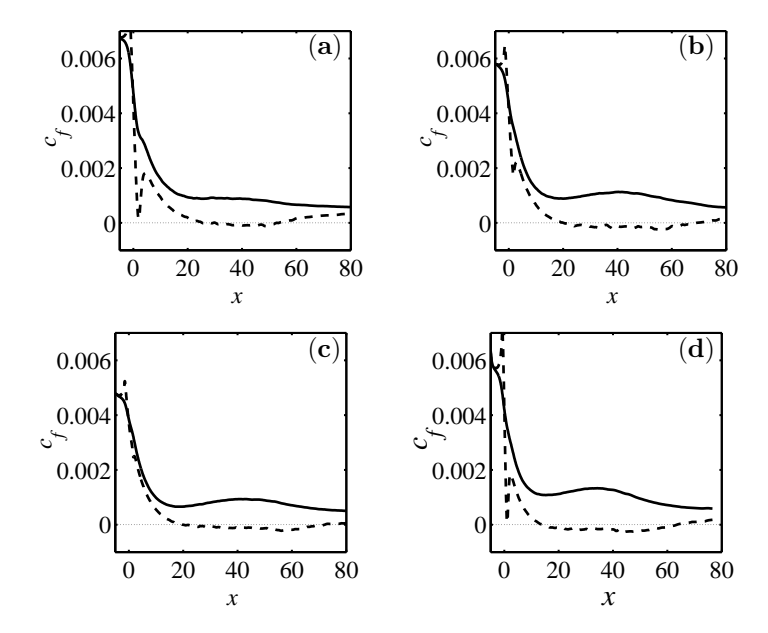
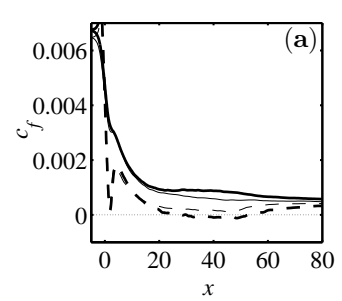


FIGURE 11. Reynolds-number dependence of the skin-friction coefficient at lower wall (dashed line) and upper wall (solid line): (a) $Re_b = 4500$ (case L3), (b) $Re_b = 9000$ (case M3), (c) $Re_b = 20000$ (case H1), (d) $Re_b = 9000$, diverging angle 10° (case K1).

the turbulence intensities measured in the experiments by Törnblom (2003) at $Re_b = 20000$. A generally higher level of fluctuations is apparent in the experiments, however the gross features are captured reasonably well by the LES results as seen in figure 10(c).

4.2.3. Separation at the Diffuser Throat

Turning attention to the first part of the expanding section at the throat of the diffuser, we note by inspecting the skin-friction coefficient C_f in figure 11(a) that for the simulation at $Re_b = 4500$ a minute separation bubble exists at x = 0. On the other hand, at $Re_b = 9000$ (figure 11 (b)), only a slight decrease of C_f is present at x = 0, and the flow does not separate in the mean. At $Re_b = 20000$ (figure 11(c)) the skin friction decreases monotonically in this region without any apparent downward peak. It is important to note that this behaviour is not resolution dependent as confirmed by figure 12. For this small region at the beginning of the diffuser expansion we conclude that the boundary layer has less tendency to separate as the Reynolds number is increased. It is interesting to note that this behaviour is opposite to the trend described for the large separated region further downstream. The results thus suggest that for the separation at the diffuser throat the Reynolds-number dependency of the



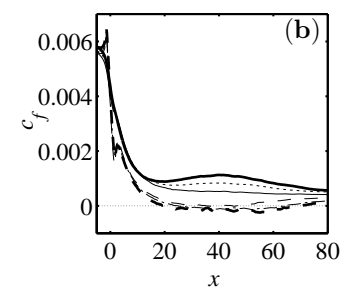


FIGURE 12. Resolution dependence of the skin-friction coefficient for (a) $Re_b = 4500$, at upper wall dashed lines, at lower wall solid lines. thin case L1, thick case L2; (b) $Re_b = 9000$: at upper wall solid M1, dotted M2, thick solid M3, at lower wall dashed M1, dashed-dotted M2, thick dashed M3.

incoming turbulent boundary layer with enhanced mixing at higher Reynolds numbers is the crucial factor preventing separation.

4.2.4. Reynolds-Number Dependence of the Internal Layer

We now focus on the flow behaviour in a region close to the upper, non-inclined wall. The section indicated by the white box in figure 10 displaying the streamwise turbulence intensity is shown as an enlargement in figure 13. For the highest Reynolds number $Re_b = 20000$, closed contour lines are visible near the upper boundary between approximately x=23 and x=37. Also from figure 13(d) showing the experimental data, a similar structure may be inferred, however not as clearly as for the simulation data. In this region we also observe an inflectional point in the mean velocity profiles. Wu et al. (2006), while considering the Obi diffuser configuration with an inclination angle of 10° at $Re_b = 9000$, associated such a closed area of contour levels close to the upper wall with the appearance of an internal layer. According to Townsend (1965), an internal layer forms as a result to sudden changes of the external conditions of boundary layers. Then the layer outside the internal layer is expected to develop in almost the same way as the original flow. Conversely, the inner layer layer is in equilibrium with respect to the local budget of turbulent kinetic energy. Wu et al. (2006) further characterise the internal layer by an inflectional point in the wall-normal profile of the mean streamwise velocity, which gives rise to a well-defined logarithmic law visible in the mean streamwise velocity underneath a linear region extending into the core region of the diffuser. They further argue that it is possible to relate the occurrence of the internal layer to the establishment and stabilisation of a new level of the skin-friction coefficient C_f . By examining frequency spectra, Wu et al. (2006) further conclude that, in the presence of a strong adverse pressure gradient, the low-frequency content of the streamwise velocity fluctuations is increased and that inside the

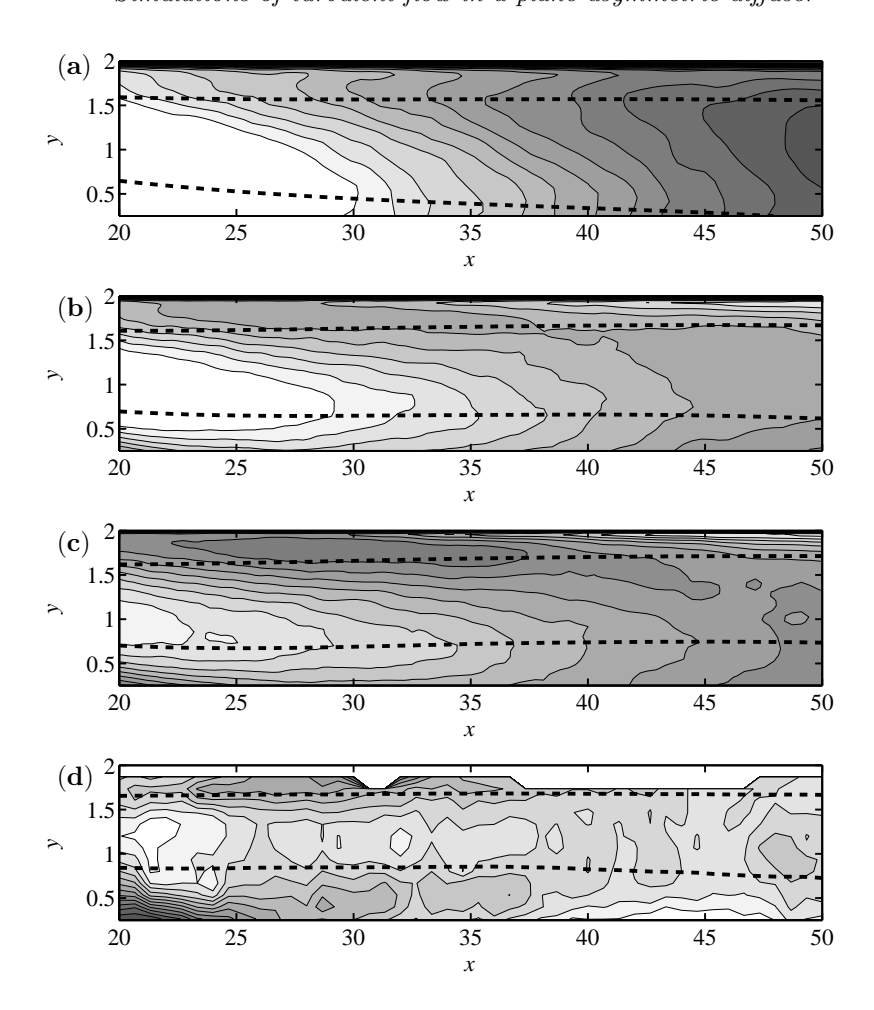


FIGURE 13. Reynolds-number dependence of the streamwise turbulence intensity: (a) $Re_b = 4500$ (case L3), (b) $Re_b = 9000$ (case M3), (c) $Re_b = 20000$ (case H1), (d) experiment by Törnblom (2003). Contour levels range from 0.02 to 0.085 with a spacing of 0.0025. *Dashed:* Contours of the stream function at $\psi = 1.5$ and 1.9.

internal layer, frequency energy spectra at different streamwise locations but with the same wall-normal coordinate, nearly collapse. They also notice that visualisations suggest the existence of organised vortices outside the internal layer.

It is interesting to see that for the present configuration with an inclination angle of 8.5°, a tendency towards the formation of such an internal layer is visible in figure 13(b); however, for $Re_b = 4500$ no such closed area can be

detected in the streamwise velocity fluctuation (figure 13(a)). Note that the stream lines superimposed in the figures are slightly deflected from the wall for the simulation at Re = 9000 whereas a slightly opposite inclination can be inferred for Re = 4500. As described above, the evolution of the skin-friction coefficient C_f is considered as a further signature of an internal layer. For comparison with the Obi configuration, we also show the results of the simulation similar to the one by Kaltenbach et al. (1999) (case K1). For that configuration, a new level of the skin-friction coefficient is clearly established (see figure 11(d)), as discussed by Wu et al. (2006). Considering figure 11, at the highest Reynolds number $Re_b = 20000$, the establishment of a new level of the skin-friction coefficient is clearly visible at the upper wall. At $Re_b = 4500$ the decrease of the skin-friction coefficient is almost monotonic and at $Re_b = 9000$ only a small elevation is present in the curve of the friction coefficient. This supports the conclusion that the development of the internal layer is more pronounced at higher Reynolds numbers.

In order to detect whether the mean streamwise velocity profiles follows a well defined logarithmic layer within the internal layer, we present in figure 14 profiles of \overline{u}^+ scaled in viscous units at different streamwise positions in dependence of the Reynolds number. On the semilogarithmic scale adopted, the different profiles collapse well at different streamwise stations for $Re_b = 20000$ (figure 14(c)), and also, however less pronounced, for $Re_b = 9000$ (figure 14(b)). At this Reynolds number the results agree well with the findings of Wu et al. (2006) who considered the Obi diffuser at the same Re_b , for which we show our own results in figure 14(d). Conversely, at the lowest Reynolds number such a collapse is clearly not observed, as can be seen from figure 14(a). Again, the above statement that the establishment of an internal layer is more distinct at higher Reynolds number, is confirmed.

4.3. Instantaneous Flow Structures

In this section we study the instantaneous features of the turbulent flow in the plane asymmetric diffuser. We first focus on the near-wall structures, in particular the turbulent near-wall streaks. These structures are well-known in turbulent boundary-layer and turbulent channel flow, and manifest themselves as spanwise alternating high- and low-speed regions relative to the local mean streamwise velocity. The size of the turbulent streaks scales with wall units, with an expected length of $\Delta x^+ \approx 1000$ and a spanwise spacing of $\Delta z^+ \approx 100$. To study the evolution of these structures as they enter the diffuser section, we have chosen to plot isosurfaces of the streamwise disturbance velocity, i.e. the variance of the velocity compared to the local spanwise and temporal mean. The flow close to the upper wall clearly features streaks in the inflow section (see figure 15). The size of the structures is seen to increase as the flow propagates downstream. For the Reynolds-number regime studied in this investigation, this downstream development can be observed at all three Reynolds numbers. For the flow at the upper wall, where the flow does not separate in the mean

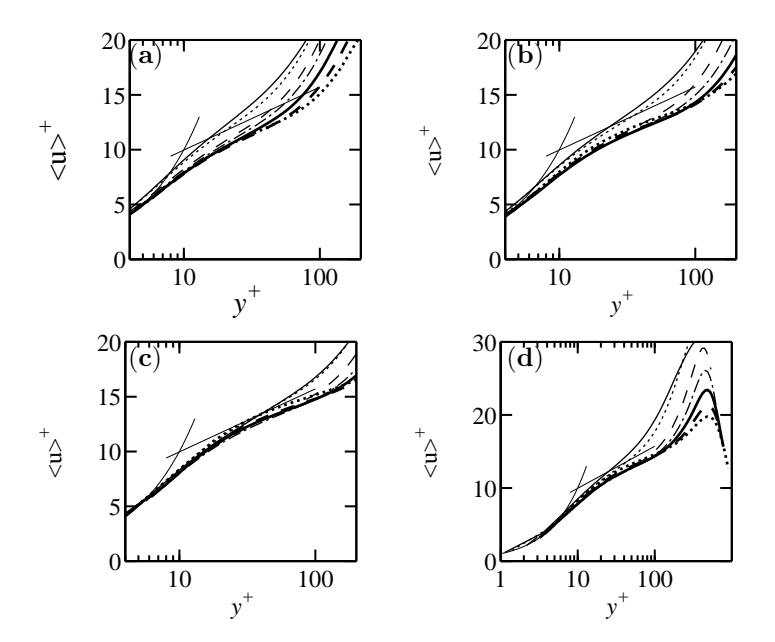


FIGURE 14. Reynolds-number dependence of the internal layer: (a) $Re_b = 4500$ (case L3), (b) $Re_b = 9000$ (case M3), (c) $Re_b = 20000$ (case H1), (d) $Re_b = 9000$, diverging angle $\phi = 10^{\circ}$ (case K1). Wall normal profile of mean streamwise velocity at positions x = 6.4 (thin solid line), x = 10.4 (thin dotted line), x = 18.4 (thin dashed line), x = 22.4 (dash-dotted line) x = 26.4 (thick solid line), x = 30.4 (thick dotted line) and x = 34.4 (thick dotted line). The analytical correlations $u^+ = y^+$ and $u^+ = 2.5 \log(y) + 4.2$ are included in the plots for reference.

for any Reynolds number studied here, the size of the structures is clearly dependent on the Reynolds number, *i.e.* it scales with viscous wall units. In the inflow section of the diffuser such a scaling is anticipated since the inflow condition is fully developed turbulent channel flow including streaks. More surprising is that the apparent size and spacing of the streaks suggests that a scaling with wall units also appears to be appropriate in the rear part of the diffuser at the upper wall.

At the lower deflected wall, for which isocontours of the streamwise disturbance velocity are shown in figure 16, the streaky structures are clearly visible, similar to the upper wall. Moreover, the same trend as at the upper wall that the streaky structures become wider as the flow propagates downstream is visible. However, even though the size of the streaks further downstream clearly depends on those of the inlet turbulence, the size of the structures increases rapidly as the flow enters the diffuser. Further downstream the size does not

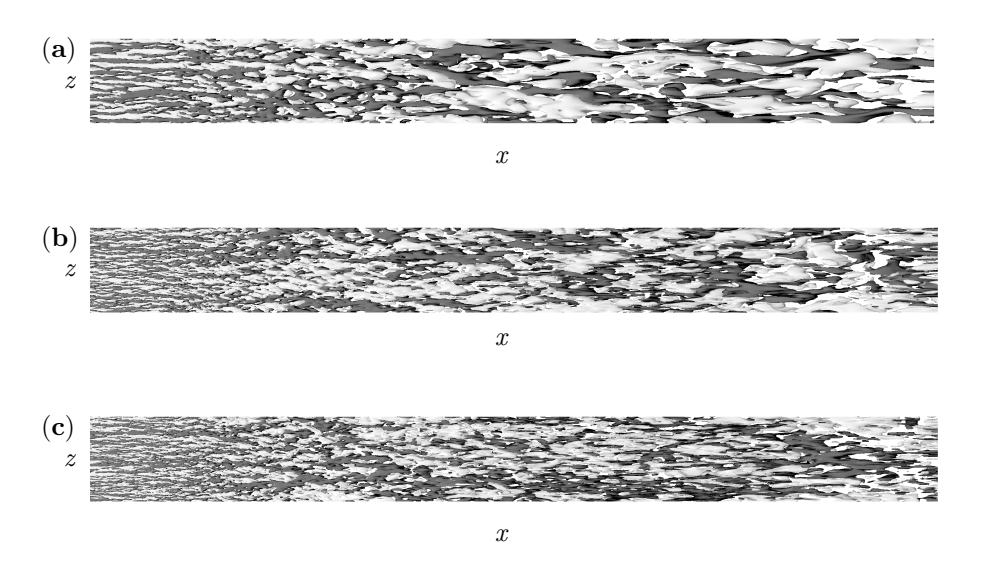


FIGURE 15. Isocontours of streamwise disturbance velocity at the upper wall with level ± 0.004 . Dark regions indicate negative, light regions positive velocity. (a) $Re_b = 4500$, (b) $Re_b = 9000$, (c) $Re_b = 20000$.

appear to be governed by the viscous scales any longer, but rather by the length scales of the outflow channel, *i.e.* the height and width of the outflow section. However, since the size of the structures in the inlet channel is different due to the varying Reynolds number, the streamwise position in the diffuser where the structures reach a similar size is different. However it must be noted that the development of the large streaky structures is somewhat restricted due the spanwise extent of the computational domain which gives a low aspect ratio in the outflow section.

In figures 17-19 three-dimensional visualisations of isosurfaces displaying the zero streamwise velocity in the diffuser are shown for the medium Reynolds number. The snapshots are separated by $\Delta t=20$ corresponding to relative times $t^*=0$, $t^*=20$ and $t^*=40$, respectively. The sequence illustrates the highly unsteady character of the separated region. Furthermore, the visualisations give a good impression of the difficulties one faces in defining a line of separation, since in the instantaneous view the separation bubble cannot be considered a smooth region of separated flow. Moreover, the separated region is highly three-dimensional in shape and size. Dependent on the time instant, one or even several distinct separated regions can be distinguished which change in shape and size demonstrating the intermittent character of the flow. This

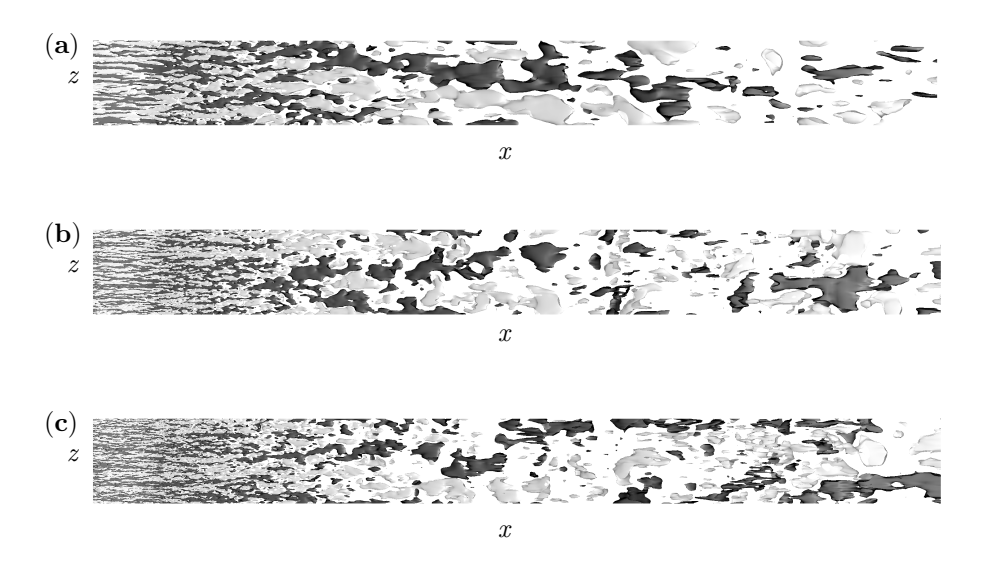


FIGURE 16. Isocontours of streamwise disturbance velocity at the lower, inclined wall with level ± 0.004 . Dark regions indicate negative, light regions positive velocity. (a) $Re_b = 4500$, (b) $Re_b = 9000$, (c) $Re_b = 20000$.

gives rise to long averaging times for obtaining converged statistical quantities. In the sequence of snapshots, a typical incident can be observed at the end of the separated region where a reverse flow region looses contact with the core separated region as time progresses, and it is further convected downstream before it finally exits the computational domain.

Turning attention to the beginning of the expansion, incipient separation is clearly encountered when the flow passes over the diffuser throat, in a region well upstream of where the flow separates in the mean (see also discussion related to figure 11). The manifestation of this first separated region is even more inhomogeneous than the larger, main separation bubble.

Varying the Reynolds number as shown in figures 20 and 21, a small separation bubble at the throat of the diffuser is visible at the lowest Reynolds number Re=4500, and as mentioned earlier, at this position separation in the mean is not present at both the medium and high Reynolds number. However, incipient separation is even encountered at these Reynolds numbers in the diffuser throat. In the Reynolds number regime studied here, the snapshots suggest that even the incipient separation encountered at the diffuser throat is less pronounced. Comparing the snapshots of isocontours of zero streamwise velocity at different Reynolds numbers, the size of the structures does not appear to vary significantly on the Reynolds number.

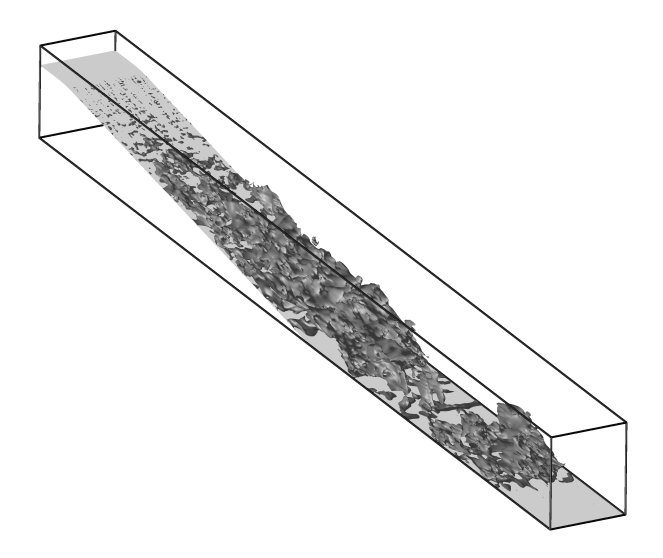


FIGURE 17. Isosurface of zero streamwise velocity for the full diffuser geometry, $Re_b = 9000$. Frame 1 at relative time $t^* = 0$.

4.4. Influence of the Inflow Condition

As described in section 3.2, the inflow boundary condition located at x=-5 is specified via an unsteady Dirichlet condition. The time-dependent data is taken from a separate simulation of fully-developed turbulent channel flow. As discussed before, distinct peaks occur in the power spectra related to the periodicity in streamwise direction in the channel flow simulation. The appearance of these peaks in the power spectra of the channel flow is clearly related to turbulent events that survive while they are convected downstream through the channel ("frozen turbulence"), see section 3.2. We now focus on the effect of these spurious temporal correlations on the diffuser simulations.

To examine this influence we conducted two diffuser simulations at the same Reynolds number $Re_b = 9000$ using the same computational grid (M2) and provided them with inflow from two channel-flow simulations that only differ in the length of the periodic domain, M2C and M2CL, respectively. The frequencies peaks present in the spectra differ due to the different domain length of the channel, with the fundamental peak being at $f_0 = 0.03$ for the simulation M2CL and $f_0 = 0.124$ for the simulation M2C.

The averaged properties of the two diffuser flow simulations are shown in figure 22. The obtained results for the full diffuser setup compare very well for the low-order statistics, in particular the mean streamwise velocity component and the cross stresses agree perfectly. The level of the streamwise turbulent

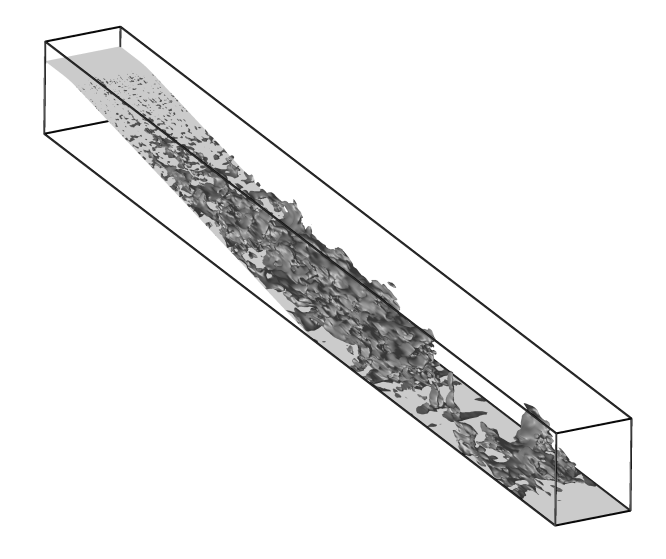


FIGURE 18. Isosurface of zero streamwise velocity for the full diffuser geometry, $Re_b = 9000$. Frame 2 at relative time $t^* = 20$.

fluctuations is slightly higher in the rear part of the diffuser for the simulation with inflow data provided by the channel flow simulation with the shorter domain length (M2C).

To study how the dynamics of the diffuser simulation is affected by the spurious time correlations present in the different channel flow simulations, we recorded power spectra of the streamwise velocity at a number of streamwise positions in the domain, more specifically close to the deflected wall from which the flow separates in the mean (figure 23), in the centreline of the diffuser (figure 24) and close to the upper wall (figure 25). Independent of the wall-normal position we observe that the energy contained in the low frequencies is generally larger for those simulation whose inflow condition is taken from the channel flow with longer periodic domain.

At the centreline of the duct (figure 24), the peaks connected to the fundamental peaks of the channel flow simulation are clearly present at the first recorded station, x=4.9. As the flow propagates downstream, the peaks gradually decrease and the differences in the spectra become less significant. Eventually, at x=79.7 the spectra exhibit reasonable agreement. The differences occurring for the highest frequencies can be attributed to the fact that the number of samples used for the computation of the spectra for the two cases is different. The trend that the differences in the power spectra decrease in the downstream direction can also be observed in the spectra recorded at

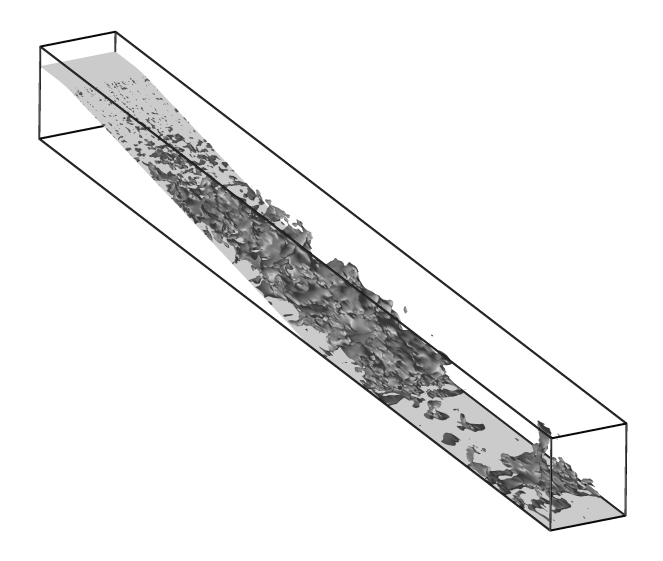


FIGURE 19. Isosurface of zero streamwise velocity for the full diffuser geometry, $Re_b = 9000$. Frame 3 at relative time $t^* = 40$.

the upper wall. At the lower deflected wall, from which the large separated region forms, the difference between the power spectra is first decreasing between position x=4.8 and x=21.0. However, the differences are most pronounced for the power spectrum recorded at x=49.4 close to the lower wall compared to all other power spectra shown, indicating that the separated region is most affected.

It should further be noted that no dominant frequency related to vortex shedding can be detected in the separated region. A similar conclusion was also drawn by Kaltenbach $et\ al.\ (1999)$ for the Obi diffuser configuration.

5. Conclusions

In the present work, large-eddy simulations (LES) of an incompressible planar, asymmetric diffuser flow have been presented. Adopting the numerical method already successfully used by Kaltenbach $et\ al.\ (1999)$, the diffuser with an opening angle of 8.5° is considered. For this configuration, recent experimental data is available at $Re_b=20000$ (Törnblom 2003). Compared to previous numerical and experimental studies, the setup is slightly modified, i.e. featuring a marginally decreased opening angle compared to the 10° used by Obi $et\ al.\ (1993)$ and Kaltenbach $et\ al.\ (1999)$. The change of setup was adopted in order to create a test case that is more sensitive and thus better suited to compare the results at different Reynolds numbers.

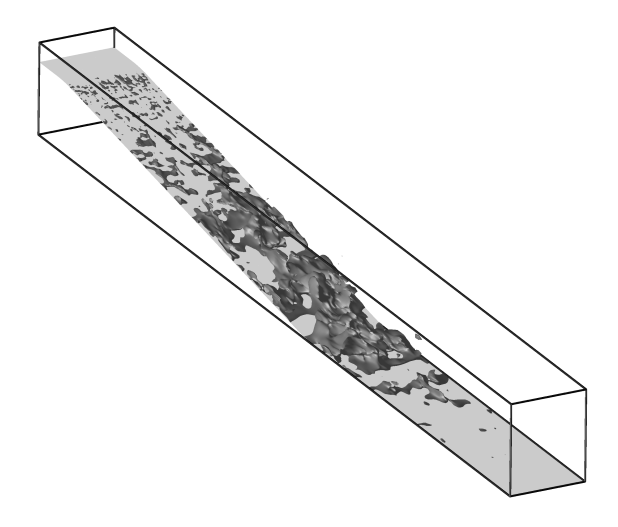


FIGURE 20. Isosurface of zero streamwise velocity for the full diffuser geometry, $Re_b=4500.$

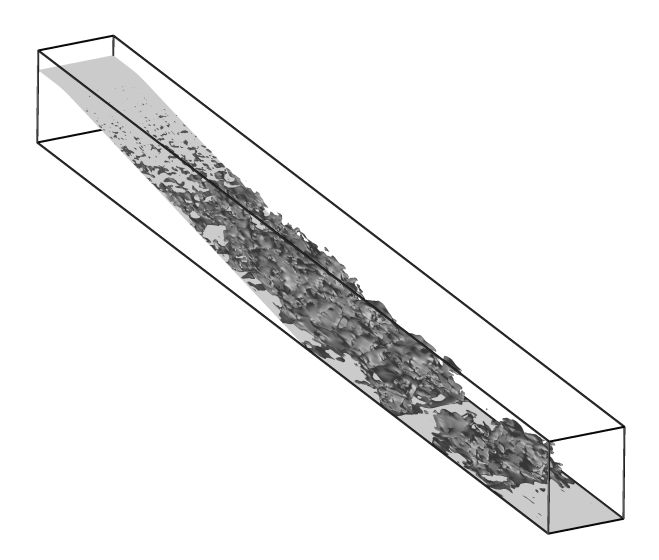


Figure 21. Isosurface of zero streamwise velocity for the full diffuser geometry, $Re_b=20000$.

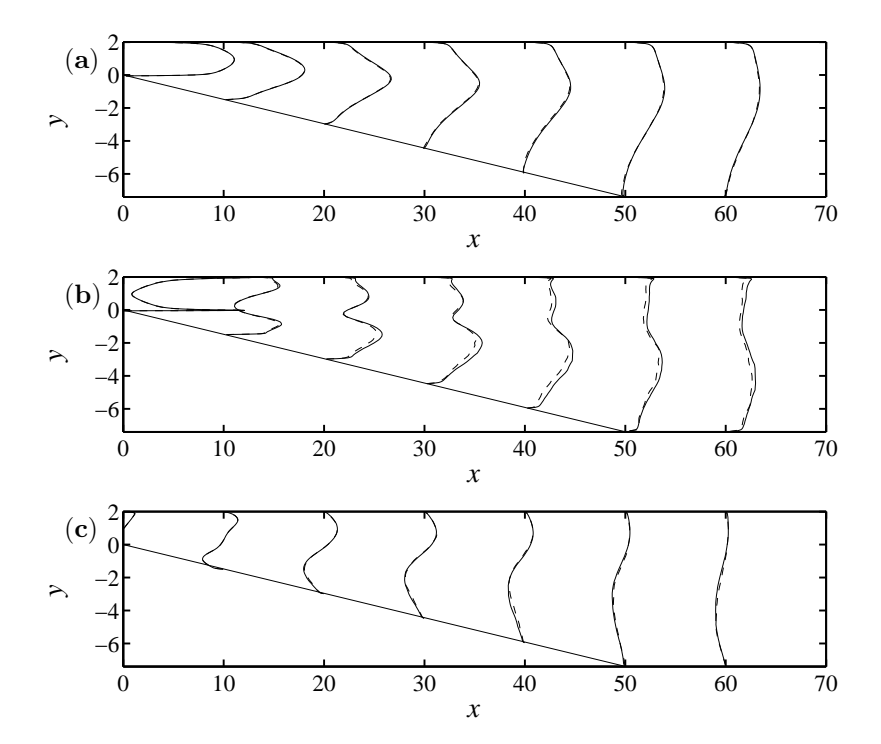


FIGURE 22. Influence of inflow channel length on statistics, dashed case MC2L, solid case MC2 (a) $10 \cdot \langle \overline{u} \rangle + x$, (b) $30 \cdot u_{\rm rms} + x$, (c) $500 \cdot \langle \overline{u'} \, \overline{v'} \rangle + x$.

For the present results, the dynamic Smagorinsky model has been used, and a resolution study has been performed, highlighting the disparity of the relevant scales and thus the sensitivity of the simulation results to the grids used. Extensive simulations of the diffuser have been conducted at three different Reynolds numbers, namely $Re_b=4500$, $Re_b=9000$ and $Re_b=20000$ corresponding to a friction Reynolds number Re_{τ} of the inflowing fully-turbulent channel flow of approximately 260, 480 and 980, respectively. These Reynolds numbers are well above the critical value for laminar-turbulent transition and allow sustained turbulent channel flow.

Regarding the flow physics, we focused on quantifying the influence of the Reynolds number on various diffuser-flow characteristics, in particular the extent of the separated region, the properties of the internal layer at the upper wall and the size of the turbulent scales. To our knowledge, there is no detailed study in the literature clarifying these influences. To this end, it is consistently shown that by increasing the Reynolds number a clear trend towards a larger separated region is evident; at least for the studied, comparably low Reynolds number regime. The Reynolds number dependence compares well with the experimental findings by Obi et al. (1999). It is further shown that the small

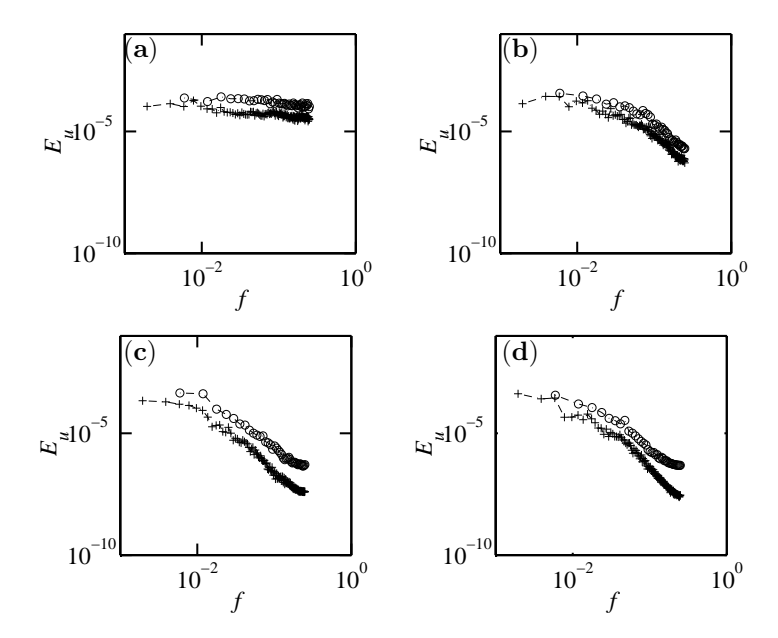


FIGURE 23. Power spectrum for streamwise velocity component near the lower wall for different streamwise positions: (a) x = 4.8, (b) x = 21.0, (c) x = 49.4, (d) x = 74.7. Crosses denote simulation M2CL.

separated region occurring at the diffuser throat shows the opposite behaviour as the main separation region, *i.e.* the boundary layer at the diffuser throat has less tendency to separate as the Reynolds number is increased. The results suggest that the size of the main separated region is governed by the 'jet-like' inflow which penetrates further into the diffuser at a higher Reynolds number. Conversely, the spatial extent of the small separated region at the diffuser throat is mainly determined by the state of the local turbulent boundary layer and its ability to withstand separation.

The influence of the Reynolds number on the internal layer occurring at the non-inclined wall described in a recent study by Wu $et\ al.\ (2006)$ has also been examined. It can be concluded that this region close to the upper, straight wall, is more distinct for larger Re.

Additionally, the influence of temporal correlations arising from the commonly used periodic turbulent channel flow as inflow condition for the diffuser is assessed. These time correlations are clearly related to turbulent events that survive while they are convected downstream. It is however found that this does not have a significant impact on the low-order statistics. Nevertheless, the examination of the power spectra at various positions in the diffuser shows that the low frequency content of spectrum is enhanced when the inflow data is taken from a longer periodic channel.

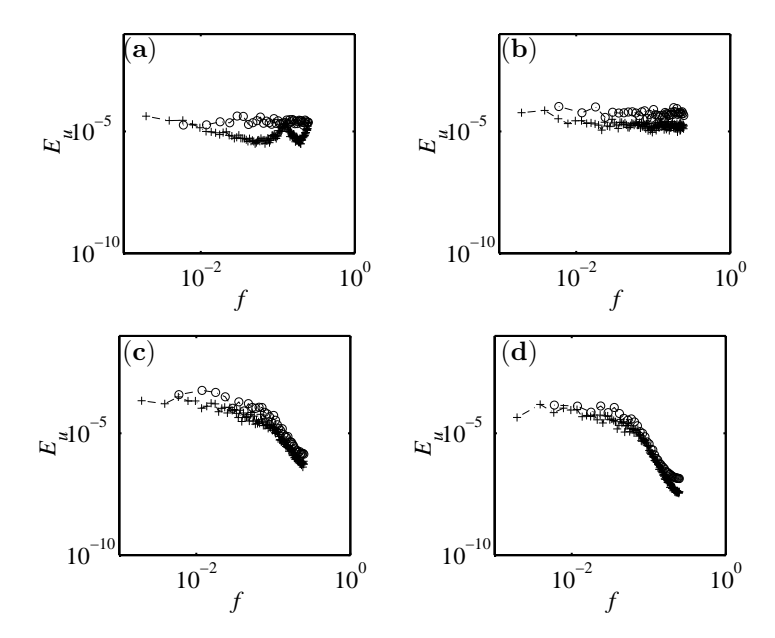


FIGURE 24. Power spectrum for streamwise velocity component at diffuser centreline for different streamwise positions: (a) x = 4.9, (b) x = 21.2, (c) x = 49.6, (d) x = 74.7. Crosses denote simulation M2C, circles denote simulation M2CL.

In general, reasonable agreement between statistical data computed from LES and the corresponding experimental measurements is obtained, e.g. for the velocity profiles and turbulent fluctuations. However, also the experimental data show a variation between different experiments and setups. Thus, there seems to be a need for more refined measurements in order to create a consistent and accurate data base. In particular, the observed Reynolds-number dependency needs to be backed up by new experimental studies. In addition, a DNS study at a higher Reynolds number than previously possible would be beneficial to validate the present findings.

Acknowledgements

Dr. Hans-Jakob Kaltenbach is thankfully acknowledged for providing the simulation code. Dr. Luca Brandt (KTH) is thanked for his help in parallelising the simulation code. The authors are also indebted to Dr. Stefan Wallin (KTH) for fruitful discussions on the temporal correlations in the inflow data. Jörg Ziefle (ETH Zürich) is thanked for providing some of the visualisation tools. Olle Törnblom (KTH) is acknowledged for giving access to the experimental data. P.S. is financially supported by the Göran Gustafsson Stiftelse. A.H. was partially funded by the Vinnova competence centre PSCI at NADA, KTH. Partial

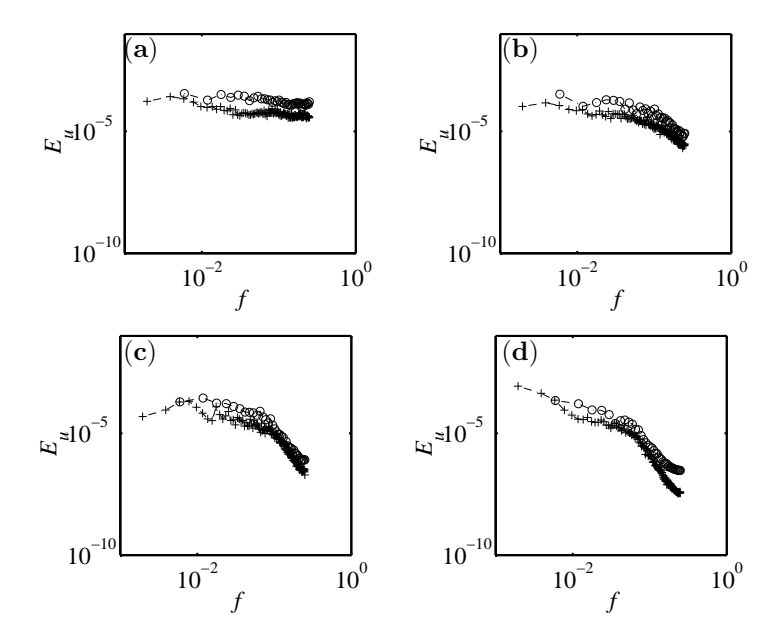


FIGURE 25. Power spectrum for streamwise velocity component near the upper wall for different streamwise positions: (a) x = 5.0, (b) x = 21.3, (c) x = 49.7, (d) x = 74.7, Crosses denote simulation M2CL.

funding from STEM is also acknowledged. Computer time was provided by the Höchstleistungsrechenzentrum Stuttgart (HLRS), Germany, through the HPC-Europe programme and Bundesprojekt SOSCIAD.

References

Breuer, M., Jaffrézic, B., Peller, N., Manhart, M., Fröhlich, J., Hinterberger, C., Rodi, W., Deng, G., Chikhaoui, O., Šarić, S. & Jakirlić, S. 2006 A comparative study of the turbulent flow over a periodic arrangement of smoothly contoured hills. In *Direct and Large-Eddy Simulation VI*. To appear.

Buice, C. U. & Eaton, J. K. 1996 Experimental investigation of flow through an asymmetric plane diffuser. CTR Annual Research Briefs pp. 243–248.

Buice, C. U. & Eaton, J. K. 2000 Experimental investigation of flow through an asymmetric plane diffuser. *J. Fluids Eng.* **122**, 433–435.

Fröhlich, J., Mellen, C. P., Rodi, W., Temmerman, L. & Leschziner, M. A. 2005 Highly resolved large-eddy simulation of separated flow in a channel with streamwise periodic constrictions. *J. Fluid Mech.* **526**, 19–66.

GERMANO, M., PIOMELLI, U., MOIN, P. & CABOT, W. H. 1991 A dynamic subgrid-scale eddy viscosity model. *Phys. Fluids A* **3** (7), 1760–1765.

- Gravemeier, V. 2005 Variational multiscale large eddy simulation of turbulent flow in a planar asymmetric diffuser. CTR Annual Research Briefs pp. 257–268.
- GULLMAN-STRAND, J., TÖRNBLOM, O., LINDGREN, B., AMBERG, G. & JOHANSSON, A. V. 2004 Numerical and experimental study of separated flow in a plane asymmetric diffuser. *Int. J. Heat Fluid Flow* 25, 451–460.
- IACCARINO, G. 2001 Prediction of a turbulent separated flow using commercial CFD codes. J. Fluids Eng. 123, 819–828.
- Kaltenbach, H.-J., Fatica, M., Mittal, R., Lund, T. S. & Moin, P. 1999 Study of flow in a planar asymmetric diffuser using large-eddy simulation. *J. Fluid Mech.* **390**, 151–185.
- Leschziner, M. A. 2006 Modelling turbulent separated flow in the context of aerodynamic applications. *Fluid Dynamics Research* 38, 174–210.
- Lesieur, M. & Métais, O. 1996 New trends in large-eddy simulations of turbulence. Annu. Rev. Fluid Mech. 28, 45–82.
- LILLY, D. K. 1992 A proposed modification of the Germano subgrid-scale closure method. *Phys. Fluids A* **4** (3), 633–635.
- MENEVEAU, C. & KATZ, J. 2000 Scale-invariance and turbulence models for large-eddy simulation. *Annu. Rev. Fluid Mech.* **32**, 1–32.
- Moin, P. & Kim, J. 1982 Numerical investigation of turbulent channel flow. J. Fluid Mech. 118, 341–377.
- NA, Y. & Moin, P. 1998 Direct numerical simulation of a separated turbulent boundary layer. J. Fluid Mech. 374, 379–405.
- Obi, S., Aoki, K. & Masuda, S. 1993 Experimental and computational study of turbulent separating flow in an asymmetric diffuser. In *Proc. Ninth Symposium on Turbulent Shear Flows, Kyoto, Japan*, pp. P305.1–P305.4.
- Obi, S., Nikaido, H. & Masuda, S. 1999 Reynolds number effect on the turbulent separating flow in an asymmetric plane diffuser. In *ASME/JSMR Fluids Engineering Division Summer Meeting* 1999, FEDSM 99-6976. ASME.
- Ohta, T., Kajishima, T., Fujii, S. & Nakagawa, S. 2003 Direct numerical simulation of turbulent separating flow in an asymmetric plane diffuser. In *Turbulence, Heat and Mass Transfer 4* (eds. K. Hanjalić, Y. Nagano & M. Tummers), pp. 441–448. Begell House, Redding, U.K.
- PIOMELLI, U. 1993 High Reynolds number calculations using the dynamic subgridscale stress model. *Phys. Fluids A* **5** (6), 1766–1771.
- Piomelli, U. & Balaras, E. 2002 Wall-layer models for large-eddy simulations. *Annu. Rev. Fluid Mech.* **34**, 349–374.
- SAGAUT, P. 2005 Large Eddy Simulation for Incompressible Flows, 3rd edn. Springer, Berlin, Germany.
- Schlatter, P., Stolz, S. & Kleiser, L. 2005 Evaluation of high-pass filtered eddyviscosity models for large-eddy simulation of turbulent flows. J. Turbulence 6 (5).
- Schlüter, J. U., Wu, X. & Pitsch, H. 2005 Large-eddy simulation of a separated plane diffuser. AIAA Paper 2005-0672.
- SIMPSON, R. L. 1996 Aspects of turbulent boundary-layer separation. *Prog. Aerospace Sci.* 32, 457–521.
- Skote, M. & Henningson, D. S. 2002 Direct numerical simulation of a separated turbulent boundary layer. *J. Fluid Mech.* **471**, 107–136.

- Smagorinsky, J. 1963 General circulation experiments with the primitive equations. Mon. Weath. Rev. $\bf 91$ (3), 99–164.
- TÖRNBLOM, O. 2003 Experimental study of the turbulent flow in a plane asymmetric diffuser. Licentiate thesis, Department of Mechanics, KTH Stockholm, Sweden.
- Townsend, A. A. 1965 Self-preserving flow inside a turbulent boundary layer. J. Fluid Mech. 22, 773–797.
- Wu, X., Schlüter, J., Moin, P., Pitsch, H., Iaccarino, G. & Ham, F. 2006 Computational study on the internal layer in a diffuser. *J. Fluid Mech.* **550**, 391–412.

Paper 5

Early turbulent evolution of the Blasius wall jet

By Ori Levin, Astrid H. Herbst and Dan S. Henningson

Department of Mechanics, KTH, SE-100 44 Stockholm, Sweden

Submitted

The first direct numerical simulation that is sufficiently large to study the selfsimilar behaviour of a turbulent wall iet is performed. The investigation is an extension of the simulation performed by Levin et al. (2005). The same numerical method is used, but a significantly larger computational domain enables to follow the development of the flow throughout the transition into its early turbulent evolution. Two-dimensional waves and streamwise elongated streaks, matched to measured disturbances, are introduced in the flow to trigger a natural transition mechanism. The Reynolds number is 3090 based on the inlet velocity and the nozzle height. The simulation provides detailed visualizations of the flow structures and statistics of mean flow and turbulent stresses. A weak subharmonic behaviour in the transition region is revealed by animations of the flow. The averaged data is presented in both inner and outer scaling in order to identify self-similar behaviour. Despite the low Reynolds number and the short computational domain, the turbulent flow exhibits a reasonable selfsimilar behaviour, which is most pronounced with inner scaling in the near-wall region.

1. Introduction

A plane wall jet may be considered as a flow which is created by the injection of high-velocity fluid in a thin layer close to a wall. The wall jet consists of an inner region, which is similar to a boundary layer, and an outer region wherein the flow resembles a free shear layer. These layers interact strongly and form a complex flow pattern. Besides the interesting physics, wall jets are of great interest from an engineering point of view, for instance in film cooling of gas turbine blades, in combustion chambers in defrosters and for separation control on airfoils.

The first study on a turbulent wall jet was carried out experimentally by Förthmann (1934), who found that the mean velocity field is self-similar, the half-width, which is the distance from the wall where the velocity in the outer region reaches half the local maximum velocity, grows linearly and that the maximum velocity is inversely proportional to the square-root of the streamwise distance. The experimental work on turbulent wall jets up to 1980 has been reviewed by Launder & Rodi (1981). For the turbulent plane wall jet in

a quiescent surrounding, one main feature is the displacement of the position of zero shear stress from the position of maximum velocity. Up to that time, a semi-logarithmic variation of the velocity near the wall was assumed, but considerable differences occur in the constants. For the Reynolds stresses, the early experimental data shows a considerable scatter and most of the experimental set-ups did not assure two-dimensionality.

Preserving this feature, Abrahamsson $et\ al.\ (1994)$ presented measurements of Reynolds stresses and wall shear stresses for a wall jet at Reynolds numbers $Re=10000,\,15000$ and 20000, based on the nozzle height and the inlet velocity. The streamwise development of the half-width and the maximum velocity were found to be independent of the Reynolds number using momentum scaling as proposed by Narasimha $et\ al.\ (1973)$. Abrahamsson $et\ al.\ (1994)$ questioned the existence of a constant shear-stress layer. Their measurements support Launder & Rodi (1981) claiming a transport of positive outer shear stress into the wall region.

Using Laser Doppler measurement technique, Schneider & Goldstein (1994) found for their measurements at Re=14000 that the measured turbulent normal stresses are higher compared to the existing hot-wire data. The hot wires are shown to indicate low values of the Reynolds stresses in the turbulent outer regions where they are effected by strong flow reversals. Laser Doppler measurements by Eriksson *et al.* (1998) resolved for the first time the inner peak in the streamwise turbulence intensity as well as the inner (negative) peak in the shear stress of a turbulent wall jet at Re=9600.

The applicability of various scaling laws to the turbulent wall jet was studied by Wygnanski $et\ al.\ (1992)$ based on experimental data for Reynolds numbers in the range 3000 to 30000. They discarded the traditional wall-jet scaling as earlier suggested by Narasimha $et\ al.\ (1973)$ and proposed a self-similarity scaling based on the momentum flux at the nozzle and on the viscosity of the fluid. They showed that a logarithmic velocity distribution cannot be derived based on the assumption on the constancy of the Reynolds stress or on the thinness of the logarithmic region relative to the thickness of the inner layer. In an investigation based mostly on experimental data by Eriksson $et\ al.\ (1998)$ and Abrahamsson $et\ al.\ (1994)$, George (2000) reasoned that neither the inner nor the outer scaling can perfectly collapse the data at finite Reynolds numbers due to the fact that the interaction region remains Reynolds number dependent.

Turbulent wall jets are challenging flow cases for computations. Recently Dejoan & Leschziner (2005) performed a large eddy simulation (LES) of a turbulent wall jet at Re=9600 matching the experiments of Eriksson et al. (1998). The profiles of velocity and turbulent stresses in the self-similar region are compared to the experimental data and agree well. However, with an LES, the transition process in the outer shear layer and especially in the boundary layer is extremely difficult to reproduce with high accuracy, as also pointed out by Dejoan & Leschziner (2005). Therefore some discrepancies with the experimental data occur. Examining the budgets for the turbulent energy and

the Reynolds stresses, the turbulent transport is seen to be very important where the outer shear layer overlaps with the boundary layer.

Direct numerical simulations (DNS) have to the authors current knowledge so far only been performed for transitional wall-jets. Wernz & Fasel (1996, 1997) studied the importance of three-dimensional effects in the transitional process and Visbal *et al.* (1998) investigated the breakdown process in a finite-aspect-ratio wall jet by the means of DNS. Levin *et al.* (2005) studied the breakdown initiated by the interaction between waves and streaks.

The present work is an extension of the work by Levin et al. (2005), who studied a wall jet both experimentally and numerically by means of highly resolved three-dimensional DNS. The experimental flow was matched in the vicinity of the nozzle outlet by a solution to the boundary-layer equations. In the experiment, the Kelvin–Helmholtz instability and naturally appearing streaks were observed to lead to breakdown. Two-dimensional waves and optimal streaks corresponding to the most unstable scales were calculated with the parabolized stability equations and introduced in the DNS. They found that in the presence of streaks, pairing is suppressed and breakdown to turbulence is enhanced.

In the present paper, the early turbulent evolution of the Blasius wall jet at Re=3090 is studied with DNS using the same disturbance forcing but with a four times larger box than used by Levin $et\ al.\ (2005)$. A Reynolds number matching the experimental investigations (Abrahamsson $et\ al.\ 1994$; Schneider & Goldstein 1994; Eriksson $et\ al.\ 1998$) is not feasible at the present stage, however in advantage to an LES, all scales are resolved and the transitional behaviour is reproduced correctly. In section 2, the numerical methods are briefly outlined. The animations and flow structures are discussed in section 3.1. In section 3.2, the averaged flow characteristics are presented in outer and inner scalings. Finally, conclusions are drawn in section 4.

2. Numerical methods

2.1. Base flow

Consider a wall jet where fluid is blown out through a nozzle and tangentially along a wall, where x, y and z denote the streamwise, wall-normal and spanwise coordinates, respectively. The corresponding velocity components are u = (u, v, w). The base flow consists of the Blasius wall jet, which is a solution to the boundary-layer equations with a coupling of the Blasius boundary layer and the Blasius shear layer as an initial condition. The flow is matched to an experimental set-up (Levin et al. 2005), where the nozzle height is $b = 3 \,\mathrm{mm}$ and the inlet velocity is $U_0 = 15.4 \,\mathrm{m\,s^{-1}}$, corresponding to the Reynolds number $Re = U_0 b/\nu = 3090$, where ν is the kinematic viscosity of the fluid. Figure 1(a) shows the computed base flow compared to data measured 16 mm downstream of the nozzle outlet.

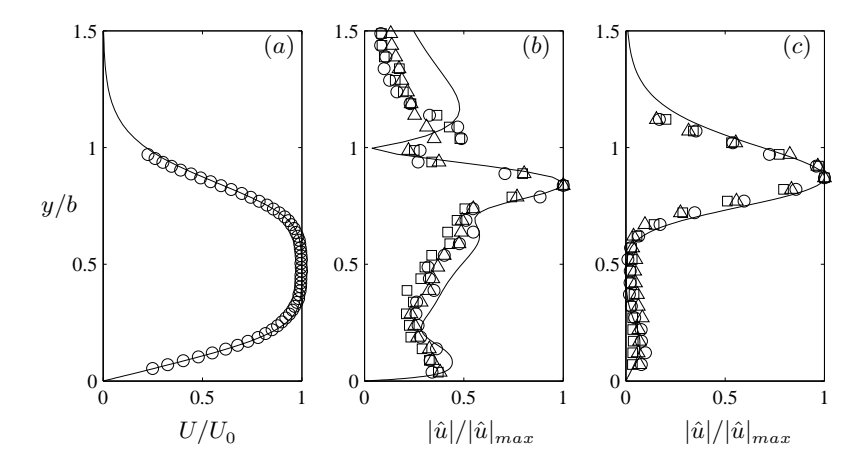


FIGURE 1. Comparison between calculations (solid lines) and experiments (symbols) from Levin et al. (2005) at x/b = 5.3 for Re = 3090. (a) Blasius wall jet. (b) Streamwise wave amplitude for $\omega b/U_0 = 1.49$. Experimental amplitudes are 0.3% (o), 1.1% (\square) and 1.7% (\triangle). (c) Streamwise streak amplitudes. The wavenumber for the PSE is $\beta b = 3.77$ and for the experiments $\beta b = 3.15$ (o), 3.90 (\square) and 4.72 (\triangle).

$2.2.\ DNS\ techniques$

The numerical code (see Lundbladh et al. 1999) uses spectral methods to solve the three-dimensional time-dependent incompressible Navier–Stokes equations. The discretization in the streamwise and spanwise directions makes use of Fourier series expansions, which enforce periodic solutions. The discretization in the normal direction is represented with Chebyshev polynomial series. A pseudospectral treatment of the nonlinear terms is used. The time advancement is a second-order Crank–Nicolson method for the linear terms and a four-step low-storage third-order Runge–Kutta method for the nonlinear terms. Aliasing errors arising from the evaluation of the convective terms are removed by dealiasing by padding and truncation using the 3/2-rule when the FFTs are calculated in the horizontal planes. In the wall-normal direction, no dealiasing is used.

Flows such as boundary layers and wall jets are spatially growing and to fulfil the necessary periodic boundary condition in the streamwise direction, required by the spectral discretization, a fringe region (see Nordström et al. 1999) is added in the downstream end of the physical domain, in which the outgoing flow is forced to its initial state. In this region, the function $\lambda(x)$ is smoothly raised from zero and the flow is forced to a desired solution \boldsymbol{v} through the forcing term $\lambda(x)(\boldsymbol{v}-\boldsymbol{u})$ added to the momentum equations, where \boldsymbol{u} is the solution vector. The forcing vector \boldsymbol{v} , which may depend on the three spatial coordinates and time, is smoothly changed (blended) from the

undisturbed wall-jet solution of the boundary-layer equations at the beginning of the fringe region to the prescribed inflow velocity vector. In the case of forcing a disturbance in the flow, it is also added to the forcing vector in the end of the fringe region.

At the wall, a no-slip boundary condition is set and at the upper edge of the computational box, a generalized boundary condition is applied in Fourier space with different coefficients for each wavenumber. It is non-local in physical space and takes the form

$$\frac{\partial \hat{\boldsymbol{u}}}{\partial y} + k\hat{\boldsymbol{u}} = \frac{\partial \hat{\boldsymbol{v}}_0}{\partial y} + k\hat{\boldsymbol{v}}_0, \tag{1}$$

where $\hat{\boldsymbol{u}}$ is the Fourier transform of \boldsymbol{u} and k is the modulus of the horizontal wavenumbers $(k^2 = \alpha^2 + \beta^2)$. Here, \boldsymbol{v}_0 denotes the blended wall-jet solution of the boundary-layer equations taken as the initial condition and $\hat{\boldsymbol{v}}_0$ its Fourier transform. The condition represents a potential-flow solution decaying away from the upper edge of the computational box. It admits the necessary entrainment of fluid, required by the spatial growth of the wall jet. In the horizontal directions, periodic boundary conditions are used.

2.3. Disturbance forcing and numerical parameters

The objective of the present paper is to study the early turbulent evolution of the wall jet, which is triggered to undergo transition through the interaction between unstable waves and streaks, the transition scenario studied in Levin et al. (2005). In the experiment presented in Levin et al. (2005), naturally appearing waves and streaks were observed to lead to breakdown. In order to simulate a natural transition mechanism of the wall jet from its laminar state to its early turbulent state, two-dimensional waves \boldsymbol{v}_w and stationary longitudinal streaks $oldsymbol{v}_s$ that are matched to the measured disturbances are introduced. These disturbances are calculated with linear disturbance equations as described in Levin et al. (2005) and are added to the blended Blasius wall-jet solution v_0 to give a forcing vector of the form $\boldsymbol{v}=\boldsymbol{v}_0+\boldsymbol{v}_w+\boldsymbol{v}_s.$ The waves and the streaks can then be forced in the fringe region. The forcing is turned on smoothly in both space and time. No noise is forced in the simulation, but a small level of noise evolving from the turbulent flow passes through the fringe region. However, the fringe region damps the energy of the incoming disturbances about seven decades.

Figures 1(b) and 1(c) show the computed amplitude functions of the wave and the streak, respectively, compared to measured data from Levin *et al.* (2005). The waves in the experiment were triggered by a loudspeaker at 1221 Hz, corresponding to an angular frequency of $\omega b/U_0=1.49$. This is close to the most amplified frequency predicted by linear stability calculations. The spanwise wavenumber of the streaks is $\beta b=3.77$, which is close to that of the naturally appearing streaks in the experiment. However, the stationary streaks in the experiment were introduced in the flow by periodically distributed roughness elements, positioned on the top lip of the nozzle. The peak in the

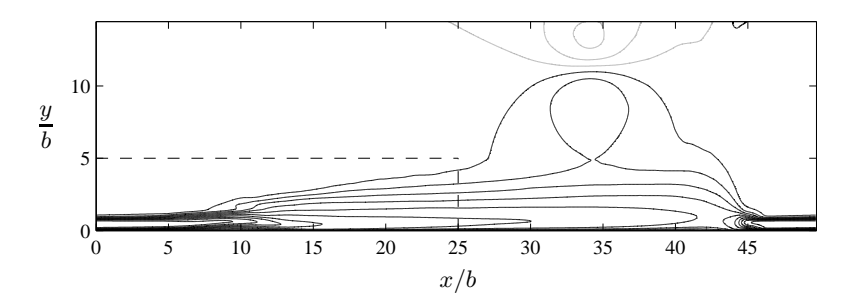


FIGURE 2. Streamwise mean velocity, averaged over a period of $213b/U_0$ and in the spanwise direction. Contour spacing is $0.1U_0$ and grey lines show negative values.

shear-layer region is in antiphase to the peak near the wall in the boundary-layer region both for the waves and the streaks. The streamwise amplitudes of the waves and the streaks are prescribed at the beginning of the computational box to $0.001U_0$ and $0.03U_0$, respectively.

The computational box is shown in figure 2. It extends from the nozzle outlet to 49.7 nozzle heights in the streamwise direction including the fringe region, which begins at x/b = 44. The height of the box is 14.4b and the width is 3.33b, which is two spanwise wavelengths of the forced streaks. There are two reasons that restrict the well represented flow quantities to the upstream half of the computational box $(x/b \lesssim 25)$. Firstly, a large external vortex exists in the downstream part of the box. This vortex can be seen in the contours of the streamwise mean flow shown in figure 2. It evolves from a start-up vortex that slowly convects downstream and then remains in the ambient flow in front of the fringe region. Such an external flow exists for wall jets in experimental set-ups as well, but as the computational box is not as large as the surrounding space in an experiment, the problem is more prominent. It is possible to avoid the vortex by specifying the entrainment velocity at the upper boundary. Dejoan & Leschziner (2005) used such a boundary condition based on the laminar free plane jet. However, we choose not to constrain the wall jet by prescribing the entrainment velocity as the laminar growth of a jet differs from its turbulent growth. Secondly, the box width is not sufficient in the downstream half of the box. However, after considering two-point correlations of the fluctuating streamwise velocity in the spanwise direction, the box proved to be sufficiently wide upstream of about x/b = 25. This does not, however, mean that the influence of the forced stationary streaks is not present. On the contrary, the early turbulent stage of the wall jet is governed by the upstream imposed streaks. It can be seen in flow visualizations (e.g. Lasheras & Choi 1988; Levin et al. 2005) that the spanwise periodicity of the streaks remains for a significant distance downstream in the early turbulent stage. To summarize, the relevant part of the computational box is the upstream half and is marked with the dashed line in figure 2.

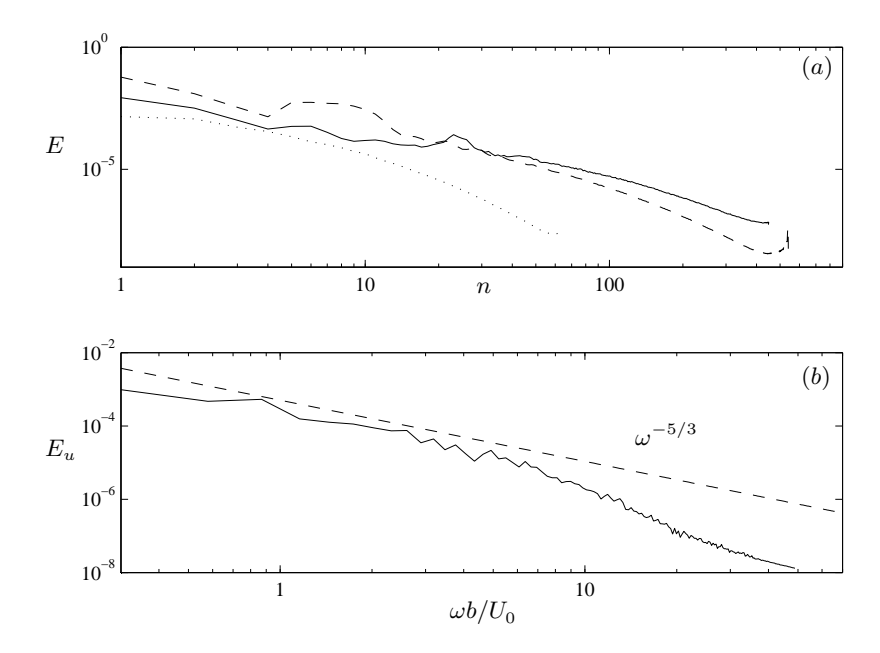


FIGURE 3. (a) Energy contained in streamwise (solid line), wall-normal (dashed line) and spanwise (dotted line) modes n. (b) Frequency spectra of streamwise velocity fluctuation averaged in the spanwise direction at x/b = 25, y/b = 0.96.

A grid of about 62.3 million modes with 900 streamwise modes, 541 wallnormal modes and 128 spanwise modes is used, corresponding to the same resolution in the horizontal plane as for the smaller box used by Levin et al. (2005), while the wall-normal resolution is 20% coarser. Dealiasing in the streamwise and spanwise directions increases the computational resolution in the simulation with a factor of 2.25 (1.5 in each direction). In figure 3(a), the energy contained in the streamwise, wall-normal and spanwise spectral modes demonstrate a decay of at least five decades. A check of the resolution for the previous study was done by Levin et al. (2005), but since the wall-normal resolution in the present study is coarser than in their work, an extra check of the wall-normal resolution is carried out for a smaller test case. An instantaneous flow field with 289 wall-normal modes (corresponding to the present resolution) is compared to the corresponding flow field with 577 wall-normal modes. In comparison to the higher resolution, the lower resolution gives acceptable results in the transitional region of the wall jet. In figure 3(a), a pile up of about one order of magnitude can be seen for the highest wall-normal modes. A similar pile up of one order of magnitude exists for the higher resolution. In order to investigate if the pile up is due to aliasing errors, an additional simulation is performed with 193 wall-normal modes and dealiasing activated even in the wall-normal direction, corresponding to the same computational cost as the test case with 289 wall-normal modes. The results are comparable with the case of 289 wall-normal modes and no conclusions can be drawn whether it is better to use dealiasing or not at the same computational cost. However, the pile up is due to aliasing errors but it does not affect the results as long as the resolution is high enough.

The time step is set adaptively to keep the CFL number close to a fixed number. Figure 3(b) shows the frequency spectra of the streamwise velocity fluctuation evaluated for a period of $21.7b/U_0$ and averaged over the spanwise direction at x/b=25, y/b=0.96. At this location, no peak of the forced frequency remains. The familiar decay law $\omega^{-5/3}$ in the inertial subrange is evident in the frequency range $0.6 < \omega b/U_0 < 6$. Beyond this range, dissipation is the dominant process giving a faster decay.

A shared memory parallelization is implemented in the numerical code. The current study uses 16 computer nodes, each with two processors. With a wall clock time of 60 h, a typical simulation calculates a period of about $3.5b/U_0$. The sampling of statistics is turned on at $tU_0/b=329$ and finished at $tU_0/b=542$, corresponding to five months of non-stop simulations.

3. Results

3.1. Flow structures

In order to visualize the whole wall jet from its laminar part in the vicinity of the nozzle outlet where the waves and the streaks grow, the transition region and its downstream turbulent part, three animations are made available. The animations show a time period of four fundamental periods of the forced waves and the streamwise extend is from the nozzle outlet to x/b = 38.5. The dark areas display regions of high streamwise velocity and the white areas display regions of backflow.

Animation I shows the (x, y)-plane in the middle of the computational domain, where the low-velocity streak is present in the outer shear layer. The height of the plane is y/b = 4.8. Figure 4(a) shows a snapshot corresponding to the first frame of the animation. In the shear-layer region, anticlockwise rotating rollers are created by the Kelvin-Helmholtz instability and follow the flow downstream. In the boundary-layer region, clockwise rotating rollers are formed and are associated with small separation bubbles. In this plane, the boundary-layer rollers move faster than the rollers in the shear-layer region. This is due to the spanwise modification of the flow by the streaks with a lowvelocity streak in the shear-layer region and a weak high-velocity streak in the boundary-layer region. The shear-layer and boundary-layer rollers move at the same rate in the plane located half a spanwise wavelength to the side where a high-velocity streak is present in the outer shear layer. A weak tendency of a subharmonic instability can be seen by looking at the roll-ups in the outer shear layer; every other roll-up is moving slightly more upwards than the roll-ups in between. The breakdown to turbulence appears first in the shear-layer region and then spreads down to the boundary-layer region. The turbulent part of

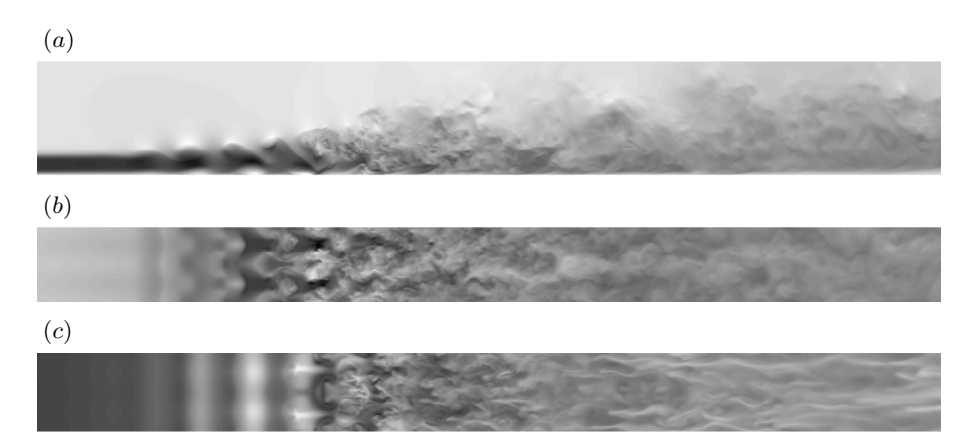


FIGURE 4. Visualization of streamwise velocity with dark areas displaying high velocity and white areas dislaying regions of backflow. The flow is from left to right and the streamwise extend of the planes are from the nozzle outlet to 38.5b. (a) (x,y)-plane at the middle of the box, the height of the plane is 4.8b. (b) Horizontal plane at y/b = 0.96. (c) Horizontal plane at y/b = 0.19.

the wall jet behaves as expected, the velocity is faster in the inner region and slower in the outer region. Downstream, the velocity in the whole wall jet slows down while the wall jet spreads and the largest scales increase.

Animation II and III show the horizontal planes at y/b = 0.96 and 0.19, respectively, which are in the middle of the outer shear layer and the inner boundary layer of the laminar part of the wall jet. The width of the planes shows the entire spanwise extend of the computational box. Figures 4(b) and 4(c) show snapshots corresponding to the first frame of animation II and III, respectively.

In animation II, two spanwise periods of the streaks are visible in the upstream part of the plane. At about four nozzle heights downstream of the nozzle outlet, the waves start to appear. Further downstream, the interaction between the waves and the streaks forms a staggered pattern. The streaks play an important role in the breakdown process, where their growth is transformed from algebraic to exponential as they become part of the secondary instability of the waves, see Levin et al. (2005). In the turbulent flow downstream of the rapid breakdown, the influence of the streaks can be seen to remain for some distance. Figure 5 shows a series of snapshots taken from the animation. The streamwise extend of the snapshots is x/b = 9 to 13, which is the region of transition, and the time period between them is half a fundamental period $T/2 = 2.11b/U_0$ of the forced waves. Figure 5(a) corresponds to the first frame of the animation. The presence of the subharmonic waves can be distinguished

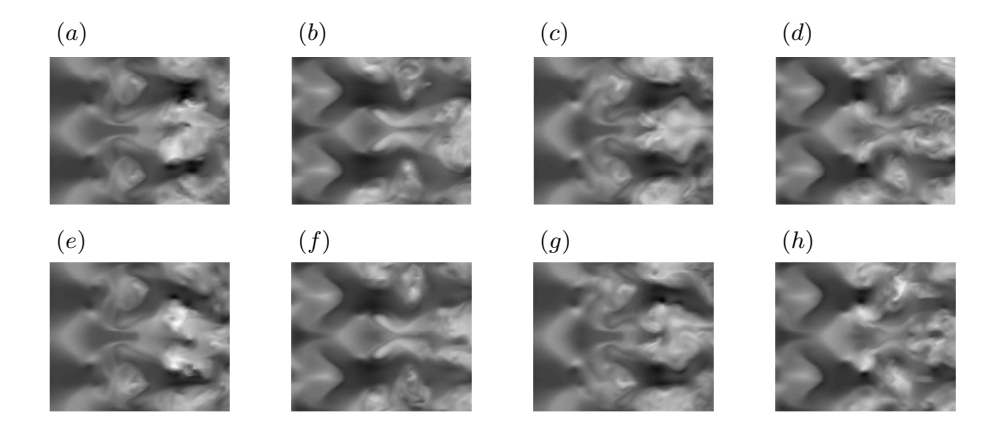


FIGURE 5. Grayscale as in figure 4. Time sequence of the flow in a horizontal plane at y/b = 0.96 with length x/b = 9 to 13. The time period between the planes is half a fundamental period $T/2 = 2.11b/U_0$: (a) t = 0, (b) t = T/2, (c) t = T, (d) t = 3T/2, (e) t = 2T, (f) t = 5T/2, (g) t = 3T, (h) t = 7T/2.

by comparing the difference of the flow structures one fundamental period apart e.g. between figure 5(b) and 5(d). The flow structures two fundamental periods apart, as shown in e.g. figure 5(b) and 5(f) look much more alike.

In animation III, the waves are more pronounced than the streaks in the beginning of plane. However, the spanwise modification of the flow becomes strong well before the breakdown, which appears about two nozzle heights downstream of the breakdown position in the upper shear layer. The influence of the forced streaks does not remain in the turbulent flow as in the shear-layer region of the wall jet. Instead, new streaky structures with smaller spanwise scales (about 100 wall units) typical for turbulent boundary layers are born and prevail throughout the length of the plane. In this plane, the presence of the subharmonic waves is easier to detect. Figure 6 shows a series of snapshots taken from the animation and the time instants are the same as for figure 5. The streamwise extend of the snapshots is x/b=11 to 15, corresponding to the more downstream transition location. By comparing the same time instants as before, i.e. figure 6(b) with 6(d) and figure 6(b) with 6(f), the subharmonic appearance becomes clear.

Vortical structures can be identified in the flow by plotting regions where the second largest eigenvalue λ_2 of the Hessian of the pressure assumes negative values (Jeong et al. 1997). Levin et al. (2005) studied these structures and observed the following five stages in the transition mechanism: (i) Spanwise rollers are formed in the wave troughs in the outer shear layer and move downstream. In the boundary layer close to the wall beneath the wave crests, counter-rotating rollers are formed. (ii) In the presence of streaks, the shear-layer rollers are

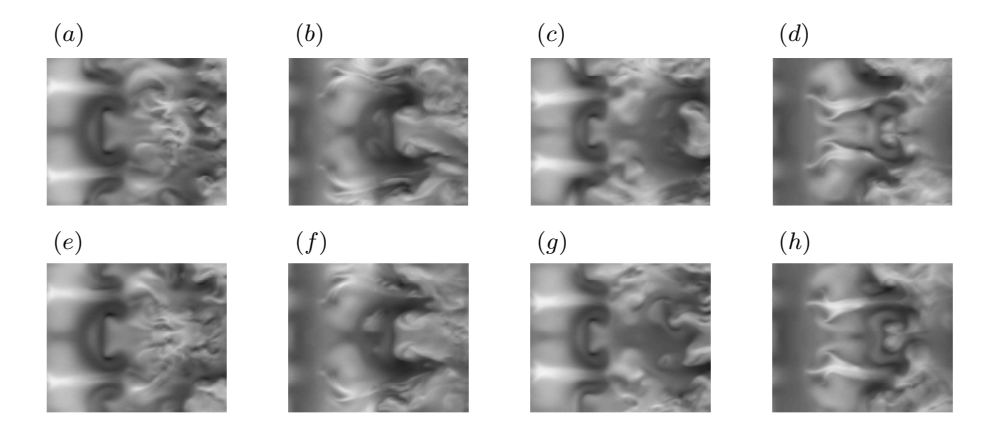


FIGURE 6. Visualization as figure 5 for a horizontal plane at y/b = 0.19 with length x/b = 11 to 15.

sinuously modified in the spanwise direction with the boundary-layer rollers deforming in the opposite direction. (iii) Vortex ribs are formed in the braids of the waves, extending from the top of the shear-layer roller to the bottom of the previous one. (iv) The vortex ribs follow the upward flow between two neighbouring shear-layer rollers and are associated with mushroom-shaped structures ejected from the wall jet into the ambient flow. (v) The tail legs of the vortex ribs, generated one fundamental period earlier, separate and form a vortex ring around the upcoming vortex ribs and additional counter-rotating vortex rings are created preceding breakdown to turbulence. Animation IV shows the development of the vortical structures during two fundamental periods. It shows a constant negative value of λ_2 in a box of streamwise extend from 6 to 13.6 nozzle heights, 4b high and one wavelength of the forced streaks wide.

To illustrate the flow structures further downstream in the turbulent wall jet, figure 7 shows the vortical structures in an instantaneous flow field. In figure 7(a), the transition and the early turbulent region where the turbulence has not yet reached the self-similar state is shown. The level of the isosurfaces is the same as in animation IV. Figure 7(b) shows the turbulent structures further downstream where the turbulence begins to reach a self-similar state. The level of the isosurfaces is one third of the level in figure 7(a). Close to the wall and at about two nozzle heights above the wall, streamwise elongated structures can be seen and correspond to the vortex stretching in the layers of maximum mean shear. The structures in the outer layer, however, are stronger consistent with the larger outer peak of turbulence kinetic energy shown in figure 13(d).

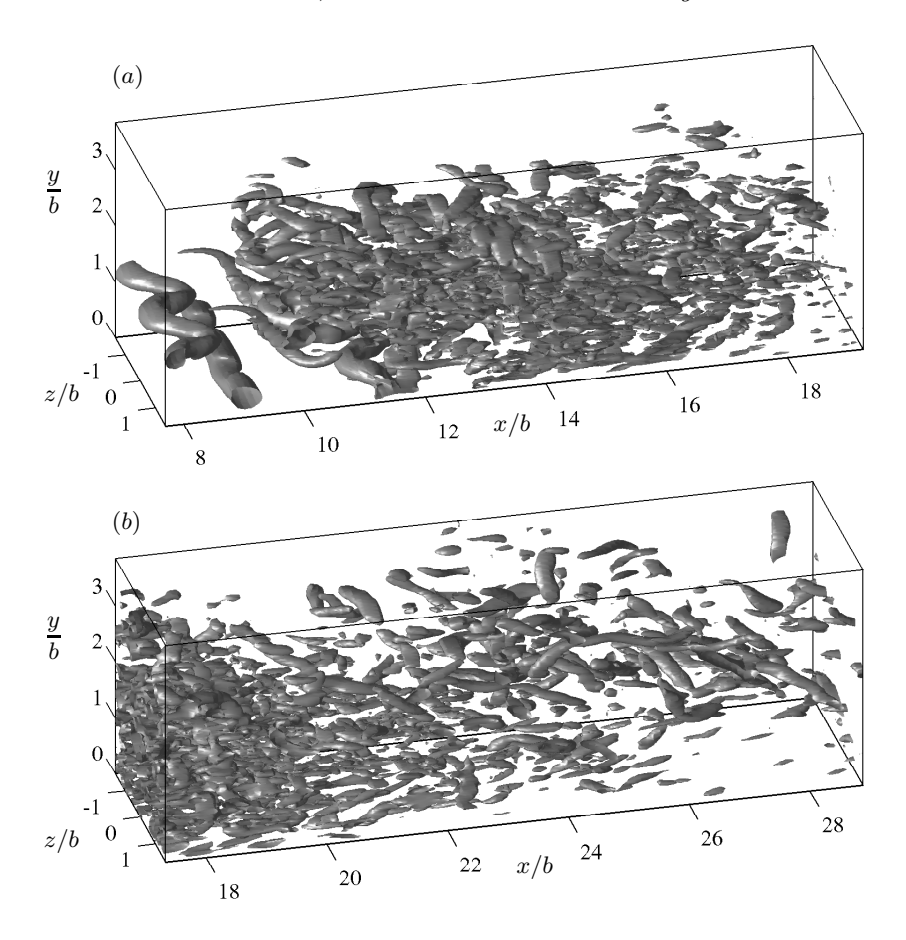


FIGURE 7. Vortex visualization of instantaneous data. The isosurfaces show a constant level of (a) $\lambda_2=-1.5$ and (b) $\lambda_2=-0.5$.

$3.2.\ Averaged\ flow\ characteristics$

While the preceding section concerned the dynamics of the flow, the following sections are designated to present the flow characteristics averaged in both time and spanwise direction. The data is presented in inner and outer scaling in order to identify self-similar behaviour. However, due to the low Reynolds number and the short computational domain, the data is not sufficient to contribute to a discussion of different approaches to scaling as presented recently by Wygnanski et al. (1992) and George (2000).

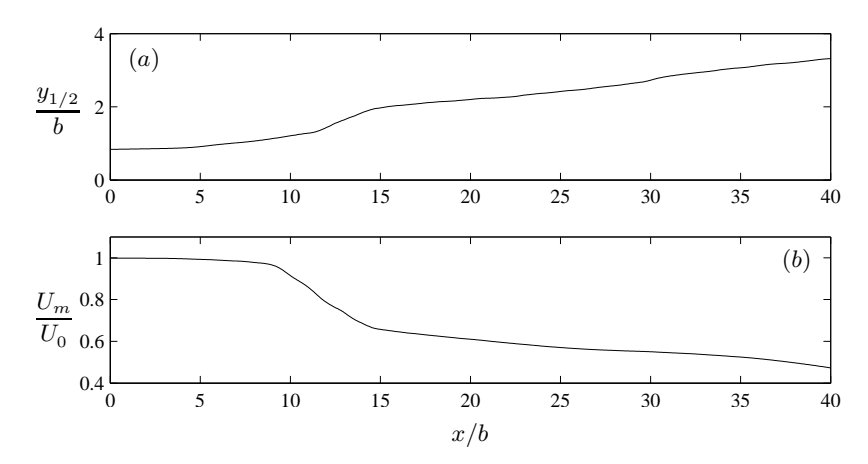


FIGURE 8. (a) Growth rate of the wall jet. (b) Decay of the wall jet velocity.

3.2.1. Outer scaling

Scaling with outer variables is used to identify self-similar behaviour in the outer shear layer. Here we apply the traditional scaling with the maximum velocity of the wall jet U_m and the half-width $y_{1/2}$. In comparison with data at higher Reynolds numbers, it has to be taken into account that the shear stress in the outer layer and therefore also the other properties are dependent on the Reynolds number.

The streamwise development of the variables $y_{1/2}$ and U_m governing the outer scaling is shown in figure 8. In the downstream direction, the thickness of the wall jet increases and its velocity decays as the wall jet spreads out in the quiescent surrounding. The laminar region in the vicinity of the inlet is followed by the clearly visible transitional region at about x/b=10 to 15. In this region, the half-width undergoes a substantial rise whereas the maximum velocity of the wall jet decays rapidly. In the downstream region, at x/b=30 to 40, the influence of the large outer vortex in the ambient flow affects the behaviour somewhat.

Figures 9(a) and 9(b) show the streamwise and wall-normal mean velocities, respectively, scaled in outer scaling. The streamwise velocity profiles between x/b=17 and 26 collapse reasonably well up to $y/y_{1/2}=1$. Further away from the wall, the profiles deviate from each other owing to a secondary flow induced by the large external vortex. For the wall-normal velocity profiles, the self-similar behaviour is only obtained between x/b=20 and 23. Further upstream, the deviation originates from the transition to turbulence. The outer vortex in the ambient flow compresses the downstream part of the wall jet slightly, causing the profile at x/b=26 to deviate towards lower values. This deviation is larger than for the streamwise component indicating that the wall-normal velocity is effected in a higher degree than the streamwise velocity.

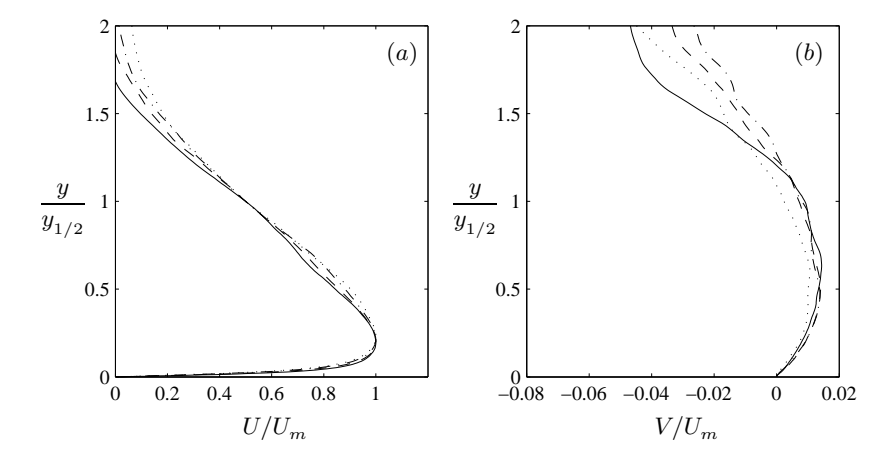


FIGURE 9. Mean velocity at x/b = 17 (solid line), 20 (dashed line), 23 (dashed-dotted line) and 26 (dotted line). (a) Streamwise component. (b) Wall-normal component.

The streamwise, wall-normal and shear stresses and the turbulent kinetic energy in outer scaling are shown in figure 10 for the same streamwise positions as in figure 9. The profiles at x/b=23 and 26 collapse reasonably well up to about $y/y_{1/2}=1$. The levels of the stresses are substantially larger at the position x/b=17 and decay thereafter in the downstream direction. In general, the turbulent quantities scaled with outer variables, are higher in the transitional region than in the self-similar region. Dejoan & Leschziner (2005) found the same tendency in their LES study, but Eriksson et al. (1998) measured the opposite trend for the streamwise Reynolds stress in outer scaling.

3.2.2. Inner scaling

The streamwise development of the wall thickness $\eta=\nu/u_{\tau}$ and the friction velocity u_{τ} , which are relevant for the inner scaling, can be interfered from figures 11(a) and 11(b). Consistent with the behaviour of a wall jet, the wall thickness increases downstream while the friction velocity decays. The streamwise evolution of the ratio between the half-width, used for the outer scaling, and the wall thickness, governing the inner scaling, is shown in figure 11(c). Quantities scaled with the inner scaling are conventionally denoted with a plus (e.g. $y^+=y/\eta$ and $u^+=\sqrt{\overline{u'u'}}/u_{\tau}$). Using this notation we can see that the half-width corresponds to about 300 units in inner scaling, a value that increases with Reynolds number.

Figure 12(a) shows the near-wall region of the streamwise mean velocity scaled with inner scaling. Within the viscous sublayer, the profiles follow a linear law $U^+ = y^+$, shown as the grey curved line, up to about $y^+ = 4$. Further away from the wall, the profiles start to deviate from the linear behaviour, earlier than for a turbulent boundary layer that typically starts to deviate for

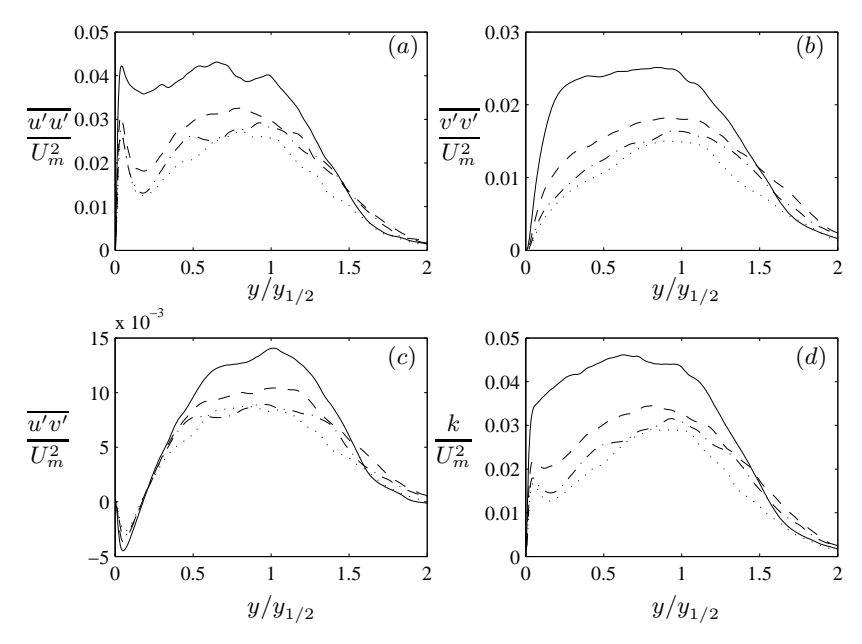


FIGURE 10. Profiles of (a) $\overline{u'u'}$, (b) $\overline{v'v'}$, (c) Reynolds shear stress and (d) turbulence kinetic energy scaled with outer variables. Lines as in figure 9.

values $y^+ \geq 8$. This observation agrees well with the behaviour interfered from the data measured by Eriksson *et al.* (1998) at Re = 9000. Due to the low Reynolds number, the data does not follow the classical log law $U^+ = 2.44 \ln y^+ + 5$, shown as the grey straight line in the figure.

In figure 12(b), the ratio between the rms of the fluctuating streamwise velocity and the mean streamwise velocity is shown. This value has previously been shown to be constant in the viscous sublayer, up to about $y^+=5$, and Alfredsson $et\ al.\ (1988)$ found the value to be 0.4 in turbulent boundary-layer and channel flows. This value seems to approximately hold even for the turbulent wall jet as can be seen in the figure. A comparison has been done to numerical data for turbulent channel flow computed by Kim $et\ al.\ (1987)$ for a low Reynolds number and by Del Alamo $et\ al.\ (2004)$ for a higher Reynolds number. The data for the low Reynolds number shows a good agreement with the present simulation.

The turbulent stresses shown in figure 10 are rescaled with inner scaling and displayed in figure 13. The profiles collapse reasonably well for the streamwise positions x/b = 20 to 26 indicating that the flow has started to exhibit a self-similar behaviour. It can be noted that the collapse provided with inner scaling is much better than with outer scaling. The profile at the position x/b = 17 is, however, still close to the transitional region and deviates from the other profiles. Downstream of the position x/b = 26, the vortex present in the end

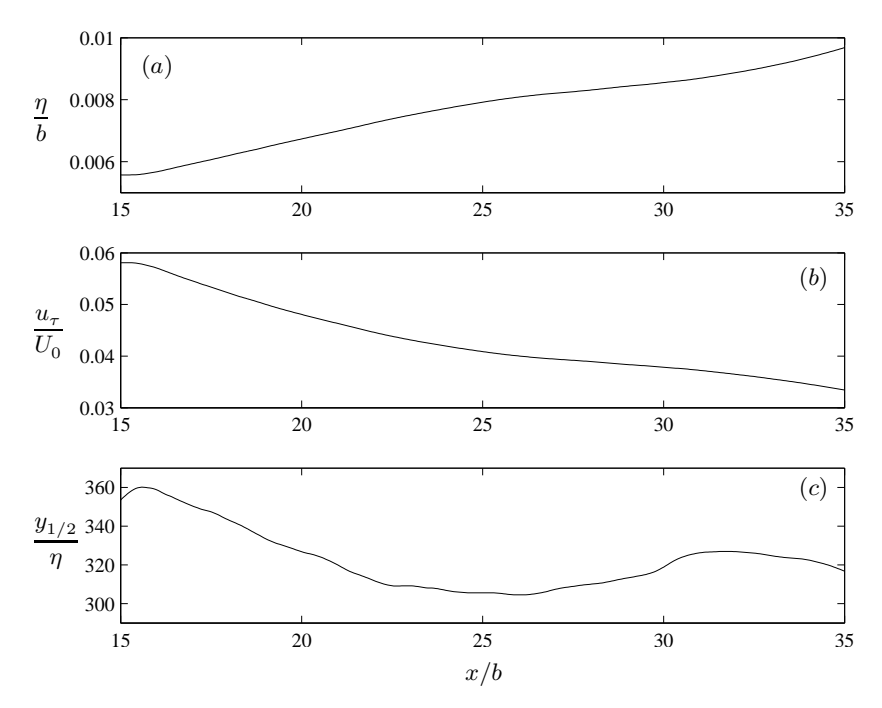


Figure 11. Streamwise evolution of (a) wall thickness, (b) friction velocity and (c) $y_{1/2}/\eta$.

of the computational domain causes the flow to depart from the self-similar behaviour and profiles from this region are therefore not taken into account.

Unfortunately, recent measurements of turbulent stresses are not available for the Reynolds number at which our simulation is performed. As pointed out in the introduction, the recent measurements of the turbulent quantities with Laser-Doppler technique show significant differences from the earlier hotwire measurements. The difference can be explained with the occurrence of reverse flow resulting in too low values for these components in the hot-wire measurements (Schneider & Goldstein 1994; Eriksson et al. 1998). However, in comparison with the data presented by Eriksson et al. (1998) at Re = 9000, the positions of the inner maxima of u^+ and k^+ agree well, whereas the levels of the turbulent fluctuations are lower due to the lower Reynolds number. The profiles of the Reynolds shear stress collapse very well in inner scaling but the inner negative peak occurs closer to the wall than in the measurements by Eriksson et al. (1998).

As can be seen in the animations, the transition starts in the shear-layer region. This process is further studied by looking at the initial development of the fluctuation v^+ as shown in figure 14. Here we have used inner scaling to draw the attention to the inner layer. However, the vertical lines indicate the

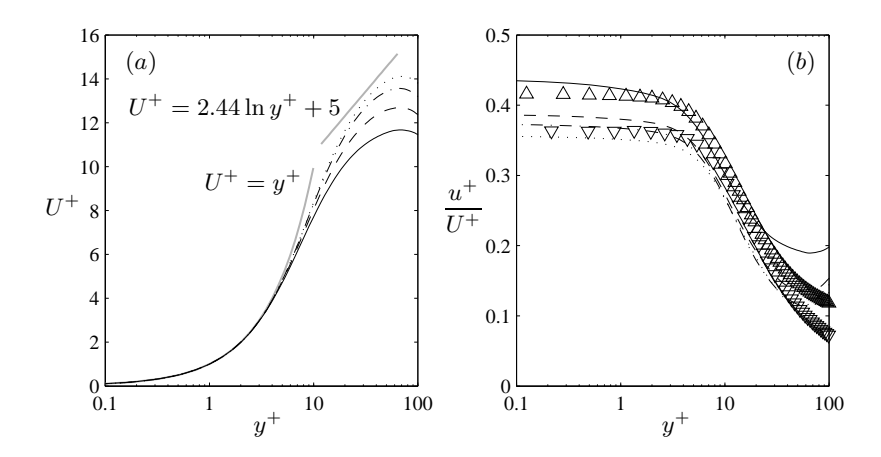


FIGURE 12. Near-wall behaviour of (a) streamwise mean velocity and (b) u^+/U^+ . Data from Kim *et al.* (1987) (∇) and Del Alamo *et al.* (2004) (\triangle) . Lines as in figure 9.

location of the half-width. A peak in the outer layer is clearly visible close to the transitional region at x/b=6, where the flow still is laminar. In the inner layer, the formation of a plateau can be seen. A new peak starts to develop out of this plateau as the flow proceeds downstream and undergoes transition. The two peaks in the inner and outer layer evolve into a new plateau for the normal stress as the turbulent mixing increases indicating that the process of merging of the inner and the outer layer is progressing (see figure 13). It is, however, less pronounced in the DNS data than in the measurements by Eriksson et al. (1998) performed at the higher Reynolds number. The plateau diminishes as the flow propagates downstream. Eriksson et al. (1998) also observed that the plateau decays in the far field.

4. Conclusions

The first direct numerical simulation that is sufficiently large to study the self-similar behaviour of a turbulent wall jet is carried out. The Blasius wall jet and its early turbulent evolution are studied at Re=3090. Two-dimensional waves and streamwise elongated streaks are introduced in the flow to trigger a natural transition mechanism. The disturbance forcing, which is matched to experimental conditions, is the same as in the previous study by Levin et al. (2005), but a four times larger computational box enables to study not only the transitional region but the early turbulent evolution. The present simulation provides detailed visualizations of the flow structures and statistics of mean flow and turbulent stresses.

In order to visualize the whole wall jet from its laminar part where the waves and streaks grow, the transition region and its downstream turbulent part, three animations are made available. They show the propagation of

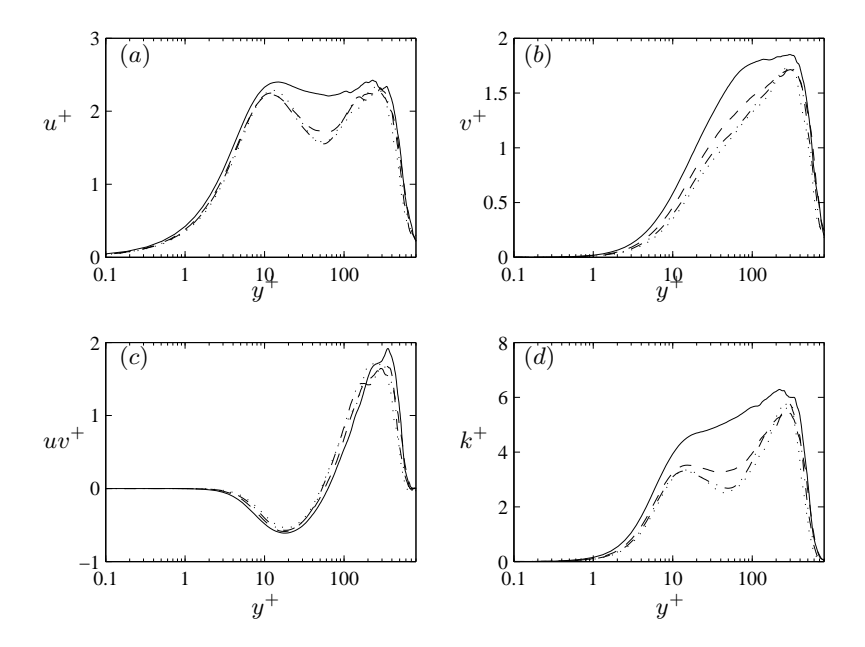


FIGURE 13. Profiles of (a) rms of u', (b) rms of v', (c) Reynolds shear stress and (d) turbulence kinetic energy. Lines as in figure 9.

spanwise modified roll-ups in the outer shear layer and in the inner shear layer. Small regions of separated flow are associated with the boundary-layer rollers. A weak subharmonic wave is present in the transition region. The breakdown to turbulence appears first in the shear-layer region where the low-velocity streak exists. In the turbulent flow downstream of the rapid breakdown, the influence of the streaks can be seen to remain for some distance. About two nozzle heights downstream of the breakdown position in the outer shear layer, the inner shear layer undergoes transition. Streaky structures typical for turbulent boundary layers are born in the near-wall region of the turbulent wall jet. A fourth animation shows the development of vortical structures in the region of transition. It shows that transition appears in the mushroom-shaped structures that are associated with vortex ribs that are ejected from the wall jet into the ambient flow.

The averaged data is presented in both inner and outer scaling in order to identify self-similar behaviour. Applying the traditional outer scaling with the maximum velocity of the wall jet and the jet half-width, the profiles of the mean streamwise velocity collapse reasonably well between x/b=17 and 26 up to the half-width of the jet. Components of the Reynolds stress agree reasonably well between x/b=23 and 26 up to the same wall-normal position. Downstream of x/b=26, a large vortex in the ambient flow exists due to the limited numerical region. Such an external flow arises for all wall jets, even

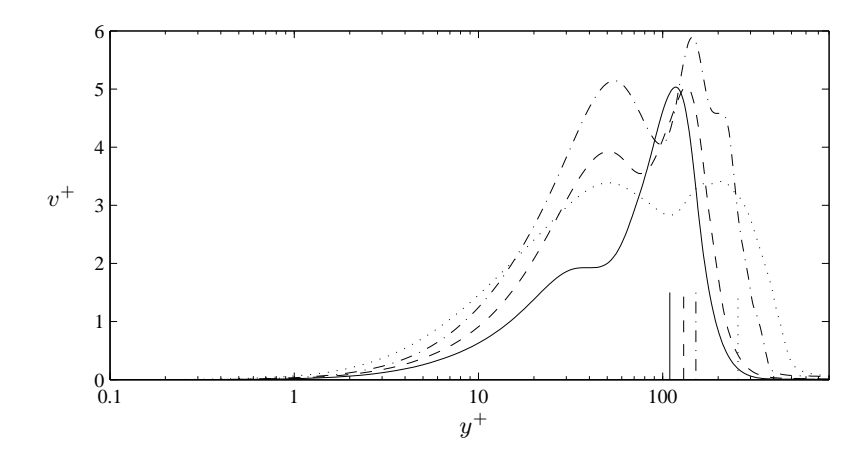


FIGURE 14. Profiles of rms of v' close to transition at x/b=6 (solid line), 8 (dashed line), 10 (dashed-dotted line) and 13 (dotted line). The vertical lines indicate the location of the half-width.

in experimental set-ups. However, the strength of the vortex decreases as the region it is allowed to occupy increases. The wall-normal velocity is effected by this vortex in a higher degree than the streamwise velocity, the self-similar behaviour is only obtained between x/b=20 and 23. The turbulent quantities scaled with outer variables are higher in the transitional region than in the self-similar region. Dejoan & Leschziner (2005) found the same tendency in their LES study, but Eriksson *et al.* (1998) measured the opposite trend for the streamwise Reynolds stress in outer scaling.

Within the viscous sublayer, the profiles follow a linear law $U^+ = y^+$ up to about $y^+ = 4$. The profiles start to deviate from the linear behaviour, earlier than for a turbulent boundary layer that typically starts to deviate for values $y^+ \geq 8$ agreeing well with the behaviour found by Eriksson $et\ al.\ (1998)$ at Re = 9000. The ratio between the rms of the fluctuating streamwise velocity and the mean streamwise velocity is found to be constant in the viscous sublayer up to about $y^+ = 3$ and the value for turbulent boundary-layer and channel flows found by Alfredsson $et\ al.\ (1988)$ seems to approximately hold even for the turbulent wall jet. The profiles of the turbulent stresses collapse well for the streamwise positions x/b = 20 to 26 indicating that the flow has started to exhibit a self-similar behaviour in the near wall region.

It can be noted that the collapse provided with inner scaling is much better than with outer scaling. Despite the low Reynolds number and the short computational domain, in comparison to available experiments, the turbulent flow exhibits a reasonable self-similar behaviour, which is most pronounced with inner scaling in the near-wall region. Despite the large computational cost, the present simulation is still too small to study a fully developed turbulent wall jet. The early turbulent state in the present simulation is governed by the upstream imposed streaks. It is, however, left for future work to study the fully developed turbulent wall jet in larger computational domains and for higher Reynolds numbers.

This work was funded by the Swedish Energy Agency (Energimyndigheten). The direct numerical simulation was performed at the Center for Parallel Computers at KTH. Many thanks to Stefan Wallin for valuable discussions about the turbulent statistics.

References

- ABRAHAMSSON, H., JOHANSSON, B. & LÖFDAHL, L. 1994 A turbulent plane two-dimensional wall-jet in a quiescent surrounding. Eur. J. Mech. B/Fluids 13 (5), 533–556.
- Alfredsson, P. H., Johansson, A. V., Haritonidis, J. H. & Eckelmann, H. 1988 The fluctuating wall-shear stress and the velocity field in the viscous sublayer. *Phys. Fluids* **31** (5), 1026–1033.
- Dejoan, A. & Leschziner, M. A. 2005 Large eddy simulation of a plane turbulent wall jet. *Phys. Fluids* 17, 025102.
- Del Alamo, J., Jimenez, J., Zadonade, P. & Moser, R. 2004 Scaling of the energy spectra in turbulent channels. *J. Fluid Mech.* **500**, 135–144.
- ERIKSSON, J. G., KARLSSON, R. I. & PERSSON, J. 1998 An experimental study of a two-dimensional plane turbulent wall-jet. *Exps. Fluids* **25**, 50–60.
- FÖRTHMANN, E. 1934 Über turbulente Strahlausbreitung. Ing. Arch. 5, 42-54.
- George, W. K. 2000 A similarity theory for the turbulent plane wall jet without external stream. J. Fluid Mech. 425, 367–411.
- Jeong, J., Hussain, F., Schoppa, W. & Kim, J. 1997 Coherent structures near the wall in a turbulent channel flow. *J. Fluid Mech.* **332**, 185–214.
- Kim, J., Moin, P. & Moser, R. 1987 Turbulence statistics in fully developed channel flow at low Reynolds number. *J. Fluid Mech.* **177**, 133–166.
- Lasheras, J. C. & Choi, H. 1988 Three-dimensional instability of a plane free shear layer: an experimental study of the formation and evolution of streamwise vortices. *J. Fluid Mech.* **189**, 53–86.
- Launder, B. E. & Rodi, W. 1981 The turbulent wall jet. *Prog. Aerospace Sci.* 19, 81–128.
- LEVIN, O., CHERNORAY, V. G., LÖFDAHL, L. & HENNINGSON, D. S. 2005 A study of the Blasius wall jet. J. Fluid Mech. 539, 313–347.
- Lundbladh, A., Berlin, S., Skote, M., Hildings, C., Choi, J., Kim, J. & Henningson, D. S. 1999 An efficient spectral method for simulation of incompressible flow over a flat plate. *Tech. Rep.*. KTH, Department of Mechanics, Stockholm, Sweden.
- NARASIMHA, R., NARAYAN, K. Y. & PARTHASARATHY, S. P. 1973 Parametric analysis of turbulent wall jets in still air. *Aeronaut. J.* 77, 335–359.

- NORDSTRÖM, J., NORDIN, N. & HENNINGSON, D. S. 1999 The fringe region technique and the Fourier method used in the direct numerical simulation of spatially evolving viscous flows. SIAM J. Sci. Comput. 20 (4), 1365–1393.
- Schneider, M. & Goldstein, R. 1994 Laser Doppler measurement of tubulence parameters in a two-dimensional plane wall jet. *Phys. Fluids* **6** (9), 3116–3129.
- VISBAL, M. R., GAITONDE, D. V. & GOGINENI, S. P. 1998 Direct numerical simulation of a forced transitional plane wall jet. AIAA Paper 98-2643.
- Wernz, S. & Fasel, H. F. 1996 Numerical investigation of unsteady phenomena in wall jets. $AIAA\ Paper\ 96\text{-}0079.$
- Wernz, S. & Fasel, H. F. 1997 Numerical investigation of forced transitional wall jets. $AIAA\ Paper\ 97\text{-}2022.$
- Wygnanski, I., Katz, Y. & Horev, E. 1992 On the applicability of various scaling laws to the turbulent wall-jet. *J. Fluid Mech.* **234**, 669–690.